From the Faculty of Medicine

at Heinrich Heine University Düsseldorf

Impact of data processing parameters on whole-brain dynamical models

Dissertation

to obtain the academic title of Doctor of Philosophy (Ph.D.) in Medical Sciences

from the Faculty of Medicine at Heinrich Heine University Düsseldorf

submitted by

Kyesam Jung

(2023)

As an inaugural dissertation printed by permission of the

Faculty of Medicine at Heinrich Heine University Düsseldorf

signed:

Dean:

Examiner/s:

“Nicht die Stärke,

sondern die Dauer der hohen Empfindung macht die hohen Menschen.”

- Friedrich Wilhelm Nietzsche

Parts of this work have been published:

Jung, K., Eickhoff, S. B., Popovych, O. V., (2021), Tractography density affects whole-brain structural architecture and resting-state dynamical modeling. Neuroimage, 237: 118176.

Popovych, O. V., Jung, K., Manos, T., Diaz-Pier, S., Hoffstaedter, F., Schreiber, J., Yeo, B. T. T., Eickhoff, S. B., (2021), Inter-subject and inter-parcellation variability of resting-state whole-brain dynamical modeling. Neuroimage, 236: 118201.

Jung, K., Florin, E., Patil, K. R., Caspers, J., Rubbert, C., Eickhoff, S. B., Popovych, O. V., (2022), Whole-brain dynamical modelling for classification of Parkinson's disease. Brain Communications, 5(1): fcac331.

Zusammenfassung

Die Magnetresonanztomographie (MRT) in den Neurowissenschaften ist eine der leistungsfähigsten nicht-invasiven Methoden zur Messung des menschlichen Gehirns. In Neuroimaging-Studien wird die MRT eingesetzt, um strukturelle und funktionelle Eigenschaften des Gehirns zu erfassen. In den computergestützten Neurowissenschaften werden bei der Ganzhirnmodellierung MRT-Daten als Grundlage verwendet, so dass Forscher die simulierte Ganzhirndynamik *in silico* untersuchen können, indem sie die freien Parameter von Ganzhirnmodellen erforschen. Allerdings gibt es für die MRT-Datenverarbeitung keine standardisierte Methode, da es keine Referenzdaten des menschlichen Gehirns gibt. Die Verwendung unterschiedlicher Softwares und Datenverarbeitungsparameter kann daher zu widersprüchlichen Ergebnissen und unterschiedlichen Schlussfolgerungen in verschiedenen Studien führen. Außerdem sind die Auswirkungen der Datenverarbeitung auf Ganzhirnmodelle noch nicht eindeutig geklärt. Daher habe ich drei Studien durchgeführt, die variierende Ansätze zur MRT-Datenverarbeitung für die Modellierung des gesamten Gehirns berücksichtigen und die Auswirkungen der Datenverarbeitungsparameter auf die Ganzhirnmodelle untersuchen. In Studie 1 wurden verschiedene Datenverarbeitungen verwendet, um das strukturelle Konnektom zu berechnen, das die Ganzhirnmodelle beeinflussen kann. In der Folge führten beeinflussten diese unterschiedlichen Ganzhirnmodelle die Simulationsergebnissen stark, und die Probanden wurden auf der Grundlage empirischer und simulierter Daten geschichtet. In Studie 2 wurden verschiedene Parzellierungsschemata des Gehirns für die Datenverarbeitung verwendet. Empirische und simulierte Ergebnisse aus verschiedenen Parzellierungsschemata zeigten interindividuelle Variabilität anhand von Datenvariablen. Vor diesem Hintergrund wurde in Studie 3 eine variierende funktionelle Datenverarbeitung für die dynamische Modellierung des gesamten Gehirns verwendet. Die empirischen und simulierten Ergebnisse unter verschiedenen Bedingungen wurden zur Klassifizierung von Parkinson-Patienten und gesunden Probanden verwendet. Dabei wurde die Klassifizierungsleistung durch die Bedingungen der funktionellen Datenverarbeitung beeinflusst. Außerdem verbesserte die Ganzhirnmodellierung die Leistung, wenn die empirischen Daten um die Simulationsergebnisse ergänzt wurden. Aus diesen Studien geht hervor, dass sich unterschiedliche Parameter der MRT-Datenverarbeitung nicht nur auf die empirischen Daten auswirken, sondern auch zu unterschiedlichen Simulationsergebnissen bei der dynamischen Modellierung des gesamten Gehirns führen.

Summary

Magnetic resonance imaging (MRI) in neuroscience is one of the most powerful non-invasive methods to measure the human brain. Neuroimaging studies have been using MRI to extract structural and functional properties from the brain. In computational neuroscience, whole-brain modeling employs MRI data as a backbone and allows researchers to scrutinize simulated whole-brain dynamics *in silico* by exploring free parameters of whole-brain models. However, MRI data processing has no standardized method because of the lack of ground truth of the human brain. Thus, using different softwares and data processing parameters can induce inconsistent results and lead to different conclusions across studies. Besides, the impact of data processing on whole-brain models has not been clearly understood. Therefore, I performed three studies considering conditions of MRI data processing for whole-brain modeling and investigated the impact of data processing parameters on whole-brain models. In study 1, varied data processing was used to calculate the structural connectome, which can directly influence whole-brain models. Subsequently, these different whole-brain models strongly influenced simulated results and the subjects were stratified based on empirical and simulated data. In study 2, different brain parcellation schemes were used for data processing. Empirical and simulated results from different parcellation schemes showed inter-individual variability via data variables. In these respects, in study 3, varied functional data processing was used for whole-brain dynamical modeling. Afterwards, the empirical and simulated results with different conditions were used for the classification of patients with Parkinson's disease against healthy subjects. The classification performance was affected by the functional data processing conditions. Furthermore, whole-brain modeling improved the performance when the empirical data are complemented by the simulation results. From these studies in the thesis, varying MRI data processing parameters does not only impact empirical data but also leads to different simulation results in whole-brain dynamical modeling and its application.

List of abbreviations

BOLD blood oxygenation-level dependent

DWI diffusion-weighted image

ECoG electrocorticography

EPI echo-planar image

FC functional connectivity

GoF goodness-of-fit

MRI magnetic resonance imaging

SC structural connectivity

T1w T1-weighted image

TVB The Virtual Brain

WBT whole-brain tractography

Table of contents

1 Introduction

Thousands of neuroimaging studies have been using magnetic resonance imaging (MRI) data for the human brain research because it provides *in vivo* (within the living) large-scale (in millimeters) structural and functional whole-brain information. MRI employs several protocols to measure brains and obtains different attributes, such as T1-weighted image (T1w) for brain anatomy (Destrieux et al., 2010; Fischl et al., 2002; Fischl et al., 2004), diffusion-weighted image (DWI) for movement of water molecules in the brain (Mori and Zhang, 2006), and echo-planar image (EPI) for blood oxygenation-level dependent (BOLD) signals (Ogawa et al., 1992; Stehling et al., 1991). Structural MRI, such as T1w, scans static brains and can be used to calculate areas or volumes of brain regions. Functional MRI records the changes of image intensities in pixels (in 2 dimensions) or voxels (in 3 dimensions) across sequential measures (through time) which represents brain dynamics, such as changes of brain activity that responses to the circumstances and causes cognitive functions and behavior. Brain activity represents responses of neurons in the brain. Changes of neural responses through time evoke variations of oxygenation of hemoglobin in red blood cells and, subsequently, it results in fluctuations of BOLD responses (Buxton et al., 2004; Logothetis et al., 2001). With these structural and functional MRI data, researchers who are interested in the brain and related topics, such as neuroscience, cognitive science, psychology, neurology, and psychiatry, have investigated the human brain and delineated relationships with human behavior or clinical symptoms.

Most raw MRI data, firstly measured through an aperture (an MRI scanner), is not directly applicable for further analysis but needs additional calculations to have a result that researchers can use for their work, for example, diffusion tensor imaging for microstructural features of the brain (Le Bihan et al., 2001), perfusion-weighted imaging for dynamics of cerebral blood flow in stroke patients (Lee et al., 2020; Neumann-Haefelin et al., 1999; Schlaug et al., 1999), functional MRI for task-driven activities of the brain (Knutson et al., 2000). Here, calculation of MRI data for further analysis is termed “data processing” in this dissertation. In other words, data processing utilizes MRI data for brain research or clinical application. Depending on research questions, raw MRI data are processed by long-take data processing procedure consists of serial calculations. A serial data processing is called “pipeline”, where the output of one data processing is the input of the next one. A pipeline can have tens of data processing steps (Fig. 1), and these steps can be rearranged based on various purposes. However, we cannot concatenate or switch data processing steps in any orders because pipelines should keep “data fidelity”. Data fidelity is the proportion of information in processed data against the information

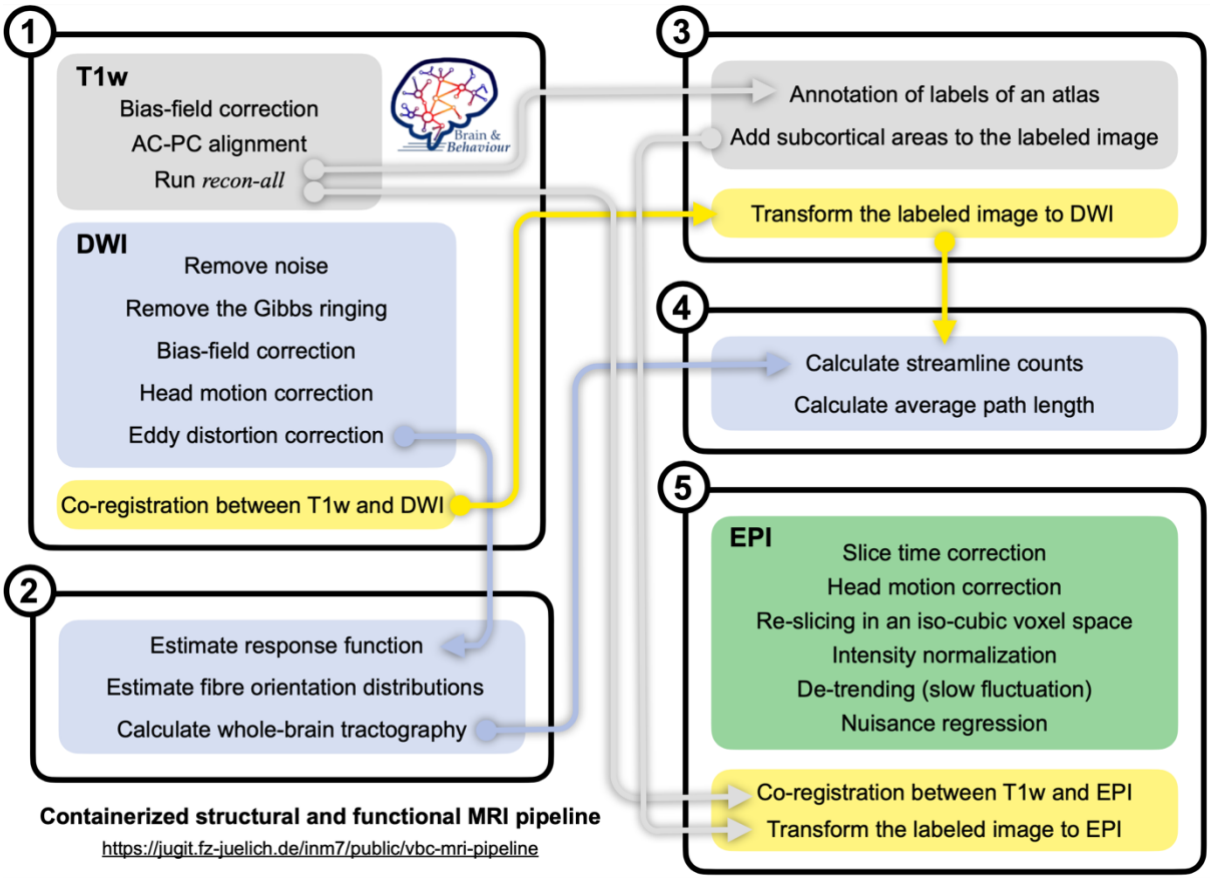

Figure 1 Workflow of an MRI pipeline for whole-brain connectome. **(1)** Preprocessing of structural T1w and DWI. **(2)** Calculation of whole-brain tractography using DWI. **(3)** Atlas labeling and transformation to DWI space. **(4)** Reconstruction of structural connectome. **(5)** Preprocessing of functional EPI. Abbreviations: AC-PC = anterior-posterior commissures; DWI = diffusion-weighted image; EPI = echo-planar image; T1w = T1-weighted image.

of directly measured data, *i.e.*, "ground truth", see the reference for an example of data fidelity in image processing (Gupta et al., 2021). For instance, if randomly generated noise is added to MRI data, its data fidelity will drop after adding the noise. Although maintaining data fidelity during MRI data processing is important for investigation, it has not been rigorously scrutinized in neuroimaging studies because obtaining ground truth from *in vivo* human brains is difficult. If the ground truth is available, MRI data processing or a pipeline can be validated based on whether the data processing brings out the information from the raw data. In other words, the validation is to evaluate data processing through agreement between directly measured data (ground truth) and processed data as to whether the data processing is applicable for further analysis (Fischl et al., 2002; Lee et al., 2020; Niedworok et al., 2016). With this respect, data fidelity can be estimated via calculating similarity, such as Pearson correlation coefficient or Dice coefficient, between ground truth and processed data. So, a validated data processing or pipeline can be expected to process data in maintaining data fidelity. Consequently, researchers can evidently interpret the results of brain MRI data processed by the validated pipeline or data

processing. The issue of validation should be considered in popular MRI processing such as a robust preprocessing pipeline for functional MRI (Esteban et al., 2019), voxel-based morphometry (Ashburner and Friston, 2000), statistical parametric mapping (Penny et al., 2011), human connectome (Sporns, 2011; Sporns et al., 2005), and whole-brain connectivity networks (Park and Friston, 2013).

1.1 Difficulty in validation of MRI data processing

One of the main issues of brain MRI data processing is that it has not been standardized upon a consensus among neuroimaging studies (Lindquist, 2020; Maier-Hein et al., 2017; Parkes et al., 2018). The lack of consensus causes that MRI data processed by different pipelines from separate studies can be different from each other (Botvinik-Nezer et al., 2020; Schilling et al., 2021). Subsequently, the different results performed by different pipelines using the same MRI data can impact data fidelity. To resolve this discrepancy, we can compare between ground truth and processed data and choose one that shows the highest agreement among data processing conditions (Maffei et al., 2022; Schilling et al., 2019). As mentioned, obtaining ground truth in brain MRI studies is difficult, nevertheless a few neuroimaging studies designed experiments to obtain ground truth for validation. Here are two validation examples of brain MRI studies using ground truth: the association of evoked neural responses to BOLD responses (neurovascular coupling) from *in vivo* animal studies (Bernal-Casas et al., 2017; Logothetis et al., 2001) and comparing anatomical (axonal) connectivity in white matter from post-mortem *ex vivo* brains with reconstructed streamlines connecting brain regions (Jones et al., 2021; Maffei et al., 2022; Yendiki et al., 2022). Even though the validation using ground truth has limitation in *in vivo* human brain, there are possible ways to obtain ground truth. For example, there is a direct way to measure electrical neural responses in the human brain *in vivo*, but only for severe clinical cases that need brain surgical operations such as electrocorticography (ECoG) for patients with epilepsy (Kuruvilla and Flink, 2003). However, the validation approach using ground truth in doing likewise is difficult to be generally applied to healthy participants or non-clinical cases.

1.2 Unclear impact of data processing parameters

One aspect that should be considered is that processed data can differ when we use different parameter values for data processing. Especially neuroimaging data processing, such as the MRI data processing in Fig. 1, has many parameters besides some of them can be essential for validation of the data processing. Because of a chain of data processing, small changes of some

of the parameters in the pipeline can also gradually impact the empirical data and its validation. Moreover, the lack of standardized MRI data processing makes the impact of the parameters complicated (Lindquist, 2020). For instance, measured (empirical) BOLD responses can differ when the pipeline works with different parameters of data processing for functional MRI, such as different temporal filters (Baria et al., 2011; Wee et al., 2012) and denoising methods (Parkes et al., 2018). Even so, these studies addressed the impact of data processing conditions on results what the researchers are interested in, but there are still unclear issues about experimental conditions concerning the effect of different data processing parameter values on conclusions of brain research. Many neuroimaging studies have been using likewise different or non-standardized parameters for further analysis without considering the impact of data processing parameters. For example, whole-brain tractography (WBT) for structural connectome (Sporns et al., 2005) has used an arbitrary turning angle criterion for streamlines (Soares et al., 2013) and different numbers of streamlines from 10 thousand to 10 million (Bajada et al., 2019; Hagmann et al., 2008; Prasad et al., 2013; Proix et al., 2016). Furthermore, there are several software tools to process DWI data (Soares et al., 2013) and tracking algorithms to calculate streamlines (Yeh et al., 2021) although it is still under debate (Maffei et al., 2022). Therefore, brain research using MRI data needs a systematic investigation of the impact of parameters of MRI data processing.

1.3 Data-driven approach for generative models

The data-driven approach belongs to systematic ways to investigate the impact of data processing parameters on empirical data via considering the parameters as variables, and besides, we can formulate study designs with experimental parameter conditions, such as control (fixed) and manipulated (varied) variables. In this way, we can probe results driven by the parameter conditions and investigate the impact of the parameters on the processed data and further analysis. If we use some parameter values from our experiences or the literature, we cannot address how the data processing parameters impact the results. In the data-driven approach, on the contrary, we vary the parameters on purpose as variables (free parameters) covering applicable ranges and obtain the results corresponding to the varied parameters. For example, when a pipeline processes data with several evenly distributed parameter values, the processed data will be calculated separately for all tested parameter values. Subsequently, each processed data can be tested step-by-step, *i.e.*, each parameter value has a value of evaluation for comparison between the processed and empirical data. Thus, we can illustrate the trajectories of varied parameters versus tested results. With these evaluation values, the data-

driven approach searches for an optimal parameter value leading to the best evaluation (the highest similarity), see the reference for an example of the data-driven approach via varying parameter values (Lee et al., 2020).

In addition, the data-driven approach is applicable for hidden variables in a generative model that mimics empirical data. In other words, when we use generative models in the data-driven approach, it is easy to apply hidden variables which represent the neuroscientific or biological circumstances to manipulating free parameters rather than experimental studies. For example, the Balloon-Windkessel model (Buxton et al., 1998; Friston et al., 2003; Havlicek et al., 2015) simulates BOLD signals using neural responses. This model contains neurovascular coupling factors as the hidden variables, which are not directly measurable from *in vivo* human brain, *i.e.*, it is difficult to manipulate parameter values in experiments, such as cerebral blood flow, cerebral blood volume and deoxyhemoglobin content. This model generates the neurovascular coupling dynamics during the calculation of BOLD responses. When we apply the data-driven approach for these neurovascular coupling factors, *i.e.*, the hidden variables as free parameters, the simulated BOLD responses can also be used to search for the optimal parameter values of the model, leading to the simulated BOLD signals that show the highest similarity with the empirical BOLD signals. For instance, dynamic causal modeling (Friston et al., 2003) simulates task-related BOLD responses based on the task design during functional MRI acquisition and varies the hidden variables of the Balloon-Windkessel model to estimate the optimal parameter values to reach out the highest explained variance between simulated and empirical BOLD signals (Friston et al., 2003; Stephan et al., 2007).

After the data-driven approach for the Balloon-Windkessel model, the optimal parameters of the model can also be used for further analysis or data-driven approaches again. For instance, Havlicek et al. (2015) found optimal parameter values of the neurovascular coupling using dynamic causal modeling, and researchers who are interested in simulated BOLD signals can apply the optimal parameter values as constant in their simulation and introduce free parameters of other models for the data-driven approach (Havlicek and Uludag, 2020; Polimeni and Lewis, 2021). In doing likewise, Maffei et al. (2022) also reported that using an optimized pipeline for DWI preprocessing as a standardized data processing minimizes discrepancies of tracking results across different algorithms and improves performance in a challenge to reconstruct axonal bundles in white matter. With predefined optimal parameters, therefore, we can systematically extend simulation models and explore simulated results driven by free parameters of additional data processing or computational models.

Searching for optimal parameter values of a given model is to fit the model to the optimal one that simulates data showing the highest similarity with the empirical data, *i.e.*, model fitting. Owing to free parameters during the data-driven approach, model fitting can be systematically probed via using methodologically unlimited parameter variations. Besides, other empirical data can also be used for model fitting. For example, functional connectivity (FC), which is calculated by Pearson correlation coefficient of BOLD signals between two brain regions, can be used for model fitting (Deco et al., 2015; Honey et al., 2009; Naskar et al., 2021). To this end, we obtain empirical FC using empirical BOLD signals between brain regions in resting-state (task-free) functional MRI and calculate simulated FC using simulated BOLD signals with the same brain regions as for the empirical FC. Afterwards, we compare simulated FC with empirical FC in separate results by using varied parameter values of models that we are interested in. Consequently, we search for the optimal parameters of the models that result in the highest similarity between simulated FC and empirical FC.

1.4 Whole-brain dynamical modeling

In the data-driven approach, whole-brain *in vivo* neuroimaging research including human subjects is limited because it is not feasible to perform many conditions corresponding to the number of varied parameter conditions in experimental study. On the contrary, whole-brain *in silico* modeling (performing on computer or computer simulation that simulates brain activity based on the entire brain connectivity) is suitable for applying parameter variation for the data-driven approach (Popovych et al., 2019). Thus, whole-brain dynamical modeling based on model fitting using free parameters allows us to apply the systematic investigation for understanding the brain as a whole system. By doing so, we can scrutinize simulated results in various perspectives based on free parameters and different objectives for model fitting.

The advantage of building whole-brain *in silico* models is that it allows us to investigate the human brain as synthetic entities in experimental virtual intervention for clinical conditions that researchers are eager to see (An et al., 2022; Bansal et al., 2018; Owen et al., 2013). For instance, Owen et al. (2013) performed virtual corpus callosotomy on empirical structural networks of healthy subjects, *i.e.*, cutting (turning non-zero values into zeros) the corpus callosum to split connections between hemispheres in the structural networks *in silico*. Afterwards, they compared the simulated structural networks of the virtual corpus callosotomy with empirical structural networks of patients with agenesis of the corpus callosum. As a result, it showed that graph-theoretical network properties of the simulated structural networks of the healthy subjects shift toward the empirical structural networks of the patients.

In addition, we can also introduce whole-brain computational models that simulate activity of the entire brain and explore simulated data in various conditions. To this end, studies in computational neuroscience have used the empirical large-scale whole-brain structural connectome (axonal connections and path lengths in the white matter) that provides the brain architecture as a backbone of whole-brain computational models, and whole-brain computational models have been developed for simulation of the brain dynamics based on the broad spectrum of updating neural activity (Cabral et al., 2012; Honey et al., 2009; Jirsa et al., 2017; Moran et al., 2013; Roberts et al., 2019; Sanz-Leon et al., 2015; Zimmermann et al., 2018). Besides Buzsaki (2006) considered the brain activities of each region as harmonized signals. Similarly, we can apply mathematical models about coupled oscillators for whole-brain models (Breakspear et al., 2010; Kuramoto, 1984; Rodrigues et al., 2016). With various computational or mathematical models, we can investigate simulated brain dynamics in different perspectives. Furthermore, we can easily manipulate parameter values of the whole-brain models and find which parameters are important for a better understanding of the brain dynamics.

As an example, The Virtual Brain (TVB) for large-scale whole-brain dynamics (Sanz-Leon et al., 2015) is applicable to whole-brain computational modeling in the data-driven approach. TVB provides various models of coupled oscillators such as Kuramoto (Kuramoto, 1984), Hopf bifurcation (Kuznetsov et al., 1998), and Fitzhugh-Nagumo type (Fitzhugh, 1961; Nagumo et al., 1962) and neural activities such as Jansen-Rit (Jansen and Rit, 1995), Wilson-Cowan (Wilson and Cowan, 1972), Wong-Wang (Deco et al., 2013; Wong and Wang, 2006), and Larter-Breakspear (Breakspear et al., 2003). These computational or mathematical models in TVB can be built based on whole-brain architecture derived from the structural connectome, and whole-brain computational models can also be utilized for investigating the impact of different modeling approaches on simulated results. However, TVB reconstruction pipeline for MRI data has only a few options for data processing parameters. For instance, it provides three parcellation atlases, *i.e.*, Desikan-Killiany (Desikan et al., 2006), Destrieux (Destrieux et al., 2010), and parcellation for virtual epileptic patients (Jirsa et al., 2017), *cf.* recent studies of brain connectivity used around 20 parcellations (Domhof et al., 2021; Messe, 2020).

Regarding the impact of data processing parameters on whole-brain dynamical models, *i.e.*, the main question of this dissertation, study designs here should be formulated by systematic approaches for manipulating data processing parameters. As a consequence, I develop an MRI pipeline that has manipulable parameters (free parameters), which is available for the data-

driven approach. With this, I can vary data processing parameters of the pipeline. After that, I search for optimal parameters of the whole-brain computational models via model fitting and obtain simulated brain responses helping me to answer research questions. By doing this, I establish a systematic whole-brain dynamical modeling against empirical data, and the simulation results will provide a way of delineating the impact of data processing parameters on whole-brain modeling. From a futuristic perspective in computational neuroscience, the cumulation through iterations of the whole-brain dynamical modeling via the data-driven approach will allow us to contemplate a whole-brain system across scales in brain cartography (Frackowiak and Markram, 2015) from microscale (individual neurons or neuronal populations) to macroscale (brain parcels) that can compute behavioral or cognitive processes like the human brains (Kriegeskorte and Douglas, 2018).

1.5 Whole-brain simulation in computational neuroscience

Hodgkin and Huxley (1952) proposed simulation of membrane potentials in individual neurons. Since this, researchers in computational neuroscience have developed many simulation models to mimic empirical neural responses in the brain. However, the main impediment to building models is the enormous number of neurons and thousands of synaptic connections of each neuron. The human brain contains around 86 billion neurons on average (Herculano-Houzel, 2012). Accordingly, reconstruction of neuronal circuits using the entire neurons for such a whole-brain neuronal system is immense and complex processing. For instance, neocortical neuronal microcircuits of 31 thousand neurons (only 0.036 % of the entire human brain) required enormous resources (Markram et al., 2015). Despite the current technological advance, it is still impossible to reconstruct whole-brain system using the entire neurons in the human brain.

1.5.1 Scale reduction of whole-brain simulation to macroscale

In spite of the difficulty, an alternative way to straighten it out is to reduce the scale from microscale to mesoscale or even further to macroscale (Sporns et al., 2005). This approach requires the entire central nervous system in multi-scale and multi-level entities across spatial scales while spanning life called human cerebral cartography (Frackowiak and Markram, 2015). To scale the micro-level down to the meso-level, we need to show that a reduced model represents the functional properties of a group of neurons. For instance, electrophysiological research of the sensory cortex in animal studies confirmed the column-columnar organization representing a receptive field, such as the orientation selectivity to visual stimuli via interacting

among tens of neurons (Hubel and Wiesel, 1962) as a group of neurons in a columnar formation (Mountcastle, 1997). In other words, the column-columnar organization model allows us to reduce nearly 100 neurons into a single minicolumn for each receptive field (see Minicolumn in Mesoscale in Fig. 2). The scale reduction regarding minicolumns was already mentioned more than 15 years ago (Sporns et al., 2005). However, the human brain still has sub-billion minicolumns, and the current technology has not reached that computational power. Therefore, by integrating the functional representations of minicolumns, we can further reduce them into a group of minicolumns, called neural groups or populations in the cortex (see Neural population in Mesoscale in Fig. 2), that also represent a collection of receptive fields such as a pinwheel structure of visual orientations in striate cortex of cat (Maldonado et al., 1997) and a center-surround modulation for facilitation and suppression via interacting among cortical columns in primary visual cortex of cat and monkey (Series et al., 2003). Following this scale reduction (Fig. 2), we can further scale them down to the level of computationally or technically manageable scales in animal studies, for instance, whole-brain neural activity in a single-cell level measured by the light-sheet microscopy (Keller and Ahrens, 2015), a reduced model for a barrel cortical column of mice (Jung et al., 2019), and a brain-wide modeling using calcium imaging (Rosch et al., 2018).

For the *in vivo* human brain, it needs further scaling down to the MRI spatial resolution on a millimeter-scale, *i.e.*, the macroscale (or large-scale). In the literature, it is stated that slightly less than 150 thousand neurons in a cortical column distribute beneath one squared millimeter cortical surface area (Herculano-Houzel, 2012), see also Neocortex in Mesoscale (Fig. 2). When we assume that the hundreds of thousand neurons play a role as a functional unit in a columnar formation (a form of neural columns) in the cerebral cortex, we can reconstruct the cortical surface with these cortical functional units. For instance, Spiegler et al. (2016) rendered the cortical surface of each hemisphere from T1w data and created 8,192 vertices on a mesh of cortical surface in each hemisphere. They also included 116 nodes for subcortical areas. Subsequently, they reconstructed a surface-based whole-brain model, following that each vertex plays as a neural mass model connected with other vertices (Spiegler and Jirsa, 2013). Thus, the total number of simulation nodes in the surface-based whole-brain model was 16,500. However, they executed the whole-brain model for only one second with 40 microseconds for time integration because the model had many simulation nodes. Although this approach scales down around 52 million times to the macroscale and assumes drastic scale reduction regarding cortical columns as functional units, it still needs more computational power. To obtain simulated whole-brain dynamics in appropriate time lengths, therefore, it is inevitable to build

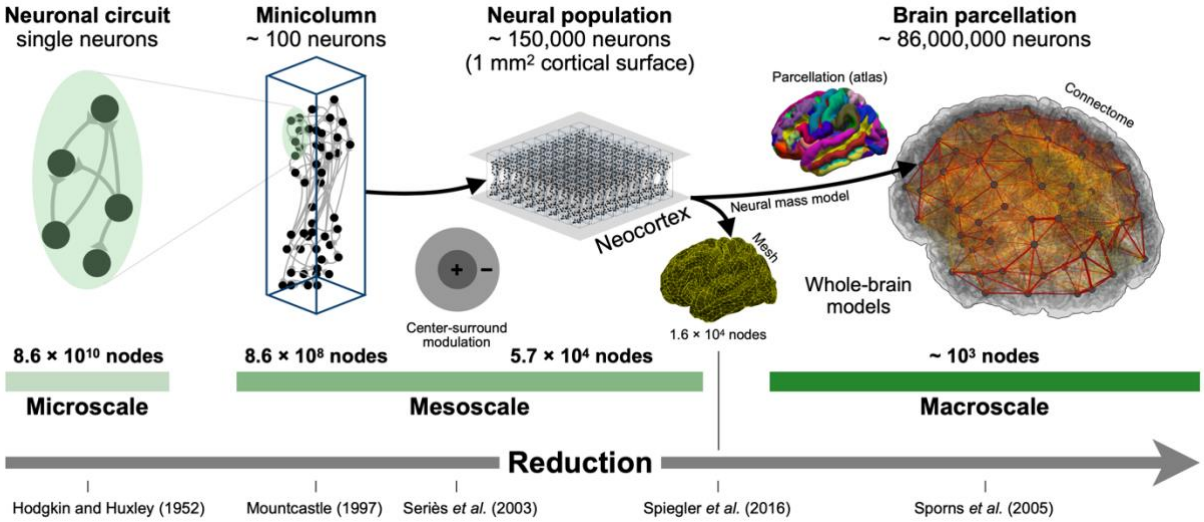

Figure 2 Schematic illustration of scale reduction for simulation models in computational neuroscience from the microscale to the macroscale. The numbers of nodes in the middle indicate the number of simulation units that shows how it strongly reduces from the entire neurons in the human brain.

a large-scale (macroscale with sub-thousand nodes) whole-brain model representing the human brain.

1.5.2 Large-scale human connectome for whole-brain modeling

Almost two decades ago, Sporns et al. (2005) introduced the human "connectome" to understand brains as a large-scale network consisting of interconnected brain regions that cover the entire human brain (see Macroscale in Fig. 2). To reconstruct the human connectome, we define brain regions with a certain criterion. For instance, brain parcellation schemes or brain atlases provide a way to split neocortical surfaces into tens or hundreds of parcels (Eickhoff et al., 2018). Various parcellation schemes have been developed for brain research based on functional properties (Schaefer et al., 2018; Shen et al., 2013), structural shapes (Desikan et al., 2006; Destrieux et al., 2010), and cytoarchitectonic variations (Amunts et al., 2020; Brodmann, 1909; von Economo and Koskinas, 1925). With this, we can split the brain into separate regions as network nodes and estimate connectivity or coupling strength between the brain regions as network edges. There are several ways to calculate whole-brain connectivity with different points of view (Park and Friston, 2013), *i.e.*, structural and functional connections. For the structural connectome, the pipeline in Fig. 1 processes T1w and DWI data in modules 1 to 4 and calculates WBT containing streamlines that delineate anatomical connections through white matter of the brain, *i.e.*, axonal bundles. Subsequently, streamlines connecting brain regions were extracted by using a given parcellation scheme, and we obtain the number of streamlines for all pairs of brain regions from the entire brain and averaged path lengths of them, *i.e.*, structural connectivity (SC). For the functional connectome, the pipeline in Fig. 1 processes

T1w and EPI data in modules 1, 3, and 5. After that, we can extract BOLD signals from the processed EPI data using the given parcellation scheme, which is the same as in the processing of SC. Then, we can calculate FC using the BOLD signals. More precisely, we apply the Pearson correlation coefficient to cross-correlate the given BOLD signals. Now the human connectome, *i.e.*, the whole-brain SC and FC, covers a computationally applicable scale (a large-scale) for dynamical modeling with hundreds of nodes. Thus, many simulation studies of the human brain have used the large-scale (or macroscale) whole-brain connectome for model validation such as the comparison between empirical FC and simulated FC (Deco et al., 2015; Honey et al., 2009; Naskar et al., 2021).

1.5.3 Data processing influences the human connectome

As aforementioned, in the whole-brain simulation, SC (streamline counts and averaged path lengths) provides a backbone of the whole-brain model that describes how strongly brain regions are coupled (interacting) with delays via streamline counts (coupling strengths) and averaged path lengths (delays). Although the estimated streamlines have around 30% of the false positive and false negative connections in the monkey brain (Girard et al., 2020), this is the method by which we can extract the large-scale structural connectome from the human brain. Recently, MRI processing pipelines and tracking algorithms have been systematically tested across around ten research teams, and the best performance showed 80% of true positive rate with only 5% false positive rate (Maffei et al., 2022). In addition, the averaged path lengths between brain regions allow us to apply delayed coupling (or neural signal propagation speed) to the whole-brain model based on the results of neurophysiological measures in the literature (Caminiti et al., 2013). Hence, varying data processing parameters in the SC pipeline (module 1 to 4 in Fig. 1) results in different SC and subsequently changes the backbone of the whole-brain model. Consequently, simulated whole-brain dynamics will be affected. From the perspective of the data-driven approach, varying data processing parameters in the SC pipeline impacts the simulated results and also allows us to investigate the impact of data processing parameters on whole-brain dynamical modeling.

The FC pipeline can also be tested via doing likewise. Sporns (2011) pointed that FC can also be critically affected by the choice of data or signal processing (Baria et al., 2011; Parkes et al., 2018; Wee et al., 2012). Thus, empirical FC and simulated FC represent dynamics of brain activity differently when we use different statistical or data processing methods for BOLD and FC calculation. Accordingly, we can also vary data processing parameters in the FC pipeline (modules 1, 3, and 5 in Fig. 1) for the data-driven approach. Therefore, by manipulating data

processing parameters in the SC and FC pipelines, we can explore whole-brain dynamical models and also search for the optimal conditions and parameter values corresponding to the highest agreement between empirical data and simulated results for model fitting.

In addition to the data processing parameters in the SC and FC pipelines, a brain parcellation scheme can also impact the results of both pipelines because SC and FC are calculated by using a region-based analysis. In other words, the large-scale whole-brain connectome of the human brain can show different results when we use different parcellation schemes (Domhof et al., 2021; Messe, 2020). Besides, as the aforementioned analysis for the human connectome, there are various parcellation schemes (functional, structural, and cytoarchitectural) to split cortical surfaces of the human brain into various levels of granularity, *i.e.*, how small brain regions are (Eickhoff et al., 2018). Parcellation schemes as different scale-reduction perspectives for large-scale whole-brain connectome can also be study- or data-dependent approaches that reflect a given condition of study design or data modality. Therefore, one of the challenges in human connectome research is also to select an appropriate parcellation scheme for whole-brain dynamical modeling.

1.6 Ethics protocols

The ethics protocols were approved by the Ethics Committee of Heinrich Heine University Düsseldorf (Study number: 4039 and 2018-317_1-RetroDEuA).

1.7 Aims of thesis

Currently, the lack of a consensus or standardized MRI processing and the unknown impacts of data processing parameters on the empirical whole-brain connectome are limiting factors in neuroimaging study. Due to this, the impact of MRI data processing parameters on whole-brain dynamical modeling should be tested by systematic approaches. The current thesis, therefore, hypothesizes that varying MRI data processing parameter values impacts whole-brain dynamical modeling. To this end, I formulate three research questions for the thesis focusing on the consequences of data processing parameters on empirical data and simulated results for whole-brain dynamical modeling. First, how does structural MRI data processing impact empirical structural architecture and whole-brain dynamical modeling? With this question, I investigate the impact of structural data processing parameters on whole-brain dynamical modeling and establish a structural pipeline for SC as a backbone of whole-brain models. Second, how do parcellation schemes influence empirical and simulated data variables? This

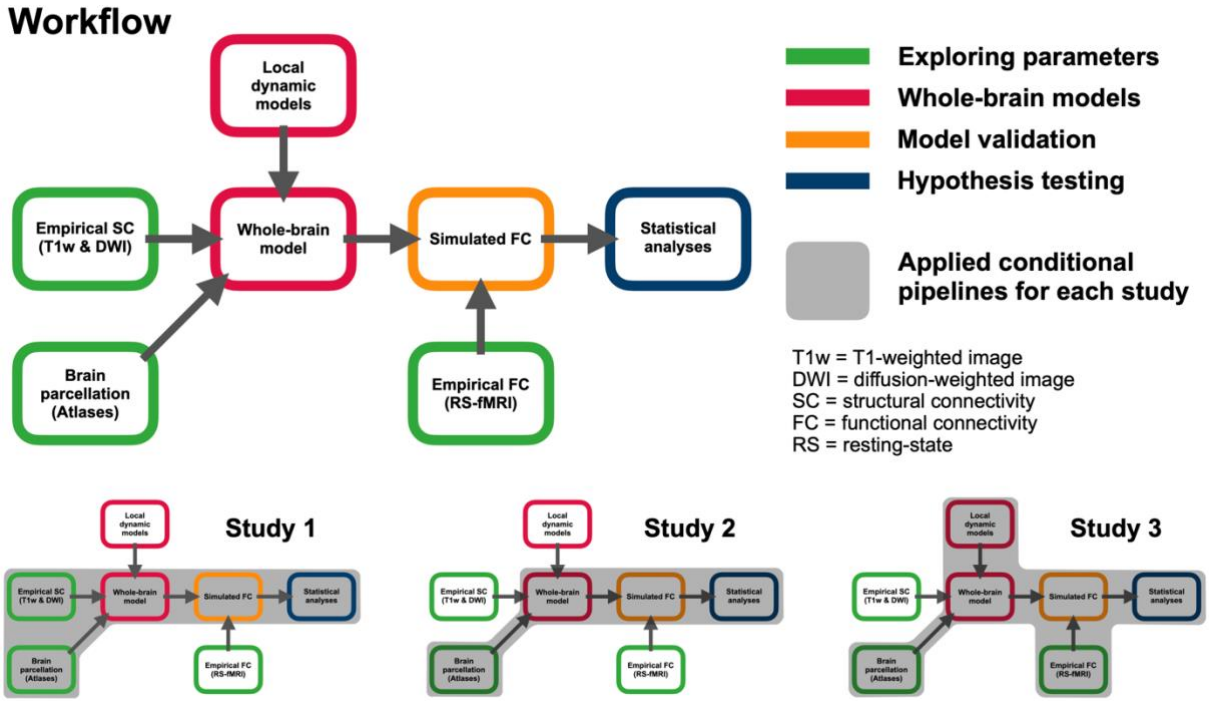

Figure 3 Illustration of workflow in the current project. The shaded workflows indicate the data processing for each study. Data processing parameters are varied in the green boxes. The red boxes are about whole-brain models for simulation. The orange boxes are about model validation. Afterwards, statistical analyses (blue boxes) are performed for hypothesis testing of each study.

question is to scrutinize the impact of parcellation schemes with varied granularity on simulated results focusing on personalized whole-brain models. Third, which functional data processing is optimal for clinical application based on whole-brain model fitting? For the third question, finally, I apply the developed MRI pipeline (Fig. 1) and whole-brain dynamical modeling to clinical data and investigate clinical applications based on whole-brain model fitting with different functional data processing conditions.

The workflow in Fig. 3 illustrates experimental designs of how data processing steps proceed with the considered research questions regarding variations of data processing parameters. The green boxes indicate data processing steps of experimental conditions for the empirical whole-brain connectome. The red boxes are about whole-brain models for simulated whole-brain dynamics. Afterwards, the model validation (orange box) compares simulated FC with empirical data and searches for the optimal model parameter corresponding to the maximal correspondence between simulated and empirical data. In the end of the hypothesis testing (blue box), I perform statistical analyses of results and address the impacts of data processing parameters on whole-brain dynamical modeling and their clinical applications.

1.7.1 Study 1: Impact of structural data processing on modeling

The first study is to investigate the impact of structural data processing parameters on SC and simulated results (see Study 1 in Fig. 3). As aforementioned, the reconstruction of WBT does not have optimal parameters in tracking algorithms, for instance, turning angles for streamline tracking or the number of streamlines of WBT. Furthermore, different numbers of streamlines have been used for WBT from 10 thousand to 10 million (Bajada et al., 2019; Hagmann et al., 2008; Prasad et al., 2013; Proix et al., 2016). Thus, I consider different WBT density conditions with two parcellation schemes, *i.e.*, functional and structural parcellation atlases. By doing so, the first study shows the impact of WBT densities on empirical structural architecture and corresponding whole-brain dynamical modeling for young and healthy participants.

1.7.2 Study 2: Impact of data processing of parcellation on modeling

The second study inquires how the parcellation schemes influence empirical and simulated data variables (see Study 2 in Fig. 3). The considered experimental conditions are about different granularities of brain parcellation and varied tissue thresholding criteria. To this end, the study contains two functional atlases with varied granularities (different numbers of parcels) and one structural atlas with varied tissue thresholding criteria (different sizes of the same parcel). In addition, two whole-brain models for all considered conditions are used for whole-brain dynamical modeling. In consequence, the second study shows that the parcellation schemes influence empirical and simulated results with inter-subject and inter-parcellation variability.

1.7.3 Study 3: Impact of functional data processing on modeling in clinical data

In the third study, I apply a convolution-based two-population model to generate electrical signals for local brain dynamics (Jansen and Rit, 1995; Lopes da Silva et al., 1974) and employ different temporal filtering conditions for empirical and simulated BOLD signals with two brain parcellation schemes, *i.e.*, structural and functional ones (see Study 3 in Fig. 3). In addition to the functional data processing conditions with the two parcellation schemes, I introduce a new model-fitting approach to detect group differences between healthy subjects and patients with Parkinson's disease. This approach can also provide a way of training machines to classify subjects into healthy control or the disease. To this end, I apply a machine learning method to train a classifier using empirical and simulated data for the patient classification. With the classification performance, I discuss the impact of signal processing (functional data processing) of BOLD signals on whole-brain dynamical modeling and corresponding classification results.

2 Study 1: Tractography density affects whole-brain structural architecture and resting-state dynamical modeling, Jung, K., Eickhoff, S. B., Popovych, O. V., Neuroimage, 237: 118176, (2021)

DOI: https://doi.org/10.1016/j.neuroimage.2021.118176

Authorship contribution statement

Kyesam Jung (Doctoral researcher, first author): Conceptualization, Data curation, Formal analysis, Investigation, Methodology, Software, Validation, Visualization, Writing - original draft, Writing - review & editing. **Simon B. Eickhoff:** Conceptualization, Funding acquisition, Resources, Writing - review & editing. **Oleksandr V. Popovych (Corresponding author):** Conceptualization, Data curation, Funding acquisition, Methodology, Project administration, Resources, Software, Supervision, Validation, Writing - review & editing.

NeuroImage 237 (2021) 118176

Contents lists available at ScienceDirect

NeuroImage

journal homepage: www.elsevier.com/locate/neuroimage

Tractography density affects whole-brain structural architecture and resting-state dynamical modeling

Kyesam Jung[a,b], Simon B. Eickhoff[a,b], Oleksandr V. Popovych[a,b,*]

[a] Institute of Neuroscience and Medicine, Brain and Behavior (INM-7), Research Center Jülich, Germany
[b] Institute for Systems Neuroscience, Medical Faculty, Heinrich Heine University Düsseldorf, Germany

ARTICLE INFO

Keywords:
Structural connectome
Functional connectivity
Kuramoto model
MRI
Whole-brain mathematical modeling

ABSTRACT

Dynamical modeling of the resting-state brain dynamics essentially relies on the empirical neuroimaging data utilized for the model derivation and validation. There is however still no standardized data processing for magnetic resonance imaging pipelines and the structural and functional connectomes involved in the models. In this study, we thus address how the parameters of diffusion-weighted data processing for structural connectivity (SC) can influence the validation results of the whole-brain mathematical models informed by SC. For this, we introduce a set of simulation conditions including the varying number of total streamlines of the whole-brain tractography (WBT) used for extraction of SC, cortical parcellations based on functional and anatomical brain properties and distinct model fitting modalities. The main objective of this study is to explore how the quality of the model validation can vary across the considered simulation conditions. We observed that the graph-theoretical network properties of structural connectome can be affected by varying tractography density and strongly relate to the model performance. We also found that the optimal number of the total streamlines of WBT can vary for different brain atlases. Consequently, we suggest a way how to improve the model performance based on the network properties and the optimal parameter configurations from multiple WBT conditions. Furthermore, the population of subjects can be stratified into subgroups with divergent behaviors induced by the varying WBT density such that different recommendations can be made with respect to the data processing for individual subjects and brain parcellations.

1. Introduction

Some 15 years ago, the human brain connectome was introduced to understand functional brain states which are emerged by structural architecture (Sporns et al., 2005). Over more than a decade, researchers have been investigating the human connectome to elucidate the relationship between structure and function (Goñi et al., 2014; van den Heuvel and Sporns, 2011; Sporns, 2011; Suárez et al., 2020). Recently, network neuroscience provides integrative perspectives to validate biophysically realistic models via structural connectome (Bassett et al., 2018). However, the lack of ground truth and golden standards for the calculation of the human connectome caused a central body of ongoing debates in the literature to validate the macroscopic structural and functional connectivity from neuroimaging data of the human brain (Lindquist, 2020; Maier-Hein et al., 2017; Parkes et al., 2018). In addition, no consensus method has been accepted so far as a standardized approach for calculating the whole-brain connectome (Schilling et al., 2019; Sotiropoulos and Zalesky, 2019). Many studies have investigated the effects of the data processing on the obtained results with respect to reproducibility with different methodologies for structural architecture (Bassett et al., 2011; Buchanan et al., 2014; Cammoun et al., 2012; Dennis et al., 2012; Messaritaki et al., 2019; Owen et al., 2013; Roine et al., 2019), functional homogeneity (Bellec et al., 2015; Thirion et al., 2014), and cortical resolutions for brain modeling (Proix et al., 2016). These studies reported good-to-excellent reliability or stable outcome (Dennis et al., 2012; Owen et al., 2013), recommendation (Messaritaki et al., 2019; Roine et al., 2019), and limitations (Buchanan et al., 2014). At this stage, researchers summarized the influence of data processing for structural brain network measures (Qi et al., 2015). Nevertheless, most of the used techniques, algorithms and parameters for processing the neuroimaging data remain at the level of the best practice lacking a solid theoretical foundation.

Without the ground truth, a model-based approach can be a possible way to investigate the impact of the data processing on the observed brain dynamics and reveal the corresponding mechanisms (Popovych et al., 2019). At this, it is assumed that the considered mathematical models derived from the interactions between brain regions can closely simulate the dynamics of the brain responses. By comparing the simulated and empirical data, we can address the model performance

* Corresponding author.
E-mail addresses: k.jung@fz-juelich.de (K. Jung), s.eickhoff@fz-juelich.de (S.B. Eickhoff), o.popovych@fz-juelich.de (O.V. Popovych).

https://doi.org/10.1016/j.neuroimage.2021.118176.
Received 16 December 2020; Received in revised form 9 May 2021; Accepted 13 May 2021
Available online 15 May 2021.

as given by the results of the model fitting and thoroughly explore the model parameters and dynamics. Consequently, we can apply the model validation to evaluate the data processing by searching for the optimal model parameters that provide the best fitting of the model against the empirical data (Cabral et al., 2011; Endo et al., 2020; Zimmermann et al., 2018). Such an evaluation procedure can be repeated for several modeling conditions, where the parameters of the data processing are varied. In this manner, we can systematically approach the optimal modeling condition and data parameters used for the data processing, which enhances the agreement between the simulated and empirical data.

Previous studies have used different whole-brain tractography (WBT) densities ranging from 5K to 100M tracked streamlines for the human connectome (Bajada et al., 2019; Hagmann et al., 2008; Honey et al., 2009; Prasad et al., 2013; Proix et al., 2016; Roine et al., 2019). In particular, Roine et al. (2019) tested the reproducibility of graph-theoretical measures across varied streamline densities from 10K to 100M and concluded that tractography density should be sufficiently high for excellent reproducibility. High tractography density is also beneficial for highlighting subtle clinical differences, and already 15K-20K streamlines may be sufficient to differentiate between patients with Alzheimer's disease or mild cognitive impairment from healthy controls (Prasad et al., 2013). However, the impact of the WBT density on the human connectome is still unclear. Besides, the derivation of the whole-brain models essentially relies on the underlying network calculated from the whole-brain empirical structural connectivity (SC). The latter provides the brain architecture serving as a backbone for the modeling of brain dynamics (Cabral et al., 2011; Endo et al., 2020; Honey et al., 2009; Zimmermann et al., 2018). It is however difficult to evaluate whether the selected parameters of the data processing for WBT density (e.g., the number of WBT streamlines) are reliably reflecting the brain architecture, and what are the optimal values for modeling, e.g., for maximal similarity between simulated and empirical data. In this study, we address the latter problem and search for the optimal configurations which could lead to the optimal SC extraction resulting in the best fit between the simulated and empirical data.

The broad spectrum of the computational models used for simulation of the brain dynamics ranges from the micro- to the macro-scale (Deco et al., 2008; Endo et al., 2020; Freeman, 1987; Hodgkin and Huxley, 1952; Jansen and Rit, 1995; Wilson and Cowan, 1973). Besides the sophisticated computational modeling concepts, the responses of brain regions can be considered as a harmonized signal (Buzsaki, 2011). Thus, we can also use simple mathematical models of coupled oscillators to generate oscillating brain activity (Breakspear et al., 2010; Kuramoto, 1984; Rodrigues et al., 2016). In particular, systems of coupled phase and generic limit-cycle oscillators were suggested by previous studies for modeling cortical oscillations of the resting-state blood oxygen level-dependent (BOLD) dynamics (Breakspear et al., 2010; Cabral et al., 2011; Deco and Kringelbach, 2016; Deco et al., 2017; Fukushima and Sporns, 2018; Ponce-Alvarez et al., 2015). These studies reported the maximal agreement between simulated and empirical data as given by the Pearson correlation between simulated and empirical functional connectivity (FC) in the range between 0.3 and 0.7. In this study, we consider such a system of coupled phase oscillators to model the slow oscillations of the resting-state BOLD dynamics.

The main topic of the current study is to investigate the impact of the WBT streamline number used for calculation of SC and the average streamline path-length (PL) between brain regions on the simulation results. We considered a system of coupled phase oscillators with delayed coupling (Yeung and Strogatz, 1999), where the anatomical information about brain structural architecture (SC and PL) from diffusion-weighted MRI (dwMRI) was used for its derivation, i.e., to build the model network and approximate the coupling weights and time delay between the network nodes. The latter are the brain regions parceled according to a given brain atlas/brain parcellation. We considered two distinct brain parcellations based on anatomical and functional brain properties. We systematically explored the model parameter space of two free parameters of global coupling and global delay in order to fit the model to empirical data. We also used two model fitting modalities as given by 1) similarity (Pearson correlation) between simulated and empirical FC as a goodness-of-fit of the model and 2) similarity between simulated FC and empirical SC to probe the dynamics of the model as related to its structural network. The obtained simulation results were compared with each other across subjects and simulation conditions, which allowed us to scrutinize the effects of structural architecture modulated by varying WBT density and brain parcellations on the model validation against empirical data. The used approach can also lead to a better understanding of the properties of the obtained data influenced by selected data processing, which can play a key role for the brain modeling as well as data analytics.

2. Materials and methods

The current study considered 351 unrelated subjects (172 males, age 28.5 ± 3.5 years) from the Human Connectome Project (HCP) S1200 dataset (Van Essen et al., 2013). HCP data (https://www.humanconnectome.org) were acquired using protocols approved by the Washington University institutional review board (Mapping the Human Connectome: Structure, Function, and Heritability; IRB #201204036). Informed consent was obtained from subjects. Anonymized data are publicly available from ConnectomeDB (https://db.humanconnectome.org). In the current study, resting-state functional MRI (fMRI), T1-weighted image (T1) and diffusion-weighted images (DWI) from 3T connectome scanners (modified Siemens PRISMA with higher gradient strength) were used for investigation. Resting-state fMRI was acquired with 2 mm isotropic voxels, T1 was in 0.7 mm isotropic voxels, and DWI consisted of 90 directions for 1000, 2000 and 3000 s/mm^2 b-values in total 270 weighted directions with 1.25 mm isotropic voxels.

We reconstructed SC and PL by using six WBT densities and two atlases for individual subjects, then calculated simulated FC from BOLD signals generated by the computational model composed of coupled phase oscillators with delayed coupling. We explored two free parameters of the model for each subject and condition and validated the model through the two model fitting modalities. We also calculated graph-theoretical network properties of SC and PL over considered conditions and compared the network properties with the goodness-of-fit of the model. The individual subjects were stratified into groups based on three criteria derived by the network properties and modeling results. The workflow of the current study is illustrated in Fig. 1.

2.1. Preprocessing of MRI data and connectivity extraction

The current study used an *in-house* pipeline for the extraction of SC and PL matrices from the DWIs. The pipeline consists of four modules: preprocessing of MRI and DWI data, WBT calculation, atlas transformation and connectivity reconstruction. The pipeline is publicly available (https://github.com/inm7/vbc_dwmri). It was optimized for parallel processing on high-performance computational clusters (Jülich Supercomputing Centre, 2018).

The pipeline was created with functions of Freesurfer (Dale et al., 1999), FSL (Smith et al., 2004), ANTs (Tustison et al., 2010), and MRtrix3 (Tournier et al., 2019). Freesurfer was used for processing the T1 including bias-field correction, tissue segmentation, cortical (surface) reconstruction, volume-surface converting, and surface deformation for parcellation as well as for the correction of the eddy-current distortions and head-motion in DWIs using the corresponding b-vectors and b-values. MRtrix3 performed de-noising and bias-field correction on the DWIs. The pre-processed images were used for co-registration between the T1 and the DWIs and linear and non-linear transformation by functions of FSL. Linear and non-linear transformation matrices and images for registration from the standard MNI space to the native space

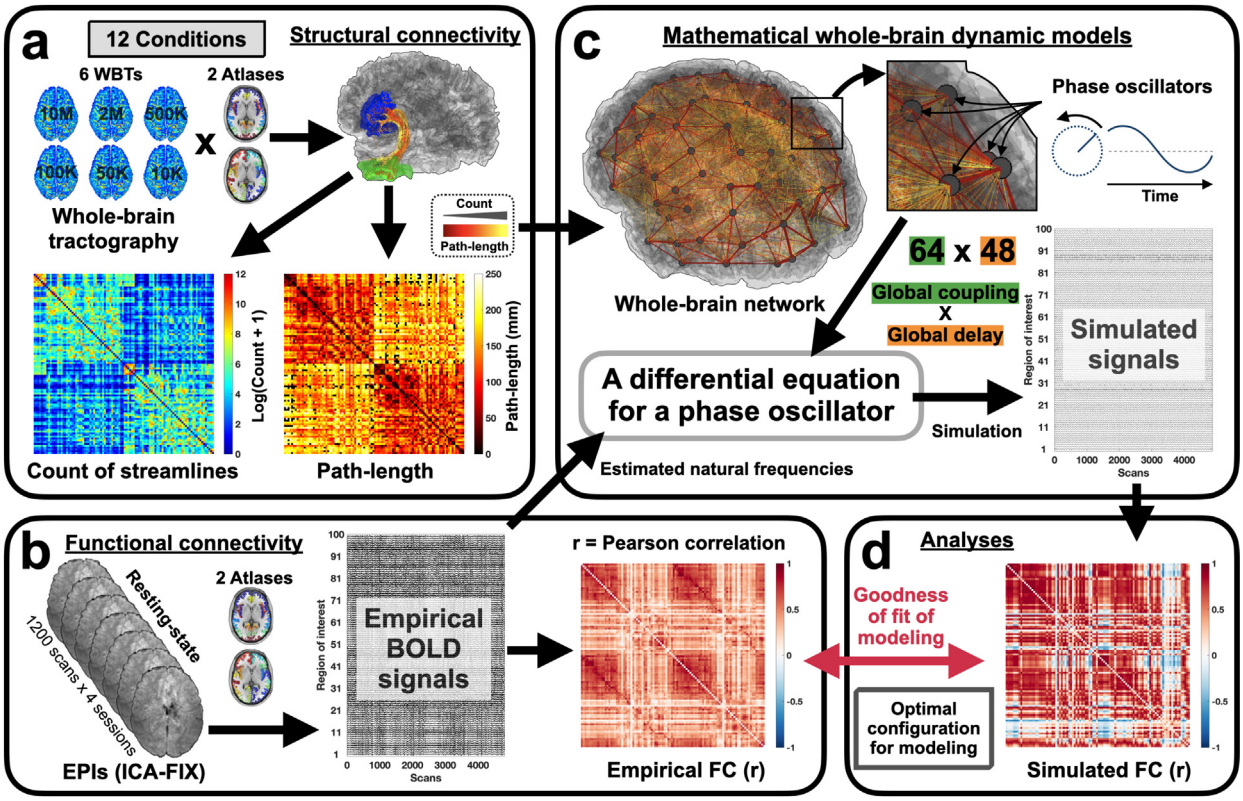

Fig. 1. Workflow of the current study. (a) The whole-brain tractography (WBT) was generated by an in-house pipeline. Structural connectivity (SC) and average path-length (PL) between brain regions were reconstructed based on a given brain parcellation/brain atlas (6 WBTs and 2 atlases). **(b)** The empirical BOLD signals were extracted for each brain region from the ICA-FIX preprocessed HCP data, and the empirical functional connectivity (FC) was calculated between BOLD signals by Pearson correlation coefficient. **(c)** By using the empirical SC and PL matrices, the whole-brain network was reconstructed. The network nodes representing the brain regions were equipped with the phase oscillators (Eq 1) coupled with the coupling weights (Eq 2) and time delays (Eq 3) extracted from the empirical SC and PL matrices, respectively. The natural frequencies of the oscillators were extracted from empirical BOLD signals. The model generated simulated BOLD signals used for the calculation of the simulated FC. **(d)** The simulated FC was compared with empirical FC and SC, and the model was validated by optimizing its parameters for the best correspondence/fitting between the simulated and empirical data. At this, the impact of the data processing on the model validation was evaluated and described.

and vice versa were estimated. Through the image registration, gray matter, white matter, cortical/subcortical, cerebellar and cerebrospinal fluid masks were generated in the native DWI space.

The WBT calculation module included only MRtrix3 functions, where the response functions for spherical deconvolution were estimated using multi-shell-multi-tissue constrained deconvolution algorithm (Jeurissen et al., 2014). Fiber oriented distributions (FOD) were estimated from the DWIs using spherical deconvolution, and the WBT was created through the fiber tracking by the second-order integration over the FOD by a probabilistic algorithm (Tournier et al., 2010). In the latter step, we used six different numbers of total streamlines for varying WBT density: 10K, 50K, 100K, 500K, 2M, and 10M, where the “K” and “M” letters stand for thousand (Kilo-) and million (Mega-), respectively. The tracking parameters were set as default values of *tckgen* function from MRtrix documentation (https://mrtrix.readthedocs.io), where the following values were used: step size = 0.625 mm, angle = 45 degrees, minimal length = 2.5 mm, maximal length = 250 mm, FOD amplitude for terminating tract = 0.06, maximum attempts per seed = 50, maximum number of sampling trials = 1000, and down sampling = 3.

The atlas transformation module applied the linear and non-linear transformation matrix and images to atlases that were sampled in the standard MNI space. We used the Schaefer atlas with 100-area parcellation (Schaefer et al., 2018) and the Harvard-Oxford atlas with 96 cortical regions (Desikan et al., 2006). After the transformation, the labeled voxels in the gray matter mask were selected for a seed and a target region. Consequently, the *tck2connectome* function of MRtrix3 reconstructed SC and PL (count and path-length matrices in Fig 1a).

For the empirical FC, the BOLD signals were extracted from the resting-state fMRI data processed by ICA-FIX as provided by HCP repository (Griffanti et al., 2014). During the ICA-FIX, a weak high-pass filtering (2000 s high-pass filter) was applied for detrending-like effect (Smith et al., 2013). The Schaefer atlas and the Harvard-Oxford atlas were applied for the parcellation of the processed fMRI into brain regions within the standard MNI 2 mm space (6th-generation in FSL). Empirical FC was calculated using Pearson correlation coefficient across BOLD signals extracted as mean signals of the parceled brain regions. There were four resting-state fMRI sessions (1200 volumes, TR = 720 ms) which consist of two different phase-encoding directions (left and right) scanned in different days. In addition, a concatenated BOLD signal was generated by using all four z-scored BOLD signals from the above four fMRI sessions, which resulted in five empirical FCs calculated for BOLD signals from the four fMRI sessions and the concatenated BOLD signals for each subject. Finally, 12 simulation conditions (6 WBTs × 2 atlases) were tested by simulation of the mathematical whole-brain model, where the model parameters were optimized for the best fit between simulated and empirical data.

2.2. Mathematical whole-brain model

We simulated a whole-brain dynamical model of N coupled phase oscillators (Cabral et al., 2011; Kuramoto, 1984; Yeung and Strogatz,

1999)

$$\dot{\varphi}_i(t) = 2\pi f_i + \frac{C}{N}\sum_{j=1}^{N} k_{ij}\sin\left(\varphi_j\left(t-\tau_{ij}\right)-\varphi_i(t)\right)+\eta_i, \quad i = 1,2,\ldots,N. \tag{1}$$

The number of oscillators N corresponds to the number of brain regions parceled as defined by a given brain atlas, where $\varphi_i(t)$ models the phase of the mean BOLD signal of the corresponding region, and the simulated BOLD was calculated as $\sin(\varphi_i(t))$. C is a global coupling which scales the level of couplings of the whole-brain network. η_i is an independent noise perturbing oscillator i, which is sampled from a random uniform distribution from the interval [-0.3,0.3]. The natural frequencies f_i were estimated from the empirical data as frequencies of the maximal spectral peaks (restricted to the frequency range from 0.01 Hz to 0.1 Hz) of the empirical BOLD signals of the corresponding brain regions. k_{ij} stands for the coupling strength between oscillators i and j, and τ_{ij} approximates the time delay of the signal propagation between oscillators i and j. They were calculated from the empirical SC and PL and determined by the following equations:

$$k_{ij} = \frac{w_{ij}}{< W >}, \tag{2}$$

where w_{ij} is the number of streamlines between i^{th} and j^{th} parceled regions and $< W >$ is an averaged number of streamlines over all connections except self-connections, and

$$\tau_{ij} = \frac{L_{ij}}{< V >} = \tau L_{ij}, \tag{3}$$

where τ is a global delay (unit: s/m) which is a reciprocal of an average speed of signal propagation $< V >$ through the whole-brain network. The time step of the numerical integration of Eq 1 by the stochastic Heun method was fixed to 0.04 s, and the simulated signals were generated for 3500 seconds after skipping 500 seconds of the transient. The simulated BOLD signals and the corresponding simulated FCs were calculated from the phases downsampled to TR = 0.72 s, which is the repetition time of HCP fMRI.

The considered mathematical model (Eq 1) has two main free parameters: the global coupling C and the global time delay τ. The global coupling ranged from 0 to 0.504 in evenly discretely distributed 64 values, and the global delay was from 0 to 423 s/m in evenly discretely distributed 48 values. Therefore, 3072 (64 × 48) simulations were performed for each subject to calculate the simulated FCs that were compared with empirical functional and structural data for each simulation condition. A total of 12,939,264 (64 × 48 × 12 × 351) simulations of model (Eq 1) were performed in this study for 351 subjects with 12 conditions (6 WBTs × 2 atlases).

We explored the 2-dimensional model parameter space as mentioned above and found the optimal parameter values for the best correspondence between simulated and empirical data. The correspondence was calculated by Pearson correlation coefficient between simulated FC (sFC) and empirical FC (eFC) and SC (eSC) depending on the model fitting modality. For each subject and simulation condition, 5 parameter planes of the *functional similarity* or *functional model fitting* modality (correlation between sFC and eFC) were obtained corresponding to 5 eFCs. In addition, one parameter plane of the *structure-functional similarity* or *structure-functional model fitting* modality (correlation between sFC and eSC) was also calculated. From each parameter plane, we selected the optimal (C, τ)-parameter point, where the maximal correlation between the simulated and the empirical data was reached. For the functional model fitting the maximal similarity can be referred to as *goodness-of-fit* of the model.

2.3. Effects of different WBT conditions

We revealed the effects of the varying WBT density on the modeling results by evaluating its impact on 1) the graph-theoretical network properties of empirical structural connectome, 2) patterns of the optimal model parameters in the model parameter space, and 3) model performance as given by the quality of the model fitting over simulation conditions. Based on the results from the three approaches, we introduced three criteria (see below) for differentiation of the influence of the WBT density on the modeling results for individual subjects. To do this, we stratified the entire subject population by splitting it into several subgroups according to the mentioned criteria based on *(i)* the relationships between the network properties and the results of the functional model fitting over WBT conditions, *(ii)* distributions of the optimal model parameters of the structure-functional model fitting, and *(iii)* positive and negative slopes (increments) of the goodness-of-fit values (model performance) across the two extreme cases of the considered 10K and 10M WBT streamlines for individual subjects.

2.3.1. Structural architecture and network properties over WBT conditions

To investigate the impact of the varying WBT density on the architecture of structural networks, we calculated graph-theoretical network properties from SC and PL for each subject, WBT condition and atlas. The considered 6 network properties (4 local properties and 2 global properties) included the weighted node degree, clustering coefficient, betweenness centrality, local efficiency, global efficiency and modularity, which were calculated by the brain connectivity toolbox version 2019-03-03 in Matlab (Rubinov and Sporns, 2010). For the local properties, both the average (Avg.) and the standard deviation (S.D.) were calculated.

For every subject, we calculated the Pearson correlation between the values of a given network measure and the maximal functional model fitting (goodness-of-fit) values across varied WBT densities. Then, for every considered network measure, we split the subjects into two subgroups with positive and negative correlations. After that, we performed the two-sample one-tail *t*-test to compare the functional model fitting between the split subgroups. Based on the results of the *t*-test, we selected the network properties, where one of the subgroups showed significantly higher functional model fitting than the other subgroup (Fig. A5 in Supplementary materials). Finally, we overlapped all selected subgroups with higher goodness-of-fit over all selected network properties and referred to this group as pattern 1. Consequently, the rest of subjects were united into the second group referred to as pattern 2. We thus stratified all subjects into two groups/patterns with potentially different impact of the WBT conditions on the modeling results.

2.3.2. Impact of time delay on the model fitting

For another stratification criterion, the optimal model parameters of the maximal correspondence between sFC and eSC were divided into two clusters as suggested by the bimodal distribution splitting small and large values of the optimal time delay (Fig 6). Since subjects can move between the parameter clusters when the total number of the WBT streamlines varies from 10M to 10K, we separated the subjects into five classes: Always staying in cluster 1 (From 1 to 1) or in cluster 2 (From 2 to 2), only once moving either from cluster 1 to cluster 2 (From 1 to 2) or in opposite direction (From 2 to 1), and performing multiple switching between the two clusters (Multiple). This approach based on the distribution of the optimal model parameters was used as the second criterion for stratification of subjects.

2.3.3. Variation of the model performance

The last stratification criterion was based on the behavior of the optimal goodness-of-fit values when the number of WBT streamlines varied. To quantify it, we calculated the increment of the maximal similarity between sFC and eFC matrices of the concatenated session for every individual subject when the number of the WBT streamlines increases from 10K to 10M. Then, all subjects were divided into two subgroups exhibiting either positive or negative slopes (increments) of the goodness-of-fit behavior versus the number of WBT streamlines (Fig 7). According to

Table 1
Sensitivity of the considered graph-theoretical network properties to the variation of the WBT density as revealed by the non-parametric one-way analysis of variance (Kruskal-Wallis ANOVA) test. The corresponding p-values are presented in the right columns of the tables, where the bold p-values indicate that the respective network property significantly changes (Bonferroni corrected $p < .05$) when the number of WBT streamlines varies in the range indicated in the left columns of the tables. The results are shown for the Schaefer atlas (upper table) and the Harvard-Oxford atlas (lower table), and the abbreviations in the upper rows denote the network properties. WD: average weighted node degree, CC: average clustering coefficient, BC: average betweenness centrality, LE: average local efficiency, GE: global efficiency, and MQ: modularity Q.

Schaefer atlas	WD	CC	BC	LE	GE	MQ
10K, 50K, 100K, 500K, 2M, 10M	**<0.001**	**<0.001**	**<0.001**	**<0.001**	**<0.001**	**<0.001**
50K, 100K, 500K, 2M, 10M	**<0.001**	**<0.001**	**<0.001**	**<0.001**	**<0.001**	**<0.001**
100K, 500K, 2M, 10M	**<0.001**	**<0.001**	**0.009**	**<0.001**	**<0.001**	**<0.001**
500K, 2M, 10M	0.994	**<0.001**	0.920	**<0.001**	0.999	**0.011**
2M, 10M	0.916	**<0.001**	0.929	**<0.001**	0.947	1.000
Harvard-Oxford atlas	**WD**	**CC**	**BC**	**LE**	**GE**	**MQ**
10K, 50K, 100K, 500K, 2M, 10M	**<0.001**	**<0.001**	**<0.001**	**<0.001**	**<0.001**	**<0.001**
50K, 100K, 500K, 2M, 10M	**<0.001**	**<0.001**	**<0.001**	**<0.001**	**<0.001**	**<0.001**
100K, 500K, 2M, 10M	0.992	**<0.001**	**0.012**	**<0.001**	1.000	**<0.001**
500K, 2M, 10M	0.996	**<0.001**	1.000	**<0.001**	1.000	**0.005**
2M, 10M	1.000	**<0.001**	1.000	**<0.001**	1.000	0.913

this criterion, the subjects were stratified into two subgroups demonstrating the best functional model fitting for either maximal or minimal number of the WBT streamlines considered. Consequently, we used all three criteria for the three-step stratification analysis (Fig 8).

3. Results

We investigate all three stratification criteria mentioned in the Methods (Section 2.3) and apply them to subject differentiation. This provides an insight into the impact of the WBT density on the model performance for individual subjects and suggests optimal configurations of the data processing parameters. To follow the stratification steps, the obtained results will be presented in parallel for the two considered brain parcellations based on the Schaefer and Harvard-Oxford atlases and compared between them.

3.1. Impacts of WBT density on structural connectome

Figure 2 illustrates the similarities between SC and PL (Fig 2 a and c) and behavior of the weighted node degree, clustering coefficient, betweenness centrality, local and global efficiencies and modularity calculated from the normalized SC matrix over 6 WBT conditions (10K, 50K, 100K, 500K, 2M, and 10M streamlines) for the two atlases (Fig 2 b and d). The similarity of the eSC matrices to the 10M case remains relatively high except for the largest drop at 10K (Fig 2 a1 and c1). On the other hand, the PL matrices have low similarity over the 6 WBT conditions, very quickly deviate from the 10M case, exhibit practically no correlation already for 100K and weakly anti-correlate for 10K (Fig 2 a2 and c2). We also performed a non-parametric one-way analysis of variance (Kruskal-Wallis ANOVA) test over the WBT conditions (Table 1).

By increasing the number of streamlines from 10K to 10M, the number of network edges increases, and the nodes become densely connected, which resulted in monotonically increasing average binarized (discarded weights of edges) node degrees as expected (Fig. A1 in Supplementary materials). However, the weighted node degree based on the normalized count matrices (SC divided by its mean) used in model (Eq 1) shows relatively stationary behavior across the WBT conditions, especially, for dense WBT (Fig 2 b1 and d1 and Table 1 WD). Decreasing the number of streamlines, for example, from 10M to 10K (by 1000 folds) resulted in the corresponding reduction of the averaged weighted node degree of the normalized SC by 6% and 33% for the Schaefer and Harvard-Oxford atlases, respectively (Fig 2 b1 and d1). Similar stationary behavior can also be observed for the average betweenness centrality and the global efficiency, especially, for dense WBT conditions (Fig 2 b3, b5, d3, and d5 and Table 1 BC and GE). The network modularity shows a weak monotonic increase when the WBT density increases (Fig 2 b6 and d6). For these network measures, relatively moderate changes were observed when the number of streamlines varies from 10M to 10K. This indicates that the connectivity in the model is still relatively strong, and some other properties of the network architecture are to a large extent preserved even for the extreme case of 10K WBT.

On the other hand, the average clustering coefficient, local efficiency and their variances strongly decrease when the WBT density increases (Fig 2 b2, b4, d2, and d4 and Table 1 CC and LE). In summary, WBT density modulates the graph-theoretical network properties and results in similar tendencies at the group level through varying WBT density for both atlases. In particular, the clustering coefficient and the local efficiency are significantly different across the WBT conditions already between 2M and 10M cases (Table 1 CC and LE), where very high similarities of SC can be observed (Fig 2 a1 and c1).

3.2. Impacts of WBT density on model fitting

Figure 3 shows the obtained parameter planes and the distributions of the optimal model parameters over all subjects and simulated conditions for the two fitting modalities (sFC versus eFC and sFC versus eSC). The goodness-of-fit between sFC and eFC was observed for small delays for both atlases. This is illustrated in Fig 3 a-d, where the red dots depicting large similarity values are concentrated on the left side of the parameter plane demonstrating, however, different cluster shapes for the Schaefer and the Harvard-Oxford atlases. We also note here that the latter atlas could lead to a stronger fit between the sFC and eFC, compare Fig 3 a and c. In contrast, in the case of the structure-functional model fitting between sFC and eSC (Fig 3 e-h), both atlases demonstrate a similar range of the correspondence (correlation) between simulated and empirical data, however, the maximal similarity can also be attained for large delay.

During the model validation for individual subjects under the 12 considered conditions (6 WBTs × 2 atlases), we also searched for the optimal model parameter, where the maximal similarity between sFC and empirical data (eFC and eSC) was achieved. The distributions of such optimal parameters are depicted in Fig 3 b, d, f, and h for the two fitting modalities and the two brain atlases. In agreement with these results, the best fit between sFC and eFC is attained for small delays (Fig 3 b and d), whereas the strongest structure-function correspondence between sFC and eSC can also be observed for large delays (Fig 3 f and h).

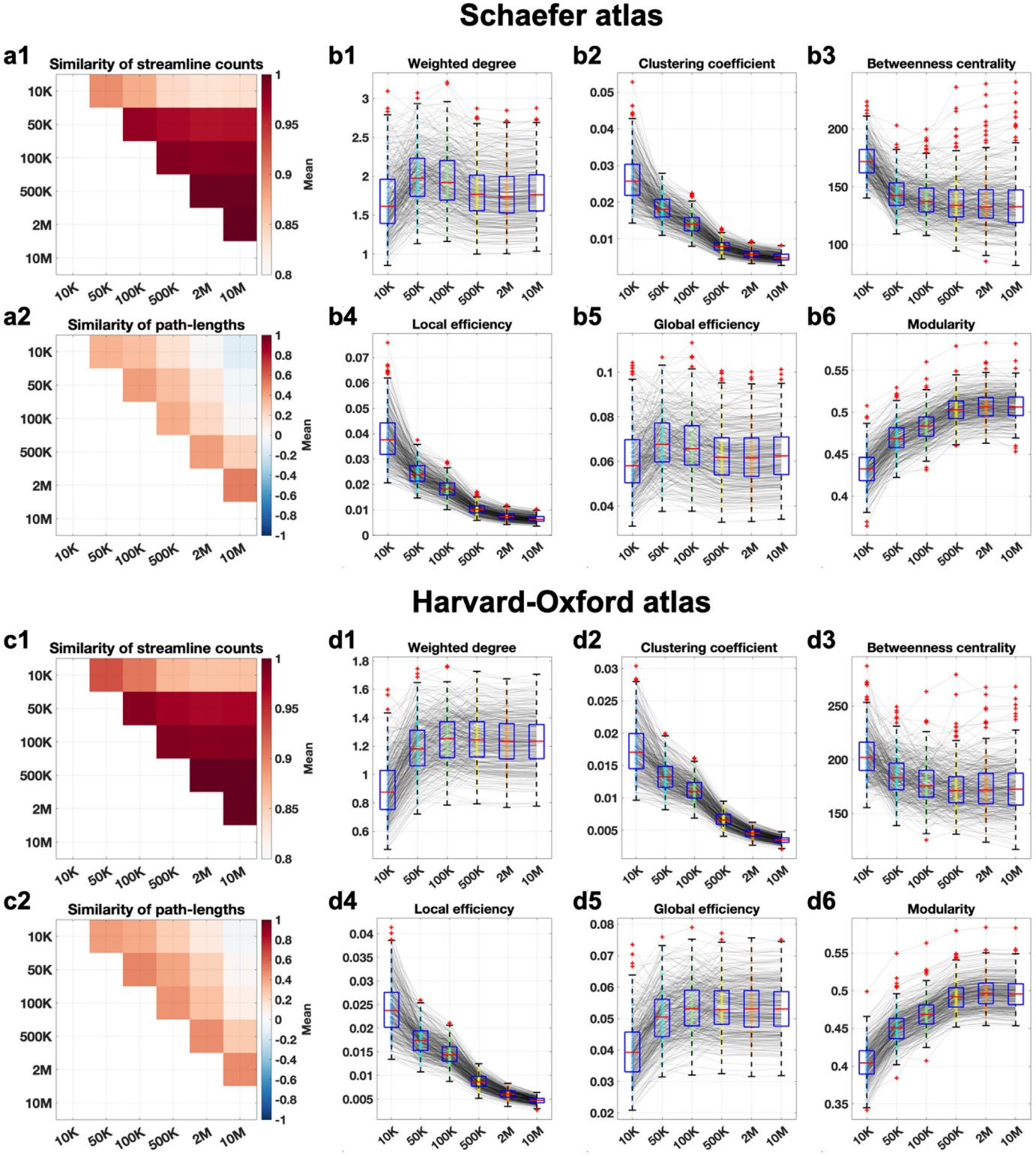

Fig. 2. Impact of the WBT density on the structural architecture. Network measures of the structural connectome and similarity between them calculated for different WBT densities (numbers of streamlines) for **(a, b)** the Schaefer atlas and **(c, d)** the Harvard-Oxford atlas. **(a, c)** Similarity of the connectivity matrices **(a1, c1)** SC and **(a2, c2)** PL calculated for different tractography densities by Pearson correlation across all subjects. **(b, d)** Variations of the network properties calculated from the normalized SC matrix versus WBT density. The plot indices stand for 1: average weighted node degree, 2: average clustering coefficient, 3: average betweenness centrality, 4: average local efficiency, 5: global efficiency, and 6: modularity as indicated in the plot titles. In each plot the thin gray lines depict the behavior of the illustrated quantities for individual subjects together with the box plots, where the red lines, blue boxes and red pluses indicate the medians, the interquartile ranges, and the outliers, respectively. (For interpretation of the references to colour in this figure legend, the reader is referred to the web version of this article.)

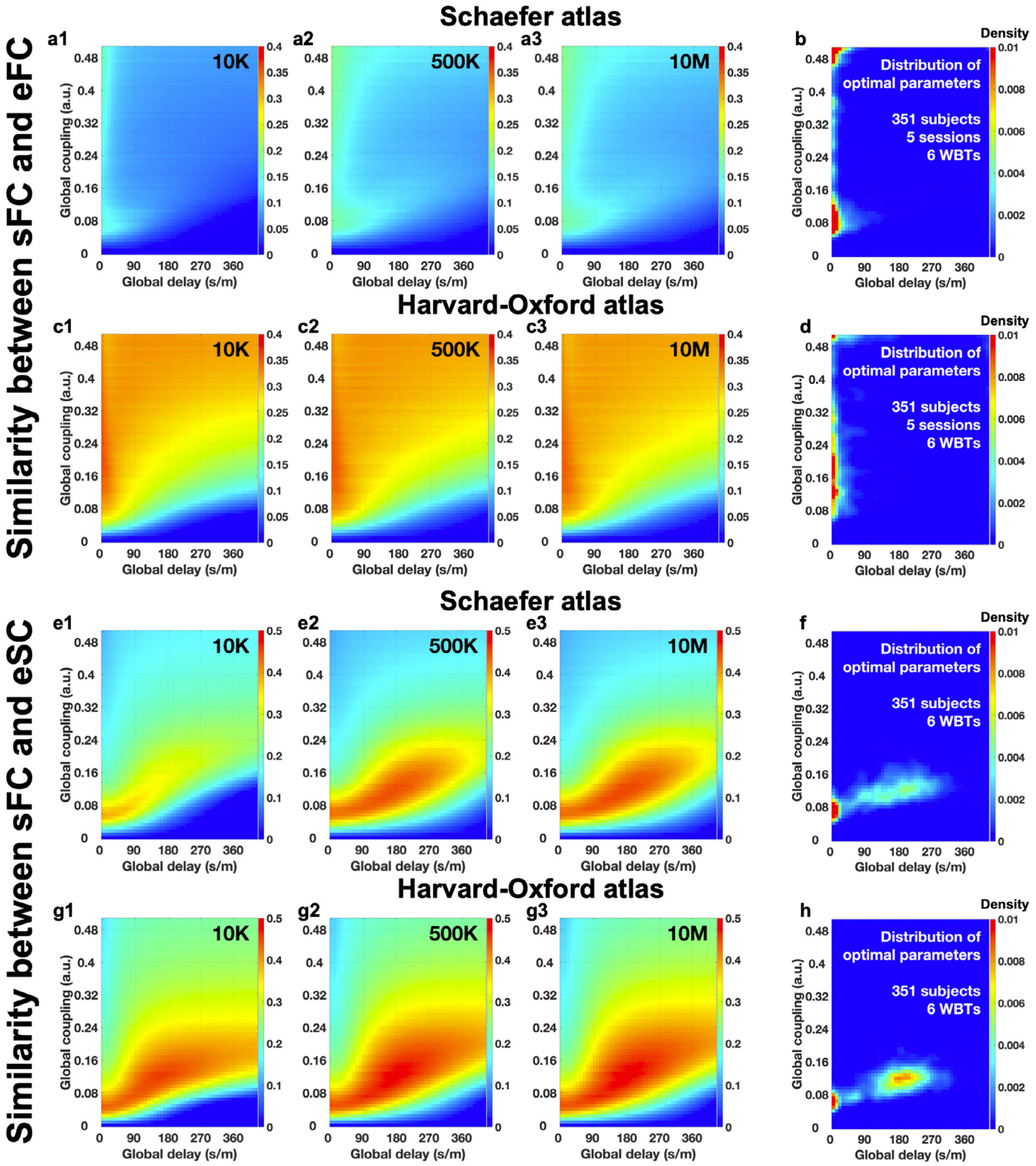

Fig. 3. Parameter planes and the distributions of the optimal model parameters (C, τ) for the two model fitting modalities between simulated and empirical data. Parameter planes are averaged **(1–3)** over all subjects (n = 351) separately for simulation conditions (10K, 500K, and 10M WBT densities) as indicated in the plots (see supplementary Fig. A10 for all conditions). The correspondence between the simulated and empirical data was calculated between **(a-d)** simulated FC and empirical FC and **(e-h)** simulated FC and empirical SC for **(a, b, e, f)** the Schaefer atlas and **(c, d, g, h)** the Harvard-Oxford atlas. The Pearson correlation between the connectivity matrices is depicted by color ranging from small (blue) to large (red) values. **(b, d, f, h)** Distributions of the optimal model parameters of the best model fitting calculated for all individual subjects and simulation conditions. (For interpretation of the references to colour in this figure legend, the reader is referred to the web version of this article.)

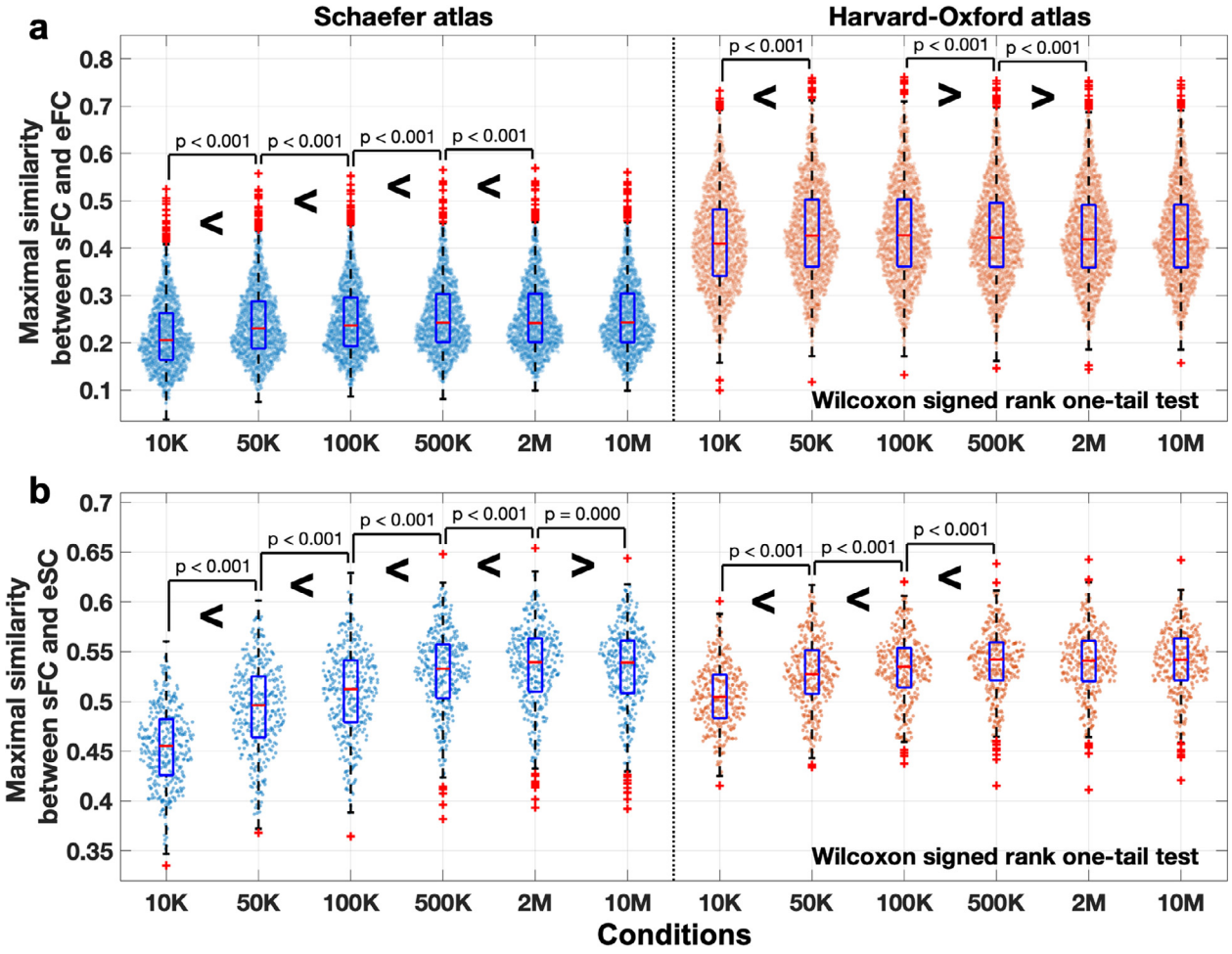

Fig. 4. Results of the model fitting to the empirical data versus 12 simulation conditions (6 WBTs ×2 atlases). The distributions of the maximal similarities for individual subjects between **(a)** simulated FC and empirical FC and **(b)** simulated FC and empirical SC are shown as violin plots for 12 conditions of the WBT streamline numbers indicated on the horizontal axes for the Schaefer atlas (blue violins) and the Harvard-Oxford atlas (orange violins). The results of the pairwise comparisons between the conditions (Wilcoxon signed rank one-tail test) are also indicated with the corresponding p-values in the cases of statistically significant differences (Bonferroni corrected $p < .05$). For the box plots the red lines, blue boxes and red pluses indicate the medians, the interquartile ranges, and the outliers, respectively. (For interpretation of the references to colour in this figure legend, the reader is referred to the web version of this article.)

In the latter case, the parameter distributions apparently demonstrate a two-cluster shape of small and large delays, which is addressed in detail below.

Together with the optimal model parameters for individual subjects, we also collected the corresponding maximal similarities between the simulated and empirical data, which are illustrated in Fig 4 for the 12 simulated conditions and for the two fitting modalities of the correspondence between sFC and eFC (Fig 4a) and between sFC and eSC (Fig 4b). Results of the functional model fitting in all conditions (Fig 4a) were not from the normal distributions, where the null hypothesis was rejected by χ^2 goodness of fit test with $p < .05$. Also in the case of the structure-functional model fitting (Fig 4b) many conditions were not from the normal distributions. Therefore, Kruskal-Wallis test was used for testing significant difference in all conditions (across tractography densities). Consequently, we performed Wilcoxon signed rank one-tail test to evaluate whether the maximal similarities between the simulated and empirical data for one condition are significantly higher or lower than those for the other conditions (see p values in Fig 4).

For the functional model fitting (sFC versus eFC) and the Schaefer atlas (Fig 4a, blue violins), the models with 2M and 10M WBTs performed better than with the other WBTs, and the performance of the model decreased when the number of streamlines decreased. On the other hand, the functional model fitting for the Harvard-Oxford atlas revealed the optimal condition at 50K or 100K WBT (Fig 4a, orange violins). Furthermore, the model could fit better to eFC for the Harvard-Oxford atlas, which was also observed in Fig 3. For the structure-functional model fitting (sFC versus eSC), the situation is different, where 2M or 10M WBTs are preferable for the strongest correspondence between the simulated and empirical data for both atlases demonstrating approximately similar extent of the maximal model fitting (Fig 4b, see also Fig 3).

3.3. Relationships between network properties and the functional model fitting

As discussed above, the WBT density modulates the structural connectome. Consequently, it can also influence the dynamics of the model (Figs 3 and 4). In this section, we investigate the effects of the graph-theoretical network properties modulated by WBT density on the model performance.

For each of the considered 6 network properties, we tested the relationships between their values and the maximal similarity between sFC and eFC as given by the Pearson correlation across 6 WBT conditions for each individual subject. The considered network properties demonstrate a pronounced agreement with the goodness-of-fit values at the level of individual subjects (Fig 5 a1 and b1). Some distributions of the correlation coefficients are significantly shifted from zero except

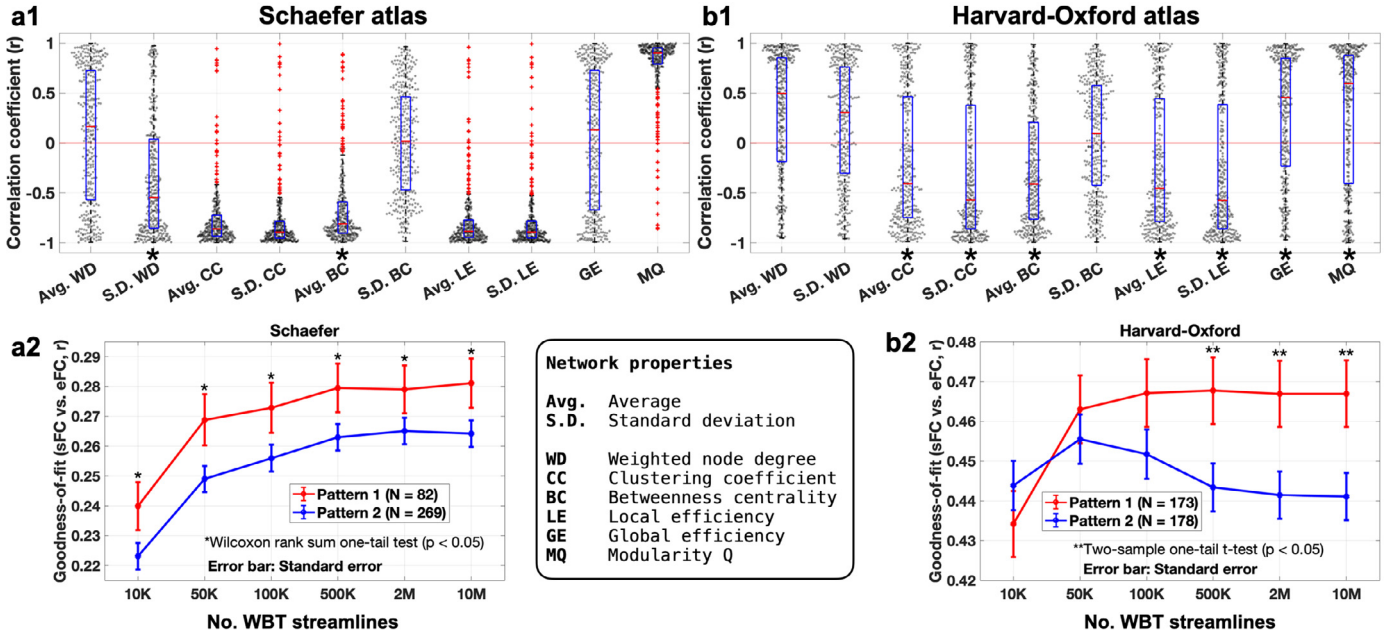

Fig. 5. Relationships between the network properties and the results of the functional model fitting. Correlation between the network properties and maximal similarity between sFC and eFC for individual subjects and fitting results for stratified subjects are shown for **(a)** the Schaefer atlas and **(b)** the Harvard-Oxford atlas. **(a1, b1)** Distributions of the Pearson correlation coefficients calculated across 6 WBT conditions for individual subjects between a given network property indicated on the horizontal axes and the goodness-of-fit values. The gray dots represent the values for individual subjects, and the box plots illustrate the medians (red lines), the interquartile ranges (blue boxes) and the outliers (red pluses). The asterisks on the x-axes indicate statistically significant differences in the goodness-of-fit values between the two subgroups of subjects with positive and negative correlations ($p < .05$ of two-sample one-tail t-test). **(a2, b2)** The results of the functional model fitting versus different numbers of the WBT streamlines for the two subject subgroups of pattern 1 and pattern 2 as indicated in the legends based on the statistically significant split of the subjects for the network properties marked by asterisks in plots a1 and b1, see the Methods Section 2.3.1 for details. The error bars indicate the standard error, and the asterisks denote the simulation conditions, where the pattern 1 and 2 exhibit significantly different extend of the similarity between simulated and empirical data. (For interpretation of the references to colour in this figure legend, the reader is referred to the web version of this article.)

for Avg. WD, S.D. BC, and GE for the Schaefer atlas and S.D. BC for the Harvard-Oxford atlas (see Fig 5 for abbreviations). The presented results are reproducible to retest over individual 5 sessions (4 fMRI sessions and the concatenated case) and merged data of the goodness-of-fit values (see supplementary Fig. A2). Based on the results illustrated in Fig 5 a1 and b1 and supplementary Fig. A2, we can conclude that the changes in the model performance for the individual subjects are related to the changes in the network properties across different WBTs.

The distributions of the correlation coefficients between the network properties and the goodness-of-fit values may differ for different atlases (Fig 5 a1 and b1) indicating a complex relationship between the structural connectome and modeling results. To address such relationships in more detail, we split the subjects into two subgroups of positive or negative correlation for every considered network metric. Then we intersect the groups with highest goodness-of-fit for the network metrics marked by asterisks in Fig 5 a1 and b1 with significant difference between the subgroups and stratify the subjects into two patterns as explained in Methods (Section 2.3.1, see also Figs. A3 - A5 in Supplementary materials).

Based on the results of the tests, for the Schaefer atlas, we selected subjects exhibiting positive correlation with the standard deviation of weighted node degree (S.D. WD+) and negative correlation with the average betweenness centrality (Avg. BC-) for pattern 1, which have significantly higher values of the goodness-of-fit of the model than those of the complementing subgroups (S.D. WD- and Avg. BC+), respectively. The intersection of the two selected subgroups, i.e., S.D. WD+ (n = 93) ∩ Avg. BC- (n = 329) = 82, constituted the stratified pattern 1, whereas the rest of the subjects (n = 269) were grouped into pattern 2.

We found that the two patterns of the split subjects subgroups demonstrate significantly different quality of the goodness-of-fit of the model depending on the WBT conditions (Fig 5a2). For statistical testing of the differences between the patterns 1 and 2, χ^2 goodness of fit test was used to test for a normal distribution for each condition of pattern 1 and pattern 2. The Wilcoxon rank sum one-tail test was then used for a non-parametric test of the difference between the patterns if the null-hypothesis for a normal distribution was rejected by the χ^2 test. Otherwise, two-sample one-tail t-test was used for comparing normal distributions of pattern 1 and pattern 2. The significant differences between the patterns are indicated by asterisks in Fig 5a2, which is the case for any WBT density. We also found that the fitting values for both patterns 1 and 2 monotonically increase for higher WBT density (Fig 5a2). In addition, we tested the changes of the goodness-of-fit of the model for each pattern when the WBT density varies by using Wilcoxon signed rank test. As a result, for the Schaefer atlas, 500K or more streamlines of the pattern 1 and 2M or more streamlines of the pattern 2 showed significantly higher goodness-of-fit values than for any sparser WBT conditions.

For stratification for the Harvard-Oxford atlas, we selected subjects from the intersection of the following subgroups derived as above of positive and negative correlations with the network metrics, which showed significantly higher goodness-of-fit values than the complementing subgroups: Avg. CC-, S.D. CC-, Avg. BC-, Avg. LE-, S.D. LE-, GE+, and MQ+ (see Fig 5 for abbreviations). As above, the sign "+" or "-" after the property name indicates the corresponding subgroups of subjects exhibiting positive or negative correlations with the considered network properties, respectively. Such an intersection of the subgroups resulted in a stratified pattern 1 containing 173 subjects complemented by the others, i.e., 178 subjects of pattern 2.

We here found that patterns 1 and 2 exhibit different behavior of the goodness-of-fit values when the WBT density varies (Fig 5b2). Pattern 1 monotonically increases for large WBT density as before, whereas pattern 2 apparently demonstrates a non-monotonic behavior with an

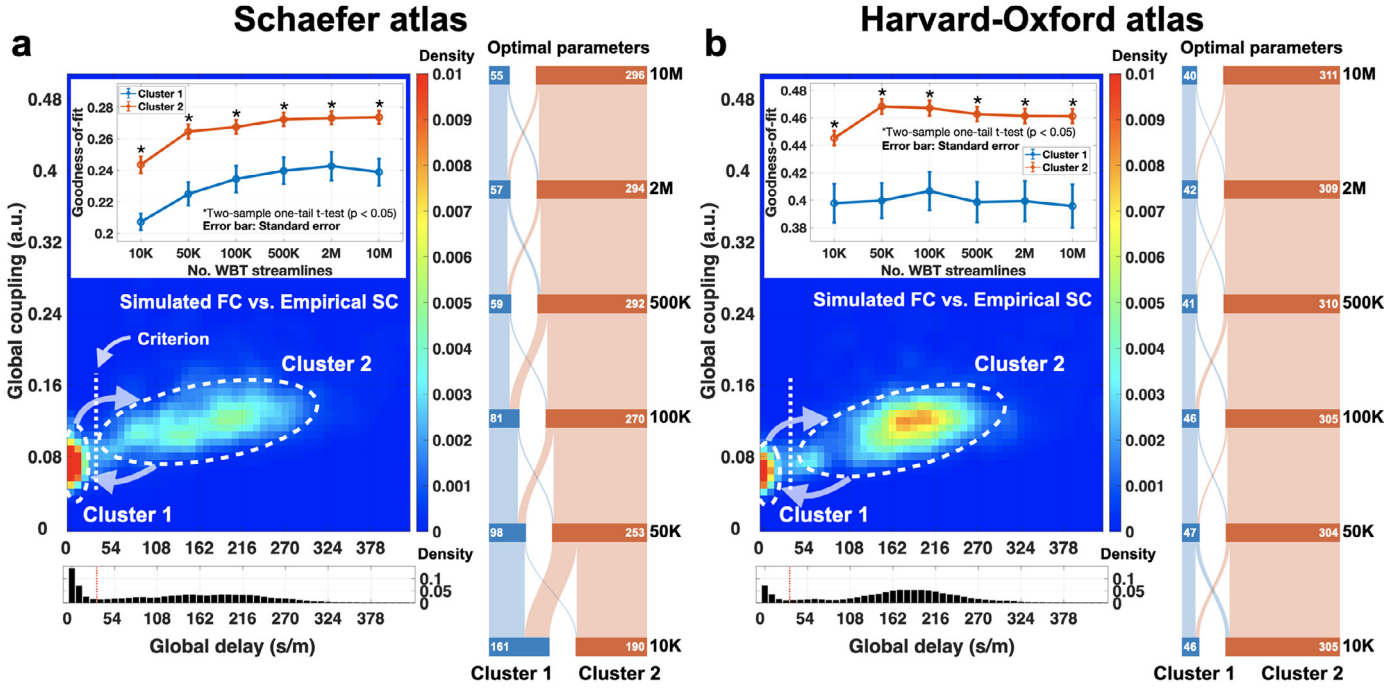

Fig. 6. Clusters of the optimal model parameters of the maximal similarity between simulated FC and empirical SC. The optimal parameters for **(a)** the Schaefer atlas and **(b)** the Harvard-Oxford atlas from Fig 3 f and h, respectively, (n = 2106 values for 351 subjects and 6 WBTs) were split into two subgroups as illustrated in the two lower plots, where the one- and two-dimensional distributions of the optimal parameters are depicted. The upper plots with error bars show the maximal similarity of the functional model fitting between simulated FC and empirical FC of the concatenated fMRI session for the subjects from the two clusters versus the number of the WBT streamlines. The alluvial plots to the right schematically illustrate the interchange of the cluster members when the number of streamlines varies from 10M to 10K. The white numbers in each WBT step indicate the number of subjects in the clusters.

optimal point at 50K of the WBT streamlines. Statistical testing with Wilcoxon signed rank test demonstrated that 100K or more streamlines of pattern 1 showed significantly higher goodness-of-fit values than any sparser WBT condition. However, 50K streamlines of pattern 2 is the optimal condition that shows significantly higher correspondence between the simulated and empirical data than for any other condition, sparser of denser WBT.

Based on the presented results, we can conclude that the optimal number of the WBT streamlines should be considered large (~500K-10M) for the Schaefer atlas (Fig 5a2). Interestingly, the best goodness-of-fit of the model for the Harvard-Oxford atlas can be reached for much sparser WBT at ~50K streamlines for more than 50% of subjects (Fig 5b2).

3.4. *Effects of time delay on model validation*

Based on the clustered distributions of the optimal model parameters of the maximal structure-functional similarity between sFC and eSC (Fig 3 f and h), we divided the optimal parameter points and the corresponding subjects into two clusters (Fig 6). In such a way, the cluster of parameter points with small delay (cluster 1) was split from the other points characterized by relatively large delay (cluster 2) based on their bimodal distributions (Fig 6, the red dotted lines in the histograms in the bottom plots). By dividing the subjects into the two subgroups corresponding to the above clustering of their optimal parameters, we found that the goodness-of-fit values of the functional model fitting are significantly higher in cluster 2 than in cluster 1 consistently for all simulation conditions (all WBTs and both atlases), see Fig 6 (upper plots). Similar effects can also be observed for the structure-functional model fitting between sFC and eSC (see Fig. A6 a2 and b2 in Supplementary materials). The time delay in coupling thus played a constructive role in the model validation against empirical data and led to a better correspondence for structure-functional as well as functional model fitting.

These results also establish a connection between the two fitting modalities and the time delay, where the impact of the latter was not observed in the distributions of the optimal parameters of the functional similarity between sFC and eFC (Fig 3 b and d) and can only be revealed by mediation of the structure-functional correspondence. Another correspondence can be established between the values of the optimal global delays and the natural frequencies of the phase oscillators (Eq 1). To evaluate such a dependence, the broadly distributed positive global delays in cluster 2 were correlated with the mean natural frequencies $\langle f_i \rangle$ averaged over all oscillators (Eq 1). The mean natural frequency of the model is also varying across subjects, and we found a well-pronounced negative correlation between the mean natural frequencies and the optimal delays for the maximal structure-functional similarity between sFC and eSC (see Figs. A7 and A8 in Supplementary materials). This indicates that subjects with slow BOLD oscillations are modeled by system (Eq 1) with large optimal delay if the best correspondence between structure and function has to be achieved.

When the number of the WBT streamlines varies, subjects may exchange their membership in the two clusters (Fig 6, the vertical alluvial plots). Interestingly, for the Schaefer atlas, the ratio of subjects in the two clusters is gradually changing when WBT is getting sparser (from 10M to 10K), where more and more subjects move to cluster 1 approximately balancing the subgroup sizes at 10K case (Fig 6a, the alluvial plot). In contrast, there are only small exchanges of the subjects between clusters for the Harvard-Oxford atlas keeping the group sizes approximately constant for all WBT conditions (Fig 6b, the alluvial plot). Cluster 2 contains most of the subjects as is for both atlases for the case of 10M of the WBT streamlines. We used the splitting of the subjects into the discussed two clusters as the second criterion of the stratification analysis.

It is also important to observe that the structure-functional correspondence between the empirical connectomes eFC and eSC exhibited weak opposite relationships between parameter clusters and across the

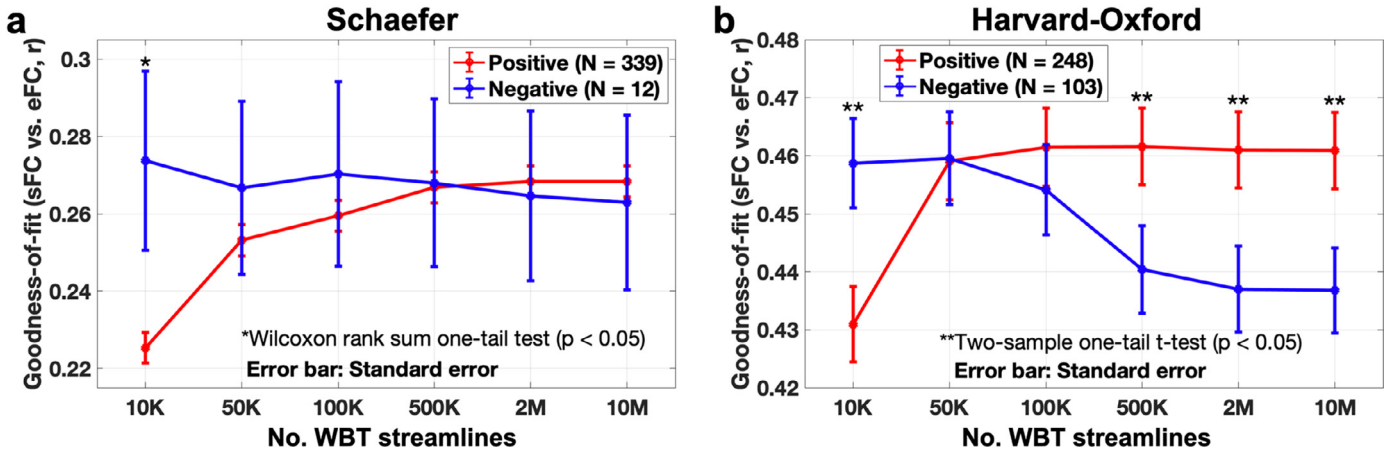

Fig. 7. Subject stratification according to the model performance across 6 WBTs. (a, b) Goodness-of-fit values of the functional correspondence between simulated FC and empirical FC for **(a)** the Schaefer atlas and **(b)** the Harvard-Oxford atlas and for the two groups of the subjects stratified according to the third criterion (see Methods Section 2.3.3). The latter is based on the behavior (positive/negative slopes) of the maximal similarity versus the WBT conditions (see text for details) as indicated in the legends, where the number of subjects in each group is also pointed out. The asterisks indicate the statistically significant differences between the two subject groups ($p < .05$, two-sample one-tail t-test for normal distributions and Wilcoxon rank sum one-tail test for non-parametric test).

number of the WBT streamlines as compared to the correspondence between simulated and empirical data (see Fig. A6 a1 and b1 in Supplementary materials). This indicates a nontrivial character of the reported results that do not directly follow from the empirical structure-function correspondence.

3.5. WBT-Induced changes of model performance

In the previous sections, we observed that the behavior of the goodness-of-fit values versus the WBT conditions is not akin to that of the other atlas. We, therefore, explicitly searched for such divergent dynamics and looked for the subjects with the best model performance for the most sparse or the most dense WBT. The subjects are then split into two subgroups based on the opposite behavior of the model performance when the number of WBT streamlines varies, see Methods (Section 2.3.3) for detail. Figure 7 illustrates the different dynamics of the goodness-of-fit values of the two subgroups of subjects for the two atlases.

As reported before, the maximal similarity between sFC and eFC monotonically increases for the Schaefer atlas when the WBT is getting denser (Figs. 4 - 6). We thus explicitly searched for such conditions, i.e., when the goodness-of-fit was larger for 10M case than for 10K case, and the corresponding line of the model performance had a positive slope. We found that the subjects split very unevenly according to such criterion, and most of them (n = 339) exhibited positive slope, where the similarity between simulated and empirical data monotonically increases when the number of streamlines increases (Fig 7a). Each split subgroup was tested for a normal distribution by χ^2 goodness of fit test over WBT densities. The null hypothesis of the χ^2 test was rejected for each subgroup and each condition. Therefore, we performed Wilcoxon signed rank test. As a result, for the subject subgroup with the positive slope the case of 2M or more WBT streamlines showed significantly higher goodness-of-fit of the model than any sparser WBT condition (Fig 7a, red curve).

In the case of the Harvard-Oxford atlas, the goodness-of-fit values may exhibit a non-monotonic behavior and attained the maximal values at 50K WBTs (Figs. 4 and 5). After stratification according to the third criterion, the both subgroups contain large fractions of the entire subject population with the positive slope (n = 248) and the negative slope (n = 103) (Fig 7b). For the statistic analysis, the null hypothesis of the χ^2 test was not rejected, and we thus performed the two-sample paired t-test. The test resulted in the subgroup with the positive slope showed significantly higher goodness-of-fit of the model with 100K or more WBT streamlines than any sparser WBT condition (Fig 7b, red curve). On the other hand, the subgroup with the negative slope showed significantly higher goodness-of-fit of the model with 50K or less WBT streamlines than any denser WBT condition (Fig 7b, blue curve).

3.6. Stratification analysis

As investigated in the previous sections, the entire subject population can first be split into two groups based on the two patterns of the relationships between network properties and the functional model performance (Fig 5). Second, the subjects can be split based on the clustered distribution of the optimal parameters of the structure-functional maximal similarity between sFC and eSC (Fig 6). Third, different behavior of the goodness-of-fit values of the best correspondence between sFC and eFC can result in positive and negative slopes versus the WBT conditions, which can also be used for subject stratification (Fig 7). By combining all three approaches, we illustrated stratification results in the alluvial plots in Fig 8. Here the proportions of the stratified subjects are shown when the above stratifying criteria are consequently applied to the entire subject population for each atlas. The stratified subjects show different extent and behavior of the goodness-of-fit values of the functional model fitting over the WBT conditions (Fig 8).

In the case of the Schaefer atlas, according to the first criterion, we can expect that subjects of pattern 1 form a relatively small fraction (23%) of the entire subject population, but they have shown higher goodness-of-fit (Fig 5a2 and Fig 8a2). The second stratification step in Fig 8 reflects the interchanging behavior between the parameter clusters observed in Fig 6a. In particular, the stratified group 3 (parameter cluster 2 of large delay) show better performance than the stratified group 2. Finally, the third criterion practically does not differentiate the subjects into positive and negative slopes, see also Fig 7. The declining curves of the goodness-of-fit when the number of the WBT streamlines decreases imply that the optimal number of the total streamlines for the simulation should be considered large, for example, more than 500K: 2M or 10M of the WBT streamlines (Fig 8a2).

For the Harvard-Oxford atlas, subjects stratified into pattern 1 by the first criterion show a monotonic increment of the goodness-of-fit for dense WBT as expected (Fig 8b2, see also Fig 5b2). In addition, we can also expect that the subjects from pattern 2 will have the maximal model performance for sparse WBTs (Fig 5b2 and Fig 8b2). In the second stratification step, the overwhelming majority of subjects from pattern 1 were sorted to the group of persistent members of cluster 2, i.e., the subgroup with large delay for the best structure-functional model fitting

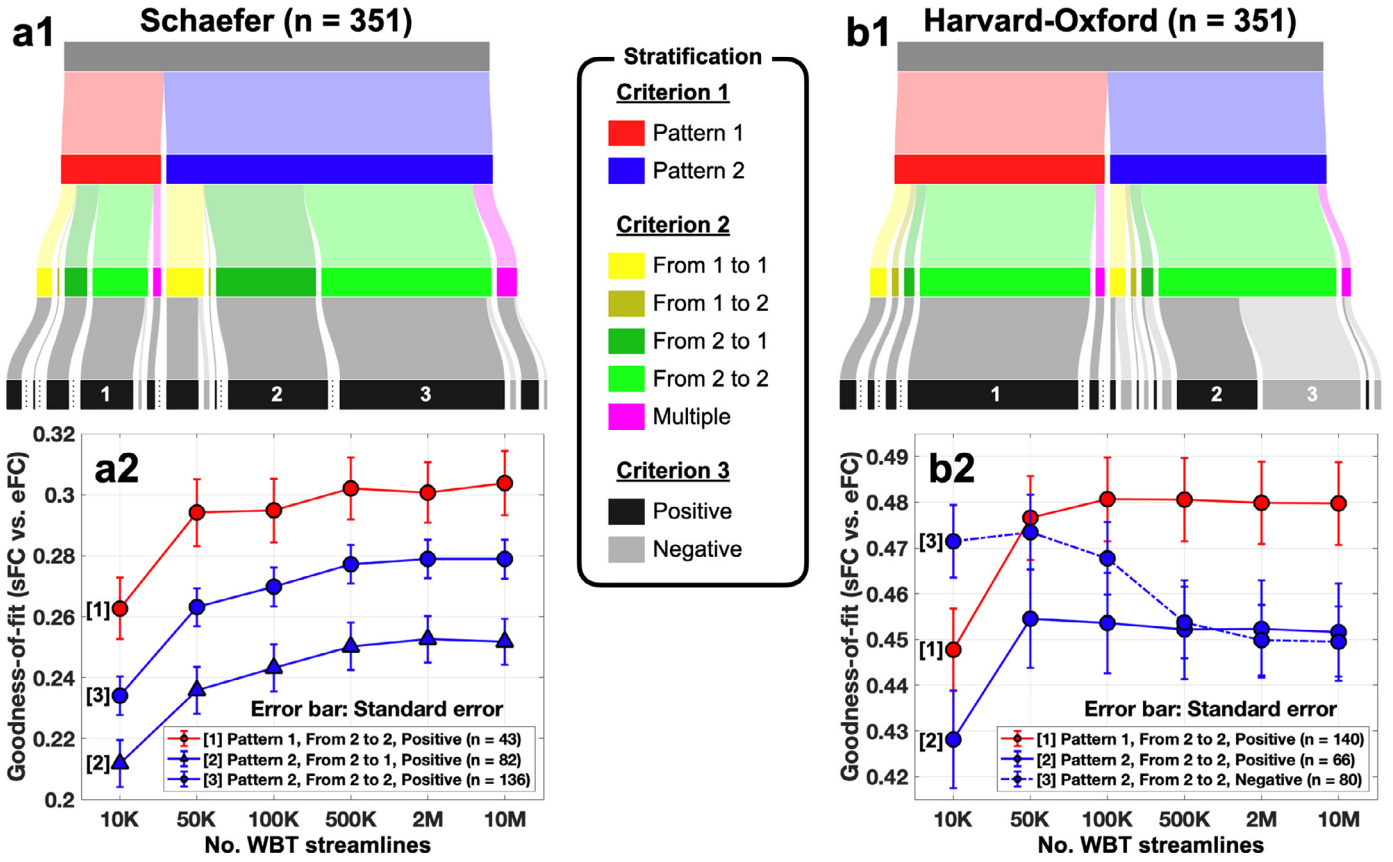

Fig. 8. Stratification analysis with three criteria for two atlases. (a1) The alluvial plot shows all stratified subjects via three criteria and **(a2)** the bottom plot shows goodness-of-fits through 6 WBT conditions for large stratified groups (>35) in the case of the Schaefer atlas. **(b)** The plots by the same analyses for the Harvard-Oxford atlas.

(Fig 8b1, see also Fig 6). Finally, the subjects in pattern 2 can still be split into two subgroups with the inclining and the declining curves of the goodness-of-fit values by the third criterion (Fig 8b2, stratified groups 2 and 3). This can further refine the differentiation of subjects of the best model performance at sparse WBT density (see also Fig 7).

The model evaluation with the Harvard-Oxford atlas shows different optimal conditions than that for the Schaefer atlas (Fig 8b2). The optimal streamline number may depend on the stratification subgroups to which the subject belongs, and which exhibited very different behavior of the goodness-of-fit when the number of streamlines varied (Fig 8b2). For example, the optimal number of streamlines for a better model performance could range from 10M to 100K for the subjects from subgroup 1 in Fig 8b2 (solid red curve). On the other hand, for more than 20% of subjects (n = 80) of the entire subject population, i.e., for those from the stratified group 3 (Fig 8b2, dashed blue curve), the optimal conditions are at ~50K WBT streamlines, and more streamlines may lead to the degradation of the quality of the model validation. For other 18% of subjects (n = 66, group 3 in Fig 8b2, solid blue curve) a sparse WBT can also be a reasonable option.

4. Discussion

The purpose of the current study was to explore how the processing of the neuroimaging data can influence the dynamics and validation of the whole-brain mathematical dynamical models informed by the empirical data. We considered several simulation conditions based on varying data processing parameters, such as the number of total streamlines of WBT and brain atlases. While the latter defined how the brain is parceled into several brain regions that are considered as network nodes in the model, the former influenced the underlying SC (streamline counts) and PL (streamline path lengths) used for the calculation of the coupling weights and time delays in the coupling between nodes. A straightforward interpretation of the investigated number of WBT streamlines as a count of anatomical fiber bundles should be made with caution which was extensively discussed by Jones et al. (2013). Instead, the *reconstructed* streamlines can be considered as a good guess of the white matter connectivity (Caminiti et al., 2013; Jones et al., 2013; Vergani et al., 2014). We discussed how the WBT density can influence the structural information fed to the model and the corresponding modeling results for the considered brain atlases. We found that the parcellation with different atlases showed similar changes of the architecture of the structural networks, but distinct trends of the goodness-of-fit of the model to the empirical data across the number of WBT streamlines. Consequently, we suggested optimal configurations of the considered data and model parameters for the best model fit at the group level as well as for personalized models of individual subjects based on the properties of the empirical and simulated data.

The applied model-based approach followed the line of research suggested and developed in many modeling studies, see, for example, the papers (Breakspear et al., 2010; Cabral et al., 2011; Deco et al., 2017; Fukushima and Sporns, 2018; Honey et al., 2009; Ponce-Alvarez et al., 2015; Popovych et al., 2019) and references therein. The potential of the whole-brain dynamical models to explain the properties of the brain dynamics and structure-function relationship was demonstrated by a detailed investigation of the correspondence between empirical and simulated brain connectomes. At this, the connectivity patterns of the underlying structural network as related to the inter-node coupling strengths and delays can play a crucial role for observing a pronounced structure-function agreement (Popovych et al., 2011; Ton et al., 2014). It is thus important to extract the empirical SC and PL used for evaluation of pa-

rameters of the model connectivity as plausible as possible in order to obtain biologically realistic modeling results (Knock et al., 2009). With this respect, the structure-functional model fitting can be higher than the functional goodness-of-fit as we observed in the current study. One possible explanation might be related to that the empirical SC serves as the underlying backbone of the whole-brain modeling, and simulated FC generated by such models may better replicate the underlying network structure than empirical FC. However, additional investigation is necessary to clarify this question. The current study focuses on the impact of tractography density on the modeling.

4.1. Evaluating structural architecture for modeling

Within the framework of the modeling approach, the model parameters can be varied in a broad range and sense to evaluate their impact on the simulated dynamics. As related to the discussed network topology, beyond the variation of the global coupling strength, the network edges approximating the anatomical connections between brain regions can be removed to obtain a better fit between simulated and empirical FC (Cabral et al., 2012). Aiming at the best correspondence between simulated and empirical data, new inter-region anatomical connections were allowed to be created, or existing structural connections to be rewired according to algorithms based on the differences between the simulated and empirical FC including the gradient-descent method (Deco et al., 2019; 2014). The model connectivity can be composed of both empirical SC extracted from dwMRI data and local intra-cortical connections incorporated into the model based on the distance-dependent approximations (Proix et al., 2016).

Among many possible ways of SC variation for the best model fitting, which might also require additional justifications, we propose to stay within the framework of realistically extracted signals from dwMRI data and consider the well-established approaches for the data processing. In this study, we used state-of-the-art techniques for calculation of WBT and SC (Tournier et al., 2019) and investigated the impact of a constructive parameter for the structural connectome, the number of extracted streamlines on graph-theoretical measures of SC, and their influence on the modeling results.

As discussed in Fig 2 and Table 1, the variation of the WBT density affects the properties of the model networks calculated from the structural connectome, especially, the PL matrices, where the edges with relatively small numbers of streamlines are sensitive to reducing the total number of tracking trials. Therefore, SC extracted from relatively sparse WBT with small number of streamlines may not guarantee a higher reproducibility with stable network properties, where some edges will be disconnected or reconnected from time-to-time, when streamlines will be generated. We, nevertheless, considered an extreme case of 10K WBT streamlines in this study to illustrate the effects observed for very sparse WBT density.

4.2. Graph-theoretical network properties across conditions

For the extraction of the brain structural and functional connectomes and for setting up the model network, we used two paradigmatically distinct brain atlases. These are the Schaefer atlas (Schaefer et al., 2018) that is based on functional MRI data, and the Harvard-Oxford atlas of anatomy-related parcellation (Desikan et al., 2006) that is based on the landscape of gyri and sulci on the cortical surface. We found that the graph-theoretical properties of the structural networks built based on these two parcellations are changing with similar tendencies across the considered WBT conditions for both atlases (Fig 2 and Table 1).

Some of the considered network properties exhibit high sensitivity to the variations of the WBT density, for example, the clustering coefficient (CC) or the local efficiency (LE), see Table 1. On the other hand, the weighted node degree (WD) or the global efficiency (GE) manifested significant changes only when the number of the calculated WBT streamlines was decreased from 10M to 100K or 50K, i.e., 100–200 times. The sensitivity was stronger for the Schaefer atlas. These findings might be of importance when the discussed network properties influence the modeling results. We also found that the mentioned network metrics (CC and LE) with sensitive dependence on the WBT density strongly anti-correlate with the goodness-of-fit of the model for the Schaefer atlas (Fig 5a1), while the dependence is weak with insensitive network measures (WD and GE). Given the impact of the WBT density on the properties of the structural networks (Fig 2), this may explain the clear monotonic behavior of the goodness-of-fit for the Schaefer atlas versus the number of streamlines (Fig 5a2). The situation is different for the Harvard-Oxford atlas, where the relationship with CC and LE is in average less pronounced, whereas the correlation with WD and GE is more enhanced (Fig 5b1). This may explain the apparently mixed behavior of the goodness-of-fit for this brain atlas (Fig 5b2).

In summary, some of the network metrics are characterized by different relationships with the results of the model validation for the varying WBT density for different parcellations, see also supplementary Figs. A3 and A4 for the relationships of all considered network properties. Therefore, even if the tractography density modulates the graph-theoretical network properties in similar changes for the considered atlases as we observed, it can however influence the dynamics of mathematical models in different ways depending on the used brain parcellation.

4.3. Role of time delay in the modeling

It is interesting to note here that the best agreement between simulated and empirical functional data (sFC and eFC) was attained for the considered model at small (zero) delays (Fig 3). It is therefore safe to consider such a type of model simulating ultra slow BOLD dynamics without delay in coupling (Deco et al., 2019; 2017; Ponce-Alvarez et al., 2015). Nevertheless, the goodness-of-fit for the model with delay (including zero delay) exhibits around 9% larger values than that without delay (zero delay only), see Fig. A9 a and b in Supplementary materials. On the other hand, the role of delay in coupling is apparent for the structure-functional (sFC-eSC) model fitting, where the correspondence between sFC and eSC is also enhanced by around 14% for the model with delay when compared to the case without delay (Fig. A9 c and d in Supplementary materials).

We also reported on the clustered distributions of the optimal model parameters for the structure-functional model fitting sFC-eSC and their behavior (migration between clusters) when the WBT density varies for the two considered brain atlases (Fig 6). Such a behavior of the optimal parameters might be related to the performance of the model at the group level. Indeed, we observed that subjects from the parameter cluster with large delay demonstrated better quality of the model validation for both functional and structure-functional model fittings (Fig 6 and supplementary Fig. A6). In other words, if the optimal parameters for the maximal sFC-eSC correspondence have a large delay, we might expect a better correspondence between sFC and eFC. Accordingly, we might also expect that the group-averaged goodness-of-fit for the Schaefer atlas will decay faster than that for the Harvard-Oxford atlas when the number of streamlines decreases as observed in Fig 4. This is because parameter points (subjects) migrate to the cluster with small delay, and fewer optimal parameter points with large delay can be found for a sparser WBT for the Schaefer atlas. These arguments can suggest a possible mechanism associated with the impact of time delay in coupling on the model fitting results.

The values of the optimal non-zero delays for the structure-functional fitting modality can be influenced by the natural frequencies of oscillators (Eq 1) demonstrating relatively strong negative correlations with the structure-functional model fitting as illustrated in supplementary Figs. A7 and A8. Therefore, the average frequency of BOLD oscillation for a given subject can influence the values of the optimal delay for the best structure-functional correspondence. The parameter of the global delay scales the average velocity of signal propagation between brain regions. Consequently, the optimal speed of the signal propagation in the

brain as revealed by the modeling results can be regulated by the mean intrinsic time scale of oscillatory activity of individual brain regions.

4.4. Stratification analysis and optimal conditions

The problem of the optimal number of the total WBT streamlines was also addressed in this study beyond the group-level analysis and aimed at the best fitting of the personalized models for individual subjects. To investigate the impact of the WBT density at the level of individual subjects, we stratified the entire subject population into smaller subgroups with more homogeneous (heterogeneous) model dynamics within (between) subgroups. One of the stratification approaches is to show the effect of the graph-theoretical network properties modulated by the WBT density on performance of the model. We found that such correlations for individual subjects are well-pronounced for the Schaefer atlas, but they are somewhat less expressed for the Harvard-Oxford atlas (Fig 5 a1 and b1). Nevertheless, the stratification can be designed by combining the splitting results for different network properties, which resulted in a clear differentiation of the impact of the WBT streamline number on the model validation across stratified subgroups and brain parcellations (Fig 5).

Another approach to stratification of the subjects was based on the clustering of the optimal delay for the structure-functional model fitting discussed above. It can provide an informed view on the validation results for the functional model fitting (Fig 6). One more stratification approach is illustrated in Fig 7, where the subjects were split into two subgroups of qualitatively different individual behavior of the goodness-of-fit versus the streamline number. Based on the obtained results, we can propose to use the large number (~2M-10M) of the WBT streamlines for the best functional model validation, if the Schaefer atlas was used for the brain parcellation.

On the other hand, the recommendation is completely opposite for more than 20% of subjects for the brain parcellation based on the Harvard-Oxford atlas (Fig 8b2, blue dashed curve 3). For such subjects, the large number of streamlines can lead to a lower quality of the model fitting as compared to rather sparse WBT containing, for example, only 50K streamlines. Differentiating the subjects according to the discussed stratification criteria can help to design an individual data processing workflow and configurations of parameters for the optimal personalized modeling of the brain dynamics. In particular, based on the obtained results, we can suggest a personalized optimal number of the WBT streamlines for the considered brain parcellation for the better model performance at the modeling of the resting-state brain dynamics.

Based on the results of the stratification analysis, we may suggest a few tentative guidelines to possible evaluation of personalized optimal number of the WBT streamlines for the whole-brain model of the resting-state brain dynamics.

- Around 50K WBT streamlines can be considered as a sparse WBT condition.
- More than 2M WBT streamlines can be considered as a dense WBT condition.
- Graph-theoretical network properties of the structural connectome can influence the goodness-of-fit of the model over different tractography densities. Such relationships to the data variables may contribute to the mechanism of the fitting variability and subject stratification into qualitatively different subgroups.
- Modeling with time delay in coupling can enhance goodness-of-fit of the model.
- A dense WBT is not always the best condition for the whole-brain modeling.
- Brain parcellation may affect the optimal parameters of the data processing and should be taken into account already at early stages of the data analytics.

To understand the underlying mechanism of the stratification results, more detailed investigation aimed at quantitative validations and generalization of the results should be performed. From the results of the current study we can already conclude that optimal configurations of the data processing and quantitative guidelines are important for personalized data processing and modeling.

4.5. Limitations and future direction

Although we used the data with high quality of the data preprocessing and physiological noise reduction, however, we note that the reported results were obtained from the neuroimaging data of young adults with relatively narrow age ranges. In order to generalize our conclusions, they have to be verified for other datasets with broader distribution of the phenotypic parameters and other data quality such as clinical-grade scans.

The current study used empirical FC based on the resting-state fMRI measurements for evaluation of the model performance. Regarding other data modalities, future works can include electrophysiological data with electrical modeling for general outcomes. Furthermore, other fitting modalities can also be possible metrics to evaluate whole-brain modeling, for instance, dynamic FC or effective connectivity. Detailed investigation under such conditions can contribute to a better coverage and optimization of the model validation for personalized modeling.

5. Summary and conclusion

We found that varying number of total streamlines for WBT affects the network properties of the structural connectome and performance of the mathematical modeling of the resting-state brain dynamics. The results showed that a dense WBT is not always the best condition for the whole-brain mathematical modeling represented by a system of interacting oscillators with time delay in coupling. We also demonstrated that the optimal parameters of the data processing may be affected by the utilized brain parcellation that should be taken into account already at early steps of the data processing workflow. The present study did not aim to provide any quantitative conclusion concerning the optimal number of WBT streamlines, but rather to illustrate possible qualitative effects caused by the varying WBT density on the structural connectome and modeling results in combination with functional and anatomical brain parcellations. Our results can contribute to a better understanding of the interplay between the data processing and model parameters and their influence on data analytics of dwMRI and modeling of the resting-state fMRI data.

Data and Code Availability Statement

Anonymized data are publicly available from ConnectomeDB (https://db.humanconnectome.org).

The structural connectivity pipeline is available from GitHub (https://github.com/inm7/vbc_dwmri).

Declaration of Competing Interest

The authors have declared that no competing interests exist.

Credit authorship contribution statement

Kyesam Jung: Conceptualization, Data curation, Formal analysis, Investigation, Methodology, Software, Validation, Visualization, Writing - original draft, Writing - review & editing. **Simon B. Eickhoff:** Conceptualization, Funding acquisition, Resources, Writing - review & editing. **Oleksandr V. Popovych:** Conceptualization, Data curation, Funding acquisition, Methodology, Project administration, Resources, Software, Supervision, Validation, Writing - review & editing.

Acknowlgedgments

The authors are grateful to Esther Florin for fruitful discussions, helpful comments on the manuscript and advices concerning statistical analysis. The authors gratefully acknowledge the computing time granted through JARA on the supercomputer JURECA at Forschungszentrum Jülich. This work was supported by the Portfolio Theme Supercomputing and Modeling for the Human Brain by the Helmholtz association (https://www.helmholtz.de/en), the Human Brain Project, and the European Union's Horizon 2020 Research and Innovation Programme (https://cordis.europa.eu) under Grant Agreements 720270 (HBP SGA1), 785907 (HBP SGA2), 945539 (HBP SGA3), and 826421 (VirtualBrainCloud). The funders had no role in study design, data collection and analysis, decision to publish, or preparation of the manuscript.

Data were provided S1200 by the Human Connectome Project, WU-Minn Consortium (Principal Investigators: David Van Essen and Kamil Ugurbil; 1U54MH091657) funded by the 16 NIH Institutes and Centers that support the NIH Blueprint for Neuroscience Research; and by the McDonnell Center for Systems Neuroscience at Washington University.

Supplementary material

Supplementary material associated with this article can be found, in the online version, at 10.1016/j.neuroimage.2021.118176

References

Bajada, C.J., Schreiber, J., Caspers, S., 2019. Fiber length profiling: a novel approach to structural brain organization. Neuroimage 186, 164–173. doi:10.1016/j.neuroimage.2018.10.070.

Bassett, D.S., Brown, J.A., Deshpande, V., Carlson, J.M., Grafton, S.T., 2011. Conserved and variable architecture of human white matter connectivity. Neuroimage 54 (2), 1262–1279. doi:10.1016/j.neuroimage.2010.09.006.

Bassett, D.S., Zurn, P., Gold, J.I., 2018. On the nature and use of models in network neuroscience. Nat. Rev. Neurosci. 19 (9), 566–578. doi:10.1038/s41583-018-0038-8.

Bellec, P., Benhajali, Y., Carbonell, F., Dansereau, C., Albouy, G., Pelland, M., Craddock, C., Collignon, O., Doyon, J., Stip, E., Orban, P., 2015. Impact of the resolution of brain parcels on connectome-wide association studies in fmri. Neuroimage 123, 212–228. doi:10.1016/j.neuroimage.2015.07.071.

Breakspear, M., Heitmann, S., Daffertshofer, A., 2010. Generative models of cortical oscillations: neurobiological implications of the kuramoto model. Front. Hum. Neurosci. 4. doi:10.3389/fnhum.2010.00190.

Buchanan, C.R., Pernet, C.R., Gorgolewski, K.J., Storkey, A.J., Bastin, M.E., 2014. Test–retest reliability of structural brain networks from diffusion mri. Neuroimage 86, 231–243. doi:10.1016/j.neuroimage.2013.09.054.

Buzsaki, G., 2011. Rhythms of the brain. Cary: Oxford University Press doi:10.1093/acprof:oso/9780195301069.001.0001.

Cabral, J., Hugues, E., Kringelbach, M.L., Deco, G., 2012. Modeling the outcome of structural disconnection on resting-state functional connectivity. Neuroimage 62 (3), 1342—1353. doi:10.1016/j.neuroimage.2012.06.007.

Cabral, J., Hugues, E., Sporns, O., Deco, G., 2011. Role of local network oscillations in resting-state functional connectivity. Neuroimage 57 (1), 130–139. doi:10.1016/j.neuroimage.2011.04.010.

Caminiti, R., Carducci, F., Piervincenzi, C., Battaglia-Mayer, A., Confalone, G., Visco-Comandini, F., Pantano, P., Innocenti, G., 2013. Diameter, length, speed, and conduction delay of callosal axons in macaque monkeys and humans: comparing data from histology and magnetic resonance imaging diffusion tractography. J. Neurosci. 33 (36), 14501–14511. doi:10.1523/JNEUROSCI.0761-13.2013.

Cammoun, L., Gigandet, X., Meskaldji, D., Thiran, J.P., Sporns, O., Do, K.Q., Maeder, P., Meuli, R., Hagmann, P., 2012. Mapping the human connectome at multiple scales with diffusion spectrum mri. J. Neurosci. Methods 203 (2), 386–397. doi:10.1016/j.jneumeth.2011.09.031.

Dale, A.M., Fischl, B., Sereno, M.I., 1999. Cortical surface-based analysis: i. segmentation and surface reconstruction. Neuroimage 9 (2), 179–194. doi:10.1006/nimg.1998.0395.

Deco, G., Cruzat, J., Cabral, J., Tagliazucchi, E., Laufs, H., Logothetis, N.K., Kringelbach, M.L., 2019. Awakening: predicting external stimulation to force transitions between different brain states. PNAS; Proceedings of the National Academy of Sciences 116 (36), 18088–18097. doi:10.1073/pnas.1905534116.

Deco, G., Jirsa, V.K., Robinson, P.A., Breakspear, M., Friston, K., 2008. The dynamic brain: from spiking neurons to neural masses and cortical fields. PLoS Comput. Biol. 4 (8), e1000092. doi:10.1371/journal.pcbi.1000092.

Deco, G., Kringelbach, M.L., 2016. Metastability and coherence: extending the communication through coherence hypothesis using a whole-brain computational perspective. Trends Neurosci. 39 (3), 125–135. doi:10.1016/j.tins.2016.01.001.

Deco, G., Kringelbach, M.L., Jirsa, V.K., Ritter, P., 2017. The dynamics of resting fluctuations in the brain: metastability and its dynamical cortical core. Sci. Rep. 7 (1). doi:10.1038/s41598-017-03073-5.

Deco, G., McIntosh, A.R., Shen, K., Hutchison, R.M., Menon, R.S., Everling, S., Hagmann, P., Jirsa, V.K., 2014. Identification of optimal structural connectivity using functional connectivity and neural modeling. J. Neurosci. 34 (23), 7910—7916. doi:10.1523/JNEUROSCI.4423-13.2014.

Dennis, E.L., Jahanshad, N., Toga, A.W., McMahon, K.L., de Zubicaray, G.I., Martin, N.G., Wright, M.J., Thompson, P.M., 2012. Test-retest reliability of graph theory measures of structural brain connectivity. In: Ayache, N., Delingette, H., Golland, P., Mori, K. (Eds.), Medical Image Computing and Computer-Assisted Intervention – MICCAI 2012. Springer Berlin Heidelberg, Berlin, Heidelberg, pp. 305–312. doi:10.1007/978-3-642-33454-2_38.

Desikan, R.S., Ségonne, F., Fischl, B., Quinn, B.T., Dickerson, B.C., Blacker, D., Buckner, R.L., Dale, A.M., Maguire, R.P., Hyman, B.T., Albert, M.S., Killiany, R.J., 2006. An automated labeling system for subdividing the human cerebral cortex on mri scans into gyral based regions of interest. Neuroimage 31 (3), 968–980. doi:10.1016/j.neuroimage.2006.01.021.

Endo, H., Hiroe, N., Yamashita, O., 2020. Evaluation of resting spatio-temporal dynamics of a neural mass model using resting fmri connectivity and EEG microstates. Front. Comput. Neurosci. 13. doi:10.3389/fncom.2019.00091.

Freeman, W.J., 1987. Simulation of chaotic EEG patterns with a dynamic model of the olfactory system. Biol. Cybern. 56 (2–3), 139–150. doi:10.1007/bf00317988.

Fukushima, M., Sporns, O., 2018. Comparison of fluctuations in global network topology of modeled and empirical brain functional connectivity. PLoS Comput. Biol. 14 (9), e1006497. doi:10.1371/journal.pcbi.1006497.

Goñi, J., van den Heuvel, M.P., Avena-Koenigsberger, A., Velez de Mendizabal, N., Betzel, R.F., Griffa, A., Hagmann, P., Corominas-Murtra, B., Thiran, J.-P., Sporns, O., 2014. Resting-brain functional connectivity predicted by analytic measures of network communication. PNAS; Proceedings of the National Academy of Sciences 111 (2), 833. doi:10.1073/pnas.1315529111.

Griffanti, L., Salimi-Khorshidi, G., Beckmann, C.F., Auerbach, E.J., Douaud, G., Sexton, C.E., Zsoldos, E., Ebmeier, K.P., Filippini, N., Mackay, C.E., Moeller, S., Xu, J., Yacoub, E., Baselli, G., Ugurbil, K., Miller, K.L., Smith, S.M., 2014. Ica-based artefact removal and accelerated fmri acquisition for improved resting state network imaging. Neuroimage 95, 232–247. doi:10.1016/j.neuroimage.2014.03.034.

Hagmann, P., Cammoun, L., Gigandet, X., Meuli, R., Honey, C.J., Wedeen, V.J., Sporns, O., 2008. Mapping the structural core of human cerebral cortex. PLoS Biol. 6 (7), e159. doi:10.1371/journal.pbio.0060159.

van den Heuvel, M.P., Sporns, O., 2011. Rich-club organization of the human connectome. J. Neurosci. 31 (44), 15775–15786. doi:10.1523/JNEUROSCI.3539-11.2011.

Hodgkin, A.L., Huxley, A.F., 1952. A quantitative description of membrane current and its application to conduction and excitation in nerve. J. Physiol. (Lond.) 117 (4), 500–544. doi:10.1113/jphysiol.1952.sp004764.

Honey, C., Sporns, O., Cammoun, L., Gigandet, X., Thiran, J., Meuli, R., Hagmann, P., 2009. Predicting human resting-state functional connectivity from structural connectivity. PNAS; Proceedings of the National Academy of Sciences 106 (6), 2035–2040. doi:10.1073/pnas.0811168106.

Jansen, B.H., Rit, V.G., 1995. Electroencephalogram and visual evoked potential generation in a mathematical model of coupled cortical columns. Biol. Cybern. 73 (4), 357–366. doi:10.1007/bf00199471.

Jeurissen, B., Tournier, J.-D., Dhollander, T., Connelly, A., Sijbers, J., 2014. Multi-tissue constrained spherical deconvolution for improved analysis of multi-shell diffusion mri data. Neuroimage 103, 411–426. doi:10.1016/j.neuroimage.2014.07.061.

Jones, D.K., Knösche, T.R., Turner, R., 2013. White matter integrity, fiber count, and other fallacies: the do's and don'ts of diffusion mri. Neuroimage 73, 239–254. doi:10.1016/j.neuroimage.2012.06.081.

Jülich Supercomputing Centre, 2018. JURECA: Modular supercomputer at jülich supercomputing centre. Journal of large-scale research facilities 4 (A132). doi:10.17815/jlsrf-4-121-1.

Knock, S.A., McIntosh, A.R., Sporns, O., Kotter, R., Hagmann, P., Jirsa, V.K., 2009. The effects of physiologically plausible connectivity structure on local and global dynamics in large scale brain models. J. Neurosci. Methods 183, 86–94. doi:10.1016/j.jneumeth.2009.07.007.

Kuramoto, Y., 1984. Chemical oscillations, waves, and turbulence. Springer Berlin Heidelberg doi:10.1007/978-3-642-69689-3.

Lindquist, M., 2020. Neuroimaging results altered by varying analysis pipelines. Nature 582 (7810), 36–37. doi:10.1038/d41586-020-01282-z.

Maier-Hein, K.H., Neher, P.F., Houde, J.-C., Côté, M.-A., Garyfallidis, E., Zhong, J., Chamberland, M., Yeh, F.-C., Lin, Y.-C., Ji, Q., Reddick, W.E., Glass, J.O., Chen, D.Q., Feng, Y., Gao, C., Wu, Y., Ma, J., He, R., Li, Q., Westin, C.-F., Deslauriers-Gauthier, S., González, J.O.O., Paquette, M., St-Jean, S., Girard, G., Rheault, F., Sidhu, J., Tax, C.M.W., Guo, F., Mesri, H.Y., Dávid, S., Froeling, M., Heemskerk, A.M., Leemans, A., Boré, A., Pinsard, B., Bedetti, C., Desrosiers, M., Brambati, S., Doyon, J., Sarica, A., Vasta, R., Cerasa, A., Quattrone, A., Yeatman, J., Khan, A.R., Hodges, W., Alexander, S., Romascano, D., Barakovic, M., Auría, A., Esteban, O., Lemkaddem, A., Thiran, J.-P., Cetingul, H.E., Odry, B.L., Mailhe, B., Nadar, M.S., Pizzagalli, F., Prasad, G., Villalon-Reina, J.E., Galvis, J., Thompson, P.M., Requejo, F.D.S., Laguna, P.L., Lacerda, L.M., Barrett, R., Dell'Acqua, F., Catani, M., Petit, L., Caruyer, E., Daducci, A., Dyrby, T.B., Holland-Letz, T., Hilgetag, C.C., Stieltjes, B., Descoteaux, M., 2017. The challenge of mapping the human connectome based on diffusion tractography. Nat. Commun. 8 (1). doi:10.1038/s41467-017-01285-x.

Messaritaki, E., Dimitriadis, S.I., Jones, D.K., 2019. Optimization of graph construction can significantly increase the power of structural brain network studies. Neuroimage 199, 495–511. doi:10.1016/j.neuroimage.2019.05.052.

Owen, J.P., Ziv, E., Bukshpun, P., Pojman, N., Wakahiro, M., Berman, J.I., Roberts, T.P., Friedman, E.J., Sherr, E.H., Mukherjee, P., 2013. Test–retest reliability of computational network measurements derived from the structural connectome of the human brain. Brain Connect. 3 (2), 160–176. doi:10.1089/brain.2012.0121.

Parkes, L., Fulcher, B., Yücel, M., Fornito, A., 2018. An evaluation of the efficacy, reliability, and sensitivity of motion correction strategies for resting-state functional mri. Neuroimage 171, 415–436. doi:10.1016/j.neuroimage.2017.12.073.

Ponce-Alvarez, A., Deco, G., Hagmann, P., Romani, G.L., Mantini, D., Corbetta, M., 2015. Resting-state temporal synchronization networks emerge from connectivity topology and heterogeneity. PLoS Comput. Biol. 11 (2), e1004100. doi:10.1371/journal.pcbi.1004100.

Popovych, O.V., Manos, T., Hoffstaedter, F., Eickhoff, S.B., 2019. What can computational models contribute to neuroimaging data analytics? Front. Syst. Neurosci. 12. doi:10.3389/fnsys.2018.00068.

Popovych, O.V., Yanchuk, S., Tass, P.A., 2011. Delay- and coupling-induced firing patterns in oscillatory neural loops. Phys. Rev. Lett. 107, 228102. doi:10.1103/PhysRevLett.107.228102.

Prasad, G., Nir, T.M., Toga, A.W., Thompson, P.M., 2013. Tractography density and network measures in alzheimer's disease. In: 2013 IEEE 10th International Symposium on Biomedical Imaging, pp. 692–695. doi:10.1109/ISBI.2013.6556569.

Proix, T., Spiegler, A., Schirner, M., Rothmeier, S., Ritter, P., Jirsa, V.K., 2016. How do parcellation size and short-range connectivity affect dynamics in large-scale brain network models? Neuroimage 142, 135–149. doi:10.1016/j.neuroimage.2016.06.016.

Qi, S., Meesters, S., Nicolay, K., ter Haar Romeny, B.M., Ossenblok, P., 2015. The influence of construction methodology on structural brain network measures: a review. J. Neurosci. Methods 253, 170–182. doi:10.1016/j.jneumeth.2015.06.016.

Rodrigues, F.A., Peron, T.K.D., Ji, P., Kurths, J., 2016. The kuramoto model in complex networks. Phys Rep 610, 1–98. doi:10.1016/j.physrep.2015.10.008.

Roine, T., Jeurissen, B., Perrone, D., Aelterman, J., Philips, W., Sijbers, J., Leemans, A., 2019. Reproducibility and intercorrelation of graph theoretical measures in structural brain connectivity networks. Med. Image Anal. 52, 56–67. doi:10.1016/j.media.2018.10.009.

Rubinov, M., Sporns, O., 2010. Complex network measures of brain connectivity: uses and interpretations. Neuroimage 52 (3), 1059–1069. doi:10.1016/j.neuroimage.2009.10.003.

Schaefer, A., Kong, R., Gordon, E.M., Laumann, T.O., Zuo, X.-N., Holmes, A.J., Eickhoff, S.B., Yeo, B.T.T., 2018. Local-Global parcellation of the human cerebral cortex from intrinsic functional connectivity MRI. Cerebral Cortex 28 (9), 3095–3114. doi:10.1093/cercor/bhx179.

Schilling, K.G., Nath, V., Hansen, C., Parvathaneni, P., Blaber, J., Gao, Y., Neher, P., Aydogan, D.B., Shi, Y., Ocampo-Pineda, M., Schiavi, S., Daducci, A., Girard, G., Barakovic, M., Rafael-Patino, J., Romascano, D., Rensonnet, G., Pizzolato, M., Bates, A., Fischi, E., Thiran, J.-P., Canales-Rodríguez, E.J., Huang, C., Zhu, H., Zhong, L., Cabeen, R., Toga, A.W., Rheault, F., Theaud, G., Houde, J.-C., Sidhu, J., Chamberland, M., Westin, C.-F., Dyrby, T.B., Verma, R., Rathi, Y., Irfanoglu, M.O., Thomas, C., Pierpaoli, C., Descoteaux, M., Anderson, A.W., Landman, B.A., 2019. Limits to anatomical accuracy of diffusion tractography using modern approaches. Neuroimage 185, 1–11. doi:10.1016/j.neuroimage.2018.10.029.

Smith, S.M., Beckmann, C.F., Andersson, J., Auerbach, E.J., Bijsterbosch, J., Douaud, G., Duff, E., Feinberg, D.A., Griffanti, L., Harms, M.P., Kelly, M., Laumann, T., Miller, K.L., Moeller, S., Petersen, S., Power, J., Salimi-Khorshidi, G., Snyder, A.Z., Vu, A.T., Woolrich, M.W., Xu, J., Yacoub, E., Ugurbil, K., Van Essen, D.C., Glasser, M.F., 2013. Resting-state fmri in the human connectome project. Neuroimage 80, 144–168. doi:10.1016/j.neuroimage.2013.05.039.

Smith, S.M., Jenkinson, M., Woolrich, M.W., Beckmann, C.F., Behrens, T.E., Johansen-Berg, H., Bannister, P.R., De Luca, M., Drobnjak, I., Flitney, D.E., Niazy, R.K., Saunders, J., Vickers, J., Zhang, Y., De Stefano, N., Brady, J.M., Matthews, P.M., 2004. Advances in functional and structural mr image analysis and implementation as fsl. Neuroimage 23, S208–S219. doi:10.1016/j.neuroimage.2004.07.051.

Sotiropoulos, S.N., Zalesky, A., 2019. Building connectomes using diffusion mri: why, how and but. NMR Biomed. 32 (4), e3752. doi:10.1002/nbm.3752.

Sporns, O., 2011. The human connectome: a complex network. Ann. N. Y. Acad. Sci. 1224 (1), 109–125. doi:10.1111/j.1749-6632.2010.05888.x.

Sporns, O., Tononi, G., Kötter, R., 2005. The human connectome: a structural description of the human brain. PLoS Comput. Biol. 1 (4). doi:10.1371/journal.pcbi.0010042.

Suárez, L.E., Markello, R.D., Betzel, R.F., Misic, B., 2020. Linking structure and function in macroscale brain networks. Trends Cogn. Sci. (Regul. Ed.) 24 (4), 302–315. doi:10.1016/j.tics.2020.01.008.

Thirion, B., Varoquaux, G., Dohmatob, E., Poline, J.-B., 2014. Which fmri clustering gives good brain parcellations? Front. Neurosci. 8, 167. doi:10.3389/fnins.2014.00167.

Ton, R., Deco, G., Daffertshofer, A., 2014. Structure-function discrepancy: inhomogeneity and delays in synchronized neural networks. PLoS Comput. Biol. 10 (7), e1003736. doi:10.1371/journal.pcbi.1003736.

Tournier, J.D., Calamante, F., Connelly, A., 2010. Improved probabilistic streamlines tractography by 2nd order integration over fibre orientation distributions. In: Proceedings of the international society for magnetic resonance in medicine, 1670. ISMRM.

Tournier, J.-D., Smith, R., Raffelt, D., Tabbara, R., Dhollander, T., Pietsch, M., Christiaens, D., Jeurissen, B., Yeh, C.-H., Connelly, A., 2019. Mrtrix3: a fast, flexible and open software framework for medical image processing and visualisation. Neuroimage 202, 116137. doi:10.1016/j.neuroimage.2019.116137.

Tustison, N.J., Avants, B.B., Cook, P.A., Zheng, Y., Egan, A., Yushkevich, P.A., Gee, J.C., 2010. N4itk: Improved n3 bias correction. IEEE Trans. Med. Imaging 29 (6), 1310–1320. doi:10.1109/TMI.2010.2046908.

Van Essen, D.C., Smith, S.M., Barch, D.M., Behrens, T.E., Yacoub, E., Ugurbil, K., 2013. The wu-minn human connectome project: an overview. Neuroimage 80, 62–79. doi:10.1016/j.neuroimage.2013.05.041.

Vergani, F., Lacerda, L., Martino, J., Attems, J., Morris, C., Mitchell, P., de Schotten, M.T., Dell'Acqua, F., 2014. White matter connections of the supplementary motor area in humans. Journal of Neurology, Neurosurgery & Psychiatry 85 (12), 1377–1385. doi:10.1136/jnnp-2013-307492.

Wilson, H.R., Cowan, J.D., 1973. A mathematical theory of the functional dynamics of cortical and thalamic nervous tissue. Kybernetik 13 (2), 55–80. doi:10.1007/bf00288786.

Yeung, M.K.S., Strogatz, S.H., 1999. Time delay in the kuramoto model of coupled oscillators. Phys. Rev. Lett. 82, 648–651. doi:10.1103/PhysRevLett.82.648.

Zimmermann, J., Perry, A., Breakspear, M., Schirner, M., Sachdev, P., Wen, W., Kochan, N., Mapstone, M., Ritter, P., McIntosh, A., Solodkin, A., 2018. Differentiation of alzheimer's disease based on local and global parameters in personalized virtual brain models. NeuroImage: Clinical 19, 240–251. doi:10.1016/j.nicl.2018.04.017.

A. Supplementary materials

Fig. A1 Average binarized node degrees over the WBT conditions for **(a)** the Schaefer atlas and **(b)** the Harvard-Oxford atlas.

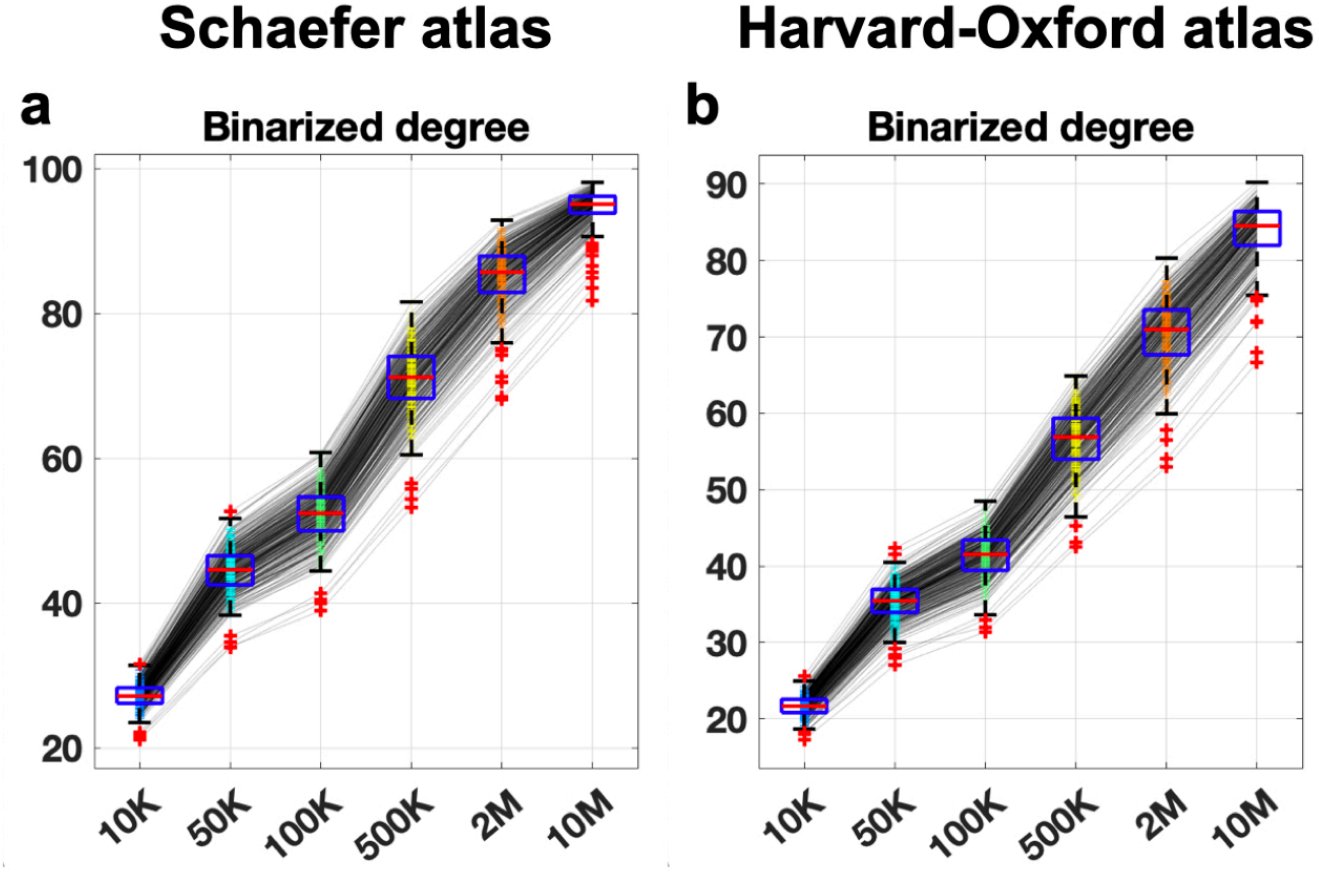

Fig. A2 Relationships between the network properties and the results of the maximal functional model fitting (sFC vs. eFC) for individual subjects and 5 sessions for **(a)** the Schaefer atlas and **(b)** the Harvard-Oxford atlas. Correlation coefficients of merged z-scored all sessions between the network properties and the maximal functional model fitting for **(c)** the Schaefer atlas and **(d)** the Harvard-Oxford atlas. The asterisks below the x-axes indicate statistically significant differences in the goodness-of-fit values between the two subgroups of subjects with positive and negative correlations ($p < 0.05$ of two-sample one-tail t-test). **(a2, b2)** The gray dots represent the values for individual subjects, and the box plots illustrate the medians (red lines), the interquartile ranges (blue boxes) and the outliers (red pluses). Abbreviations of the network property names: binarized node degree (BD), weighted node degree (WD), clustering coefficient (CC), betweenness centrality (BC), local efficiency (LE), global efficiency (GE), and modularity Q (MQ).

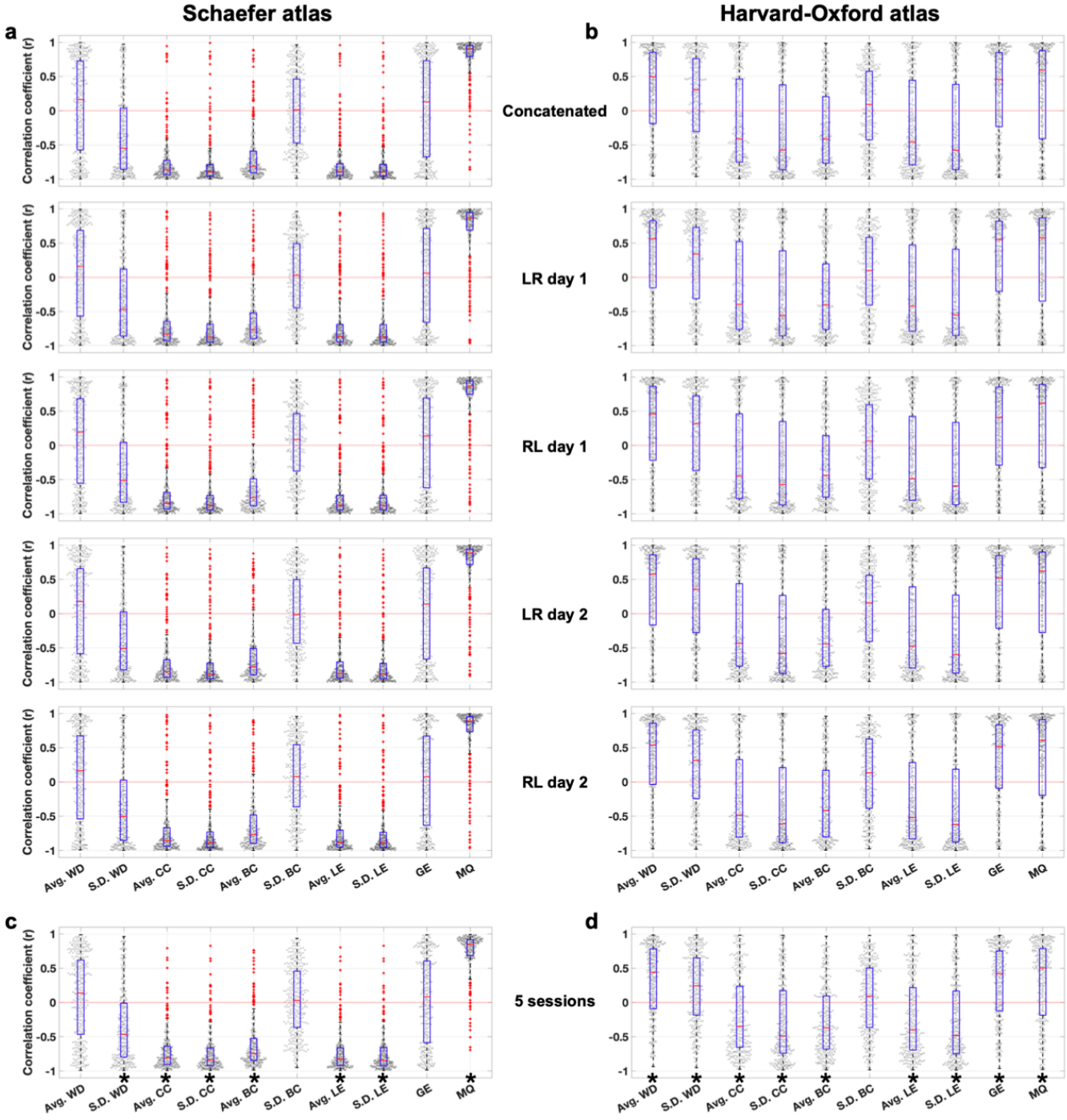

Fig. A3 Pearson correlation coefficients between network properties and the goodness-of-fit of the model (similarity between sFC and eFC) for the Schaefer atlas.

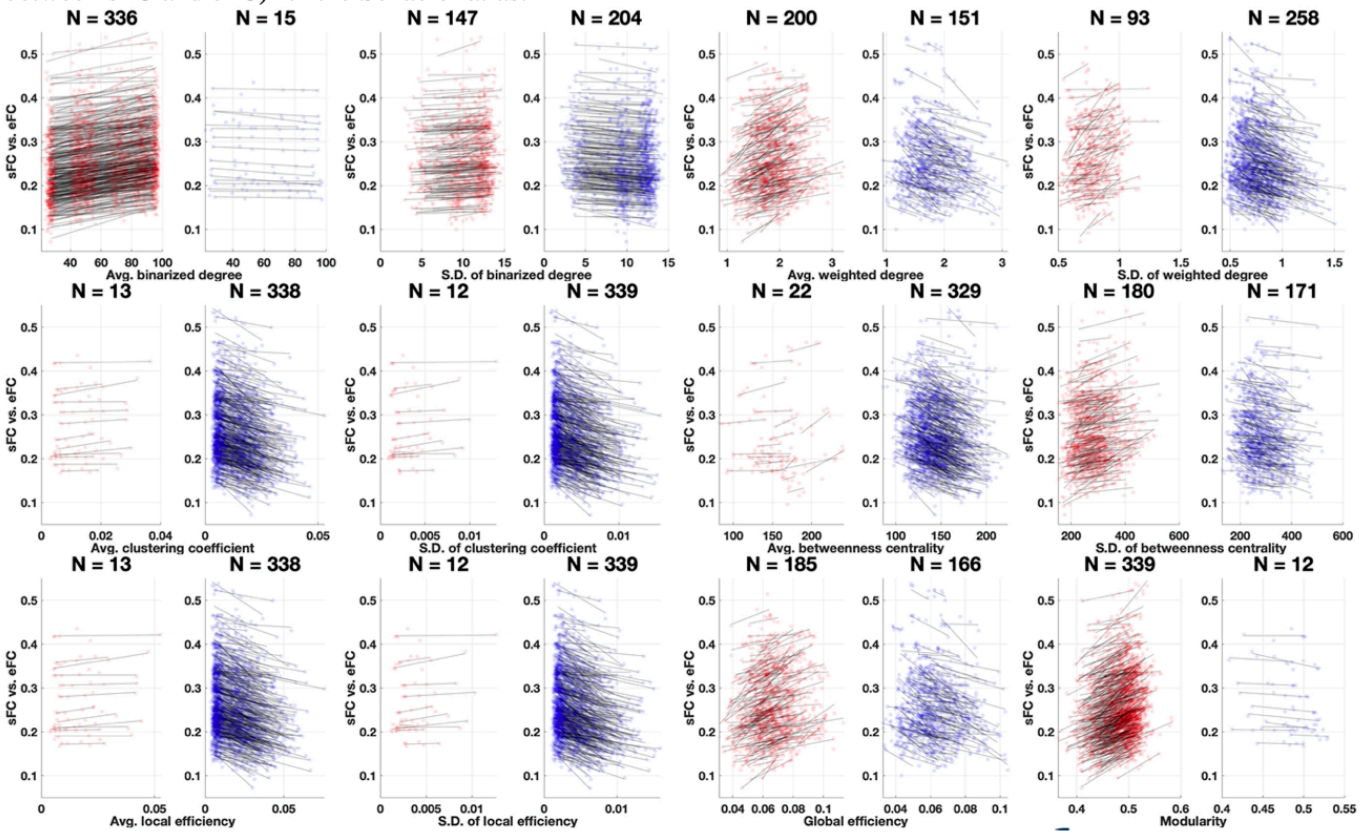

Fig. A4 Pearson correlation coefficients between network properties and the goodness-of-fit of the model (similarity between sFC and eFC) for the Harvard-Oxford atlas.

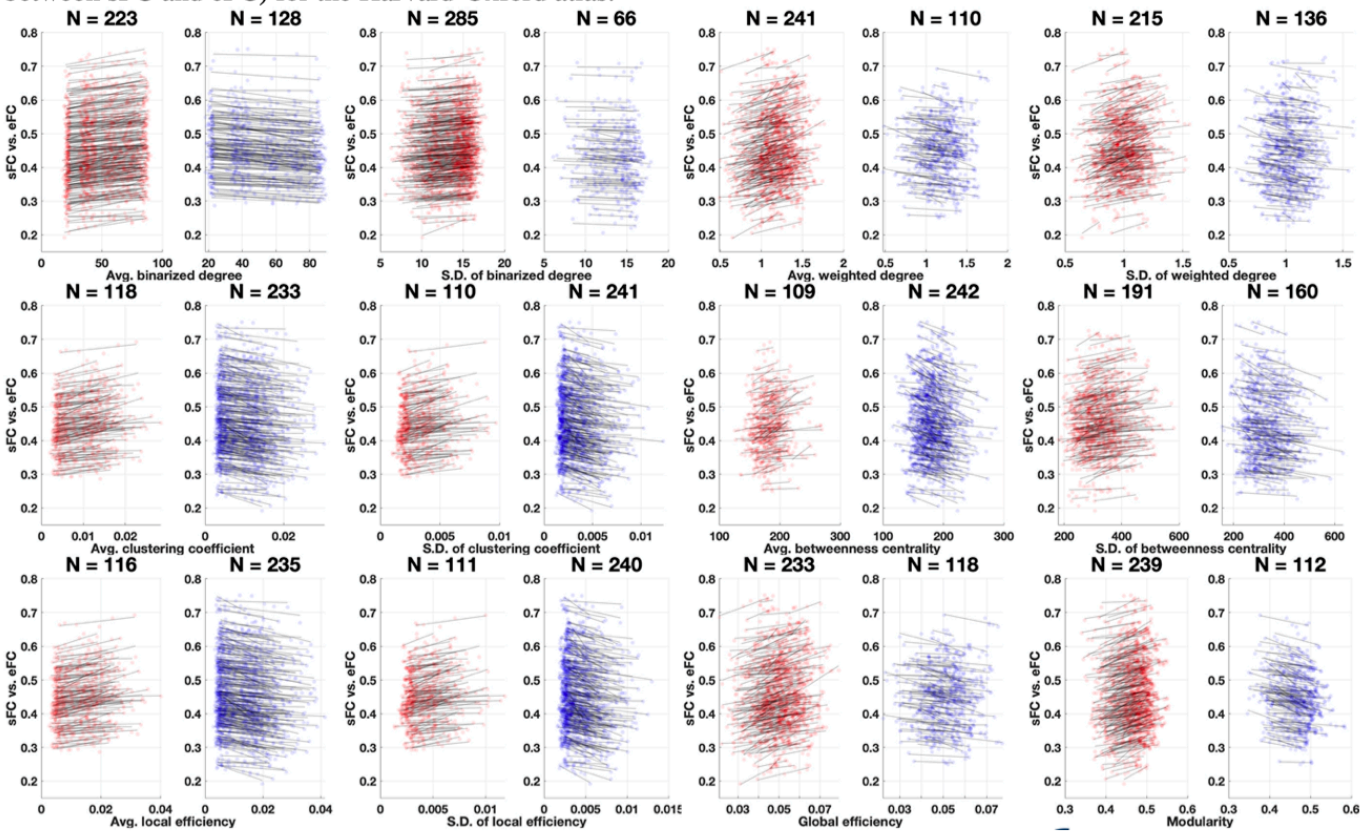

Fig. A5 Stratification of subjects based on the distributions of the correlation coefficients between the network properties and the functional goodness-of-fit values of the model for **(a)** the Schaefer atlas and **(b)** the Harvard-Oxford atlas. **(a, b)** p-values of the two-sample one-tail t-test for the differences of the model fitting between the two subject subgroups split based on the positive or negative correlation coefficients whose distributions are illustrated in Fig 5 a1 and b1. The corresponding network properties and the number of WBT streamlines are indicated on the horizontal and vertical axes, respectively. The black squares in the tables indicate significant results with $p < 0.05$. Red cells mean the subgroup of positive correlations showed higher goodness-of-fit of the model than the subgroup of negative correlations. Blue cells mean the subgroup of negative correlations showed higher goodness-of-fit of the model than the subgroup of positive correlations. Abbreviations of the network property names are as in Fig 5. The plus (+) or minus (-) sign after the property name in the black boxes, e.g., **S.D. WD+**, indicates a group of subjects with positive, respectively, negative correlation coefficients between the corresponding network property and the model goodness-of-fit values. The results of 10K condition were excluded from this analysis because the network properties from 10K show remarkably different tendencies.

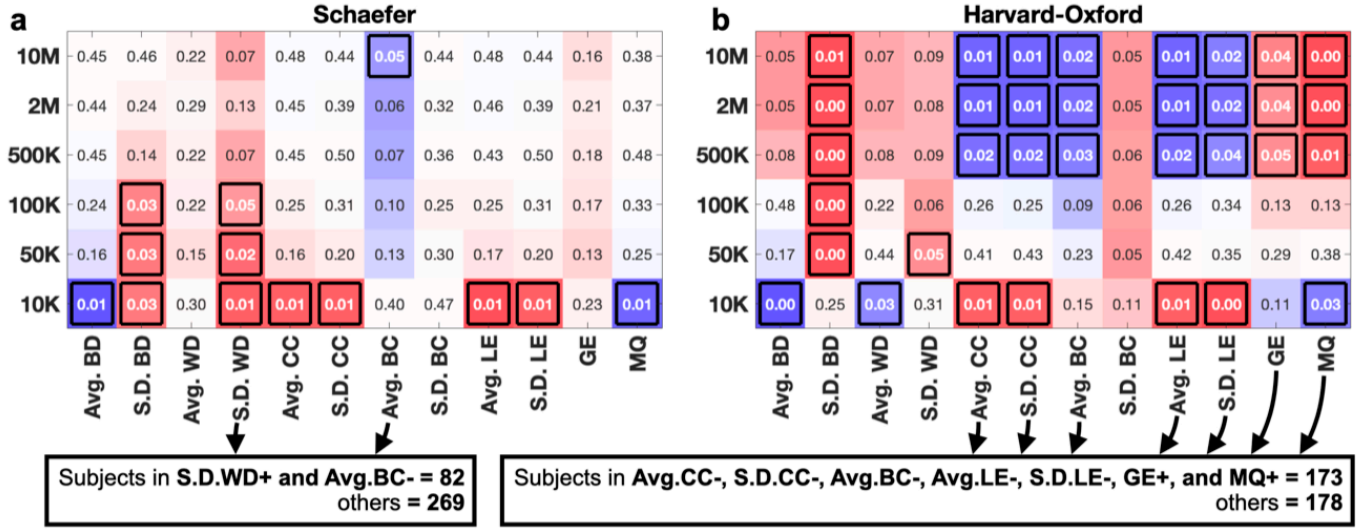

Fig. A6 **(a1 and b1)** Agreements between eFC and eSC for two subgroups by the second criterion of the stratification. **(a2 and b2)** Agreements between sFC and eSC for two subgroups by the second criterion of the stratification. The subgroup 1 means the cluster 1 and the subgroup 2 means the cluster 2 in Fig 6.

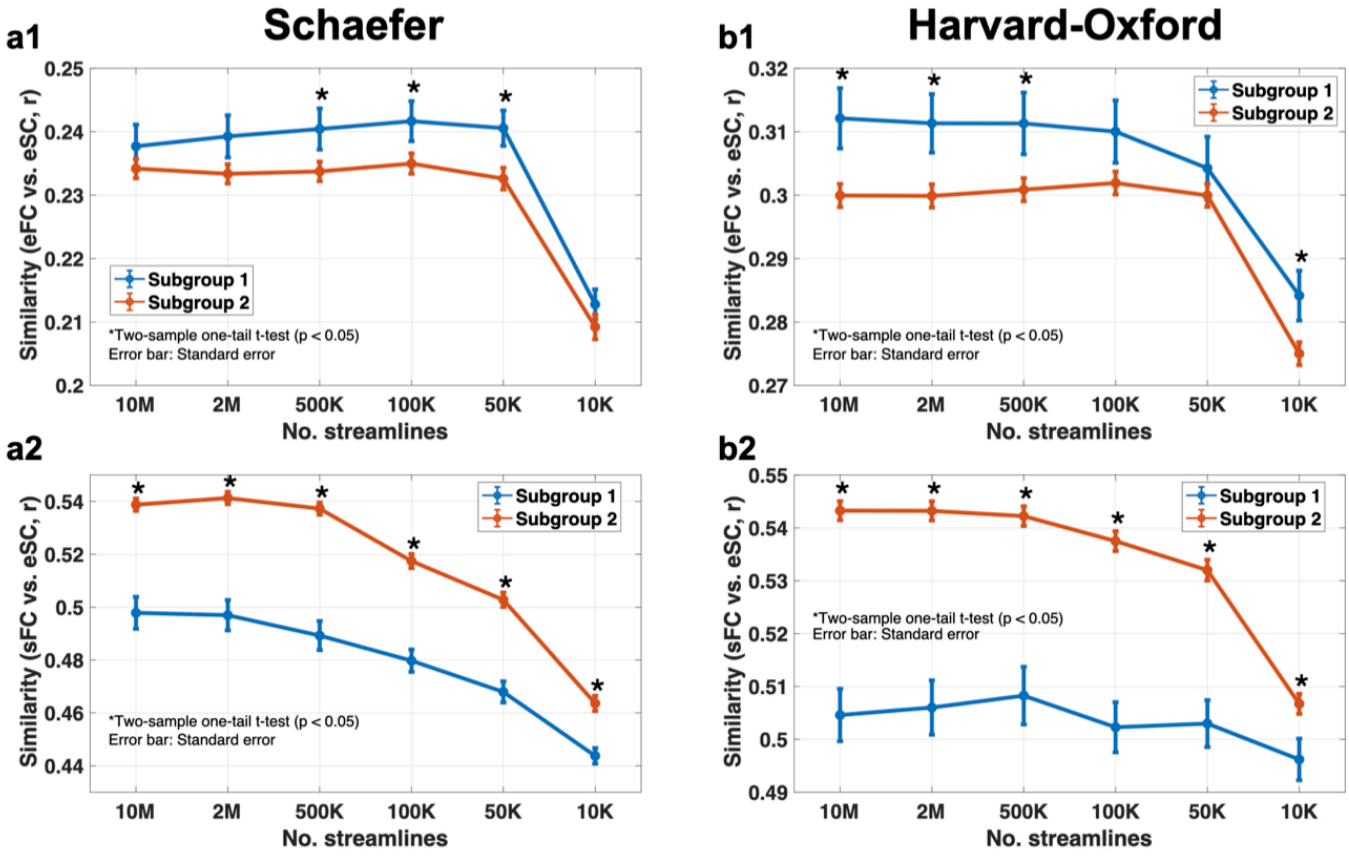

Fig. A7 Relations between the mean estimated natural frequencies and the optimal global delays for the similarities of sFC versus eSC for the Schaefer atlas. Red dots are the optimal parameter sets of subgroup 1 and blue dots are that of subgroup 2 in Fig 6. The subgroup 1 means the cluster 1 and the subgroup 2 means the cluster 2 in Fig 6.

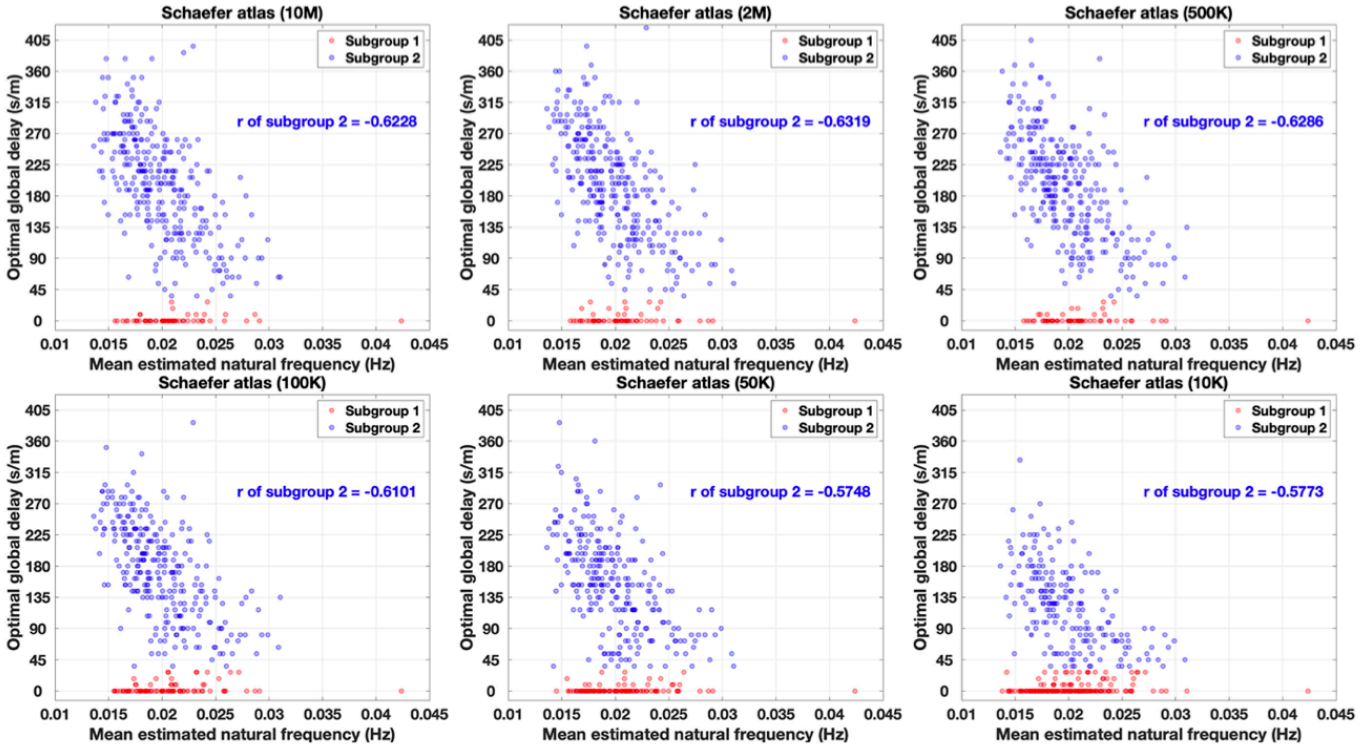

Fig. A8 Relations between the mean estimated natural frequencies and the optimal global delays for the similarities of sFC versus eSC for the Harvard-Oxford atlas. Red dots are the optimal parameter sets of subgroup 1 and blue dots are that of subgroup 2 in Fig 6. The subgroup 1 means the cluster 1 and the subgroup 2 means the cluster 2 in Fig 6.

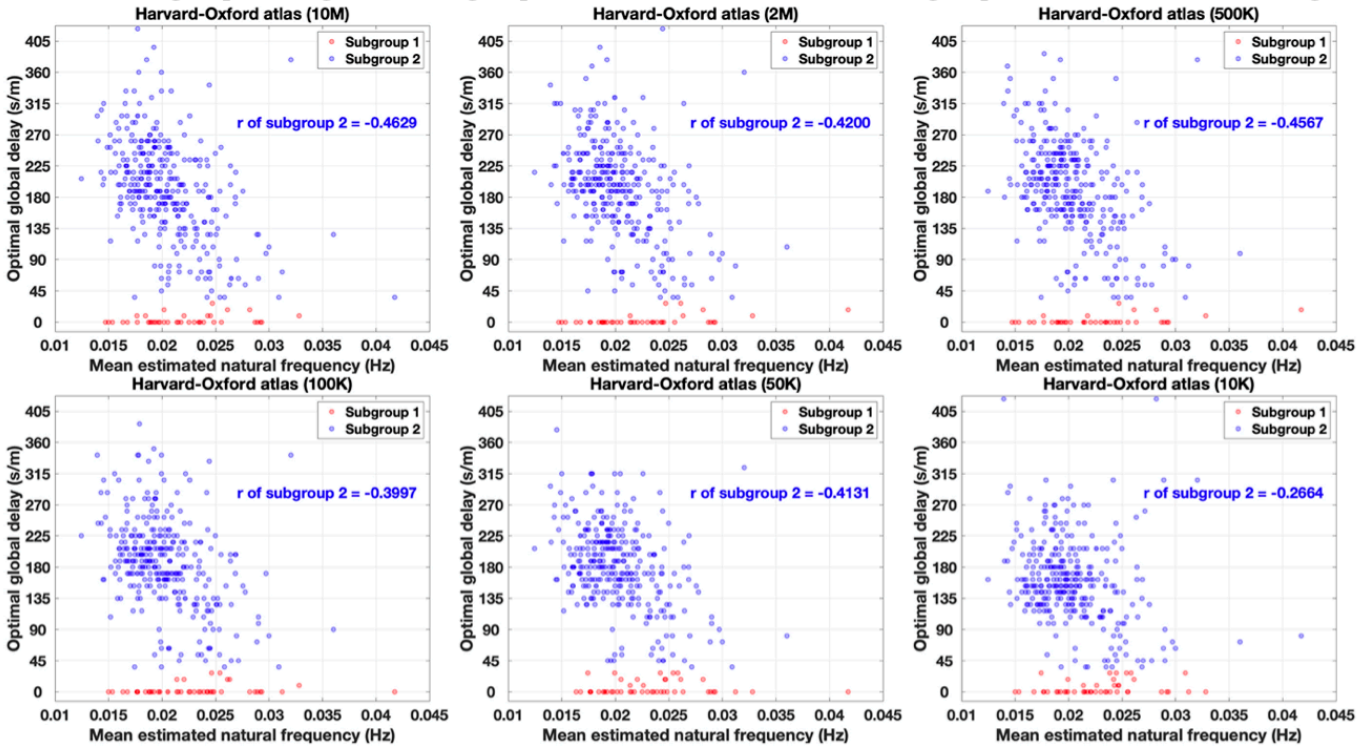

Fig. A9 Comparison between maximal functional fitting with and without delay (i.e., zero delay) of the current modeling. **(a, b)** Comparison of the functional model fitting for the Schaefer and Harvard-Oxford atlases. With delay, it increased by 9.0% for the Schaefer atlas and 8.2% for the Harvard-Oxford atlas. **(c, d)** Comparison of the structure-functional model fitting for the Schaefer and Harvard-Oxford atlases. With delay, it increased by 13.7% for the Schaefer atlas and 14.6% for the Harvard-Oxford atlas.

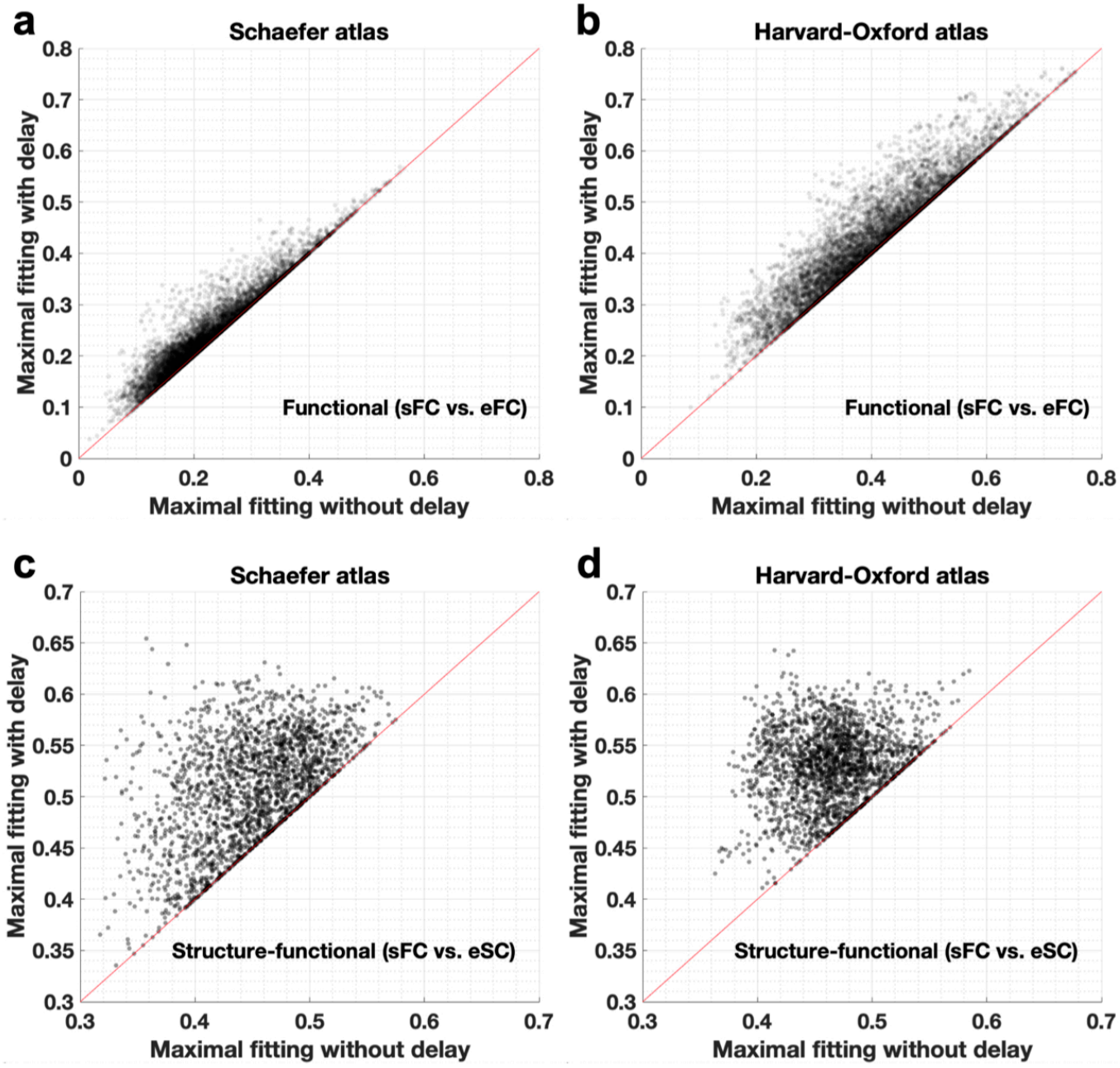

Fig. A10 Parameter planes for the two model fitting modalities between simulated and empirical data.

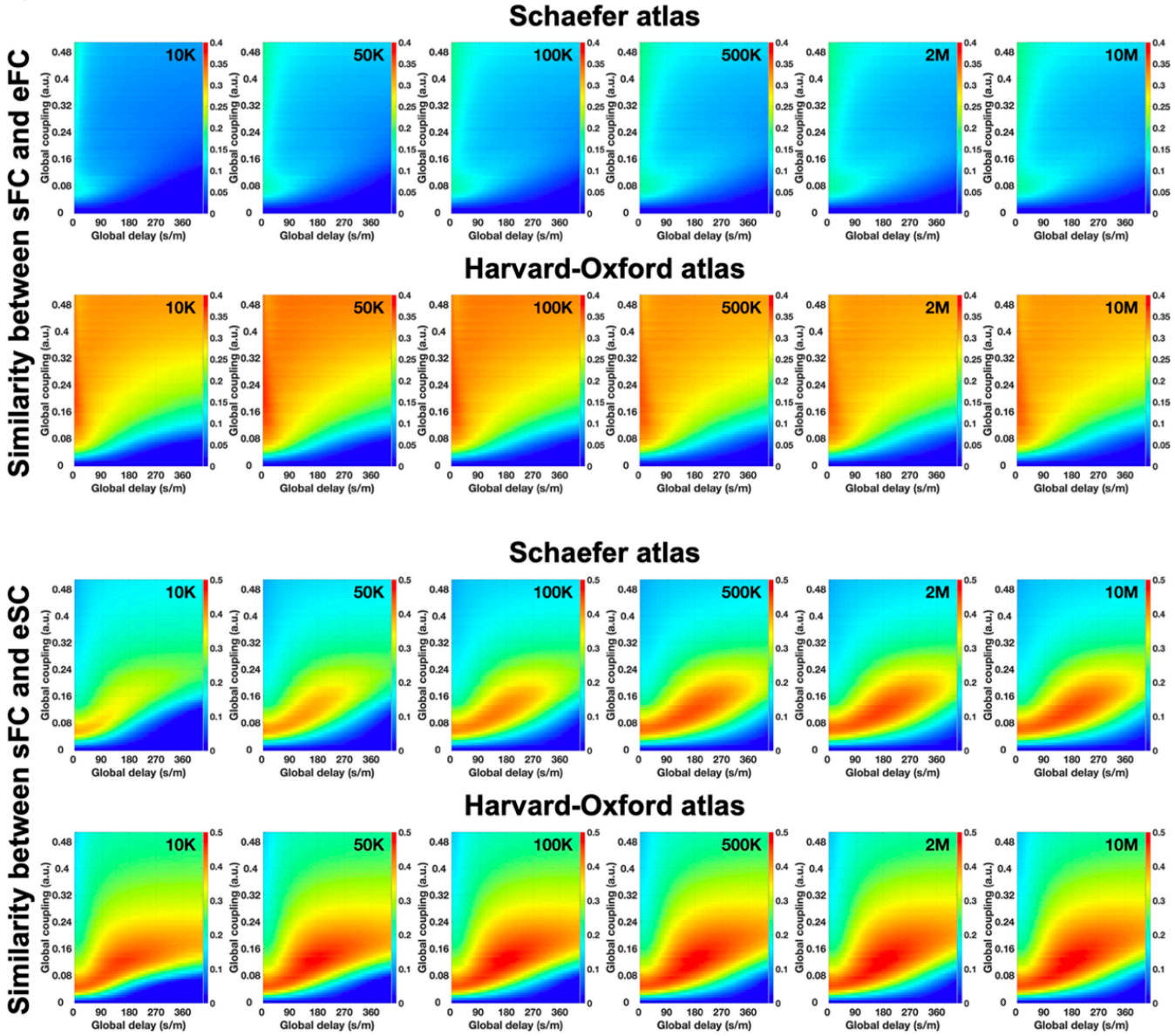

3 Study 2: Inter-subject and inter-parcellation variability of resting-state whole-brain dynamical modeling, Popovych, O. V., Jung, K., Manos, T., Diaz-Pier, S., Hoffstaedter, F., Schreiber, J., Yeo, B. T. T., Eickhoff, S. B., Neuroimage, 236: 118201 (2021)

DOI: https://doi.org/10.1016/j.neuroimage.2021.118201

Authorship contribution statement

Oleksandr V. Popovych (Corresponding author): Conceptualization, Resources, Data curation, Software, Formal analysis, Validation, Investigation, Visualization, Methodology, Writing - original draft, Writing - review & editing. **Kyesam Jung (Doctoral researcher):** Data curation, Software, Validation, Methodology, Writing - review & editing. **Thanos Manos:** Conceptualization, Resources, Data curation, Methodology, Writing - review & editing. **Sandra Diaz-Pier:** Resources, Software, Methodology, Writing - review & editing. **Felix Hoffstaedter:** Data curation, Software, Methodology, Writing - review & editing. **Jan Schreiber:** Data curation, Software, Methodology, Writing - review & editing. **B.T. Thomas Yeo:** Resources, Validation, Methodology, Writing - review & editing. **Simon B. Eickhoff:** Conceptualization, Resources, Supervision, Funding acquisition, Validation, Methodology, Project administration, Writing - review & editing.

NeuroImage 236 (2021) 118201

Contents lists available at ScienceDirect

NeuroImage

journal homepage: www.elsevier.com/locate/neuroimage

Inter-subject and inter-parcellation variability of resting-state whole-brain dynamical modeling

Oleksandr V. Popovych[a,b,*], Kyesam Jung[a,b], Thanos Manos[a,b,c], Sandra Diaz-Pier[d], Felix Hoffstaedter[a,b], Jan Schreiber[e], B.T. Thomas Yeo[f,g,h,i], Simon B. Eickhoff[a,b]

[a] Institute of Neuroscience and Medicine (INM-7), Research Centre Juelich, Juelich, Germany
[b] Institute of Systems Neuroscience, Medical Faculty, Heinrich-Heine, University Duesseldorf, Duesseldorf, Germany
[c] Laboratoire de Physique Théorique et Modélisation, CY Cergy Paris Université, CNRS, UMR 8089, Cergy-Pontoise cedex 95302, France
[d] Institute for Advanced Simulation, Juelich Supercomputing Centre (JSC), Research Centre Juelich, Juelich, Germany
[e] Institute of Neuroscience and Medicine (INM-1), Research Centre Juelich, Juelich, Germany
[f] Centre for Sleep and Cognition, Centre for Translational MR Research & N.1 Institute for Health, National University of Singapore, Singapore
[g] Department of Electrical and Computer Engineering, National University of Singapore, Singapore
[h] Martinos Center for Biomedical Imaging, Massachusetts General Hospital, Charlestown, MA, USA
[i] Integrative Sciences and Engineering Programme (ISEP), Singapore

ARTICLE INFO

Keywords:
Brain atlas
Whole-brain model
Resting-state brain dynamics
Simulations
Brain connectome
Model validation

ABSTRACT

Modern approaches to investigate complex brain dynamics suggest to represent the brain as a functional network of brain regions defined by a brain atlas, while edges represent the structural or functional connectivity among them. This approach is also utilized for mathematical modeling of the resting-state brain dynamics, where the applied brain parcellation plays an essential role in deriving the model network and governing the modeling results. There is however no consensus and empirical evidence on how a given brain atlas affects the model outcome, and the choice of parcellation is still rather arbitrary. Accordingly, we explore the impact of brain parcellation on inter-subject and inter-parcellation variability of model fitting to empirical data. Our objective is to provide a comprehensive empirical evidence of potential influences of parcellation choice on resting-state whole-brain dynamical modeling. We show that brain atlases strongly influence the quality of model validation and propose several variables calculated from empirical data to account for the observed variability. A few classes of such data variables can be distinguished depending on their inter-subject and inter-parcellation explanatory power.

1. Introduction

Investigation of brain dynamics during task-evoked and resting-state activity is frequently based on the inspection of corresponding functional networks that are collections of brain regions with enhanced synchronization among them (Bolt et al., 2017; Cole et al., 2014; Park and Friston, 2013). Neither nodes nor edges of such networks can uniquely be defined, especially, for the resting-state brain activity. State-of-the-art approaches range from voxel-wise nodes resulting in huge networks defined by the number of voxels in the underlying neuroimaging data to nodes encircling entire brain regions either as neuronal foci co-activated during a specific task or parcellated according to other criteria (Stanley et al., 2013). In the latter case, the brain regions are defined based on a certain brain parcellation (Eickhoff et al., 2018b; Stanley et al., 2013; Thirion et al., 2014), which reduces the dimensionality of the brain data by merging hundred thousands of voxels from high-resolution neuroimaging data into a few hundreds up to thousand of brain regions. A unified brain parcellation could improve the interpretability and comparability of results for different subjects and studies and increase the effective signal-to-noise ratio. However, there are many ways to parcellate the brain into separate regions (or parcels), which is actively debated in the literature (Eickhoff et al., 2018b; Stanley et al., 2013; Thirion et al., 2014). There is a sparse empirical evidence for the effect of a particular atlas choice, but see Refs. (Messe, 2019; Pervaiz et al., 2020; Zimmermann et al., 2019) for recent reports.

The great variety of possible techniques for creating brain parcellations and existing brain atlases makes the choice of a particular parcellation for a given analysis very difficult (Eickhoff et al., 2018a). At least two paradigmatically distinct approaches can be used for the parcellation, where the brain regions are defined based either on their anatomical or functional properties. For example, the cortex can be parcellated into regions according to its folding properties, e.g., into gyral-based

* Corresponding author at: Institute of Neuroscience and Medicine (INM-7), Research Centre Juelich, Juelich, Germany.
E-mail address: o.popovych@fz-juelich.de (O.V. Popovych).

https://doi.org/10.1016/j.neuroimage.2021.118201.
Received 1 March 2021; Received in revised form 21 May 2021; Accepted 22 May 2021
Available online 24 May 2021.

parcels encircled by tracing from the depth of one sulcus to another (Desikan et al., 2006). A very different parcellation approach is based on the brain function, where the patterns of the resting-state functional connectivity (FC) can be used to group the voxels (or vertices) into parcels of similar connectivity (Schaefer et al., 2018; Shen et al., 2013). The latter can be evaluated either according to a global similarity measure combined with abrupt changes in the local gradient of the whole-brain intrinsic FC (Schaefer et al., 2018) or based on the graph theory with application of a multigraph clustering approach to the resting-state FC (Shen et al., 2013). From the above anatomical and functional approaches to brain parcellation, one may assume that the latter could be more appropriate for calculation of the whole-brain FC, where the parcels are suspected to be composed of voxels with higher functional homogeneity. However, the detailed effects of these two distinct parcellation techniques on the results of data analysis and modeling can hardly be predicted by a simple theoretical reasoning.

Utilizing a brain parcellation is essential for dynamical modeling of brain activity, where the brain regions are represented as nodes of a network model (Honey et al., 2009). The selected brain parcellation is involved in the extraction of the structural connectivity (SC), inferred from diffusion-weighted magnetic resonance imaging (dwMRI), which serves as proxies for anatomical connections between brain regions at the meso- and macroscopic level (Hagmann et al., 2010). This SC can then be used to estimate the coupling strength and communication delay between the nodes of the model network contributing in such a way to the model derivation (Deco et al., 2011; Ghosh et al., 2008). Furthermore, the selected parcellation can be used to extract the blood oxygen level-dependent (BOLD) signals inferred from functional magnetic resonance imaging (fMRI) and calculate the empirical FC. The latter can be compared to simulated FC calculated from simulated BOLD time series generated by the derived model, thus validating the simulation results against the empirical data (Cabral et al., 2011; Deco and Jirsa, 2012). As a consequence, this process crucially depends on the empirical data used for the model derivation (e.g., SC) and fitting (e.g., FC), which in turn is affected by the data processing, in particular, by the selected brain parcellation (Messe, 2019; Pervaiz et al., 2020; Popovych et al., 2019; Zimmermann et al., 2019).

In this study we therefore simulate the resting-state brain activity using dynamical mathematical models to investigate the effects of brain parcellations. Functional and anatomical brain atlases with different resolutions are used for model validation against empirical resting-state functional and structural connectivity data. We consider three representatives from the above parcellation classes as given by the anatomical Harvard-Oxford atlas (Desikan et al., 2006) and the functional Schaefer (Schaefer et al., 2018) and Shen (Shen et al., 2013) atlases. The effects of brain parcellation are studied in detail with two systems of coupled phase and limit-cycle oscillators suggested for modeling cortical oscillations and resting-state BOLD dynamics (Breakspear et al., 2010; Cabral et al., 2011; Deco et al., 2019; 2017; Fukushima and Sporns, 2018; Ponce-Alvarez et al., 2015). The effects are investigated by an extensive exploration of the model parameter space. The models are fitted against empirical data of individual subjects for a set of varying conditions, in particular, the granularity of the parcellation for Schaefer and Shen atlases and the maximal probability threshold for Harvard-Oxford atlas affecting the size of brain regions.

The number of parcels is an important parameter, which may influence the results of the mathematical modeling, the empirical structure-function relationship as well as the prediction of human behavior from the patterns of brain connectivity (Honey et al., 2009; Messe, 2019; Pervaiz et al., 2020; Proix et al., 2016; Zimmermann et al., 2019) and deserves a systematic modeling investigation (Popovych et al., 2019). In the paper (Proix et al., 2016) the authors explored the impact of parcellations and local connectivity on the dynamics of neural mass models with and without delays, where the different parcellations were obtained by randomly splitting the brain regions of the Desikan-Killiany atlas into smaller subregions. It was in particular identified that spatial attractors of slow brain dynamics were qualitatively not affected by the number of regions in the cortical parcellation, whereas the parcellation granularity influenced their critical range in the global coupling strength. On the other hand, the richness of fast dynamics of the response to perturbations increased only if delays were considered in the model, suggesting an optimal parcellation scale, which can be decomposed into only a few spatial patterns. The work of Zimmermann et al. (2019) exposed a subject specificity to the association between empirical structural and functional connectomes for six different datasets and brain parcellations. It was however shown that intra-subject specificity of the SC-FC fit was achieved only for one of the considered cases indicating that selecting an appropriate brain parcellation was critical to provide enough statistical information to individually link SC and FC. The structure-function relationships between empirical SC and FC were also investigated for several brain parcellations with various spatial resolutions by Messe (2019) revealing a significant effect of brain parcellation on the SC-FC correlation driven by the number of brain regions. In the paper (Pervaiz et al., 2020) the impact of brain parcellation on the predictive power of data-driven models was analyzed regarding the relationship between whole brain functional connectivity patterns and behavioral traits in an attempt to find the optimal parcellation among other conditions.

In this study we analyze the parcellation-induced differences of model validation against empirical data for two approaches to brain parcellation based on anatomical or functional brain data. Furthermore, we test for an effect on two different models of limit-cycle and phase oscillators distinguished whether the amplitude of the simulated BOLD signals is taken into account or not, respectively. We consider functional and structure-functional fitting modalities for the model validation against empirical data. We aim to evaluate whether and how different parcellations may influence the modeling results and suggest possible approaches to explain inter-subject and inter-parcellation variation of model fitting. In our approach, we study the contribution of different features of the experimental data, which can vary with the pre-processing and chosen parcellation, to the ability of mathematical models to make an individualized link between simulated and empirical connectomes. We demonstrate that the considered atlases lead to substantially different results when comparing the model fit for parcellations within and between the anatomical and functional parcellation families. This is especially the case for the quality of the model validation, structure of the model parameter space and reliability of the fitting results. To understand the origin of the observed behavior of the model fitting, we also evaluate how the properties of the empirical data used for model derivation and validation may influence the modeling results (Messe et al., 2014). We show that several data variables calculated from the empirical neuroimaging data can be classified into a few correlative types depending on their contribution to the model fitting for individual subjects and for the brain parcellations from the same or different brain atlases. In this respect, the variation of the fitting results for personalized models across subjects and parcellations can, to a greater extent, be accounted for by the variation of the considered data variables.

2. Methods and materials

2.1. Empirical data

Empirical SC and FC used for the derivation and validation of the mathematical models were extracted for 272 healthy unrelated subjects (144 females, average age 28.5 ± 3.5 [mean±std] years) from the Human Connectome Project (HCP; https://www.humanconnectome.org/) (Van Essen et al., 2013) S1200 public release with complete dwMRI and resting-state fMRI data.

Structural connectivity Empirical SC approximating the anatomical axonal tracts in the brain (Conturo et al., 1999) was extracted from pre-

processed dwMRI data. To do this, we developed an in-house pipeline consisting of FSL version 5.0 (Jenkinson et al., 2012), Freesurfer 6.0 (Fischl et al., 2001), ANTs 3.0 (Tustison et al., 2014), and MRtrix3 3.0 (Tournier et al., 2019). The main pre-processing steps included denoising, bias-field correction, removal of eddy-current-induced distortions and motion correction (dwMRI), normalization of image intensity (T1-weighted image), co-registering the diffusion data with the T1-weighted image, estimation of the transformation function from the MNI standard template to the native diffusion space, and segmentation and application of tissue masks in the diffusion space. Then the whole-brain tractography (WBT) was calculated by the probabilistic fiber tracking algorithm (iFOD2) based on the multi-shell-multi-tissue constrained spherical deconvolution algorithm (Jeurissen et al., 2014), which was realized in MRtrix3, where 10 million streamlines were obtained. The tracking algorithm used voxels in the white-mater mask for seeding of tracts with the maximal angle in 45 degrees between successive steps. Finally, the resulting SC was extracted from the calculated WBT according to a given brain parcellation defining a set of brain regions (parcels), where any two parcels were selected as seed and target regions for the compression of WBT to the parcellation-based SC. The output is two $N \times N$ matrices of SC containing the empirical streamline counts (eSC) and the averaged empirical streamline path lengths (ePL) between any pair from N brain regions of the considered brain parcellation.

Resting-state functional connectivity The empirical FC was calculated from the resting-state fMRI data which was ICA FIX denoised as provided by the HCP repository (Glasser et al., 2013; Griffanti et al., 2014; Salimi-Khorshidi et al., 2014). Similar to the extraction of the empirical SC, also for the calculation of the empirical FC, the brain was split into a set of regions according to a given brain parcellation, and the mean BOLD signals (averaged over all voxels in any region) were calculated for all parcels. The extracted BOLD signals were then cross-correlated by Pearson correlation resulting in $N \times N$ empirical FC (eFC) matrices for each subject. The HCP repository provided 4 resting-state fMRI sessions (1200 volumes, TR = 720 ms) for each considered subject corresponding to the scans with two different phase-encoding directions repeated on two different days. This accordingly resulted in 4 eFC matrices for each subject. Additionally, the BOLD signals from all 4 scanning sessions were concatenated, and 5 eFC matrices were obtained in total for each subject.

Brain parcellation The empirical SC and FC were calculated for 11 brain parcellations using the Schaefer and Shen atlases based on the resting-state functional connectivity (Schaefer et al., 2018; Shen et al., 2013), and the Harvard-Oxford atlas based on the anatomy of cortical folding (Desikan et al., 2006). Several variations of these atlases were considered: the Schaefer atlas with 100, 200, 400 and 600 cortical parcels (denoted as S100, S200, S400 and S600, respectively), the Shen atlas with 79, 156 and 232 cortical regions (denoted as Shen79, Shen156 and Shen232), and the probabilistic Harvard-Oxford atlas with 96 non-overlapping cortical parcels with thresholds at 0%, 25%, 35%, and 45% of the maximal probability (denoted as HO96 0%, HO96 25%, HO96 35%, and HO96 45%, respectively). For higher thresholding, voxels that did not reach the threshold level were excluded, and for 45% threshold the left supracalcarine cortex region contained no supra threshold voxels reducing the number of parcels to 95 for HO96 45%.

Finer granularity for the Schaefer and Shen atlases and larger threshold for the Harvard-Oxford atlas led to smaller brain regions of the corresponding parcellations as illustrated in Fig. 1A. The main difference between the considered atlases is that the brain regions are more homogeneous in size for the Schaefer and Shen atlases than for the Harvard-Oxford atlas. However, the size spread decayed together with the average size such that the relations between them little changed for varying granularity and probability threshold, albeit overall differences between the three parcellation families [Fig. 1B]. The variation of the atlases, their parcellation granularity and probability threshold affected

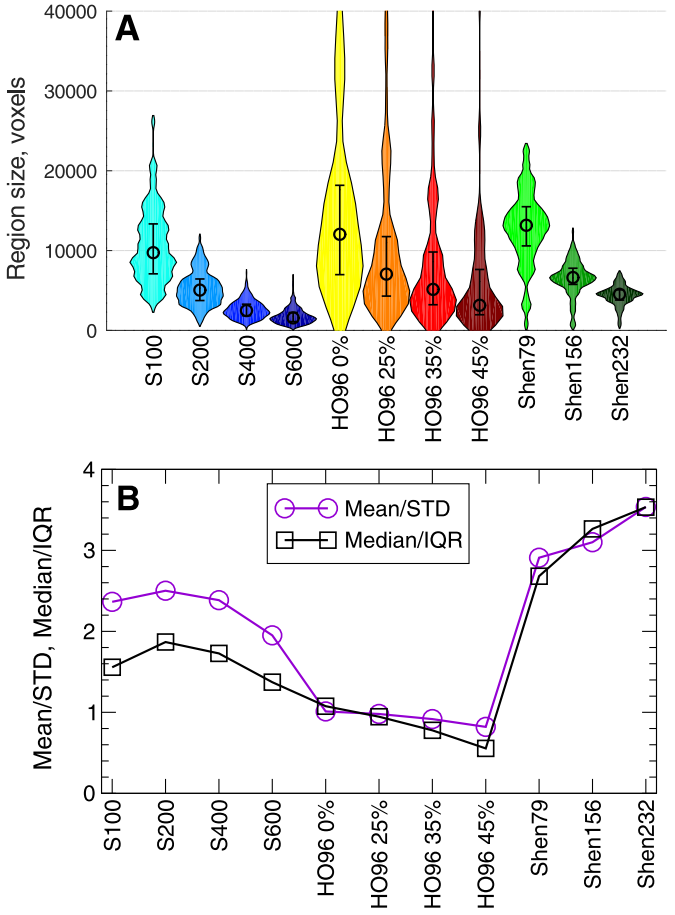

Fig. 1. Variation of the region size for the considered brain parcellations. (**A**) Distributions of the region size (the number of 1 mm isocubic voxels) and (**B**) the corresponding relations between the mean or median and the spread of the region size are depicted versus all considered parcellations. The spread of the region size is reflected by the standard deviation (STD) or interquartile range (IQR) as indicated in the legends.

the properties of the empirical data used for the model derivation and validation as discussed in Section 3.3 below.

2.2. Models and simulated data

In this study we considered two models. The first model is an ensemble of coupled phase oscillators of Kuramoto type (Kuramoto, 1984)

$$\dot{\varphi}_j(t) = 2\pi f_j + \frac{C}{N}\sum_{n=1}^{N} w_{jn}\sin(\varphi_n(t-\tau_{jn}) - \varphi_j(t)) + \eta_j, \qquad (1)$$

$$j = 1, 2, \ldots, N,$$

where φ_j are the phases, N is the number of oscillators, f_j are the natural frequencies (frequencies of the uncoupled oscillators, measured in hertz (Hz), and the time t in the model and delay in coupling are thus measured in seconds), and C is the parameter of the global coupling. Parameters w_{jn} and τ_{jn} represent the individual coupling weight and propagation delay in the coupling, respectively, from oscillator n to oscillator j, and η_j is an independent noise uniformly distributed in the interval $[-0.3, 0.3]$. This system was used to model by the observable $x_j = \sin(\varphi_j)$ the dynamics of the empirical BOLD signal of the jth brain region (parcel) according to a given brain parcellation as explained above, where the number of oscillators N in model (1) was equal to the number of brain parcels.

Another investigated model is a system of coupled generic limit-cycle (LC) oscillators that are the normal form of the supercritical Hopf bifur-

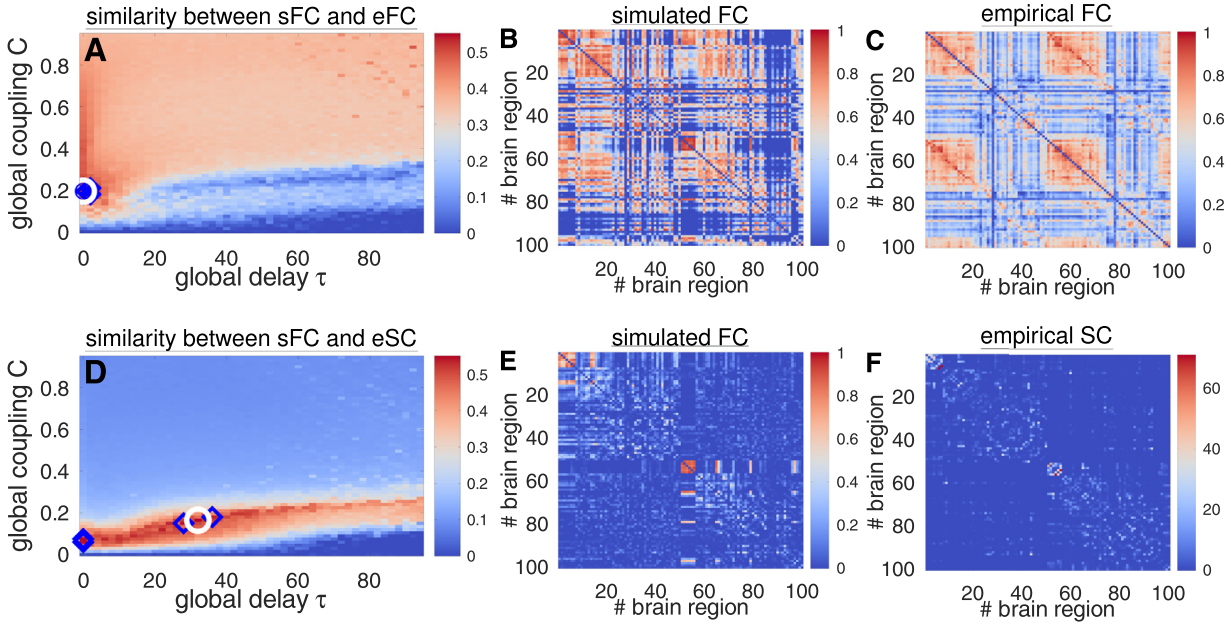

Fig. 2. Examples of model (1) validation against empirical data. Fitting of the simulated FC (sFC) to eFC (upper row, **A-C**) and to eSC (lower row, **D-F**) for S100 parcellation. (**A, D**) Similarity (Pearson correlation coefficient) between the simulated and empirical data is encoded in color versus parameters of the global delay τ and coupling C, where the optimal parameter points of the best fit are indicated by white circles, and the next 4 largest values are depicted by blue diamonds. The corresponding sFC matrices of the best fit compared with eFC and eSC, respectively, are depicted in the middle column (**B** and **E**), whereas the corresponding eFC matrix and normalized by its mean eSC matrix are shown in the right column of the upper (**C**) and lower (**F**) row, respectively. The simulated and empirical FC matrices are shown in the same scale for comparison. (For interpretation of the references to colour in this figure legend, the reader is referred to the web version of this article.)

cation (Kuznetsov, 1998)

$$\dot{z}_j(t) = \left(a_j + \mathrm{i}2\pi f_j - |z_j(t)|^2\right) z_j(t) + \frac{C}{N}\sum_{n=1}^{N} w_{jn}\left(z_n(t-\tau_{jn}) - z_j(t)\right) + \xi_j, \quad j = 1, 2, \ldots, N, \tag{2}$$

where $z_j(t) = x_j(t) + \mathrm{i}y_j(t)$ are the complex variables of individual oscillators, and $\mathrm{i} = \sqrt{-1}$ is the imaginary unit. Without coupling ($C = 0$), all oscillators of ensemble (2) independently and uniformly rotate around the origin on the limit cycles with individual radii $\sqrt{a_j}$ and with individual natural frequencies f_j measured in Hz. The independent complex noise ξ_j is uniformly distributed in the interval $[-0.3, 0.3]$. The empirical BOLD signal of region j was modeled by the variable $x_j(t)$.

The model parameters f_j, a_j, w_{jn} and τ_{jn} are extracted from the empirical data for each individual subject, and the personalized models (1) and (2) were simulated separately for each subject. The natural frequencies f_j of the phase and LC oscillators were calculated from the empirical BOLD signals extracted from the corresponding brain regions as the frequencies of the maximal spectral peaks discarding the frequencies below 0.01 Hz and above 0.1 Hz. Similar approach for defining the local model parameters was also used in other studies for the phase and LC oscillators (Deco et al., 2019; 2017; Ponce-Alvarez et al., 2015). The amplitude parameters a_j of LC oscillators (2) were selected proportionally to the extent of time fluctuations of empirical BOLD signals of individual parcels. For this, the normalized standard deviation $std(\mathrm{BOLD}_j)$ was used to calculate a_j such that the mean and the standard deviation over all parcels were $\langle a_j \rangle = 0.5$ and $std(a_j) = 0.4$, respectively.

The coupling weights w_{jn} and delays τ_{jn} were derived from the eSC and ePL, respectively. The parameters w_{jn} were calculated as the normalized number of SC streamlines $w_{jn} = k_{jn}/\langle k_{jn} \rangle$, where k_{jn} is the number of streamlines connecting regions j and n, and $\langle \cdot \rangle$ denotes the ensemble averaging over the entire $N \times N$ matrix with zero diagonal. The matrix of the streamline counts $eSC = \{k_{jn}\}$ thus defined the coupling weights and the graph of the model network. The delays τ_{jn} were calculated as $\tau_{jn} = L_{jn}/V$, where L_{jn} is the average path length of the streamlines connecting regions j and n, and V is an average velocity of signal propagation. The matrix $ePL = \{L_{jn}\}$ can thus be used to calculate the delays τ_{jn} in the coupling, which can be rewritten as $\tau_{jn} = \tau \cdot L_{jn}/\langle L_{jn} \rangle$, where $\tau = \langle L_{jn} \rangle / V$ is the global (or average) delay. In models (1) and (2) the self-connections were excluded ($w_{jj} = 0$) by putting the diagonal elements in the matrices eSC and ePL to zero: $k_{jj} = L_{jj} = 0$. The parameters of the global coupling C and the global delay τ can be used to scale the extent of the coupling in the system and the average velocity V, respectively, and were varied to fit the model to empirical data.

2.2.1. Model validation

For each set of the model parameters, the models (1) and (2) were numerically simulated, and the matrix of the simulated functional connectivity (sFC) was calculated by Pearson correlation between the simulated BOLD signals x_j, $j = 1, 2, \ldots, N$. sFC was compared with the matrices of the empirical connectivity eFC and eSC, where the similarity between them was calculated by Pearson correlation, i.e., $\mathrm{corr}(\mathrm{sFC}, \mathrm{eFC})$ or $\mathrm{corr}(\mathrm{sFC}, \mathrm{eSC})$ between the corresponding upper triangular parts. The model fitting for the phase oscillators (1) is illustrated in Fig. 2. For given eFC and eSC [Fig. 2C and F], the model parameters τ and C were varied, and the similarity between sFC and the empirical connectivity matrices was calculated for each parameter point (τ, C) [Fig. 2A and D]. Among all tested parameter values, the optimal values were selected corresponding to the best model fit, i.e., where the similarity is maximal [Fig. 2A and D, while circles]:

$$\begin{aligned} \mathrm{Fit}(\mathrm{sFC}, \mathrm{eFC}) &= \max_{(C,\tau)} \mathrm{corr}(\mathrm{sFC}, \mathrm{eFC}), \\ \mathrm{Fit}(\mathrm{sFC}, \mathrm{eSC}) &= \max_{(C,\tau)} \mathrm{corr}(\mathrm{sFC}, \mathrm{eSC}). \end{aligned} \tag{3}$$

The goodness-of-fit values $\mathrm{Fit}(\mathrm{sFC}, \mathrm{eFC})$ of the functional model fitting can be used to evaluate the similarity between the simulated patterns of synchronization between oscillators of systems (1) and (2) and the resting-state BOLD dynamics as given by eFC matrix. On the other

hand, the structure-functional model fitting Fit(sFC, eSC) evaluates how strongly the model dynamics can replicate the underlying network structure as for the structure-function relationship in the brain (Honey et al., 2009; Messe, 2019; Park and Friston, 2013; Zimmermann et al., 2019) and for which parameters and dynamical regimes. Examples of the correspondence between sFC and empirical data are illustrated in Fig. 2, compare sFC matrices in Fig. 2B and E with eFC and eSC in Fig. 2C and F, respectively. For further analysis, optimal model parameters were selected from each parameter space as in Fig. 2A and D (white circles) together with the corresponding maximal similarity values $\mathrm{Fit}(\cdot,\cdot)$, i.e., goodness-of-fit of the model defined by Eq. (3).

As mentioned above, the two models were simulated for 11 brain parcellations (4 for the Schaefer atlas, 4 for the Harvard-Oxford atlas and 3 for the Shen atlas) defining 11 simulation conditions for each subject. Simulation for each condition resulted in 5 parameter planes like in Fig. 2A and D of comparison between sFC and eFC (each subject had 5 eFCs), and one plane of comparison between sFC and eSC. Each parameter plane spanned the range $[0, 94] \times [0, 0.945]$ of the coupling delay τ and strength C, respectively, and contained a grid of 48×64 parameter points. For each of these parameter points the models were numerically simulated (model run) for random initial conditions by the stochastic Heun integration method with fixed $\Delta t = 0.06$ s integration step during 4000 s, where the last 3500 s were used for sFC evaluation (the first 500 s were skipped as transient). From each parameter plane one optimal parameter point (τ, C) was extracted and collected for further analysis [Fig. 2A and D, white circles], where the maximal similarities (3) were reached. For the considered 272 subjects we analyzed $272 \times 5 = 1360$ maximal similarities $\mathrm{Fit}_i(\mathrm{sFC}, \mathrm{eFC})$ $(i = 1, 2, \ldots, 1360)$ and 272 values of $\mathrm{Fit}_i(\mathrm{sFC}, \mathrm{eSC})$ $(i = 1, 2, \ldots, 272)$ and the corresponding optimal parameters (τ_i, C_i) for each of 11 simulation conditions (brain parcellations) and 2 models. These values were derived from more than 18 millions of model runs.

For statistical analyses, we related the vectors $\mathrm{Fit}_i(\cdot,\cdot)$ (we omit the subscripts in what follows) across subjects between different brain parcellations and models to evaluate the similarity and interdependencies between modeling results with regard to simulation conditions (parcellations and models) as well as statistical properties of the empirical data. The similarity was evaluated by the Pearson correlation coefficients and their statistical significance as provided by the *corrcoeff* function in Octave. Fischers z-transform was applied to the correlation coefficients before (and after) performing arithmetic operations (e.g., averaging) and testing. For multivariate analysis the standard multiple linear regression model (MLR) was employed.

3. Results

In what follows we first illustrate the results of the model fitting for all considered subjects, parcellations, fitting modalities and models. Then we present two approaches to evaluate and explain the impact of brain parcellations on the inter-subject and inter-parcellation variability of the obtained modeling results. As our first approach, the results of the model fitting, i.e., the Fit-values of the maximal similarity (3) and the corresponding optimal model parameters (τ, C) were compared across individual subjects and between different brain parcellations and models. We evaluated the inter-parcellation variability of the fitting patterns across individual subjects. In the second approach, several data variables were calculated from individual empirical data and used to account for the variation of the goodness-of-fit across subjects for each of the considered brain parcellations as well as among them. Thereby, we assess the influence of individual data properties on intra- and inter-parcellation variability of the model fitting.

3.1. Results of model fitting

The distributions of the maximal similarity Fit(sFC, eFC) of the fitting sFC to eFC are illustrated in Fig. 3A and E for the considered brain atlases and the two simulation models. The impact of the atlases is apparent when comparing the differences between Fit(sFC, eFC) for the Schaefer atlas (S100-S600, blue violins), the Harvard-Oxford atlas (HO96 0%-45%, yellow - dark red violins) and the Shen atlas (Shen79-Shen232, green violins). In the latter cases (HO96 and Shen) the both models demonstrate much higher fitting to the empirical data with up to 80% of the relative increase of Fit(sFC, eFC) with respect to S100-S600 cases [supplementary Table A.1]. The differences in the model fitting can also be observed between the parcellations of the same type, i.e., from the same atlas. In particular, the best fit for the Schaefer atlas was obtained for S200 case providing an optimal spatial scale for this brain atlas. For other atlases Fit(sFC, eFC) monotonically decays when the threshold for HO96 atlas or the number of parcels for the Shen atlas increases [Fig. 3A and E].

Results of a systematic statistical testing of Fit(sFC, eFC) for all considered simulation conditions (11 parcellations) are illustrated in Fig. 3B and F, where the p-values of the paired Wilcoxon signed-rank test are depicted in color for comparisons between different parcellations. The dark color (darker than yellow) at the intersection of a particular row and column of the shown matrices indicates that the goodness-of-fit for the condition from the vertical axis $\mathrm{Fit}^{(\mathrm{row})}$ is statistically larger (with $p < .05$ at least) than $\mathrm{Fit}^{(\mathrm{column})}$ for the condition from the horizontal axis accordingly. For example, $\mathrm{Fit}^{(\mathrm{S200})} > \mathrm{Fit}^{(\mathrm{S100})}$ as well as $\mathrm{Fit}^{(\mathrm{S200})} > \mathrm{Fit}^{(\mathrm{S400})}$ and $\mathrm{Fit}^{(\mathrm{S200})} > \mathrm{Fit}^{(\mathrm{S600})}$, where the cells at the intersection of the row "S200" and columns "S100", "S400" and "S600" are dark and marked by ">" implying $p < .05$. We also confirm that the quality of the model fitting decays for larger probability threshold for HO96 atlas and for more parcels for the Shen atlas [Fig. 3B and F]. Shen79 provides the best fit for both models, whereas the lowest goodness-of-fit was obtained for S100 for the phase model and for S400 and S600 for the LC model, see the row "Shen79" and columns "S100", "S400" and "S600" in Fig. 3B and F. The effect size associated with the presented p-values is illustrated in supplementary Fig. A.1.

The maximal similarity Fit(sFC, eFC) is achieved at the optimal model parameters as illustrated in Fig. 2A (white circle). Distributions of the optimal model parameters (τ, C) for the model fitting to the empirical functional data eFC for all subjects are shown as one-dimensional histograms in Fig. 3C and G, and as two-dimensional histograms in Fig. 3D and H for a few selected parcellations. We found that Fit(sFC, eFC) is attained at the optimal parameters remarkably concentrated towards small delay τ and moderate values of coupling C for all considered brain parcellations and models. Somewhat broader distribution of the optimal coupling can be observed for the Shen atlas for the phase model but not for the LC model [Fig. 3C6 and G6]. Further examples of the parameter planes averaged over all subjects are illustrated in supplementary Fig. A.2 together with the distributions of the optimal model parameters taking into account up to 5 largest similarity values per individual parameter plane [Fig. 2A and D, white circles and blue diamonds].

The situation is different for the structure-function relationship, where sFC is fitted to eSC (count matrix) [Fig. 2D-F] as illustrated in Fig. 4. In particular, the maximal similarity monotonically decays in a well-pronounced manner when the granularity of the Schaefer and Shen atlases decreases for both models [Fig. 4A and E, blue and green violins, supplementary Table A.1]. In contrast, Fit(sFC, eSC) increases for larger threshold for HO96 atlas and the LC model [Fig. 4E and F, yellow-red violins]. On the other hand, the behavior of the Fit-values is non-monotonic for the phase model, where the thresholds of 25% and 35% are optimal for the structure-functional model fitting for HO96 atlas and phase model [Fig. 4A and B]. The highest and the lowest correspondence between the simulated and empirical data was obtained for Shen79 and S600, respectively, for both models, see also supplementary Fig. A.1 for effect size.

The distributions of the optimal model parameters for Fit(sFC, eSC) also exhibit a deviation from those for Fit(sFC, eFC) as illustrated in Fig. 4 (compare to Fig. 3). Interestingly, the best structure-functional model fitting can be achieved for small and very well localized values

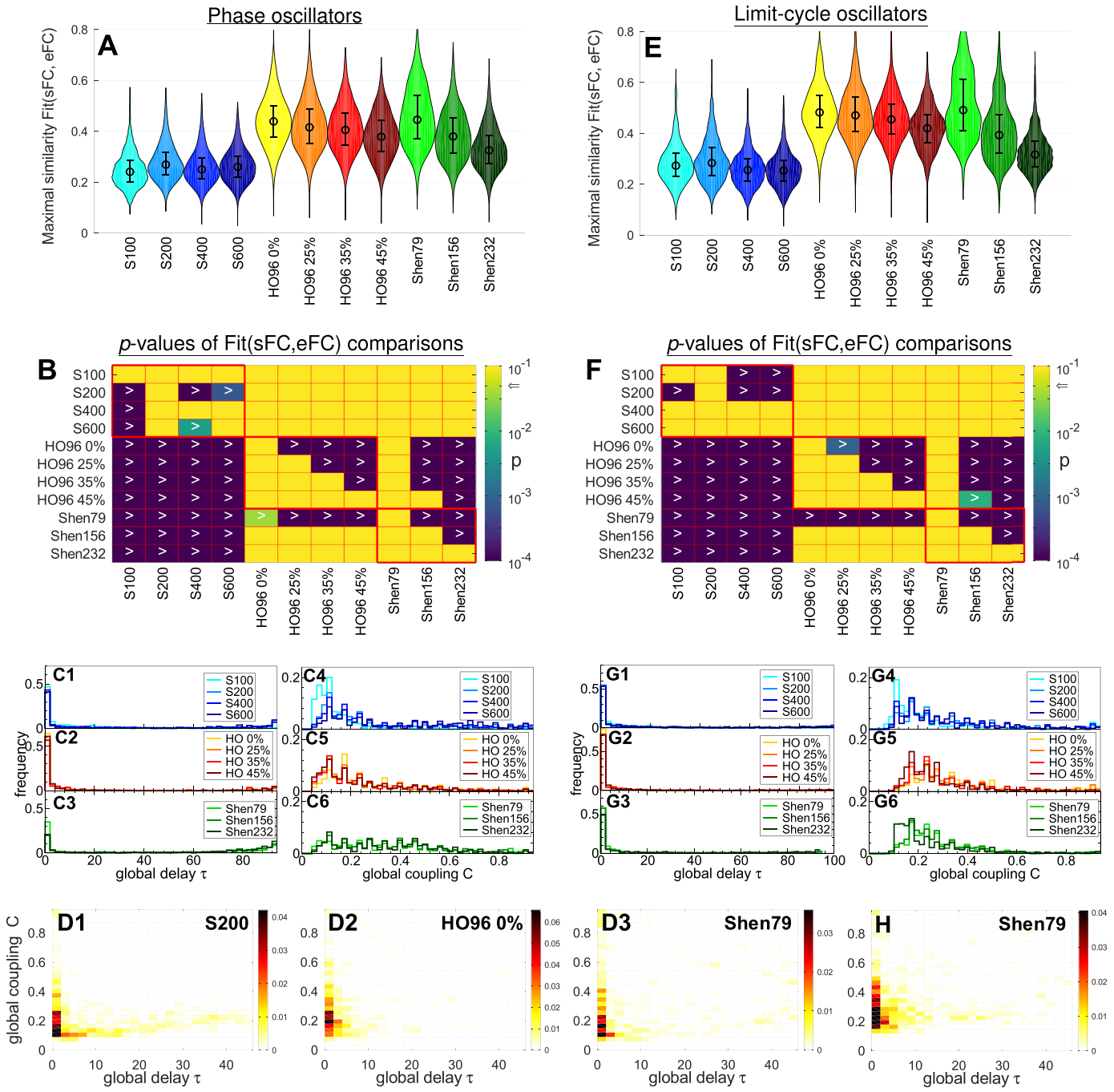

Fig. 3. Results of the functional model fitting for (**A - D**) phase model (1) and (**E - H**) LC model (2). (**A, E**) Distributions of the maximal similarity values Fit(sFC, eFC) as violin plots for the considered brain parcellations denoted on the horizontal axes as introduced in Methods, where the medians and the interquartile ranges are also shown. (**B, F**) Outcomes of statistical tests, where the *p*-values (corrected for multiple comparisons) of the paired Wilcoxon signed-rank test of the Fit(sFC, eFC) values between the parcellations indicated on the axes are depicted by color in logarithmic scale (see color bar). The null hypothesis is rejected with $p < .05$ (indicated by arrow on the color bar) in favor of the alternative hypothesis $\mathrm{Fit}^{(\mathrm{row})} > \mathrm{Fit}^{(\mathrm{column})}$ for parcellations in the row and column, respectively, where the corresponding cell is dark (small *p*-value) and contains the inequality sign ">". (**C,D,G,H**) Distributions of the corresponding optimal model parameters, where the one- and two-dimensional histograms of the occurrence frequency of the optimal parameters are, respectively, plotted as step-wise curves (**C, G**) and depicted in color (**D, H**) ranging from white (small values) to black (large values) for the parcellations indicated in the legends and plots. (For interpretation of the references to colour in this figure legend, the reader is referred to the web version of this article.)

of the global coupling C and for broadly distributed delay τ [Fig. 4C and D] when compared to the functional fitting modality. The latter property is somewhat reduced for the LC model as compared to the phase model [Fig. 4G and H]. Nevertheless, positive delay in coupling is still important to obtain the best model fitting in this case for both models, see supplementary Fig. A.2 for more details and comparison between the phase and LC models.

3.2. Inter-parcellation variability of fitting results

To explore the variability of the fitting results over brain parcellation, in this section we analyze the similarity among the goodness-of-fit vectors $\mathrm{Fit}(\cdot,\cdot)$ (3) collected for all subjects and fMRI scan sessions (see Methods) calculated for different parcellations and models. The Fit-values were correlated across subjects for any two parcellations for the

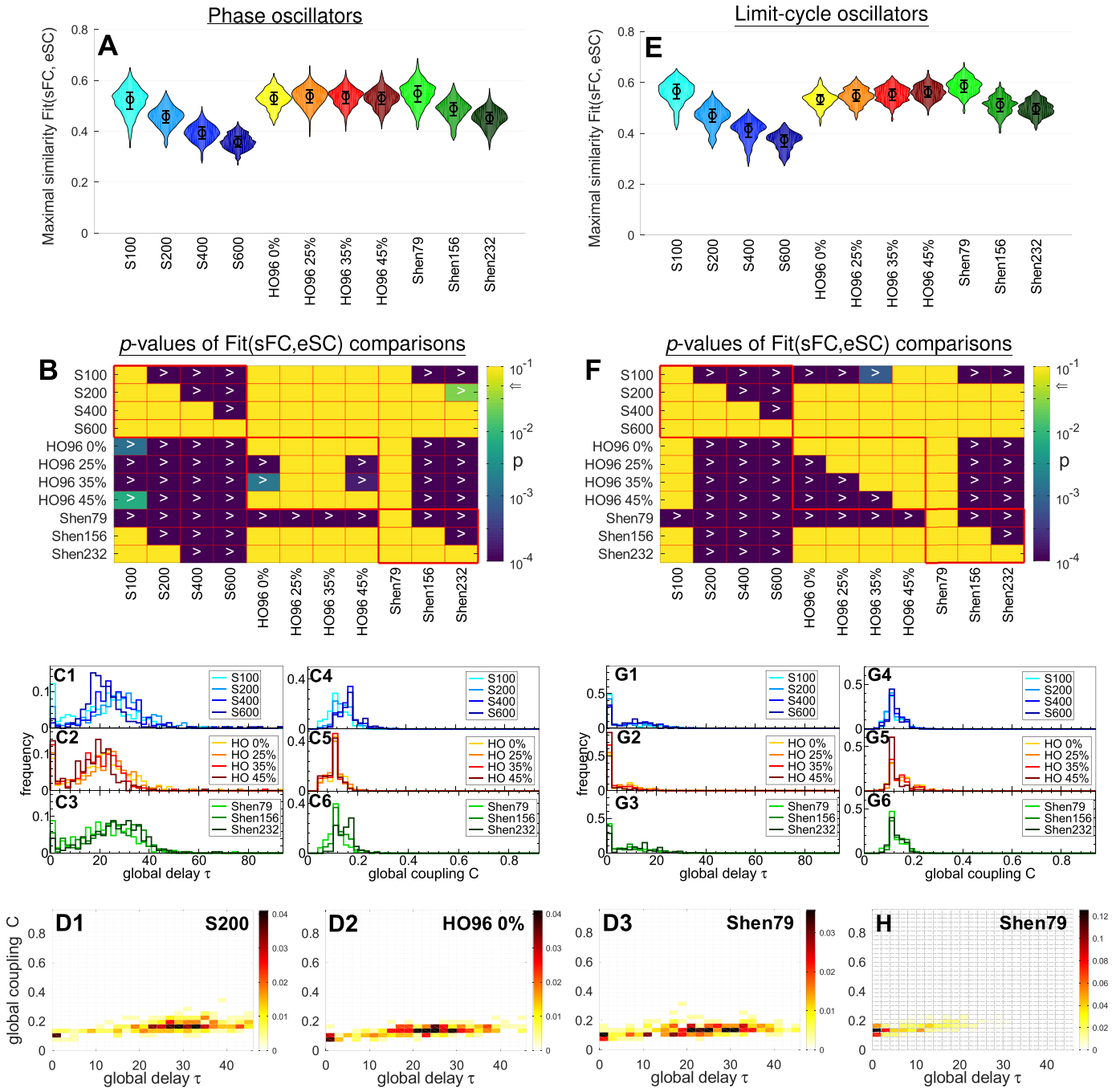

Fig. 4. Results of the structure-functional model fitting for (**A - D**) phase model (1) and (**E - H**) LC model (2). (**A, E**) Distributions of the maximal similarity values Fit(sFC, eSC) for the considered brain parcellations, where the medians and the interquartile ranges are also shown. (**B, F**) Outcomes of statistical tests, where the corrected for multiple comparisons p-values of the paired Wilcoxon signed-rank test of the Fit(sFC, eSC) values between the parcellations indicated on the axes are depicted by color in logarithmic scale (see color bar). The null hypothesis is rejected with $p < .05$ (indicated by arrow on the color bar) in favor of the alternative hypothesis $\mathrm{Fit}^{(\mathrm{row})} > \mathrm{Fit}^{(\mathrm{column})}$ for parcellations in the row and column, respectively, where the corresponding cell is dark (small p-value) containing the inequality sign ">". (**C,D,G,H**) Distributions of the corresponding optimal model parameters, where the one- and two-dimensional histograms of the occurrence frequency are, respectively, plotted as step-wise curves (**C, G**) and depicted in color (**D, H**) ranging from white (small values) to black (large values) for the parcellations indicated in the legends and plots. (For interpretation of the references to colour in this figure legend, the reader is referred to the web version of this article.)

same as well as different models to evaluate how strongly the variation of the brain parcellation and model can affect the inter-subject patterns of the goodness-of-fit and assess the reliability of the fitting results.

The pairwise correlations of the maximal similarity Fit(sFC, eFC) between any two of the considered brain parcellations are shown for the phase model in Fig. 5A and LC model in Fig. 5B. We observe that the fitting results are well correlated for parcellations within the same atlas/parcellation family, i.e., among S100-S600 parcellations and within HO96 and Shen atlases. The average intra-atlas correlations are 0.82 for the phase model [Fig. 5A] and 0.86 for the LC model [Fig. 5B]. On the other hand, the similarity of the model fitting patterns between different atlases is reduced, which holds for both models, and the corresponding average inter-atlas correlations are 0.59 and 0.71, for the phase and LC models, respectively. The inter-subject patterns of the goodness-of-fit Fit(sFC, eFC) are preserved for both dynamical models as illustrated in Fig. 5C, where the phase model was used for parcellations on the vertical

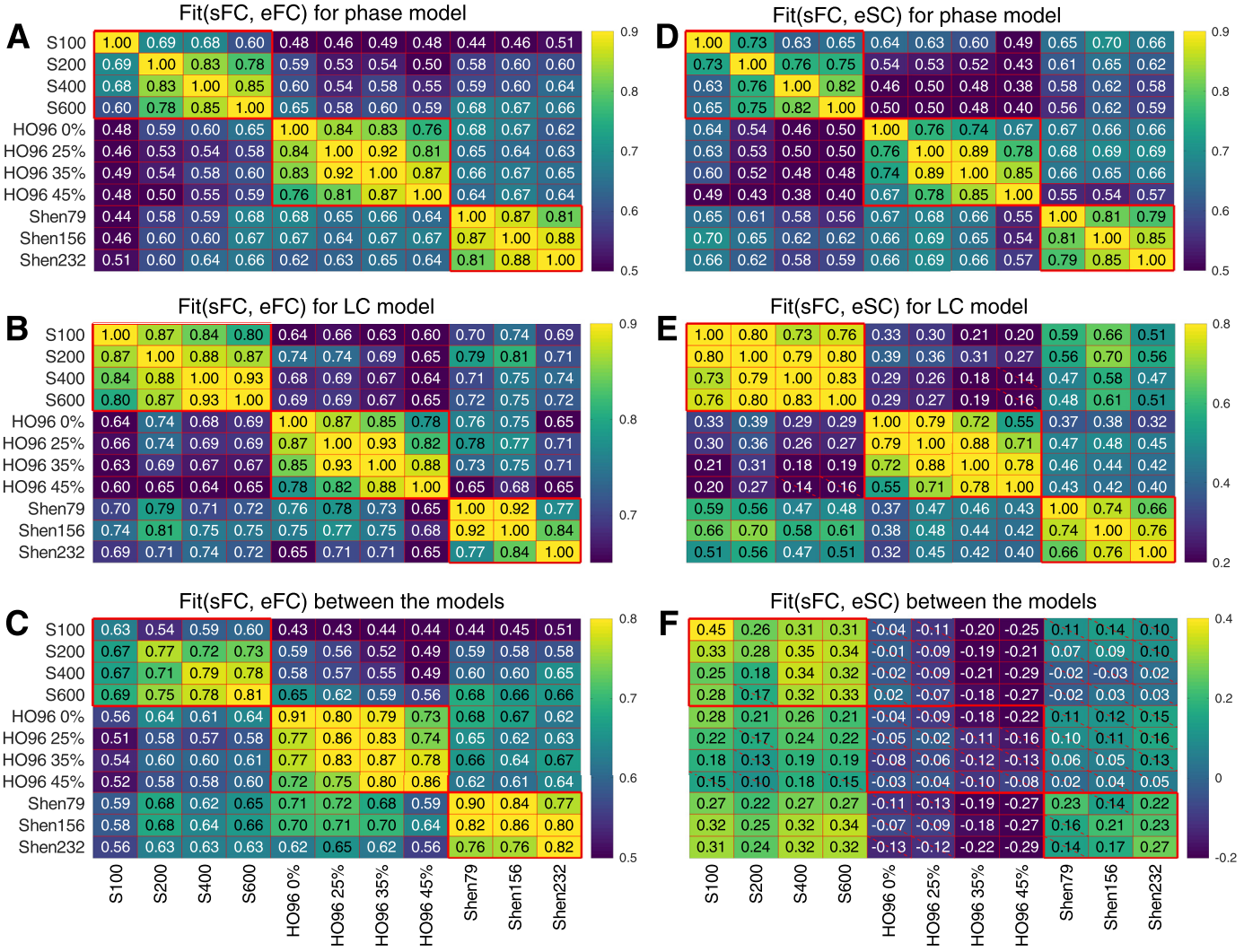

Fig. 5. Correspondence between the patterns of the inter-individual variation of the fitting results (Fit-values (3)) for the considered parcellations and models. The vectors of the Fit-values collected over all subjects and scans (see Methods for details) were Pearson correlated with each other for any two parcellations (indicated on the axes) for (**A - C**) Fit(sFC, eFC) and (**D - F**) Fit(sFC, eSC), and for (**A, D**) phase model and (**B, E**) LC model. In plots (**C** and **F**) the correspondence between the phase model (parcellations on the vertical axes) and LC model (parcellations on the horizontal axes) is illustrated. The results are depicted by color, and their magnitudes are indicated in the plots. The crossed out cells indicate that the corresponding correlation does not reach the statistical significance with $p < .05$. The heavy red lines delineate the parcellations from the same atlas (parcellation family). (For interpretation of the references to colour in this figure legend, the reader is referred to the web version of this article.)

axis, and the LC model was simulated for parcellations on the horizontal axis. As for the inter-parcellation correspondence of the fitting results for the same model [Fig. 5A and B], similar amount of stronger intra- and weaker inter-atlas correlation is observed for the between-model comparison [Fig. 5C].

The same conclusion can be drawn for the structure-functional model fitting Fit(sFC, eSC) as illustrated in Fig. 5D for the phase model and in Fig. 5E for the LC model. Here, the parcellations from the same atlas also agree much better with each other than for the parcellations from different atlases. The results also demonstrate that Fit-values obtained for HO96 parcellations and the LC model [Fig. 5E] are relatively dissimilar to the other two atlases of brain parcellations. Furthermore, the similarity Fit(sFC, eSC) seems to be sensitive to the model used for simulation as illustrated in Fig. 5F. The fitting results of the LC model for S100-S600 parcellations weakly correlate with those obtained for all other parcellations for the phase model. For other atlases, the fitting results of LC model are either practically independent of those obtained for the phase model (for the Shen atlas), or even weakly anti-correlate with the other model (for HO96 atlas) even for the same brain parcellation/atlas [Fig. 5F].

Changing the brain parcellation can also influence the values of the optimal parameters, where the maximal similarity (3) is achieved. The pairwise parameter differences are illustrated in supplementary Fig. A.3 for the considered parcellations and models. Similar to the correlation between the Fit-values [Fig. 5], the parcellations from the same atlas are expected to lead to smaller variations of the optimal parameters than between those from different atlases. Interestingly, the variation of the optimal parameters is larger for the functional model fitting modality, especially, for the between-model comparison than for the structure-function correspondence. In the latter case the parameter distance between models remarkably mimics the similarity patterns of the correlation between fitting results, compare Fig. 5F and supplementary Fig. A.3F.

3.3. Data variables

In the next Section 3.4 we evaluate how the maximal model-data similarity (3) obtained for the optimal model parameters depends on selected statistical properties of the empirical data used for the model derivation and validation. To this end, we calculated several data vari-

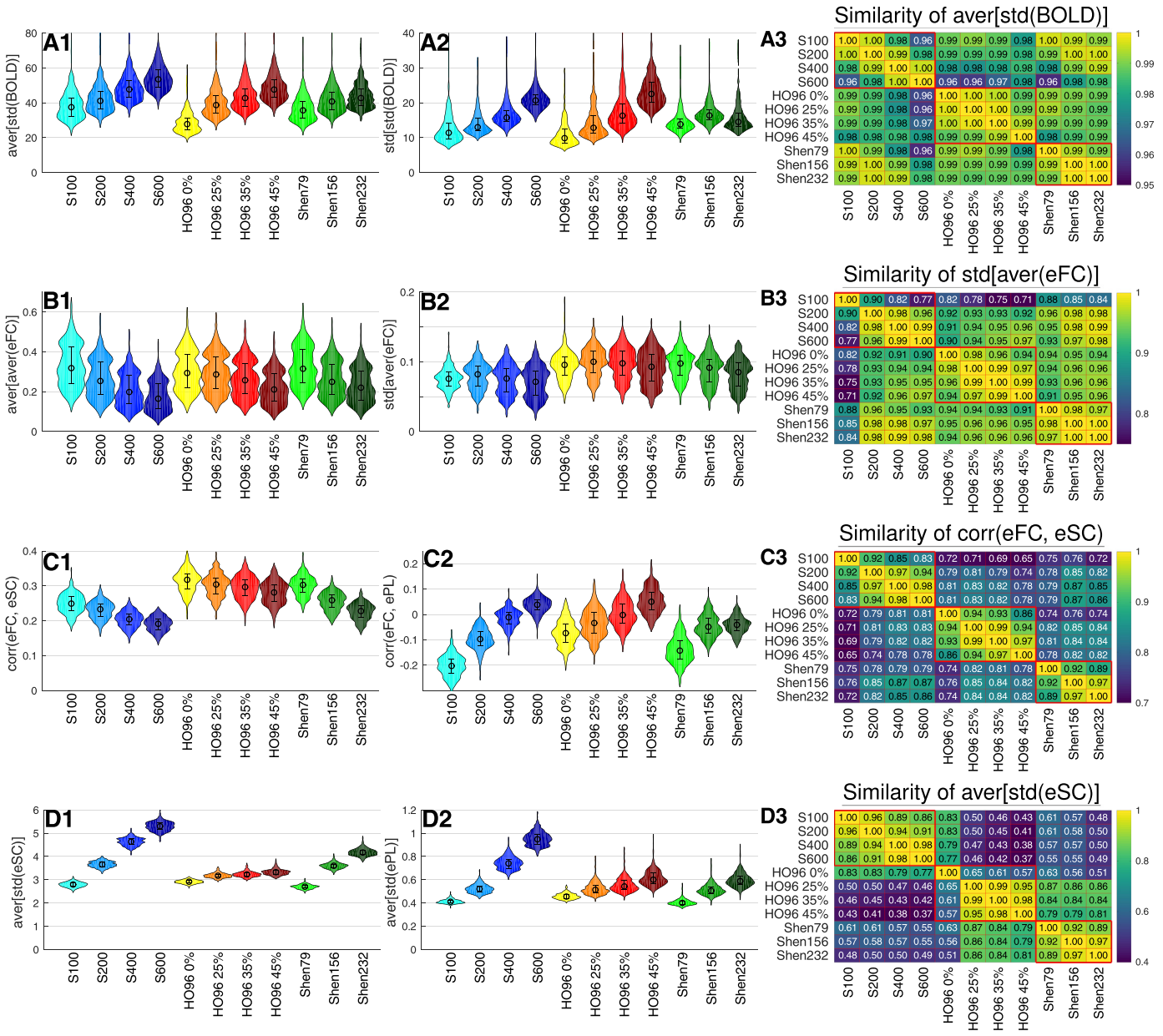

Fig. 6. Variation of the data variables extracted for the considered brain parcellations. In columns **1** and **2**, the distributions of the data variables (indicated on the vertical axes) for all subjects/fMRI sessions are depicted versus the parcellations (indicated on the horizontal axes). In column **3**, the correspondence between the data variables among all considered parcellations is illustrated. For any two parcellations (indicated on the axes), the Pearson cross-correlation between the corresponding data variables was calculated across all subjects for (**A3**) $aver[std(\text{BOLD})]$, (**B3**) $std[aver(\text{eFC})]$, (**C3**) $corr(\text{eFC}, \text{eSC})$, and (**D3**) $aver[std(\text{eSC})]$ as indicated in the titles of the plots. The results are depicted by color, and their magnitudes are also printed in the plots. The crossed out cells indicate that the corresponding correlation does not reach the statistical significance with $p < .05$. The heavy red lines delineate the parcellations from the same atlas (parcellation family). (For interpretation of the references to colour in this figure legend, the reader is referred to the web version of this article.)

ables (or indices) for each subject and fMRI scan session. For the empirical BOLD signals we calculated the standard deviation of their time fluctuations $std(\text{BOLD})$ averaged over all parcels $aver[std(\text{BOLD})]$. Since the BOLD signals were extracted as mean signals averaged over all voxels in the parcels, the latter data variable may reflect the extent of synchronization of BOLD dynamics within the individual brain regions. Indeed, the amplitude of the mean signal is expected to increase with enhanced synchronization as the theory of synchronization implies (Kuramoto, 1984). On the other hand, calculating the variability of time fluctuations among parcels $std[std(\text{BOLD})]$ may give an insight into the difference of individual parcels in this respect.

Smaller brain regions, e.g., for finer granularity (Schaefer, Shen) or larger probability threshold (HO96) can be suspected to be more homogeneous with respect to the BOLD dynamics. We observed that mean BOLD signals exhibit enhanced fluctuations for smaller parcels demonstrating larger standard deviation $std(\text{BOLD})$ [Fig. 6A1], where the distributions of $aver[std(\text{BOLD})]$ exhibit the behavior inverse to that of the parcels' size versus the considered brain parcellations [Fig. 1A]. The same holds for $std[std(\text{BOLD})]$ [Fig. 6A2, but see Shen232]. Our calculations thus indicate that the intra-region dynamical homogeneity (synchronization) may increase together with the inter-region variability of it. However, a systematic investigation of the collective dynamics of

BOLD signals within parcels is necessary to assess the intra-region dynamical homogeneity (Schaefer et al., 2018). Interestingly, the distributions of both mentioned data variables across individual subjects exhibit very similar patterns for any of the considered atlases and strongly correlate across subjects for any pair of parcellations, see Fig. 6 A3 for $aver[std(\mathrm{BOLD})]$, where the minimal correlation $r \approx 0.96$ is attained for S600.

Additional data variables can be calculated from eFC by evaluation of its column-wise mean $aver(\mathrm{eFC})$ and the standard deviation $std(\mathrm{eFC})$, where the former represents the average functional connectivity (synchronization) of a region to the rest of the brain (i.e., other regions), and the latter stands for the extent of variation of the individual connections of a given brain region. Evaluating the mean and the standard deviation once more across all brain regions we obtain four data variables: $aver[aver(\mathrm{eFC})]$, $std[aver(\mathrm{eFC})]$, $aver[std(\mathrm{eFC})]$, and $std[std(\mathrm{eFC})]$. The distributions of the first two are illustrated in Fig. 6B1 and B2, where the total average inter-region synchronization $aver[aver(\mathrm{eFC})]$ in the brain decays with decreasing region size, which is also in agreement with the behavior observed for BOLD signals [Fig. 6A2]. The inter-region variation of the regional synchronization to the rest of the brain $std[aver(\mathrm{eFC})]$ does not demonstrate very pronounced dynamics with respect to the considered parcellations [Fig. 6B2]. However, the inter-parcellation patterns of its distribution appears to be similar to those observed for the functional similarity Fit(sFC, eFC) [Fig. 3A and E]. An example of the cross-parcellation correlation for the later data variable is illustrated in Fig. 6B3, where the level of correlation is still very high with $r \gtrsim 0.91$ except for S100 which distinguishes from the other parcellations.

Further data variables can be the extent of correlation between the empirical connectivity matrices eFC, eSC and ePL, which may influence the quality of the model fitting and are denoted as $corr(\mathrm{eFC}, \mathrm{eSC})$, $corr(\mathrm{eFC}, \mathrm{ePL})$ and $corr(\mathrm{eSC}, \mathrm{ePL})$. Examples of the distributions of these variables are shown in Fig. 6C1 and C2, where both illustrated variables apparently demonstrate a monotonic behavior with respect to the parcel size, but in opposite directions, i.e., $corr(\mathrm{eFC}, \mathrm{eSC})$ decreases, and $corr(\mathrm{eFC}, \mathrm{ePL})$ increases when the region size decays. The impact of the state-of-the-art brain parcellations on the structure-function relationship $corr(\mathrm{eFC}, \mathrm{eSC})$ was investigated by Messe (2019), and a similar global decrease in correlation with decreasing the parcellation granularity and regions size was reported. For these data variables the difference between the atlases becomes more pronounced, where the correspondence (correlation) between the data indices for the parcellations of the same atlas are stronger than for those from different atlases [Fig. 6C3] as was shown for the results of the model validation and optimal parameters [Fig. 5 and supplementary Fig. A.3].

This effect is further enhanced for the data variables derived from SC matrices, for example, for $aver[std(eSC)]$ [Fig. 6D3]. The data variables $aver[std(\mathrm{eSC})]$ and $aver[std(\mathrm{ePL})]$ calculated from the eSC and ePL matrices normalized by their mean as used in the models always attain larger values for finer granularity/smaller brain regions [Fig. 6D1 and D2]. This is similar to the variables $corr(\mathrm{eFC}, \mathrm{ePL})$ [Fig. 6C2] and those derived from BOLD signals [Fig. 6A1 and A2]. This is however in contrast to the data variables calculated from eFC, where the behavior is different [Fig. 6B1, B2 and C1]. The observed increase of the average inter-region variability of SC matrices [Fig. 6D1 and D2] might be suspected when the brain is parcellated into smaller regions that stronger deviate from each other with respect to individual connectivity properties. However, a detailed investigation is necessary to clarify the underlying mechanisms of the illustrated behavior of the considered data variables [Fig. 6].

Further considered data variables in the form $std[aver(\cdot)]$ and $std[std(\cdot)]$ were calculated from the eSC and ePL matrices. The natural frequencies f_i of the models (1) and (2) extracted from the frequency spectra of the empirical BOLD signals (see Methods) were also taken into account, and the mean $aver(f_i)$ and the standard deviation $std(f_i)$ were involved in the analysis.

3.4. Correlation between data variables and model fitting

The variation of the empirical data illustrated in Fig. 6 may influence the observed variability of the modeling results [Figs. 3 and 4]. Therefore, to inquire into where the variance of the fitting results across subjects and parcellations may come from, we investigate how the discussed data variables and the maximal similarity (3) correlate with each other. Several such correlative relationships are illustrated in the scatter plots in Fig. 7A–C, where, together with linear regressions for individual parcellations (color dots and dashed lines), the joint linear regression for all data points in the plots (for all 11 parcellations) is also shown by solid black lines. The observed distinct constellations between the individual (color dashed) and joint (black solid) regression lines can be used to differentiate between a few classes of the data variables with respect to their relationships to the overall model fitting. For example, for the data variable $aver[std(\mathrm{BOLD})]$ [Fig. 7A] we found that the joint correlation indicated in the plot appears to be much smaller than the correlative relationships obtained separately for each individual parcellation. Therefore, the variation of the mentioned data variable can relatively well account for the variability of the model fitting across individual subjects for a given parcellation, i.e., for the intra-parcellation inter-subject variance. However, its explanatory power for the variation of Fit(sFC, eFC) across considered parcellations is limited. We may thus refer to such data indices as intra-parcellation variables.

Another class of the data variables can be illustrated by the data index $corr(\mathrm{eFC}, \mathrm{eSC})$ [Fig. 7B]. Here, the joint correlation between the empirical data and the model goodness-of-fit across subject data from different parcellations can be much higher than the correspondence across subjects within individual parcellations. In the considered example, the across-subject correlations between the empirical data and results of the model fitting are mostly small and negative for individual parcellations. Therefore this data variable can hardly explain the variance of the model fitting across subjects for a given brain parcellation. Nevertheless, the joint correlation for the data merged over all parcellations is much stronger contributing to our understanding of the variance of the fitting results across different parcellations. We may thus refer to such data indices as inter-parcellation variables.

For some other data variables, for example, for $std[aver(\mathrm{eFC})]$ the joint correlation is comparable to the relatively large correlations for individual parcellations [Fig. 7C]. The explanatory power of such variables can thus be extended from single to many parcellations. This indicates that such data variables can therefore well account for both the variability of the model fitting across subjects within individual parcellations and the differences of Fit-values across parcellations. We may thus refer to such data indices as the variables of both intra- and inter-parcellation types.

The correlations across subjects and scanning sessions between the similarity Fit(sFC, eFC) and all mentioned data variables are shown in Fig. 7D for all considered parcellations. One in particular observes that there are several data variables that only weakly correlate with Fit(sFC, eFC), which may indicate that the results of the model fitting may little depend on them. Such conclusion could be made for the mean of the natural frequencies $aver(f_i)$, average variability of eFC $aver[std(\mathrm{eFC})]$ (except for S100 and S200), and also for the data indices derived from eSC and ePL. Notably, the extent of the empirical structure-function relationship $corr(\mathrm{eFC}, \mathrm{eSC})$ also little correlates with the correspondence between simulated and empirical functional data, see also Fig. 7B. Put otherwise, increasing/decreasing the agreement between the empirical structure (eSC) and function (eFC) seems not to essentially influence the quality of the model fitting (the similarity between sFC and eFC) or may even have a negative effect. This takes place in spite of that the network model is constructed from eSC and its output is compared with eFC.

Other data variables consistently exhibit (anti-)correlation with Fit(sFC, eFC) ranging from moderate to relatively strong for most of the parcellations. This for instance applies to the spread of the natural frequencies $std(f_i)$, amplitude $aver[std(\mathrm{BOLD})]$ of the BOLD signals and

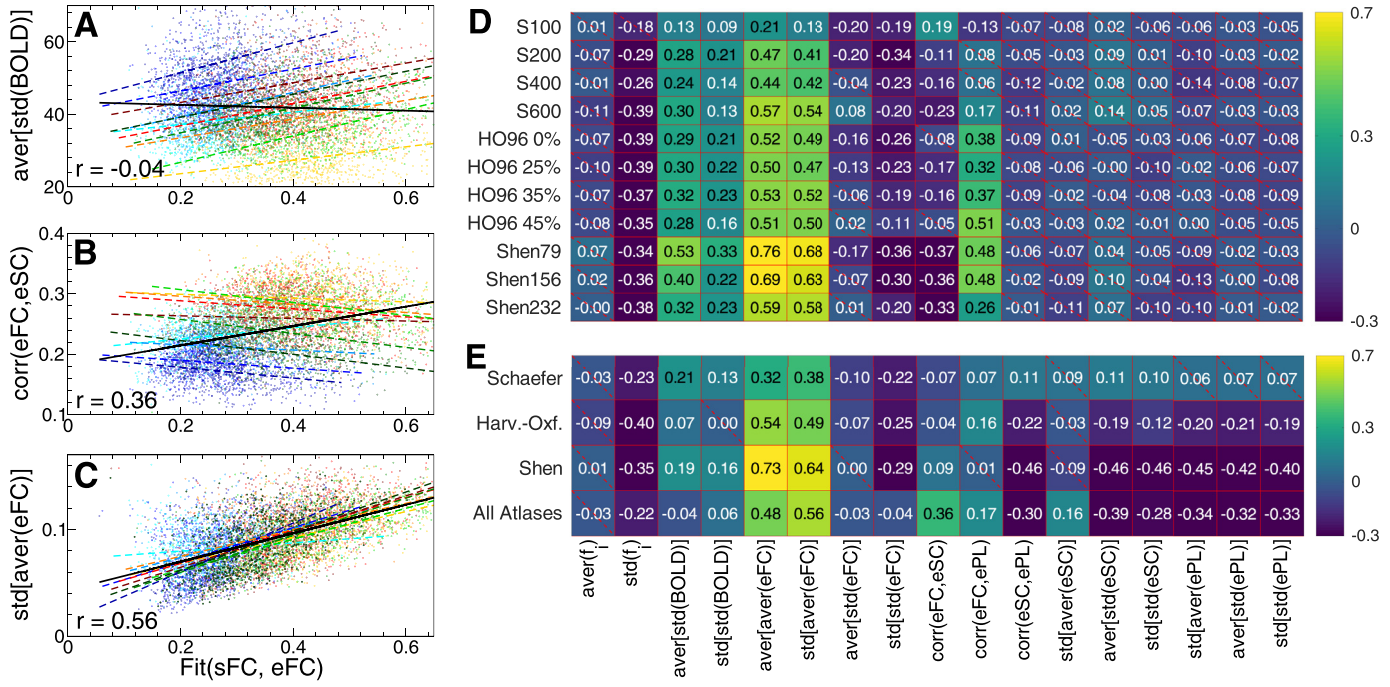

Fig. 7. Relationship between the fitting results (3) of the phase model (1) and empirical data. (**A-C**) Scatter plots and the corresponding linear regression (straight lines) are shown for a few selected data variables from Fig. 6 indicated on the vertical axes versus the maximal similarity Fit(sFC, eFC) (horizontal axes). Each dot represents one subject/MRI session, and color corresponds to that used to differentiate between the parcellations in Fig. 6. The black solid lines depict the joint linear regressions for all data in the plots, and the joint correlations r are also indicated. (**D, E**) Pearson correlation across individual subjects between the maximal similarity Fit(sFC, eFC) and several data variables indicated on the horizontal axis. The correlation was calculated for (**D**) different individual parcellations indicated on the vertical axis and (**E**) joint data merged over a few combinations of the considered parcellations as indicated on the vertical axis: all parcellations of the Schaefer atlas, Harvard-Oxford atlas, Shen atlas and all 11 considered parcellations (last row). The correlation is depicted by color, and its magnitude is indicated in the plot. The crossed out cells indicate that the corresponding correlation does not reach the statistical significance with $p < .05$.

some properties of eFC [Fig. 7D]. These data variables may be used to provide an initial guess of the pattern of the functional model fitting for new subjects that supposed to be included in the analysis. However, the correlation between eFC and ePL matrices $corr(\text{eFC}, \text{ePL})$ seems to have a different impact on the model validation for different atlases, where Fit(sFC, eFC) is practically independent of this data index for the Schaefer atlas, which is distinct for other atlases [Fig. 7D]. Such effects may also be useful for understanding the observed differences in the quality of the model fitting for individual subjects and may also be applied for explaining the impact of the considered brain parcellations on the model fitting [Fig. 3A].

The above classification of the data variables with respect to their intra- or inter-parcellation correlative relationships with the modeling results [Fig. 7A–C] can be evaluated by comparing the individual correlations in Fig. 7D to the joint correlation calculated for the data merged over the considered parcellations for simultaneous analysis. This is illustrated in Fig. 7E for the phase model and functional model fitting. More systematic comparison of the individual and joint correlations between the results of the model fitting (3) and the data variables is summarized in Fig. 8 for both models (1) and (2) and both fitting modalities Fit(sFC, eFC) and Fit(sFC, eSC). Much larger individual (joint) correlation than the joint (individual) one is indicative for an intra- (inter-) parcellation data variable.

The constellation obtained for the phase model [Fig. 8A] is well preserved also for the LC model [Fig. 8B, see also supplementary Fig. A.4 for individual and joint correlations]. The correlation patterns are different for the structure-functional fitting modality [Fig. 8C and D], where the results obtained for the phase and LC models may deviate from each other, see also supplementary Fig. A.5 for individual and joint correlations for the structure-functional fitting modality Fit(sFC, eSC). Although most of the considered data indices exhibiting large correlation are of inter-parcellation type [Fig. 8], still there are a few data variables of intra-parcellation type like $std(f_i)$, $aver[std(\text{BOLD})]$ or $std[std(\text{eFC})]$ for the functional similarity Fit(sFC, eFC) or $std(f_i)$ (phase model) and $aver(f_i)$ (LC model) for Fit(sFC, eSC). The most pronounced data variables of both types for Fit(sFC, eFC) are given by the total average inter-region synchronization $aver[aver(\text{eFC})]$ or inter-region variation of the regional synchronization $std[aver(\text{eFC})]$ [Fig. 8A,B].

3.5. Multiple linear regression model

The variation of the model fitting across subjects and brain parcellations can be investigated by combining several data variables in a MLR model, where they serve as independent (explanatory) variables, and the maximal similarity Fit(sFC, eFC) is the MLR output, i.e., the dependent variable. The calculated data variables can be used in the MLR model to evaluate which variation of the Fit-values across subjects and parcellations can be explained by the individual empirical data used for the model derivation and validation. The results of such a regression with respect to all data variables [Fig. 7] are illustrated in Fig. 9 for investigated individual parcellations as well as for the joint data merged over all parcellations. The fraction of the explained variance increases when more data variables get involved in the regression, see Fig. 9A–C and compare the indicated R^2-values to the correlation coefficients in Figs. 7 and 8. The results of the model fitting for the anatomical Harvard-Oxford and the functional Shen atlases seem to be somewhat better explained by the empirical data used for the model derivation than for the functional Schaefer atlas [Fig. 9E, but see Shen232 for LC model]. The strongest regression results are obtained for the joint regression for the data merged over all considered parcellations [Fig. 9D and E].

The weights of the discussed data variables within the maximal similarity Fit(sFC, eFC) as reflected by the regression coefficients [Fig. 9 A2-D2] highlight several data variables that are of importance for under-

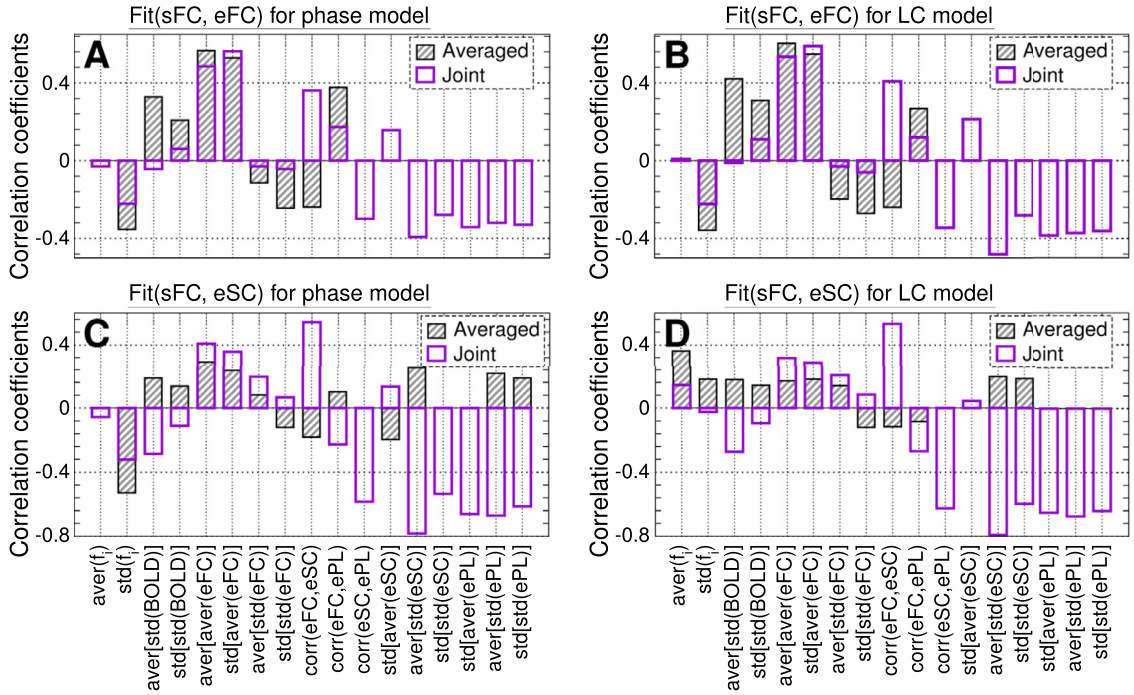

Fig. 8. Correlation between the Fit-values (3) and data variables from Fig. 7 jointly for all considered brain parcellations. For the data variables indicated on the horizontal axes, the joint correlation for the data merged over all considered parcellations [Fig. 7E, last row] is depicted by empty bars. The hatched bars represent the correlation for individual parcellations from Fig. 7D averaged over all parcellations and significant values (i.e., excluding the crossed out cells in Fig. 7D) as indicated in the legends. The data is shown for (**A, B**) functional fitting Fit(sFC, eFC) and (**C, D**) structure-functional fitting Fit(sFC, eSC), and for (**A, C**) phase model (1) and (**B, D**) LC model (2) as indicated in the titles of the plots.

standing of the modeling results. All regression coefficients for the interdependency between Fit(sFC, eFC) and the data variables are shown in Fig. 10 for both models including the case of joint data (last rows in the plots). Comparing the obtained results for individual parcellations and models, we observe that the regression coefficients well agree between the two models. There are several data indices that consistently and strongly contribute to the Fit-values and seem to have a major impact on the model fitting for many parcellations, see Figs. 9 and 10. In particular, the variables $std[aver(\mathrm{eFC})]$, $aver[std(\mathrm{eFC})]$ and $corr(\mathrm{eFC},\mathrm{eSC})$ have the most notable regression coefficients. At the level of individual parcellations, there is also a minor impact of other variables, for example, the natural frequencies $std(f_i)$, average total connectivity $aver[aver(\mathrm{eFC})]$ and its variability $std[std(\mathrm{eFC})]$ as well as structure-function relationship with ePL matrix $corr(\mathrm{eFC},\mathrm{ePL})$. For the inter-parcellation variance of Fit(sFC, eFC), additional variables can be taken into account, that are $corr(\mathrm{eFC},\mathrm{ePL})$ and $aver[std(\mathrm{eSC})]$ as suggested by the MLR model [Fig. 10].

Similar results can also be obtained for the structure-functional model fitting and the maximal similarity Fit(sFC, eSC) [supplementary Fig. A.6]. Here we however find that Fit(sFC, eSC) less consistently depends on the data variables over individual parcellations and with a reduced agreement between different models as reflected by the MLR coefficients. The only data indices that reliably contribute to the inter-individual variation of the Fit-values for most of the parcellations are those extracted from the natural frequencies $aver(f_i)$ and $std(f_i)$, while the latter is again less reliable for the LC model [supplementary Fig. A.6 A and B]. The fractions of the Fit(sFC, eSC) variance explained by the data variables for individual parcellations is reduced as compared to the functional model fitting [compare Fig. 9E and supplementary Fig. A.6 D]. However, the inter-parcellation variance as reflected by the joint data can still be relatively well accounted for by the empirical data [supplementary Fig. A.6 C], and the largest MLR coefficients of the joint data for both models are obtained for the structural connectome eSC and ePL [supplementary Fig. A.6 A and B].

3.6. Group-level inter-parcellation variations

In the previous sections the interdependence between the results of the model validation and empirical data were evaluated by correlation of the Fit-values with the data variables across individual subjects either for any parcellation separately or for joint data merged over all considered parcellations. While the former approach investigates the inter-subject intra-parcellation variance, the latter also considers the variation of the variables among parcellations. The inter-parcellation variation of the fitting results can also be addressed at the group level only, i.e, separated from the inter-subject variations. This can be accomplished when the data calculated for individual subjects is compressed into single values, for example, to medians, see Figs. 3 and 4. The behavior of the group-averaged values across individual parcellations can provide an informed expectation on how a given parcellation may in average influence the considered variables, for example, the Fit-values or the data indices.

In this section we correlate the medians of the Fit-values and the considered data variables across parcellations. The results of the calculations are illustrated in Fig. 11. Several data variables exhibit strong correspondence with the Fit-values for both models. However, only a few of them are significantly correlated as indicated by hatched bars for the phase model and empty bars with heavy borders for the LC model [Fig. 11A and D]. For the functional modal fitting, only two data indices $std[aver(\mathrm{eFC})]$ and $corr(\mathrm{eFC},\mathrm{eSC})$ significantly and strongly contribute to the inter-parcellation variance of Fit(sFC, eFC) at the group level for both models [Fig. 11A], see also Fig. 11B and C for the corresponding scatter plots, where the fraction of the explained variance can reach 93%.

For the structure-functional model fitting, more data variables significantly correlate with the maximal similarity Fit(sFC, eSC) [Fig. 11D]. However, only four of them fulfill this requirement for both models simultaneously: $corr(\mathrm{eFC},\mathrm{eSC})$ that also contributes to Fit(sFC, eFC), as well as data variables $aver[std(\mathrm{eSC})]$, $std[aver(\mathrm{ePL})]$ and $aver[std(\mathrm{ePL})]$ calculated from the structural connectome as given by eSC and ePL ma-

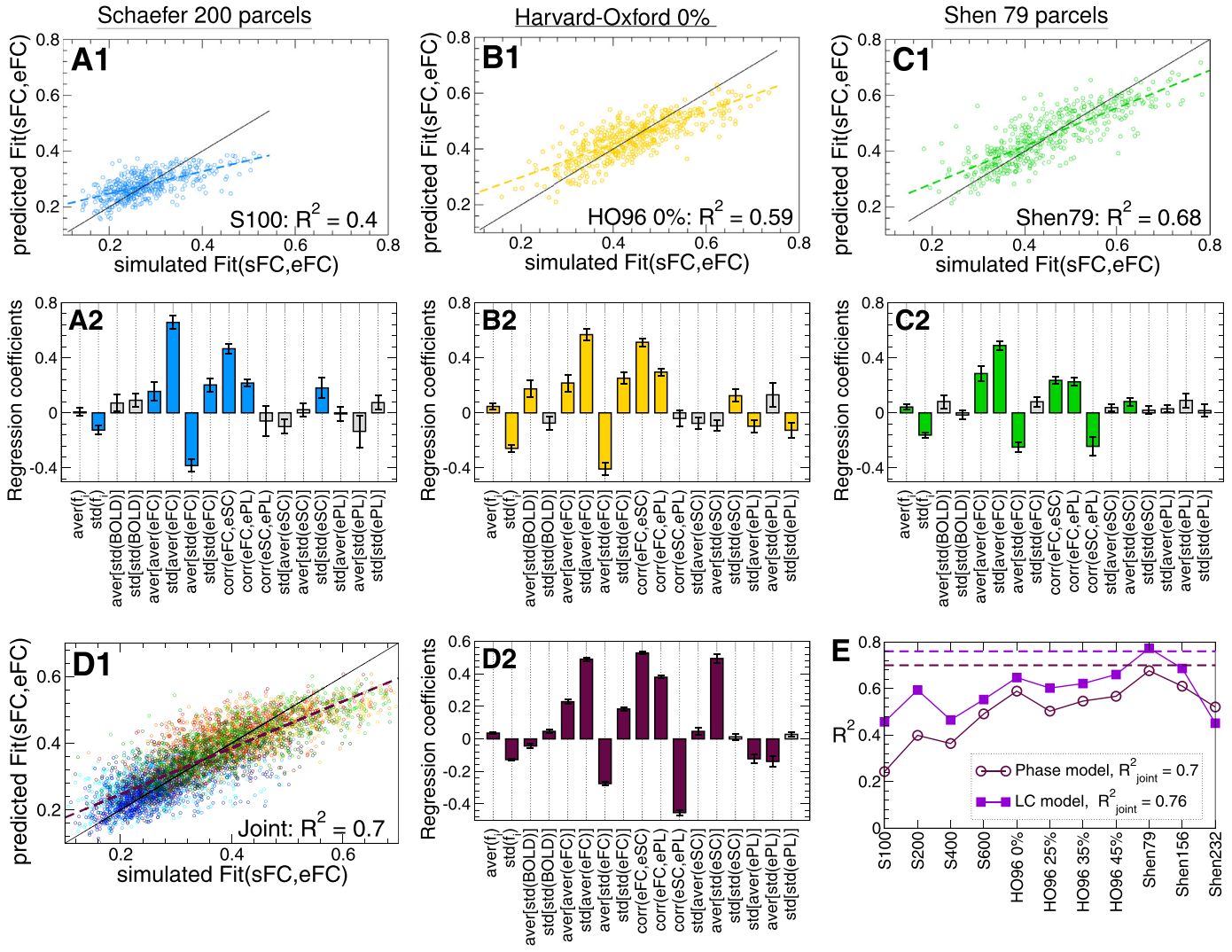

Fig. 9. Modeling the maximal similarity Fit(sFC, eFC) by the multiple linear regression (MLR) model with data variables from Fig. 7 as independent variables. (**A1** - **D1**) Scatter plots with regression lines of the Fit-values predicted by MLR versus Fit(sFC, eFC) obtained by simulations of the phase model (1). The diagonals are depicted by thin black lines for comparison. (**A2** - **D2**) The corresponding regression coefficients with the standard deviation for z-scored data obtained from the model fitting for parcellations (**A**) S200 and (**B**) HO96 0%, (**C**) Shen79 and (**D**) for joint data merged over all considered parcellations as indicated in the corresponding scatter plots. The gray bars indicate the regression coefficients, where the statistical significance with $p < .05$ was not achieved. The fractions of the explained variance R^2 are also shown in the scatter plots and in plot (**E**) for all individual parcellations for both phase and LC models as indicated in the legend. The dashed lines depict R^2 for the joint data also indicated in the legend.

trices. Again, the fraction of the explained variance can reach 93% for the data index calculated from eSC, see Fig. 11D-F also for the corresponding scatter plots. Interestingly, for the structure-functional fitting modality also the data indices derived from eFC matrices seem to significantly contribute to the fitting values Fit(sFC, eSC) for the phase model [Fig. 11D], although the corresponding p-values are close to the significance threshold of 0.05 after correction for multiple comparisons.

4. Discussion

We investigated the impact of data parameters used for the preprocessing of the empirical neuroimaging data on the structure and dynamics of whole-brain dynamical models derived from and validated against empirical data. In this study we focused on brain parcellations and considered three brain atlases as defined by the functional Schaefer atlas with 100, 200, 400 and 600 cortical regions (Schaefer et al., 2018), functional Shen atlas with 79, 156 and 232 cortical regions (Shen et al., 2013), and the anatomical Harvard-Oxford atlas of 96 cortical regions with a few thresholds of the maximal probability (Desikan et al., 2006) that also influenced the region size. Here we did not aim to suggest an optimal atlas, which is a complex task given the numerous existing parcellation approaches, brain atlases and multiplicity of possible optimization criteria. Instead, we illustrated possible effects that the considered brain parcellations can have on the modeling results. For this we analyzed the results of the model validation for two fitting modalities as given by the maximal similarities Fit(sFC, eFC) and Fit(sFC, eSC) and for two models of coupled phase and limit-cycle oscillators. We also suggested an approach to account for the parcellation-induced inter-subject and inter-parcellation variability of the fitting results.

We compared the distributions of the Fit-values and the corresponding optimal parameters for individual subjects and reported on pronounced differences in the model fitting between the considered brain parcellations. In particular, Fit(sFC, eFC) for the Schaefer atlas is much smaller than that for the Harvard-Oxford and Shen atlases [Fig. 3]. The latter atlases seem to provide appropriate parcellations for high correspondence between simulated and empirical functional data. The better

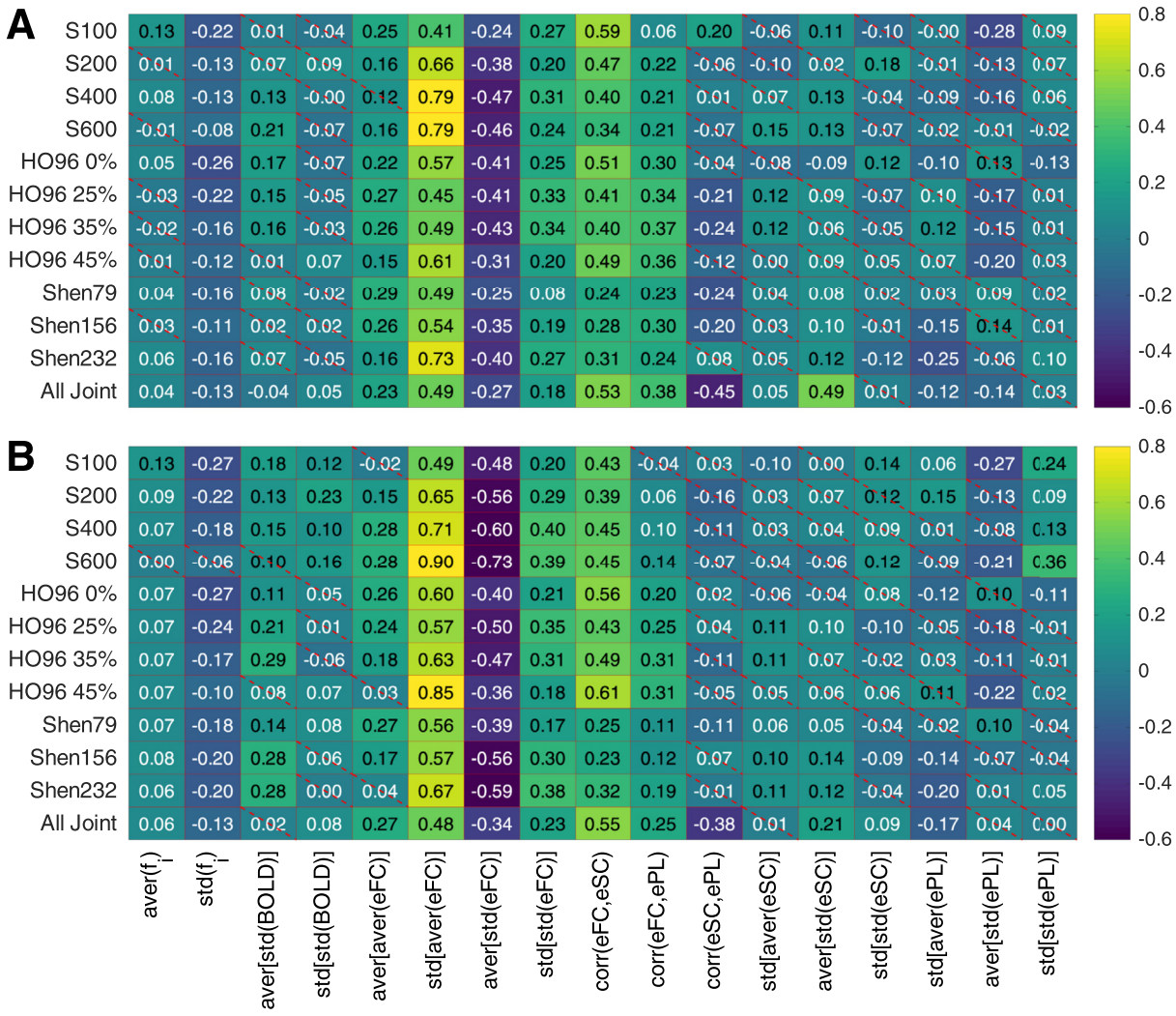

Fig. 10. Regression coefficients of the MLR model for Fit(sFC, eFC), for all considered parcellations including the joint data as indicated on the vertical axes and for (**A**) phase model and (**B**) LC model. The values are depicted by color, and they magnitudes are shown in the plots. The crossed out cells indicate that the corresponding coefficient does not reach the statistical significance with $p < .05$.

fitting for HO96 0% as compared to S100 was also observed for the model of coupled phase oscillators simulating the high-frequency electrical activity of brain regions in α and γ frequency bands (Manos et al., 2019). For the structure-functional model fitting Fit(sFC, eSC) the situation is different, and the difference between the atlases is less pronounced [Fig. 4].

We demonstrated that the best correspondence Fit(sFC,eFC) between simulated and empirical FCs was achieved at 200 parcels for the Schaefer atlas [Fig. 3] suggesting that an optimal spatial scale may exist, see also (Arslan et al., 2018; Proix et al., 2016). However, the best functional model fitting for the other brain atlases was achieved at the coarsest granularity (Shen atlas) or smallest probability threshold (Harvard-Oxford atlas), where the parcel size is maximal. On the other hand, the maximal values of the structure-functional model fitting Fit(sFC, eSC) were achieved at the largest region size for the Schaefer and Shen atlases [Fig. 4]. For the Harvard-Oxford atlas, Fit(sFC, eSC) exhibited either non-monotonic behavior with the optimal probability thresholds at 25%–35% for the phase model or even monotonically increased for the LC model when the region size decreased. We thus observed a remarkable exchange of the distribution patterns of Fit(sFC, eFC) and Fit(sFC, eSC) between the Schaefer and Harvard-Oxford atlases and different behavior of the Fit-values with respect to the parcel size. These findings complicate the problem of the optimal spatial scale of brain parcellation.

The corresponding distributions of the optimal model parameters however manifest very similar shapes for the same fitting modality also for different atlases and parcellations, but differ across fitting modalities [Figs. 3 and 4]. In particular, the optimal parameters for Fit(sFC, eFC) are strongly concentrated towards zero delay, whereas the structure-function correspondence Fit(sFC, eSC) for many subjects was also achieved for large delay, especially, for the phase model. This is accompanied by a narrow interval of the coupling strength in the latter case, whereas this parameter can broadly be distributed for the functional fitting, especially, for the Shen atlas and phase model. Therefore, the direct modeling of the resting-state BOLD dynamics by slowly oscillating phase or limit-cycle oscillators can safely be performed by systems without delay (Deco et al., 2019; 2017; Ponce-Alvarez et al., 2015), however, only for the fitting of the simulated and empirical functional data.

The impact of the brain parcellations on the model validation can be investigated by evaluation of how the fitting results Fit$(\cdot,\cdot)$ calculated for individual subjects and a given parcellation agree with those found for other parcellations. We thus correlated Fit-values for different parcellations across subjects and calculated the distance between the corresponding optimal model parameters. It appeared that Fit-values for the parcellations within the same atlas better correlate with each other than across different atlases for both fitting modalities Fit(sFC,

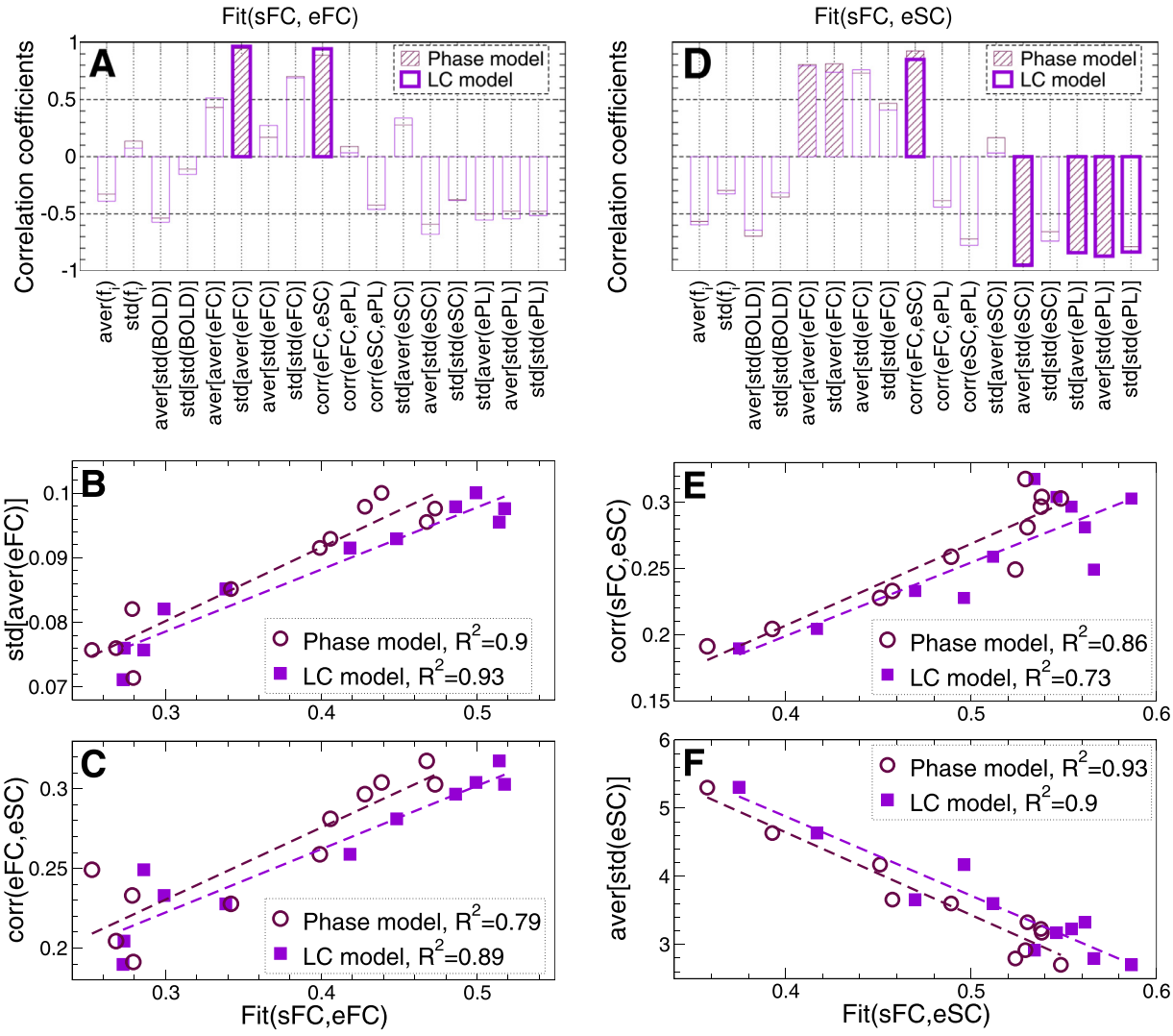

Fig. 11. Correlation between the results of the model fitting and data variables at the group level. (**A, D**) Pearson correlation across pacellations between the medians evaluated over all subjects of the data variables and the corresponding medians of (**A**) Fit(sFC, eFC) and (**D**) Fit(sFC, eSC). The hatched bars for the phase model and empty violet bars with heavy borders for the LC model stand for statistically significant ($p < .05$) correlation coefficients. (**B,C,E,F**) Scatter plots of the medians of the data variables versus (**B, C**) Fit(sFC, eFC) and (**E, F**) Fit(sFC, eSC) with the corresponding regression lines. Each plot symbol corresponds to one of the considered parcellations. The fractions of the explained variance (squared correlation) for both models are indicated in the legends.

eFC) and Fit(sFC, eSC) and both considered models [Fig. 5]. The same is true for the distance between the optimal parameters, where they less deviate from each other for the parcellations from the same atlas than between atlases [supplementary Fig. A.3]. It is interesting to note that neither different numbers of brain regions for the Schaefer and Shen atlases nor different level of thresholding for the Harvard-Oxford atlas can cause differences in the cross-subject correspondence in the model fitting larger than those between different atlases even for parcellations with similar region size. The inter-atlas differences cannot simply be reduced to differentiation between anatomical and functional parcellation approaches considered in this study. This indicates that a parcellation family (atlas) shares some particular properties that are reflected in the results of the model fitting and preserved even for varying other "internal" parcellation parameters (e.g., granularity or probability threshold affecting region size). This conclusion is also preserved for between-model comparison for Fit(sFC, eFC), whereas the structure-functional fitting results Fit(sFC, eSC) obtained for the LC model demonstrated enhanced sensitivity, especially, for the Harvard-Oxford atlas [Fig. 5].

To understand the origin of the observed variation of the fitting results across subjects and brain parcellations, we suggested to evaluate how the Fit-values depend on a few data variables (or data indices) reflecting some statistical properties of the empirical data used for the model derivation and validation. The performed regressive analysis between Fit-values and data variables suggested that the latter can be split into a few classes depending on their explanatory power for (*i*) inter-subject Fit-variance for individual parcellations; (*ii*) inter-subject Fit-variance across parcellations for joint data; and (*iii*) both inter-subject Fit-variance within individual parcellations and across them [Figs. 7 and 8].

The bivariate analysis provided correlation between Fit-values and individual data variables, where the squared correlation with Fit(sFC, eFC) across subjects can reach $R^2 = 64\%$ for individual parcellations and 35% for joint data merged over all considered parcellations [Fig. 7 and supplementary Fig. A.4]. For the structure-functional model fitting Fit(sFC, eSC), this quantity may range up to 40% for the variance across subjects for individual parcellations and about 62% for joint data [supplementary Fig. A.5]. The inter-subject fluctuations of the Fit-values may be better accounted for if several data variables are used in the MLR model [Fig. 9]. With the multivariate approach, the inter-subject variance of Fit(sFC, eFC) and Fit(sFC, eSC) can be explained up to 77%

and 56% within individual parcellations and up to 76% and 77% for joint data, respectively [Fig. 9 and supplementary Fig. A.6]. Finally, if the variance of the fitting results across parcellations is considered at the group level only (as medians), the individual data variables correlate with the fitting values up to $R^2 = 93\%$ [Fig. 11].

Evaluating the effect that a given parcellation can have on the data variables, which reliably, strongly and significantly correlate with the fitting values as investigated in this study, can help to explain and predict the results of the model fitting before involving computationally expensive model simulations. This can be addressed by investigating the properties of the empirical data extracted for varying brain parcellation. Decrease of the region size due to finer granularity or larger cutting threshold seems to cause two main effects, where both (*i*) the intra-region dynamical homogeneity and (*ii*) inter-region heterogeneity appeared to increase. This can be concluded from the behavior of the mean BOLD signals of the brain regions and the extent of total synchronization between regions $aver[aver(\mathrm{eFC})]$ [Fig. 6]. The inter-region heterogeneity seems to increase for smaller regions also for the structural connectome as demonstrated by the data variables derived from eSC, ePL. Here, the empirical structure-function relationship $corr(\mathrm{eFC}, \mathrm{eSC})$ decays with decreasing region size as was also reported by Messe (2019). It is interesting to note that the correspondence between structure and function is larger for the Harvard-Oxford atlas and the coarsest granularity of the Shen atlas as compared to the Schaefer atlas. Investigation of the impact of brain parcellations on the data variables should also take into account inter-subject spatial variability (shape and location) of brain regions, which seems to influence the cross-subject variability of the resting-state fMRI data and functional connectivity (Bijsterbosch et al., 2018; Kong et al., 2018).

Among the considered data variables only a few indeed exhibit relatively strong interdependencies with the Fit-values across subjects and parcellations [Figs. 7–11]. These sets of the data variables may vary for different fitting modalities and models. Here, the behavior of $corr(\mathrm{eFC}, \mathrm{eSC})$ is of special interest, because the empirical structure-function correspondence might be suspected to underlie the model fitting results Fit(sFC, eFC) and Fit(sFC, eSC). Our investigations however showed that $corr(\mathrm{eFC}, \mathrm{eSC})$ only weakly anti-correlate with Fit-values across subjects for practically all of the considered parcellations [Fig. 7 and supplementary Figs. A.4 and A.5]. On the other hand, $corr(\mathrm{eFC}, \mathrm{eSC})$ relatively strongly correlates with the Fit-values for joint data [Fig. 8] and can thus potentially be used to explain the variation of the fitting results between atlases, especially, if the prediction is performed at the group-averaged level [Fig. 11]. In addition to the variable of the structure-function relationship, the attention might also be paid to other data indices including the average BOLD amplitude $aver[std(\mathrm{BOLD})]$, the total synchronization $aver[aver(\mathrm{eFC})]$, variability of the regional synchronization $std[aver(\mathrm{eFC})]$ and the average variability of inter-region structural connectivity $aver[std(\mathrm{eSC})]$. Further data indices derived from the path length matrices ePL and natural frequencies f_i might also be of importance, especially, for the structure-functional model fitting Fit(sFC, eSC).

Examining the similarities and differences in the interdependencies between the Fit-values and data variables for individual parcellations, joint and group-averaged data we may reveal the properties that are crucial for understanding the impact of brain parcellations on the empirical and simulated data. In this study we presented several interesting observations that require further detailed investigation and explanation, which could contribute to the mechanisms influencing the modeling results. In the first turn, this concerns the counter-intuitive negative dependencies (or their absence) between the empirical structure-function relationship and fitting results at the subject level in contrast to the group level as discussed above. Understanding the relationship between the fitting results and other data variables, especially, for different fitting modalities is also important. In this respect, we observed that the parcellation-induced variability of the structure-functional model fitting across subjects appears to be sensitive to the model and parcellation considered, whereas the functional fitting is relatively robust against different parcellations and models [Fig. 5]. Another issue relates with the mechanism of how the parcellation granularity and region size influence the correspondence between empirical and simulated functional and structural connectomes, which was found to be a difficult problem already for empirical data (Messe, 2019). We suggested to address these questions by separating the inter-subject and inter-parcellation variability of the modeling results and their investigation by inspecting the data indices computed from the empirical data. This approach needs to be confirmed and refined for more parcellations, models and datasets.

In this study we used the HCP dataset, where the data quality is close to a perfect physiological noise reduction. Examining different processing strategies and their parameters can be an object of investigation for further studies. In addition, other measures of similarity between simulated and empirical data can be used to verify the obtained results, for example, the amount of metastability or similarity between simulated and empirical dynamic FC (Deco et al., 2017). The generalization of the reported results should be based on profound hypothesis testing involving sophisticated statistical methods for evaluation and comparison of correlation (Wilcox and Rousselet, 2018). On the other hand, instead of similarity measures based on correlative relationships one may utilize linear models that could resolve some issues connected with heteroscedasticity of the data (Thirion et al., 2015). Some other data indices may be calculated from empirical data. For example, the graph-theoretical network properties of the empirical connectome may be involved in the analysis as well (Rubinov and Sporns, 2010). Selecting and investigating a few most important data variables with respect to their impact on the modeling results, and on a data-driven analysis of brain networks, could advance our understanding of the results' variability across subjects and parcellations.

Data and code availability statement

MRI data used in this study are publicly available from ConnectomeDB (db.humanconnectome.org). The code used for the simulation of the brain network dynamics can be found here: https://gitlab-public.fz-juelich.de/brainmodelling/resting-state-atlases.

Ethics statement

Human subjects: HCP data (https://www.humanconnectome.org/, (Van Essen et al., 2013)) were acquired using protocols approved by University institutional review board (Mapping the Human and Heritability; IRB # 201204036). Informed consent was obtained from subjects.

Declaration of Competing Interest

The authors have declared that no competing interests exist.

Credit authorship contribution statement

Oleksandr V. Popovych: Conceptualization, Resources, Data curation, Software, Formal analysis, Validation, Investigation, Visualization, Methodology, Writing - original draft, Writing - review & editing. **Kyesam Jung:** Data curation, Software, Validation, Methodology, Writing - review & editing. **Thanos Manos:** Conceptualization, Resources, Data curation, Methodology, Writing - review & editing. **Sandra Diaz-Pier:** Resources, Software, Methodology, Writing - review & editing. **Felix Hoffstaedter:** Data curation, Software, Methodology, Writing - review & editing. **Jan Schreiber:** Data curation, Software, Methodology, Writing - review & editing. **B.T. Thomas Yeo:** Resources, Validation, Methodology, Writing - review & editing. **Simon B. Eickhoff:** Conceptualization, Resources, Supervision, Funding acquisition, Validation, Methodology, Project administration, Writing - review & editing.

Acknowledgments

We gratefully acknowledge the fruitful discussions with Viktor Jirsa, Petra Ritter and Alexander Peyser. The authors also gratefully acknowledge the computing time granted by the JARA Vergabegremium and provided on the JARA Partition part of the supercomputer JURECA at Forschungszentrum Jülich (Jülich Supercomputing Centre, 2018). Data were provided by the Human Connectome Project, WU-Minn Consortium (Principal Investigators: David Van Essen and Kamil Ugurbil; 1U54MH091657) funded by the 16 NIH Institutes and Centers that support the NIH Blueprint for Neuroscience Research; and by the McDonnell Center for Systems Neuroscience at Washington University. This work was supported by the Helmholtz Portfolio Theme Supercomputing and Modeling for the Human Brain, and the European Union's Horizon 2020 Research and Innovation Programme under Grant Agreements 720270 (HBP SGA1), 785907 (HBP SGA2), and 826421 (VirtualBrainCloud). TM is supported by the Labex MME DII (ANR-11-LBX-0023-01) French national funding program. BTTY is supported by the Singapore National Research Foundation (NRF) Fellowship (Class of 2017) and the National University of Singapore Yong Loo Lin School of Medicine (NUHSRO/2020/124/TMR/LOA). Any opinions, findings and conclusions or recommendations expressed in this material are those of the author(s) and do not reflect the views of National Research Foundation, Singapore. The funders had no role in data collection, discussion of content, preparation of the manuscript, or decision to publish.

Supplementary material

Supplementary material associated with this article can be found, in the online version, at doi:10.1016/j.neuroimage.2021.118201.

References

Arslan, S., Ktena, S.I., Makropoulos, A., Robinson, E.C., Rueckert, D., Parisot, S., 2018. Human brain mapping: a systematic comparison of parcellation methods for the human cerebral cortex. Neuroimage 170, 5–30. doi:10.1016/j.neuroimage.2017.04.014.

Bijsterbosch, J.D., Woolrich, M.W., Glasser, M.F., Robinson, E.C., Beckmann, C.F., Van Essen, D.C., Harrison, S.J., Smith, S.M., 2018. The relationship between spatial configuration and functional connectivity of brain regions. eLife 7, e32992. doi:10.7554/eLife.32992.

Bolt, T., Nomi, J.S., Rubinov, M., Uddin, L.Q., 2017. Correspondence between evoked and intrinsic functional brain network configurations. Hum. Brain Mapp. 38, 1992–2007. doi:10.1002/hbm.23500.

Breakspear, M., Heitmann, S., Daffertshofer, A., 2010. Generative models of cortical oscillations: neurobiological implications of the Kuramoto model. Front. Hum. Neurosci. 4, 190. doi:10.3389/fnhum.2010.00190.

Cabral, J., Hugues, E., Sporns, O., Deco, G., 2011. Role of local network oscillations in resting-state functional connectivity. Neuroimage 57, 130–139. doi:10.1016/j.neuroimage.2011.04.010.

Cole, M.W., Bassett, D.S., Power, J.D., Braver, T.S., Petersen, S.E., 2014. Intrinsic and task-evoked network architectures of the human brain. Neuron 83, 238–251. doi:10.1016/j.neuron.2014.05.014.

Conturo, T.E., Lori, N.F., Cull, T.S., Akbudak, E., Snyder, A.Z., Shimony, J.S., McKinstry, R.C., Burton, H., Raichle, M.E., 1999. Tracking neuronal fiber pathways in the living human brain. Proc. Natl. Acad. Sci. U. S. A. 96, 10422–10427. doi:10.1073/pnas.96.18.10422.

Deco, G., Cruzat, J., Cabral, J., Tagliazucchi, E., Laufs, H., Logothetis, N.K., Kringelbach, M.L., 2019. Awakening: predicting external stimulation to force transitions between different brain states. Proc. Natl. Acad. Sci. U. S. A. 116, 18088–18097. doi:10.1073/pnas.1905534116.

Deco, G., Jirsa, V.K., 2012. Ongoing cortical activity at rest: criticality, multistability, and ghost attractors. J. Neurosci. 32, 3366–3375. doi:10.1523/JNEUROSCI.2523-11.2012.

Deco, G., Jirsa, V.K., McIntosh, A.R., 2011. Emerging concepts for the dynamical organization of resting-state activity in the brain. Nat. Rev. Neurosci. 12, 43–56. doi:10.1038/nrn2961.

Deco, G., Kringelbach, M.L., Jirsa, V.K., Ritter, P., 2017. The dynamics of resting fluctuations in the brain: metastability and its dynamical cortical core. Sci. Rep. 7, 3095. doi:10.1038/s41598-017-03073-5.

Desikan, R.S., Segonne, F., Fischl, B., Quinn, B.T., Dickerson, B.C., Blacker, D., Buckner, R.L., Dale, A.M., Maguire, R.P., Hyman, B.T., Albert, M.S., Killiany, R.J., 2006. An automated labeling system for subdividing the human cerebral cortex on MRI scans into gyral based regions of interest. Neuroimage 31, 968–980. doi:10.1016/j.neuroimage.2006.01.021.

Eickhoff, S.B., Constable, R.T., Yeo, B.T.T., 2018. Topographic organization of the cerebral cortex and brain cartography. Neuroimage 170, 332–347. doi:10.1016/j.neuroimage.2017.02.018.

Eickhoff, S.B., Yeo, B.T.T., Genon, S., 2018. Imaging-based parcellations of the human brain. Nat. Rev. Neurosci. 19, 672–686. doi:10.1038/s41583-018-0071-7.

Fischl, B., Liu, A., Dale, A.M., 2001. Automated manifold surgery: constructing geometrically accurate and topologically correct models of the human cerebral cortex. IEEE T. Med. Imaging. 20, 70–80. doi:10.1109/42.906426.

Fukushima, M., Sporns, O., 2018. Comparison of fluctuations in global network topology of modeled and empirical brain functional connectivity. PLoS Comput. Biol. 14, e1006497. doi:10.1371/journal.pcbi.1006497.

Ghosh, A., Rho, Y., McIntosh, A.R., Kotter, R., Jirsa, V.K., 2008. Noise during rest enables the exploration of the brain's dynamic repertoire. PLoS Comput. Biol. 4, e1000196. doi:10.1371/journal.pcbi.1000196.

Glasser, M.F., Sotiropoulos, S.N., Wilson, J.A., Coalson, T.S., Fischl, B., Andersson, J.L., Xu, J.Q., Jbabdi, S., Webster, M., Polimeni, J.R., Van Essen, D.C., Jenkinson, M., 2013. The minimal preprocessing pipelines for the human connectome project. Neuroimage 80, 105–124. doi:10.1016/j.neuroimage.2013.04.127.

Griffanti, L., Salimi-Khorshidi, G., Beckmann, C.F., Auerbach, E.J., Douaud, G., Sexton, C.E., Zsoldos, E., Ebmeier, K.P., Filippini, N., Mackay, C.E., Moeller, S., Xu, J.Q., Yacoub, E., Baselli, G., Ugurbil, K., Miller, K.L., Smith, S.M., 2014. ICA-based artefact removal and accelerated fMRI acquisition for improved resting state network imaging. Neuroimage 95, 232–247. doi:10.1016/j.neuroimage.2014.03.034.

Hagmann, P., Cammoun, L., Gigandet, X., Gerhard, S., Grant, P.E., Wedeen, V., Meuli, R., Thiran, J.P., Honey, C.J., Sporns, O., 2010. MR connectomics: principles and challenges. J. Neurosci. Methods 194, 34–45. doi:10.1016/j.jneumeth.2010.01.014.

Honey, C.J., Sporns, O., Cammoun, L., Gigandet, X., Thiran, J.P., Meuli, R., Hagmann, P., 2009. Predicting human resting-state functional connectivity from structural connectivity. Proc. Natl. Acad. Sci. U. S. A. 106, 2035–2040. doi:10.1073/pnas.0811168106.

Jenkinson, M., Beckmann, C.F., Behrens, T.E., Woolrich, M.W., Smith, S.M., 2012. FSL. Neuroimage 62, 782–790. doi:10.1016/j.neuroimage.2011.09.015.

Jeurissen, B., Tournier, J.D., Dhollander, T., Connelly, A., Sijbers, J., 2014. Multi-tissue constrained spherical deconvolution for improved analysis of multi-shell diffusion MRI data. Neuroimage 103, 411–426. doi:10.1016/j.neuroimage.2014.07.061.

Jülich Supercomputing Centre, 2018. JURECA: modular supercomputer at Jülich supercomputing centre. J. Large-Scale Res. Facil. 4, A132. doi:10.17815/jlsrf-4-121-1.

Kong, R., Li, J., Orban, C., Sabuncu, M.R., Liu, H., Schaefer, A., Sun, N., Zuo, X.N., Holmes, A.J., Eickhoff, S.B., Yeo, B.T.T., 2018. Spatial topography of individual-specific cortical networks predicts human cognition, personality, and emotion. Cereb. Cortex 29, 2533–2551. doi:10.1093/cercor/bhy123.

Kuramoto, Y., 1984. Chemical Oscillations, Waves, and Turbulence. Springer, Berlin.

Kuznetsov, Y.A., 1998. Elements of Applied Bifurcation Theory. Springer, New York.

Manos, T., Diaz-Pier, S., Hoffstaedter, F., J., S., Peyser, A., Eickhoff, S.B., Popovych, O.V., 2019. Impact of brain parcellation on parameter optimization of the whole-brain Dynamical Models. In: Poster at OHBM 2019 Conference, June 9–13, Rome, Italy.

Messe, A., 2019. Parcellation influence on the connectivity-based structure-function relationship in the human brain. Hum. Brain Mapp. 1–14. doi:10.1002/hbm.24866.

Messe, A., Rudrauf, D., Benali, H., Marrelec, G., 2014. Relating structure and function in the human brain: relative contributions of anatomy, stationary dynamics, and non-stationarities. PLoS Comput. Biol. 10, e1003530. doi:10.1371/journal.pcbi.1003530.

Park, H.J., Friston, K.J., 2013. Structural and functional brain networks: from connections to cognition. Science 342, 1238411. doi:10.1126/science.1238411.

Pervaiz, U., Vidaurre, D., Woolrich, M.W., Smith, S.M., 2020. Optimising network modelling methods for fMRI. Neuroimage 211, 116604. doi:10.1016/j.neuroimage.2020.116604.

Ponce-Alvarez, A., Deco, G., Hagmann, P., Romani, G.L., Mantini, D., Corbetta, M., 2015. Resting-state temporal synchronization networks emerge from connectivity topology and heterogeneity. PLoS Comput. Biol. 11. doi:10.1371/journal.pcbi.1004100. UNSP e1004100.

Popovych, O.V., Manos, T., Hoffstaedter, F., Eickhoff, S.B., 2019. What can computational models contribute to neuroimaging data analytics? Front. Syst. Neurosci. 12, 68. doi:10.3389/fnsys.2018.00068.

Proix, T., Spiegler, A., Schirner, M., Rothmeier, S., Ritter, P., Jirsa, V.K., 2016. How do parcellation size and short-range connectivity affect dynamics in large-scale brain network models? Neuroimage 142, 135–149. doi:10.1016/j.neuroimage.2016.06.016.

Rubinov, M., Sporns, O., 2010. Complex network measures of brain connectivity: uses and interpretations. Neuroimage 52, 1059–1069. doi:10.1016/j.neuroimage.2009.10.003.

Salimi-Khorshidi, G., Douaud, G., Beckmann, C.F., Glasser, M.F., Griffanti, L., Smith, S.M., 2014. Automatic denoising of functional MRI data: combining independent component analysis and hierarchical fusion of classifiers. Neuroimage 90, 449–468. doi:10.1016/j.neuroimage.2013.11.046.

Schaefer, A., Kong, R., Gordon, E.M., Laumann, T.O., Zuo, X.N., Holmes, A.J., Eickhoff, S.B., Thomas, B.T., 2018. Local-global parcellation of the human cerebral cortex from intrinsic functional connectivity MRI. Cereb. Cortex 28, 3095–3114. doi:10.1093/cercor/bhx179.

Shen, X., Tokoglu, F., Papademetris, X., Constable, R.T., 2013. Groupwise whole-brain parcellation from resting-state fMRI data for network node identification. Neuroimage 82, 403–415. doi:10.1016/j.neuroimage.2013.05.081.

Stanley, M.L., Moussa, M.N., Paolini, B.M., Lyday, R.G., Burdette, J.H., Laurienti, P.J., 2013. Defining nodes in complex brain networks. Front. Comput. Neurosci. 7, UNSP169. doi:10.3389/fncom.2013.00169.

Thirion, B., Pedregosa, F., Eickenberg, M., Varoquaux, G., 2015. Correlations of correlations are not reliable statistics: implications for multivariate pattern analysis. ICML Workshop on Statistics, Machine Learning and Neuroscience (Stamlins 2015), Bertrand Thirion, Lars Kai Hansen, Sanmi Koyejo, Lille, France.

Thirion, B., Varoquaux, G., Dohmatob, E., Poline, J.B., 2014. Which fMRI clustering gives good brain parcellations? Front. Neurosci. 8, 167. doi:10.3389/fnins.2014.00167.

Tournier, J.D., Smith, R., Raffelt, D., Tabbara, R., Dhollander, T., Pietsch, M., Christiaens, D., Jeurissen, B., Yeh, C.H., Connelly, A., 2019. Mrtrix3: a fast, flexible and open software framework for medical image processing and visualisation. Neuroimage 202, UNSP116137. doi:10.1016/j.neuroimage.2019.116137.

Tustison, N.J., Cook, P.A., Klein, A., Song, G., Das, S.R., Duda, J.T., Kandel, B.M., van Strien, N., Stone, J.R., Gee, J.C., Avants, B.B., 2014. Large-scale evaluation of ANTs and FreeSurfer cortical thickness measurements. Neuroimage 99, 166–179. doi:10.1016/j.neuroimage.2014.05.044.

Van Essen, D.C., Smith, S.M., Barch, D.M., Behrens, T.E.J., Yacoub, E., Ugurbil, K., 2013. The WU-minn human connectome project: an overview. Neuroimage 80, 62–79. doi:10.1016/j.neuroimage.2013.05.041.

Wilcox, R.R., Rousselet, G.A., 2018. A guide to robust statistical methods in neuroscience. Curr. Protocols Neurosci. 82, 8.42.1–8.42.30. doi:10.1002/cpns.41.

Zimmermann, J., Griffiths, J., Schirner, M., Ritter, P., McIntosh, A.R., 2019. Subject specificity of the correlation between large-scale structural and functional connectivity. Netw. Neurosci. 3, 90–106. doi:10.1162/netn_a_00055.

Appendix A. Supplementary Figures

Parcellation	Phase oscillators **Fit(sFC, eFC)**	Phase oscillators **Fit(sFC, eSC)**	LC oscillators **Fit(sFC, eFC)**	LC oscillators **Fit(sFC, eSC)**
S100	0.25 ± 0.07	0.52 ± 0.05	0.28 ± 0.08	0.56 ± 0.04
S200	17 ± 24 %	-14 ± 8 %	7 ± 17 %	-20 ± 5 %
S400	10± 23 %	-27 ± 7 %	-4 ± 17 %	-30 ± 5 %
S600	14± 26 %	-33 ± 6 %	-4 ± 17 %	-37 ± 5 %
HO96 0%	76 ± 47 %	3 ± 10 %	75 ± 44 %	-6 ± 11 %
HO96 25%	72 ± 49 %	5 ± 10 %	73 ± 43 %	-3 ± 11 %
HO96 35%	69 ± 46 %	5 ± 11 %	68 ± 42 %	-1 ± 12 %
HO96 45%	61 ± 42 %	3 ± 12 %	59 ± 39 %	1 ± 12 %
Shen79	80 ± 56 %	8 ± 11 %	80 ± 48 %	6 ± 9 %
Shen156	61 ± 46 %	-7 ± 9 %	52 ± 36 %	-11 ± 7 %
Shen232	43 ± 37 %	-15 ± 8 %	24 ± 29 %	-13 ± 8 %

Table A.1: Relative change of the best model fit (mean ± standard deviation, in %) with respect to the case S100 (the corresponding fitting values for S100 are included in the top row) for the two model fitting modalities Fit(sFC,eFC) [Fig. 3] and Fit(sFC, eSC) [Fig. 4], and the two considered models of coupled phase and limit-cycle (LC) oscillators as indicated in the first row.

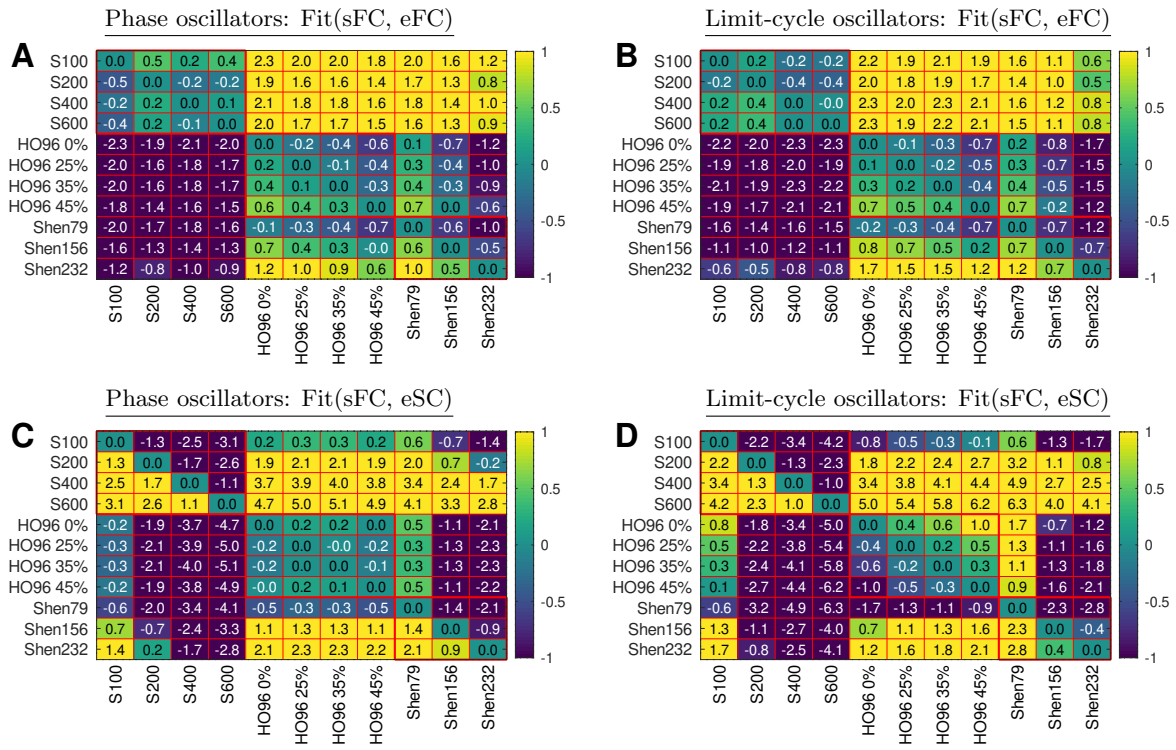

Figure A.1: Effect size as given by Cohen's d values of the paired comparison across subjects of the fitting values (**A, B**) Fit(sFC, eFC) and (**C, D**) Fit(sFC, eSC) between different parcellations and for (**A, C**) phase model and (**B, D**) limit-cycle model. The differences $\mathrm{Fit}^{(\mathrm{column})} - \mathrm{Fit}^{(\mathrm{row})}$ were examined for the Fit-values calculated for the parcellations indicated on the horizontal axes (columns) and vertical axes (rows), respectively. The corresponding cells of the table contain the calculated Cohen's d values explicitly indicated and depicted by color. The corresponding p-values of the paired Wilcoxon signed-rank test are illustrated in Figs. 3 and 4.

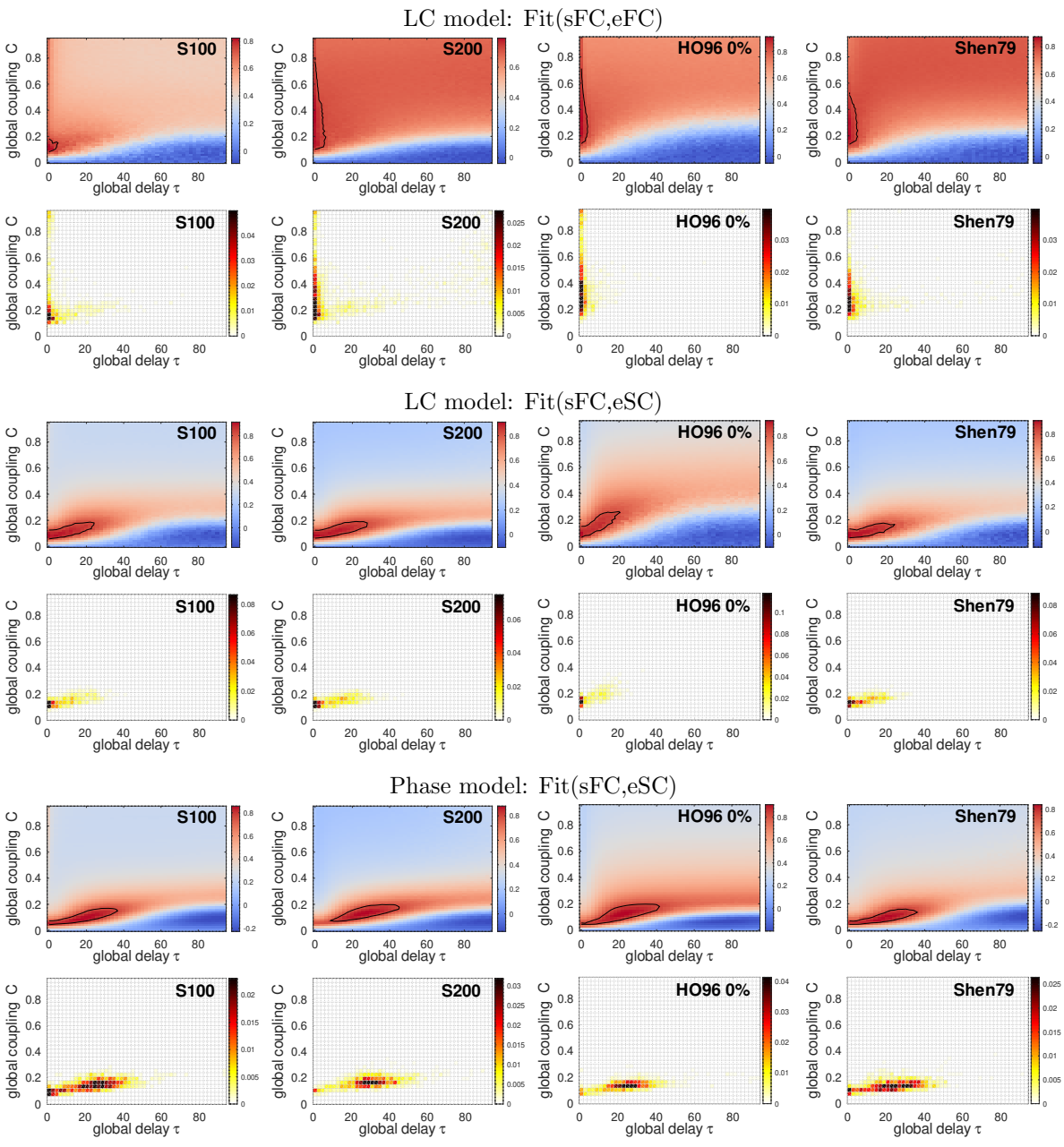

Figure A.2: Examples of parameter planes and distributions of the optimal parameters of similarity $corr(\mathrm{sFC}, \mathrm{eFC})$ (two upper rows) and $corr(\mathrm{sFC}, \mathrm{eSC})$ (four lower rows) for limit-cycle model (2) and phase model (1) as indicated on top of the plots and for parcellations indicated in the plots. The colored panels (uneven rows) are parameter planes of the model-data similarity averaged over all subjects/fMRI scans, where individual planes were first normalized by their maximal values. The black curses delineate the contour lines of 90% of maximum. The distribution of the optimal parameters (2Dim histograms in even rows) were calculated from all 5 values of the largest similarity values detected for every individual parameter plane, see Fig. 2A and D (white circles and blue diamonds).

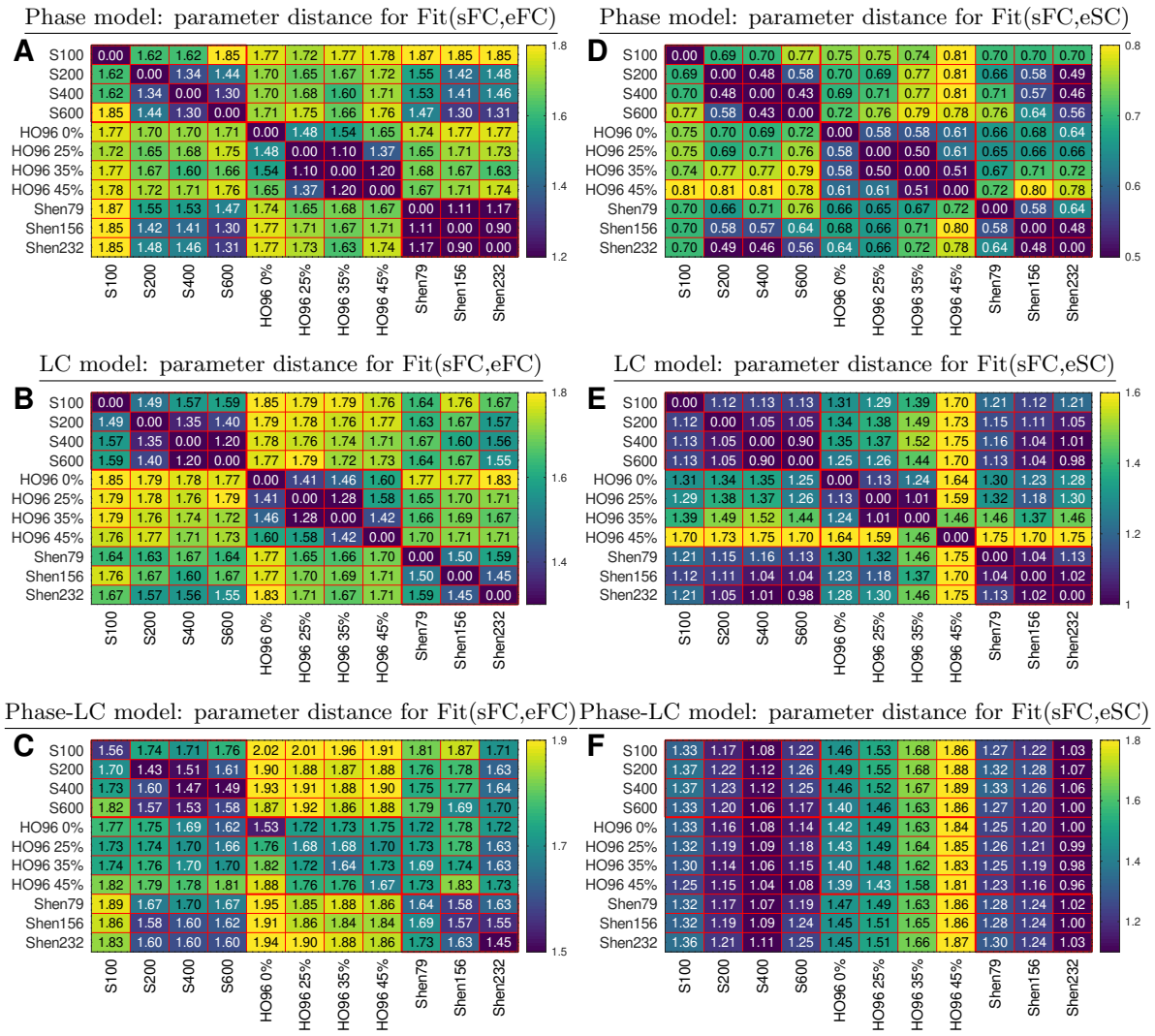

Figure A.3: Correspondence between the inter-individual variation of the optimal model parameters where the best correspondence between simulated and empirical data is achieved for the considered parcellations and models. Relative differences between the optimal parameters $P_1 = (\tau_1, C_1)$ and $P_2 = (\tau_2, C_2)$ for a given subject/fMRI session and for two different parcellations were calculated as $\left\langle \|(P_1 - P_2)\,/\,[(P_1 + P_2)\,/2]\| \right\rangle$ with element-wise division and averaging $\langle\cdot\rangle$ over all subjects/fMRI sessions. The calculation results performed for any two parcellations (indicated on the axes) are illustrated for (**A - C**) Fit(sFC, eFC) and (**D - F**) Fit(sFC, eSC), and for (**A, D**) phase model and (**B, E**) LC model. In plots (**C** and **F**) the correspondence between the phase model (parcellations on the vertical axes) and LC model (parcellations on the horizontal axes) is illustrated. The results are depicted by color, and their magnitudes are indicated in the plots. The heavy red lines delineate the parcellations from the same atlas (parcellation family).

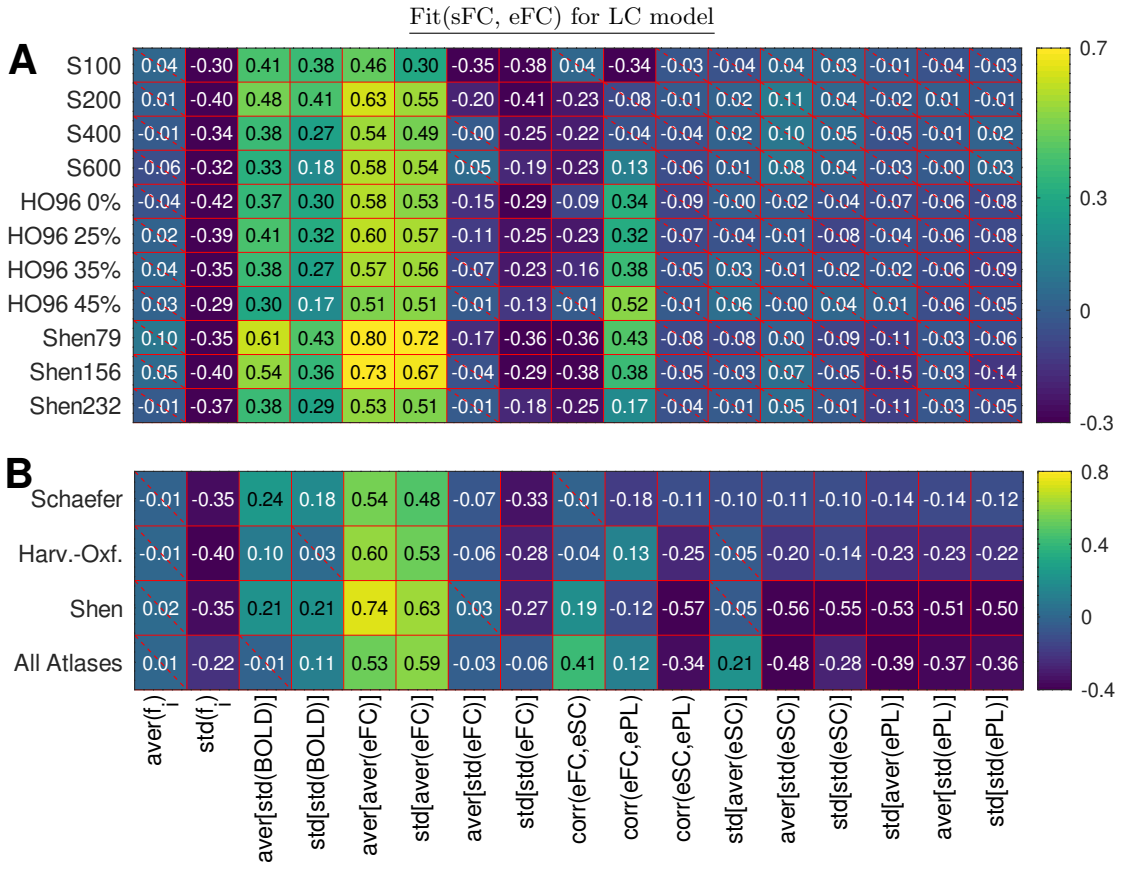

Figure A.4: Relationship between the fitting results (3) of LC model (2) and empirical data. (**A, B**) Pearson correlation across individual subjects between the maximal similarity Fit(sFC, eFC) and several data variables indicated on the horizontal axis. The correlation was calculated for (**A**) different individual parcellations indicated on the vertical axis and (**B**) joint data merged over a few combinations of the considered parcellations as indicated on the vertical axis: all parcellations of the Schaefer atlas, Harvard-Oxford atlas, Shen atlas and all 11 considered parcellations (last row). The correlation is depicted by color, and its magnitude is indicated in the plot. The crossed out cells indicate that the corresponding correlation does not reach the statistical significance with $p < 0.05$.

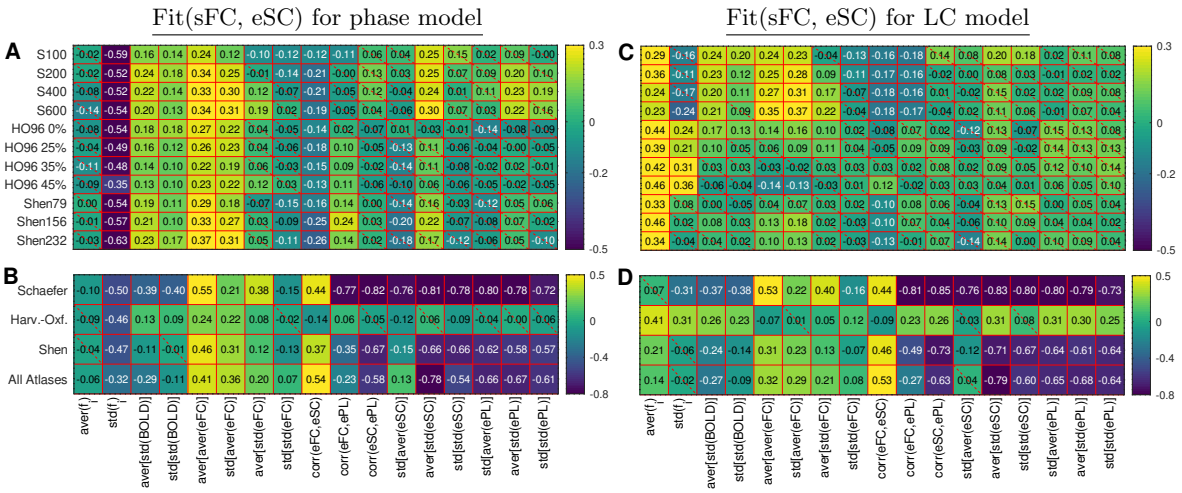

Figure A.5: Relationships between the results of the structure-functional model fitting and empirical data. Pearson correlation between the maximal similarity Fit(sFC, eSC) and several statistical properties (data variables) extracted from the empirical data (see text for details) indicated on the horizontal axes for different parcellations and their combinations (vertical axes). The correlation was calculated for (**A, B**) phase model (1) and (**C, D**) LC model (2), and for (**A, C**) different individual parcellations and (**B, D**) joint data merged over a few combinations of the considered parcellations (vertical axes): all parcellations of the Schaefer atlas, Harvard-Oxford atlas, Shen atlas and all 11 considered parcellations (last row). The correlation is depicted by color, and its magnitude is indicated in the plot. The crossed cells indicate that the corresponding correlation does not reach the statistical significance with $p < 0.05$.

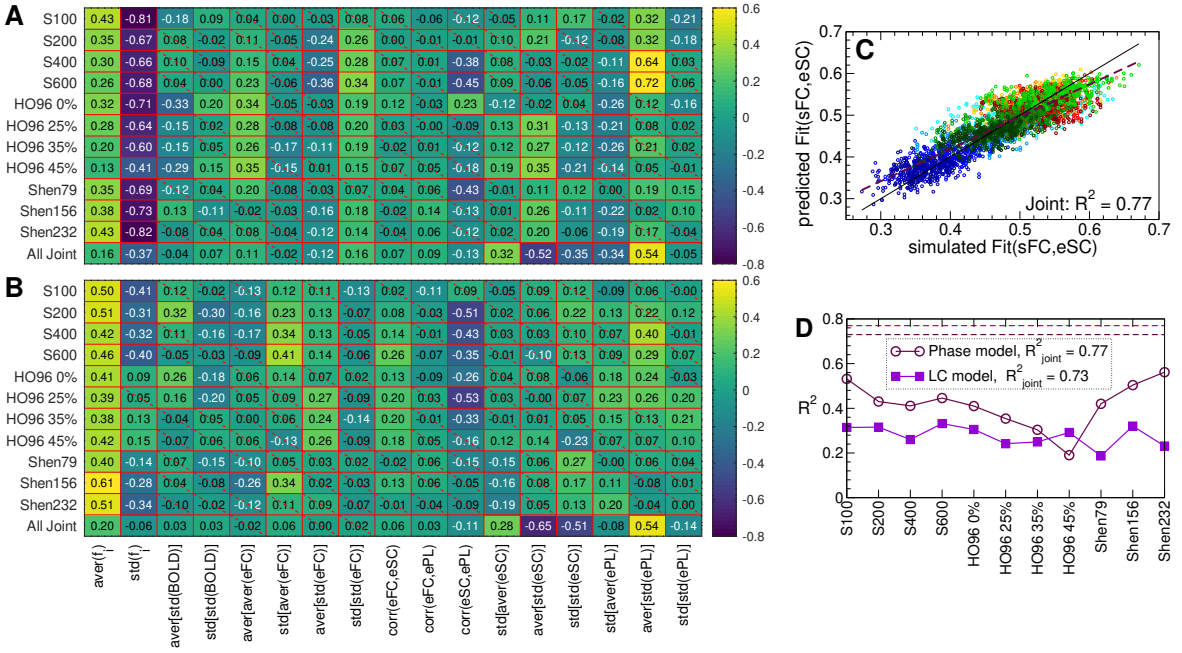

Figure A.6: Modeling the maximal structure-functional similarity Fit(sFC, eSC) by the multiple linear regression (MLR) model with data variables from Fig. 7 as independent variables. (**A, B**) Regression coefficients of the MLR model of Fit(sFC, eSC) for all considered parcellations including the joint data as indicated on the vertical axes for (**A**) phase model (1) and (**B**) LC model (2). The values are depicted by color, and they magnitudes are shown in the plots. The crossed out cells indicate that the corresponding coefficient does not reach the statistical significance with $p < 0.05$. (**C**) Scatter plot for joint data merged over all considered parcellations with the regression line of the Fit-values predicted by MLR versus Fit(sFC, eFC) obtained by simulations of the phase model (1). The diagonal is depicted by thin black line for comparison. The fractions of the explained variance R^2 is also shown in the scatter plot and in plot (**E**) for all individual parcellations for both phase and LC models as indicated in the legend. The dashed lines depict R^2 for the joint data also indicated in the legend.

4 Study 3: Whole-brain dynamical modeling for classification of Parkinson's disease, Jung, K., Florin, E., Patil, K. R., Caspers, J., Rubbert, C., Eickhoff, S. B., Popovych, O. V., Brain Communications, 5(1): fcac331 (2022)

DOI: https://doi.org/10.1093/braincomms/fcac331

Authorship contribution statement

Kyesam Jung (Doctoral researcher, first author): Conceptualization, Data curation, Formal analysis, Investigation, Methodology, Software, Validation, Visualization, Writing – original draft, Writing – review & editing. **Esther Florin:** Conceptualization, Supervision, Validation, Writing – review & editing. **Kaustubh R. Patil:** Methodology, Validation, Writing – review & editing. **Julian Capers:** Data curation. **Christian Rubbert:** Data curation. **Simon B. Eickhoff:** Conceptualization, Funding acquisition, Project administration, Resources, Writing – review & editing. **Oleksandr V. Popovych (Corresponding author):** Conceptualization, Funding acquisition, Methodology, Project administration, Resources, Software, Supervision, Validation, Writing – original draft, Writing – review & editing.

BRAIN COMMUNICATIONS

Whole-brain dynamical modelling for classification of Parkinson's disease

Kyesam Jung,[1,2] Esther Florin,[3] Kaustubh R. Patil,[1,2] Julian Caspers,[4] Christian Rubbert,[4] Simon B. Eickhoff[1,2] and Oleksandr V. Popovych[1,2]

Simulated whole-brain connectomes demonstrate enhanced inter-individual variability depending on the data processing and modelling approach. By considering the human brain connectome as an individualized attribute, we investigate how empirical and simulated whole-brain connectome-derived features can be utilized to classify patients with Parkinson's disease against healthy controls in light of varying data processing and model validation. To this end, we applied simulated blood oxygenation level-dependent signals derived by a whole-brain dynamical model simulating electrical signals of neuronal populations to reveal differences between patients and controls. In addition to the widely used model validation via fitting the dynamical model to empirical neuroimaging data, we invented a model validation against behavioural data, such as subject classes, which we refer to as behavioural model fitting and show that it can be beneficial for Parkinsonian patient classification. Furthermore, the results of machine learning reported in this study also demonstrated that the performance of the patient classification can be improved when the empirical data are complemented by the simulation results. We also showed that the temporal filtering of blood oxygenation level-dependent signals influences the prediction results, where filtering in the low-frequency band is advisable for Parkinsonian patient classification. In addition, composing the feature space of empirical and simulated data from multiple brain parcellation schemes provided complementary features that improved prediction performance. Based on our findings, we suggest that combining the simulation results with empirical data is effective for inter-individual research and its clinical application.

1 Institute of Neuroscience and Medicine, Brain and Behaviour (INM-7), Research Centre Jülich, 52425 Jülich, Germany
2 Institute for Systems Neuroscience, Medical Faculty, Heinrich-Heine University Düsseldorf, 40225 Düsseldorf, Germany
3 Institute of Clinical Neuroscience and Medical Psychology, Medical Faculty, Heinrich-Heine University Düsseldorf, 40225 Düsseldorf, Germany
4 Department of Diagnostic and Interventional Radiology, Medical Faculty, Heinrich-Heine University Dusseldorf, 40225 Düsseldorf, Germany

Correspondence to: Oleksandr V. Popovych
Institute of Neuroscience and Medicine
Brain and Behaviour (INM-7)
Research Centre Jülich, 52425 Jülich, Germany
E-mail: o.popovych@fz-juelich.de

Keywords: whole-brain simulation; MRI; Parkinson's disease; patient classification; machine learning

Abbreviations: AUC = area under a curve; BF = broad-frequency band; BOLD = blood oxygenation level-dependent; BW = Balloon–Windkessel; CV = cross-validation; DWI = diffusion-weighted image; EPSP = excitatory postsynaptic potential; FC = functional connectivity; FOD = fibre oriented distribution; GoF = goodness-of-fit; HC = healthy control; HF = high-frequency band; IPSP = inhibitory postsynaptic potential; LASSO = least absolute shrinkage and selection operator; LF = low-frequency band; NF = no filtering; PD = Parkinson's disease; PL = path length; PSP = postsynaptic potential; ROC = receiver operating characteristic; SC = streamline count; T_1w = T_1-weighted image; WBT = whole-brain tractography

Received June 29, 2022. Revised August 29, 2022. Accepted December 14, 2022. Advance access publication December 15, 2022

Graphical Abstract

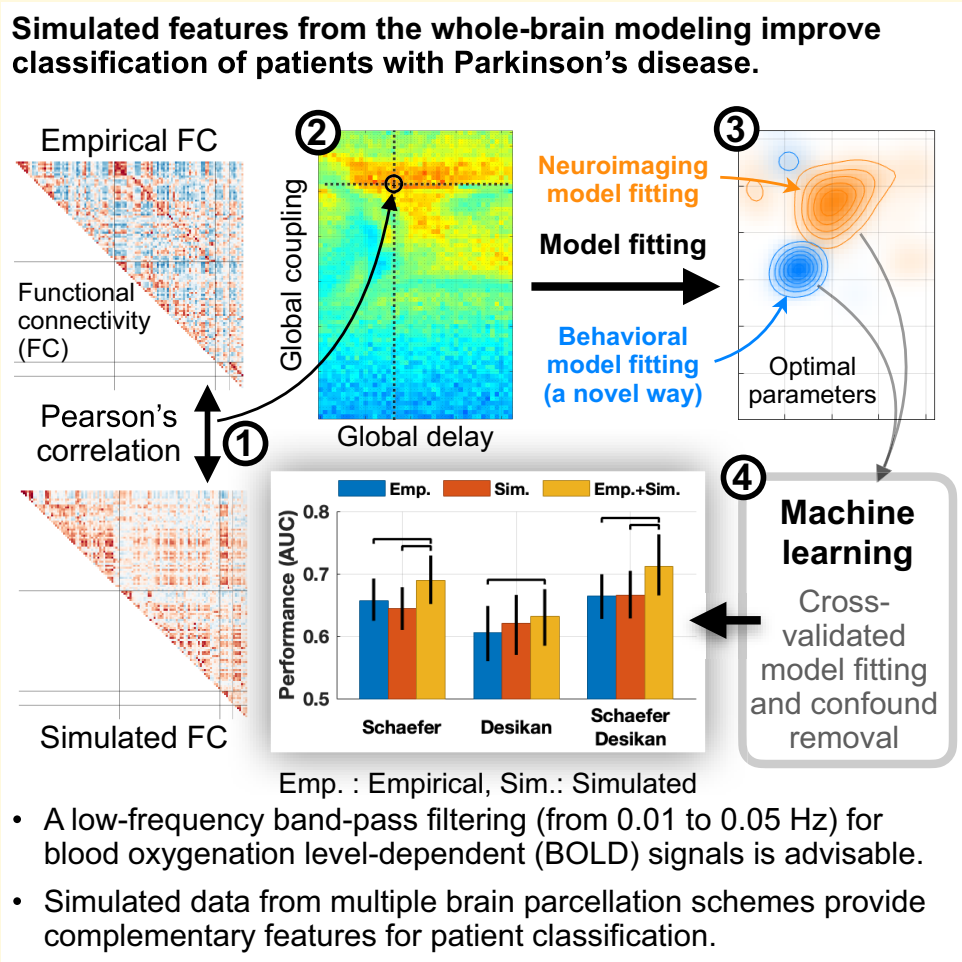

Introduction

For decades, large-scale whole-brain connectivity acquired from non-invasive *in-vivo* MRI has actively been used to study the human brain as an integrative complex system.[1] Accordingly, anatomical (or structural) and functional connectivities between brain regions have been used. Previous studies have shown that the structural architecture shapes the temporal synchronization between the blood oxygenation level-dependent (BOLD) signals in selected networks, for instance the default mode network.[2,3] However, the structure-function correspondence is not high for whole-brain connectivity.[4–6] The correspondences between the brain connectomes of the same and different subjects, samples or data modalities[7,8] have been considered to investigate the inter-individual differences[9] or diagnostic classification between healthy controls (HCs) and patients.[4,10–12]

Connectivity relationships are also commonly used when brain dynamics are modelled by mathematical whole-brain dynamical models. In particular, finding the strongest correspondence (the highest similarity) between empirical functional connectivity (eFC) and simulated functional connectivity (sFC) has been used for model validation.[13–15] Such a correspondence of the simulated data to the empirical data may undergo qualitative changes when parameters of a given model vary and the validation procedure consists in finding the most pronounced agreement between the data and the model fitted by searching for optimal parameter points.

Previous studies utilizing the discussed whole-brain modelling showed that the employed modelling approach was applicable to clinical research. The variability of the model parameters between diseased and healthy states has been investigated for brain disorders including schizophrenia,[16–19] Alzheimer's disease,[20] Parkinson's disease[21,22] and stroke patients.[23] For instance, Saenger *et al.*[22] showed that therapeutic deep brain stimulation in Parkinson's disease can be modelled by the normal form of a Hopf bifurcation model.[24] Detailed simulations of neuronal dynamics may also provide a way to test prognostic outcomes *in silico* throughout virtual operations and optimize the setup and parameters of therapeutic interventions.[25–28]

There are, however, no well-established standards for model validation against empirical data. Several fitting modalities have been suggested in the literature, including the fitting of the grand-averaged empirical and simulated FC matrices, fitting the dynamical FCs, maximization of the metastability and structure-functional model fitting.[6,13,24,29,30] On that account, it is necessary to investigate, which parameter points of a given dynamical mode and which model fitting modalities are the most suitable to answer a given research question by the modelling approach. For example, it was observed that the distributions of the optimal model parameters differ when using only functional or structure-functional model fitting and may lead to subject stratifications showing different model fitting values and optimal parameter points.[30] It is also well known that varying parameters of MRI data processing influence the empirical structural and functional connectomes and their analyses.[31–34] This subsequently affects model validation.[6,30,35] Therefore, the impact of data processing on the results of model validation should be carefully considered, especially in clinical applications.

In Parkinson's disease research, the eFC of the resting-state networks was already being used in machine learning approaches to subject classification.[36,37] When sFC is involved, it is essential to extract relevant features for Parkinson's disease classification from simulation results via searching in a given model parameter space for the optimal model. To do this, we considered two aspects of parameters regarding dynamical models and data processing. First, we find the model parameters that reveal the most prominent differences in connectome correspondence between Parkinson's disease and HC. Such an approach can be used for model validation. Here, we aim at a diagnostic classification of patients from healthy subjects, where the model fitting to behavioural (phenotypical) data might be an alternative approach for model validation. We attempt to provide a way to reveal and maximize the group difference in simulated results by varying the parameters of dynamical models. For instance, the disease status of the subjects can be used for behavioural fitting, as we show in this study. Second, we consider different temporal filters of BOLD signals, which are known to influence FC properties.[38,39] In particular, the altered frequency bands were found to retain Parkinson's disease-related neural changes.[40] The frequencies of empirical BOLD signals, when included in the whole-brain mathematical models, may influence the optimal model parameters and the quality of the model fitting.[6,30] In this context, investigation of the impact of temporal filtering conditions on the model validation in Parkinson's disease data is important.

In the current study, we advance the classification of clinical data by application of machine learning to empirical and simulated connectomes. The functional connectomes were calculated from empirical and simulated BOLD signals, respectively, filtered in broad-, low- and high-frequency bands for two different brain parcellations as given by the Schaefer[41] and Desikan–Killiany[42] brain atlases. As compared with purely empirical studies, we take the next step based on the two aspects of parameters for model fitting modality and data processing and employ the simulated data to improve the prediction results in a machine learning setting.

The current study employs whole-brain dynamical modelling of the resting-state functional MRI data based on the Jansen–Rit model type of interacting excitatory and inhibitory neuronal populations.[43,44] The simulated FCs generated for the optimal model parameters based on model fitting modalities were used to calculate the connectome relationships (Pearson's correlation) with empirical structural and functional connectivities. We also introduced a simple but effective method for model validation against behavioural data more suitable for differentiation between patients with Parkinson's disease and HCs than the conventionally used model fit to neuroimaging data. Consequently, the personalized features derived from the connectome relationships were used in this study for classification of Parkinson's disease and HC using machine learning. We in particular show that complementing empirical data with simulated FC can improve the prediction performance for unseen subjects. Our results suggest that the personalized whole-brain models can serve as an additional source of information relevant for disease diagnosis and possibly for their treatment as well.

Materials and methods

We performed three main steps to obtain the whole-brain connectivities eFC, eSC (empirical streamline counts), ePL (empirical average path length) and sFC. Figure 1 schematically illustrates the data processing and simulation workflow. We applied four temporal filtering conditions to empirical and simulated resting-state BOLD signals. Subsequently, we considered three types of connectivity relationship corresponding to the correlation between eFC and eSC, the correlation between eSC and sFC and the correlation between eFC and sFC. Since sFC was calculated by varying the two free model parameters of global coupling and global delay, the correlations involving sFC change, as illustrated by the eFC-sFC correlation landscape in the parameter space in Fig. 1 (the rightmost colour plot). We used these three connectivity relationships as features for the Parkinson's disease classification via a machine learning approach. To this end, we trained Parkinson's disease classifiers and evaluated their performance based on prediction probabilities obtained on unseen subjects.

Subjects and demography

The three considered whole-brain connectivities (eFC, eSC and sFC) were calculated for 51 (30 males) HC and 65 (45 males) patients with Parkinson's disease, see Table 1 for the demography. Patients and controls were included in an MRI data pool acquired at the University Hospital Düsseldorf, Germany, which was also used in several recent studies,[36,37,45,46] where additional details about the data

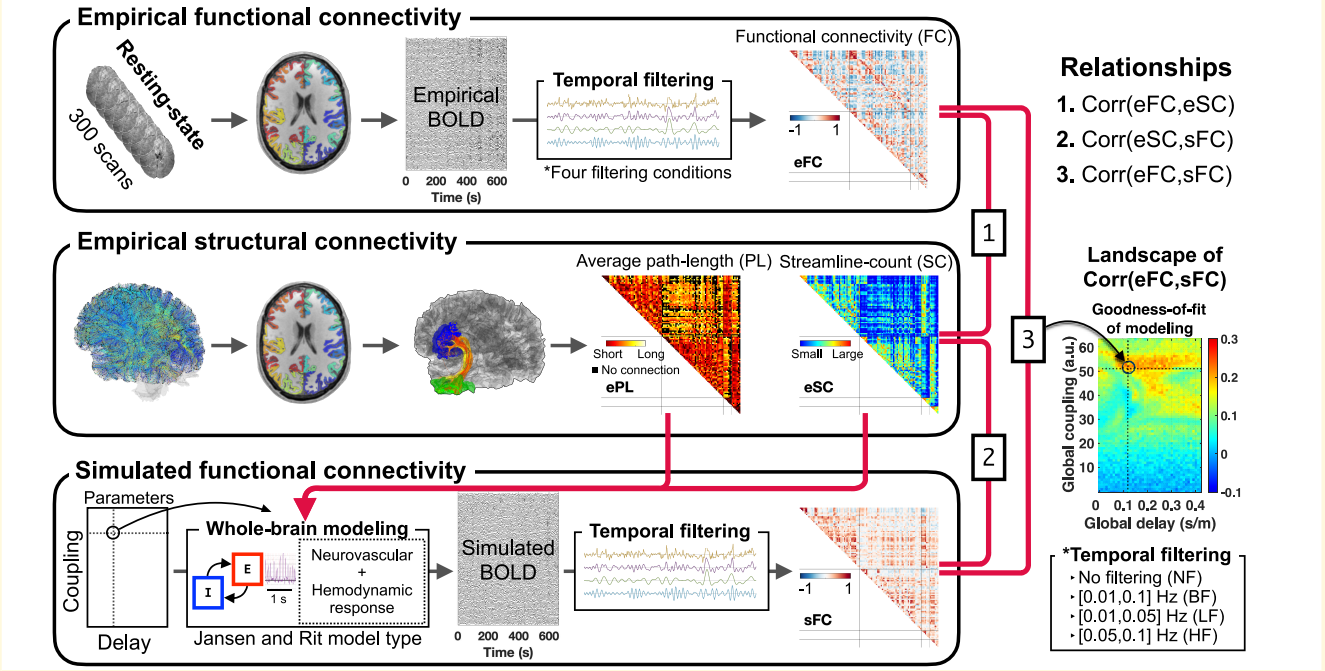

Figure 1 Data processing and simulation overview. First (upper box), brain parcellations in the native space of T_1w were prepared and applied to the processed functional MRI data, BOLD signals were extracted from the corresponding brain regions and filtered according to four temporal filtering conditions (right *bottom* box) and four respective eFCs were calculated. Second (*middle* box), the parcellations were also used for the calculation of the structural connectivity by extracting streamlines from the WBT reconstructed using DWIs, where the number and length of streamlines connecting any two brain regions were collected into matrices of eSC and ePL. Third (lower box), the structural connectome (eSC and ePL) was used to build a brain network for the whole-brain modelling that simulates BOLD signals, which were filtered according to the considered filtering conditions (right *bottom* box) and used to calculate sFC. Subsequently, we calculated connectivity relationships (Pearson's correlation) using these three connectivity matrices: (i) corr (eFC, eSC); (ii) corr (sFC, eSC); and (ii) corr (eFC, sFC). Model parameters for global coupling and global delay were varied to validate the model against empirical data. In particular, the correspondence (correlation) between eSC and eFC and sFC was calculated for each parameter point, resulting in similarity landscapes in the model parameter space, see the example of the relationship between eFC and sFC in the rightmost colour plot. The most pronounced correspondence (correlation) between the empirical and simulated connectomes was selected, together with the respective optimal model parameters, as a result of the neuroimaging model fitting for further analysis.

Table 1 Demography of subjects included in the study

Groups	Mean (standard deviation) years		Statistical tests	*P*-values
	All subjects		**χ^2 goodness-of-fit test**	
All	58.93 (10.25)		116 subjects	0.149
	HC	**Patients**	**Wilcoxon rank-sum two-tail test**	
All	55.02 (9.69)	62.00 (9.62)	51 HC versus 65 patients	0.000
Female	56.52 (9.40)	60.80 (8.96)	21 HC versus 20 patients	0.201
Male	53.97 (9.74)	62.53 (9.85)	30 HC versus 45 patients	0.001
	Females	**Males**	**Wilcoxon rank-sum two-tail test**	
All	58.61 (9.43)	59.11 (10.67)	41 females versus 75 males	0.751

can be found. All patients were diagnosed with Parkinson's disease by an experienced movement disorder specialist. All HC subjects had no history of any neurological or psychiatric disease and no abnormalities were detected in cranial MRI. The ages of 116 subjects (mean: 58.9 years and standard deviation: 10.3 years) are in a normal distribution (the null hypothesis was not rejected by a χ^2 goodness-of-fit test with $P = 0.15$). The age of patients was significantly higher than that of controls (Wilcoxon rank-sum two-tail test). The age of male patients was significantly higher than that of male controls, but the age of females was not from distributions with different medians. There was no age difference between females and males (Table 1). The study was approved by the local ethics committee and performed in accordance with the Declaration of Helsinki. All subjects provided written informed consent prior to study inclusion.

MRI acquisition

Structural and functional MRI data were acquired using a 3 T scanner (Siemens Trio). A structural brain image was acquired using a 3D T_1-weighted image (T_1w) sequence (TR = 2.3 s, TE = 2.96 ms, TI = 900 ms, flip-angle = 9°, field-of-view = 240 × 256 mm^2 in sagittal, the number of slices = 160, voxel dimension = 240 × 256 × 160, voxel size = 1.0 × 1.0 × 1.1 mm^3). Diffusion-weighted images (DWI) comprised a single non-weighted (B_0) image and weighted (B = 1000 s/mm^2) images with 64 directions (TR = 6.7 s, TE = 81 ms, phase encoding: anterior to posterior, field-of-view = 216 × 216 mm^2 in axial, the number of slices = 55, voxel dimension = 90 × 90 × 55, voxel size = 2.4 × 2.4 × 2.4 mm^3). Resting-state functional MRI was obtained using an echo-planar imaging sequence during 663 s (TR = 2.21 s, TE = 30 ms, field-of-view = 200 × 200 mm^2 in axial, the number of slices = 36, voxel dimension = 64 × 64 × 36, voxel size = 3.125 × 3.125 × 3.565 mm^3). To prevent the distraction of streamline tracking, artefact volumes of DWI were removed from the data based on evaluation by two raters.

Preprocessing of MRI

For the personalized data processing, we developed a containerized in-house pipeline to process structural and functional MRI in the native spaces. The pipeline consists of five modules: preprocessing of structural MRI (T_1w and DWI), whole-brain tractography (WBT) calculation, atlas transformation, reconstruction of structural connectivity (eSC and ePL) and preprocessing of functional MRI. The pipeline comprises Freesurfer,[47] FSL,[48] ANTs,[49] MRtrix3[50] and AFNI.[51] It is publicly available (https://jugit.fz-juelich.de/inm7/public/vbc-mri-pipeline).

The preprocessing module of structural MRI performed the following steps: bias-field correction for T_1w, alignment of anterior-posterior commissures of T_1w, *recon-all* by Freesurfer, removing the Gibbs ringing artefacts of DWIs, bias-field correction for DWIs, corrections of head motion, b-vector rotations and eddy distortion of DWIs and co-registration between averaged DWI and T_1w. This module segmented subcortical areas based on voxel intensities of the T_1w. It also prepared labelling annotations using a brain atlas, for which a classifier was available from the literature. The annotation can also be created based on a subject cohort by capturing region data either drawn by neuroanatomists or according to dedicated algorithms.[52]

The WBT calculation module included only MRtrix3 functions. They estimated response functions for spherical deconvolution using the constrained deconvolution algorithm.[53] Fibre oriented distributions (FODs) were estimated from the DWIs using spherical deconvolution, and the WBT was created through the fibre tracking by the second-order integration over the FOD by a probabilistic algorithm.[54] In the latter step, we used 10 million total streamlines for the WBT density. The tracking parameters of the *tckgen* function were set as in the previous study:[30] step size = 0.625 mm, angle = 45°, minimal length = 2.5 mm, maximal length = 250 mm, FOD amplitude for terminating tract = 0.06, maximum attempts per seed = 50, the maximum number of sampling trials = 1000 and downsampling = 3 (FOD samples per steps−1).

The atlas transformation module annotated labels using a classifier to parcel cortical regions in the native T_1w space using Freesurfer. In the present study, we applied two atlas classifiers for brain parcellations, the Schaefer atlas with 100 parcels[41] and the Desikan–Killiany atlas with 68 parcels.[42] Both atlases provide cortical parcellations, where the former is based on functional MRI data, while the latter is labelled by gyral-based anatomical parcellation. After this, the subcortical areas segmented by the preprocessing module were included and combined with the labelled cortical parcels. Finally, the pipeline transformed the labelled image (cortical parcels and subcortical regions) from the T_1w to DWI native spaces.

The reconstruction module calculated the matrices of the streamline counts (SCs) and the matrices of the average path lengths (PLs) of the streamlines extracted between any two parcellated brain regions from the calculated WBT with the transformed, labelled image in the DWI space.

The preprocessing module of functional MRI performed slice time correction, head motion correction, re-slicing in a 2 mm iso-cubic voxel space, intensity normalization, detrending with filtering of very slow fluctuations out (high pass), co-registration to the T_1w and calculation of regressors for the white matter, cerebrospinal fluid (CSF) and brain global signals as well as for the head motion. The pipeline also transformed the labelled image of the brain parcellation generated in the native T_1w space to the functional MRI native space. Finally, we performed a nuisance regression with the prepared regressors (white matter, CSF and the brain global signals, as well as head motions).

Post-processing of functional MRI

After preprocessing of MRI, we extracted mean BOLD signals based on the annotated atlas labels and applied three temporal band-pass filtering conditions in the frequency ranges of (0.01,0.1) Hz (broad-frequency band; BF), (0.01,0.05) Hz (low-frequency band; LF) and (0.05,0.1) Hz (high-frequency band; HF). Therefore, four filtering conditions were considered: no filtering (NF), BF, LF and HF. The filtering was done using a script in the Python programming language (version 3.8, Python Software Foundation, https://www.python.org/) using the SciPy (version 1.5) signal processing module[55] and NumPy[56] (version 1.19) for the temporal band-pass filtering. We used the Butterworth digital filter of order 6, *scipy.signal.butter*.

Whole-brain model

Convolution-based two-population model for electrical signals

The whole-brain resting-state dynamics considered in this study was simulated by a system of N coupled neuronal

models representing the mean brain regional activity. Each region contains two populations for each neuronal type (excitatory and inhibitory) that interact with each other via postsynaptic potentials (PSPs).[43] The considered convolution-based model is of the Jansen–Rit type[44,57] and simulates the PSP signals involving other brain regions that interact with time delay in coupling according to the calculated structural connectivity, i.e. SC and PL matrices. The following set of differential equations describes the mean dynamics of the excitatory and inhibitory PSPs of region $n = 1, 2, \ldots, N$,

$$\dot{y}_{n,e}(t) = z_{n,e}(t), \tag{1}$$

$$\dot{y}_{n,i}(t) = z_{n,i}(t), \tag{2}$$

$$\dot{z}_{n,e}(t) = P_{n,e}(t) - 2aR_n z_{n,e}(t) - a^2 R_n^2 y_{n,e}(t) + \eta_{n,e}, \tag{3}$$

$$\dot{z}_{n,i}(t) = P_{n,i}(t) - 2bR_n z_{n,i}(t) - b^2 R_n^2 y_{n,i}(t) + \eta_{n,i}, \quad n = 1, 2, \ldots, N. \tag{4}$$

Here, $z_{n,e}$, $z_{n,i}$, $y_{n,e}$ and $y_{n,i}$ are the excitatory postsynaptic current, the inhibitory postsynaptic current, the excitatory PSP (EPSP) and the inhibitory PSP (IPSP) of the brain region n, respectively, where the subscripts e and i stand for *excitatory* and *inhibitory*, accordingly. The model (1)–(4) is a system of driven harmonic oscillators in a critical damping regime, where the system quickly returns to its steady state after perturbation without undershooting. Parameters a and b represent the reciprocal of the time constants of the PSP kernel for the two populations for EPSP and IPSP, respectively. $\eta_{n,e}$ and $\eta_{n,i}$ are independent noise sampled from a random uniform distribution between -1.5 and $1.5\ V/s^2$. For frequency of oscillations, we also introduced a scaling factor R. By increasing R, the spectral power of the PSP signals shifts to higher frequencies. Perturbation $P_{n,e}$ drives EPSP oscillations regarding input signals from other regions, i.e. it models the coupling between the network nodes/brain regions and $P_{n,i}$ perturbs IPSP oscillations by the input from the excitatory population in the same region n,

$$P_{n,e}(t) = AaR_n^2 \sigma_e\left(\frac{C}{N}\sum_{m\neq n}^{N} C_{nm} y_{m,e}(t - \tau_{nm}) - C_{ei} y_{n,i}(t)\right), \tag{5}$$

$$P_{n,i}(t) = BbR_n^2 \sigma_i(C_{ie} y_{n,e}(t)), \quad n = 1, 2, \cdots, N. \tag{6}$$

A and B are the maximum amplitudes of the PSP kernels for EPSP and IPSP, respectively. N is the total number of brain regions/network nodes for the whole-brain model. In Equation (5), C is a global coupling parameter, which scales the couplings throughout the whole-brain network. C_{nm} is the strength of the individual coupling from region m to region n, which is realized via weighting the EPSP signal of the m-*th* network node $y_{m,e}$ considered with time delay τ_{nm}. Parameter C_{ei} weights an input coming from the inhibitory population of the same brain region, i.e. IPSP $y_{n,i}$. The individual time delays and coupling strengths between regions m and n can be estimated from the empirical data as

$$\tau_{nm} = \tau_{global} L_{nm}, \ C_{nm} = \frac{w_{nm}}{W}, \tag{7}$$

where the averaged path length L_{nm} (from the matrix PL) of the reconstructed streamlines between regions n and m is scaled by a global delay parameter τ_{global}. C_{nm} in Equation (7) calculates an individual coupling strength by taking into account the SC matrix, where the number of streamlines w_{nm} between the two regions was normalized by an averaged number of streamlines W calculated over all connections except for the self-connections. As follows from Equation (5), the coupling between brain regions is realized between the excitatory populations, where the delayed EPSP signals from the other brain regions composed the coupling term. Together with the intra-regional coupling by the IPSP signal from the inhibitory population, the total PSP input to the excitatory population is converted by a nonlinear sigmoid function $\sigma_e(v)$ given in Equation (8) below to an averaged firing density. The inhibitory population in region n received an input EPSP signal weighted by parameter C_{ie} from the excitatory population of the same region only, which was again converted to an averaged firing density by the following sigmoid function $\sigma_i(v)$:

$$\sigma_e(v) = \frac{F_e}{1 + e^{r(v_0 - v)}}, \ \sigma_i(v) = \frac{F_i}{1 + e^{r(v_0 - v)}}. \tag{8}$$

In Equation (8) of the mentioned sigmoid functions, the parameter r is a slope, v_0 is a half of the maximal neural activity and parameters F_e and F_i are the maximal firing densities of the excitatory and inhibitory populations, respectively. Parameter values of the considered two-population model Equations (1)–(8) are given in Table 2.

Simulated BOLD signals

We calculated the regional BOLD signals using the corresponding EPSP signals simulated by the electrical model Equations (1)–(8) introduced in the previous section. Several examples of the time courses of the EPSP signals generated by the considered model and their power spectra are illustrated in Supplementary Fig. 1. Neurovascular coupling and hemodynamic responses constitute the process reflected in the Balloon–Windkessel (BW) model that was utilized to convert the simulated neural activity to BOLD signals,[58–60] see details in the Supplementary material.

Model validation: neuroimaging and behavioural model fitting

In this study, we considered two model fitting approaches: neuroimaging model fitting and behavioural model fitting. The former is well known in the literature and consists of validation of the model via comparing simulated data against neuroimaging empirical data. In this study, the Pearson's

Table 2 Parameter values of the electrical model and the BW model

Electrical model	Variables	Values	BW model	Variables	Values
Max. sigmoid (excitatory)	F_e	100 s^{-1}	Echo time	TE	30 ms
Reciprocal of the time constant of the EPSP kernel	a	100[a] s^{-1}	Mean-transit-time	t_{MTT}	2[b] s
Max. EPSP	A	3.25[a] mV	Net oxygen extraction fraction at rest	E_0	0.4[b]
Max. sigmoid (inhibitory)	F_i	50 s^{-1}	Venous blood volume fraction	V_0	4[b] %
Reciprocal of the time constant of the IPSP kernel	b	50[a] s^{-1}	Frequency offset for 3 T	ϑ_0	80.6[b] s^{-1}
Max. IPSP	B	22[a] mV	Ratio of intra/extra-vascular signal	ε	0.3[b]
Slope of sigmoid	r	0.56[a] mV^{-1}	Sensitivity (regression slope)	r_0	25[b] s^{-1}
50% neural activity	v_0	6[a] mV	Steady state flow-volume relationship	α	0.38[b]
Intra-regional coupling (from excitatory to inhibitory)	C_{ie}	6	Rate constant for damped oscillations	κ	0.64[b] Hz
Intra-regional coupling (from inhibitory to excitatory)	C_{ei}	6	Rate constant for damped oscillations	γ	0.32[b] Hz
Scaling factor	R	2.2	Values of initial conditions	$[s, f, v, q]$	[0,1,1,1][c]
Amplitude of noise		1.5 V/s^2			

aValues from Jansen and Rit study.[44]
bValues from Havlicek *et al.*[58]
cValues empirically determined based on the trajectories generated by the BW model.
EPSP, excitatory postsynaptic potential; IPSP, inhibitory postsynaptic potential.

correlation coefficient between eFC and sFC (comparing the upper triangle without self-connections of the connectivity matrices) was calculated and denoted as goodness-of-fit (GoF) values. Searching for the maximal GoF in a given parameter space is a well-established approach for model validation in whole-brain modelling studies.[13–15] In this study, we optimized the coupling and delay model parameters to maximize the GoF value on a parameter grid of 64 × 43 points (64 global couplings and 43 global delays) densely covering the parameter plane, respectively. In addition, we also considered the connectivity relationship between eSC and sFC as for separate neuroimaging model fitting. In consequence, two types of neuroimaging model fitting (eFC versus sFC and eSC versus sFC) were used in this study. As this procedure fits the model to the connectivity derived from the empirical neuroimaging data, we term it *neuroimaging model fitting*.

We also introduce *behavioural model fitting* as a procedure to validate a model against behavioural data, for example, optimizing the model to reflect some behavioural (phenotypical) properties to the best possible extent. In this study, we optimized the parameters of the model to maximally differentiate between Parkinson's disease patients and HC subjects. For this, we calculated the effect size based on the z-statistics of the Wilcoxon rank-sum two-tail test as given by the Rosenthal formula, i.e. the normal z-statistics divided by the square root of the number of observations[61] of the difference between the (neuroimaging) GoF values of the HC and Parkinson's disease subject groups. The effect size was calculated for every parameter point in the considered parameter space of 64 × 43 grid and represented as a parameter map. In this way we obtained a parameter landscape of the group differences and were able to investigate the differentiation of GoF values of Parkinson's disease patients from those of HC subjects. This parameter landscape reflects the relation of the model GoF to the behavioural data (in this study, to the differentiation based on clinical measures), and we thus used this approach as behavioural model fitting. To evaluate the parameter areas of significant group difference, we performed the Wilcoxon rank-sum two-tail test and obtained a corresponding P-value parameter map. Due to the multiple comparisons over the parameter points, we applied the random-field thresholding scheme[62,63] using a 2D Gaussian kernel smoothing. Subsequently, we obtained a Z-score map and thresholded it to retain statistically significant parameter areas (alpha = 0.05). Finally, we searched for the optimal model parameters within the significant parameter areas corresponding to the maximal effect size. We considered two connectivity relationships (eFC versus sFC and eSC versus sFC) for the behavioural model fitting.

Random sampling for optimal parameters

We performed a random sampling to test the stability of the optimal parameter points for the behavioural model fitting. To do this, the stability of the results was assessed by sex-balanced stratified subsampling. After a random sampling of 72 subjects (36 HC subjects and 36 Parkinson's disease patients) out of 116 subjects, we applied the behavioural model fitting to the sampled subjects and found optimal parameters corresponding to the largest effect size. The subsampling and the corresponding calculations were repeated 1000 times.

Regularized (least absolute shrinkage and selection operator) logistic regression

The current task is to train a binary classifier (Parkinson's disease versus HC) using 10 features (five connectivity

relationships from two parcellation schemes), which are of lower dimension than observations (116 subjects). We considered a simple regularized logistic regression that is a sparse method possessing good interpretability and is known to work well in many applications.[64–66] There might be other methods that could give better accuracy.[67] The main goal of the current study was however to compare the prediction results between several computational conditions including data processing and model validation. This could be demonstrated using such a linear (interpretable) machine learning method without an exhaustive search for the methods and conditions for the best performance. Thus, logistic regression is applicable to the current study. To this end, we used a regularized logistic regression with the least absolute shrinkage and selection operator (LASSO) for training and classification of HC versus Parkinson's disease subjects.[68] To avoid an overfit, the training error included the deviance and an L_1-penalty.[69] We used the *lassoglm* function for the logistic LASSO regression and the *glmval* function for predicted probability calculation in the Statistics and Machine Learning Toolbox of MATLAB R2020b.

Confound regression for age-controlled features

We used a cross-validation (CV) scheme to train the logistic LASSO regression for Parkinson's disease classification. As for a degenerative disease,[70,71] features for Parkinson's disease classification should be controlled by an age effect via a confound regression. Due to a random sampling from the same cohort and the usage of the same data for model validation and model training, it is important to prevent possible data leakage during the CV procedure, especially for behavioural model fitting as it uses data across subjects. Otherwise, the trained models might be biassed due to the usage of the results of the behavioural model fitting derived from Parkinson's disease classification against HC. In this respect, we followed the ideas of the cross-validated confound regression[72] as illustrated in Fig. 2. Specifically, we applied the CV-consistent approach to features derived from the empirical result, neuroimaging and behavioural model fitting. Accordingly, the subjects were split into training and test sets (Fig. 2, green and orange blocks in the outer loop) and the optimal parameter point of the behavioural model fitting was calculated on the training set at every iteration of the outer CV loop (Fig. 2, the green box with the Circle 1). Then the respective connectome relationships were calculated for every subject. Next, the age was regressed out for these subjects (cross-validated confound regressions in Fig. 2, Circles 1 and 2) from the obtained features of connectivity relationships used for subject classification. The optimal model parameters and the regression coefficients obtained for the training set were then used for the connectome calculation and the age regression for the test subjects.

Nested cross-validation

In order to avoid over-optimistic results of CV,[73] we used nested CV to train the logistic LASSO regression for Parkinson's disease classification (Fig. 2). In the outer loop, we randomly split the subjects into five subsets. One subset of 20% of subjects was considered as a test set (unseen subjects, the orange box in the outer loop in Fig. 2) and the other four subsets were pulled together and composed a training set (the green boxes in the outer loop in Fig. 2). As explained above, we first applied the cross-validated model fitting and confound regression to the features in the training set (Fig. 2, the green box with the Circle 1). Subsequently, the training set (age-controlled) was split into ten subsets for the nested CV in the inner loop. A logistic LASSO regression model was trained with the hyperparameters minimizing the 10-fold CV error. This model was then applied to predict the test set. As follows from the aforementioned, the age-controlled training and test sets were used for model training and prediction, respectively. The training and testing procedure we performed can be summarized as follows:

(i) Randomly split the entire subject cohort into five subgroups.
(ii) Select one group as a test set and compound the others into a training set.
(iii) Perform the cross-validated (behavioural) model fitting using the training set and extract respective connectome relationships corresponding to the optimal model parameters.
(iv) Perform the cross-validated confound (age) regression for the training set from the features based on the connectome relationships used for classification.
(v) Train the logistic LASSO regression model in the inner loop with a 10-fold CV that minimizes errors in the prediction model.
(vi) Apply the trained best model to predict the test set with age regression, where the optimal model parameters of the model fitting and age regression coefficients obtained for the training set were used (Fig. 2, the dashed arrow in the outer loop).
(vii) Calculate the model performance using a confusion matrix and an receiver operating characteristic (ROC) curve.
(viii) Perform Steps (ii)–(vii) for the other four subsets split in Step (i) as test sets in the outer CV loop (five prediction results).
(ix) Repeat Steps (i)–(viii), 50 times (250 prediction results in total).

Evaluation of prediction performance

For Parkinson's disease classification based on the discussed machine learning approach, we considered five features for each of the two parcellation schemes (Schaefer and Desikan–Killiany atlases), i.e. 10 features in total: corr (eFC, eSC) as an empirical feature, corr (eFC, sFC) and corr (eSC, sFC) as simulated features for each model fitting,

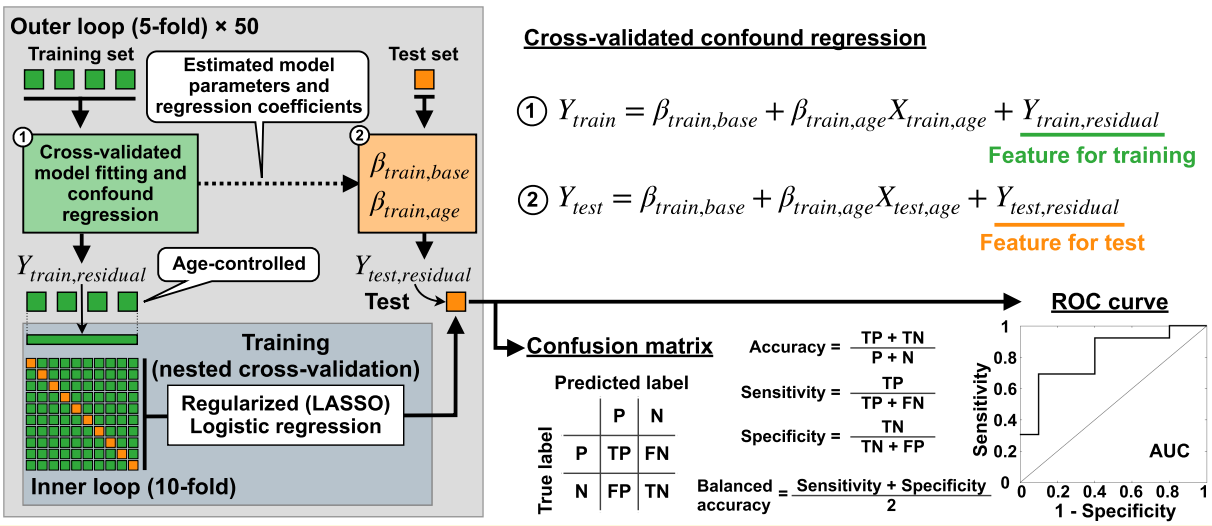

Figure 2 Schematic illustration of cross-validated model fitting, cross-validated confound regression and nested CV. The boxes under the 'Training set' in the leftmost plot illustrate randomly split subject subgroups used for training the model in the 5-fold outer loop and in the 10-fold inner loop. The box under the 'Test set' in the outer loop depicts the testing subject subgroup used for evaluation of the prediction performance of the trained model as given by accuracy, sensitivity, specificity, balanced accuracy and area under the ROC curve. *P*, positive as patients; N, negative as controls; TP, true positive; FP, false positive; TN, true negative; FN, false negative.

i.e. the neuroimaging model fitting and the behavioural model fitting. To investigate the impact of simulated results on the Parkinson's disease prediction, we composed the considered features into three conditions: (i) empirical features only (shuffle simulated features); (ii) simulated features only (shuffle empirical features); and (iii) all features (no shuffling). The shuffling was performed by a random redistribution of the values of a given feature among subjects such that the correspondence of the feature to individual subjects was destroyed. By focusing on some features (connectome relationships and parcellations), the other features were shuffled. For example, to focus on the empirical features of the Schaefer atlas, four simulated features (eFC versus sFC and eSC versus sFC for two model fitting modalities) of the Schaefer atlas and all five features (one empirical and four simulated features) of the Desikan–Killiany atlas were shuffled. The shuffling was performed for every feature separately, randomizing feature values across subjects while retaining distributional properties (Supplementary Fig. 2). After feature selection, model training and application of the trained model to the unseen test subject set, we calculated a confusion matrix from the prediction results and plotted a ROC curve.[74] The latter was calculated from the prediction results obtained by varying the subject classification threshold of a predicted probability from 0 to 1. Then, we calculated the prediction performance (accuracy, sensitivity, specificity and balanced accuracy) and the area under a curve (AUC) of the ROC curve.

In addition to the prediction considering the cross-validated confound regression with subjects' ages using the entire cohort, we also applied the same approach to a balanced subject configuration by excluding the 17 oldest Parkinson's disease patients from 116 subjects. Thus, the balanced cohort has no significant age difference between Parkinson's disease and HC groups with balanced group sizes (see Supplementary Table 1). Subsequently, we analysed the prediction performances of the balanced subject cohort (99 subjects).

Statistical analysis

Statistical analysis was performed using functions in the Statistics and Machine Learning Toolbox of MATLAB R2020b. We set significance level at $P < 0.05$. We applied the Bonferroni correction to prevent multiple comparison issues when the test was used multiple times. Statistical tests used in the results were mentioned in each legend of figures and tables. We also scrutinized the prediction probabilities for individual subjects to evaluate the model's performance. Here, the trained model estimated the predicted probabilities for each subject in the test set. Subsequently, we calculated a fraction of actual positives and showed relationships using probability calibration. The ideal case is to have the same values for the fraction of positives and the predicted probability, i.e. the graph should align to the diagonal. In clinical applications, the tight correspondence between predicted probabilities and the fraction of actual positives provides high trustworthiness for diagnosis.[75] To this end, we used the Brier score[76] to calculate the mean-squared error of each predicted probability against an ideal case. We also used the Wasserstein distance to show how much cost is required to turn a given distribution of the predicted probabilities into a uniform one.[77] In other words, this metric was used to evaluate how well predicted probabilities were

uniformly distributed. Thus, a lower Wasserstein distance means that the predicted probabilities are relatively better calibrated than those of a higher one. Accordingly, we further evaluated the model's performance regarding individual predicted probabilities in addition to the integrative performance from the confusion matrix.

Results

In this study, we investigated the application of simulation results from whole-brain dynamical models to Parkinson's disease classification using relationships between empirical and simulated connectomes as features. The whole-brain dynamical model of the Jansen–Rit type was used to simulate the electrical neuronal activity and was validated against empirical data by means of neuroimaging or behavioural model fitting. Accordingly, we calculated the connectome relationships involving the simulated connectomes corresponding to the optimal model parameters of the two fitting modalities and used them as features for Parkinson's disease classification. We show that complementing the empirical data by simulated data improves the prediction performance as compared with the case where only empirical data were used.

Neuroimaging model fitting

We calculated sFC using simulated BOLD signals for each parameter point and obtained the similarity (Pearson's correlation) values between eFC and sFC. Figure 3 shows the corresponding landscapes of the GoF values in the delay-coupling (τ_{global}, C) parameter space averaged over all subjects, the distributions of the maximal GoF values and corresponding optimal model parameters for individual subjects for the Schaefer atlas (Fig. 3A-D) and the Desikan–Killiany atlas (Fig. 3E-H). We calculated eFC and sFC for the different frequency ranges of the corresponding filtered BOLD signals, i.e. NF, BF, LF and HF conditions (see Materials and methods for details). The profiles of the parameter landscapes were different between the considered brain atlases. The Schaefer atlas showed a unimodal distribution containing maximal GoF values (the dashed circle in Fig. 3A) for the optimal global delays in the biologically feasible range[78] from 0.06 to 0.25 s/m (Fig. 3D). On the other hand, the maximal GoF for the Desikan–Killiany atlas posited a bi-modal distribution (the dashed circles in Fig. 3E) with well-separated peaks along the global coupling parameter (Fig. 3G, compare with Fig. 3C). Moreover, stronger global coupling of the maximal GoF values was accompanied by a widespread global delay (the upper dashed circle in Fig. 3E) that may get out of the biologically feasible range as compared with the weaker global couplings (the lower dashed circle in Fig. 3E).

Furthermore, we observed that applying temporal filtering to BOLD signals diminished GoF values over the entire parameter landscape (Fig. 3B and F). In particular, the narrow frequency bands (LF and HF) resulted in significantly lower maximal GoF values than in the cases of the broader (BF) or entire frequency (NF) range; see Table 3 for statistical results.

Effect size of group comparisons for behavioural model fitting

The behavioural model fitting resulted in effect sizes of group difference between HC and Parkinson's disease (Fig. 4A–B for eFC-sFC correlation, see Supplementary Fig. 3 for eSC-sFC correlation). Furthermore, we also observed that the distributions of the optimal parameter points corresponding to the maximal effect sizes are densely concentrated in the parameter space across repeated subsampling (1000 times) and filtering conditions (Fig. 4C–D, distributions in blue). Interestingly, the distributions of the optimal parameters derived from the behavioural model fitting were strikingly different from those determined by the neuroimaging model fitting (Fig. 4C–D, distributions in orange for the neuroimaging and in blue for the behavioural fitting). Both sets of optimal parameters are located in the biologically plausible range of time delay.[78]

Group difference between healthy controls and patients

The empirical structure-function relationships corr(eFC, eSC) for HC and Parkinson's disease subject groups were found to be from distributions with different medians for the Schaefer atlas and all considered filtering conditions and for the LF condition only for the Desikan–Killiany atlas (Fig. 5, the first row). The group differences obtained by involving the simulated connectomes in the neuroimaging model fitting were small and non-significant for both atlases and all filtering conditions (Fig. 5, the second and third rows). On the other hand, for behavioural model fitting, we observed that Parkinson's disease patients exhibited stronger agreements between empirical and simulated connectomes than HC subjects and can thus be better differentiated from HC (Fig. 5, the fourth and fifth rows).

Temporal filtering may influence the group differences for the empirical and also for the simulated connectomes as illustrated in Fig. 5, see the first row for the Desikan–Killiany atlas, in particular and Supplementary Fig. 4. In addition, we calculated the explained variances of the five connectivity relationships between each other for the same and different filtering conditions, which resulted in relatively low similarities for the simulated results (Supplementary Fig. 5). Accordingly, the temporal filtering can influence the considered connectivity relationships and may lead to dissimilar patterns of connectome relationships across subjects.

Prediction performance

We used the five whole-brain connectivity relationships as features for Parkinson's disease classification using machine learning based on the logistic LASSO regression algorithm.

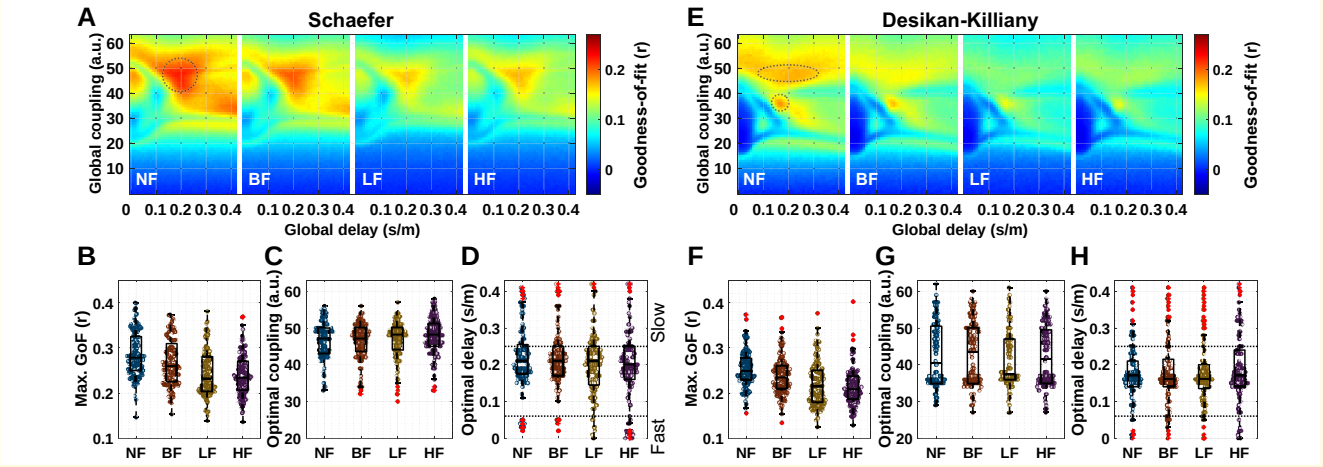

Figure 3 Results of the neuroimaging model fitting. (**A–D**) The Schaefer atlas and (**E–H**) the Desikan–Killiany atlas. (**A, E**) Parameter landscapes of the similarity (Pearson's correlation) between eFC and sFC, i.e. goodness-of-fit (GoF) values averaged over the entire subject cohort. The landscapes are illustrated for each filtering condition (NF, BF, LF and HF, see Materials and methods for details). The dashed circles delineate the hills with large GoF values. Distributions of (**B, F**) the maximal GoF values, (**C, G**) optimal coupling parameters and (**D, H**) the respective optimal delays corresponding to the maximal GoF values for each filtering condition. The distributions of the maximal GoF values are significantly different across filtering conditions ($P = 0.000$ for the Schaefer atlas and $P = 0.000$ for the Desikan–Killiany atlas; Kruskal–Wallis non-parametric one-way analysis of variance test). *Post-hoc*: Significantly different filtering conditions are NF > BF, NF > LF, NF > HF, BF > LF and BF > HF in both atlas conditions (Wilcoxon signed-rank two-tail test, Bonferroni corrected $P < 0.05$, see Table 3 for details). The distributions of the optimal coupling parameters are not significantly different ($P = 0.317$ for the Schaefer atlas and $P = 0.505$ for the Desikan–Killiany atlas; the Kruskal–Wallis test). The distributions of the optimal delays are not significantly different ($P = 0.459$ for the Schaefer atlas and $P = 0.824$ for the Desikan–Killiany atlas; the Kruskal–Wallis test). The dashed horizontal lines in plots (**D, H**) indicate the biologically feasible delay range regarding the electrophysiological conduction speed. The *middle* lines in interquartile box plots indicate the medians of distributions, and the red plus signs are the outliers.

The feature space constituted three feature conditions with ten features (five connectivity relationships for two atlases), see Supplementary Fig. 2. After the nested CV, the trained best models were relatively well balanced, with a slight tendency towards overfitting for some of the used performance measures (13.4% decreased balanced accuracy and 1.1% decreased AUC of test performance from training one, see Supplementary Fig. 6).

Figure 6 shows the prediction performance for each of the investigated conditional cases of brain parcellations, frequency bands and feature conditions. The first important observation is that involvement of the simulated connectomes can improve the classification of Parkinson's disease and HC, see Fig. 6 and compare blue dots (empirical features) to red dots (simulated features) and to yellow dots (all features) (see Supplementary Fig. 7 for the differences). In the latter case, where the empirical features are complemented by the simulated ones, the prediction performance can only be enhanced as compared with purely empirical features, which we observed for most feature conditions and performance measures (Fig. 6A–C). Interestingly, the performance further improved when using features from both atlases (Fig. 6 and Supplementary Fig. 7).

We also investigated how the prediction performance varies depending on the filtering conditions (Fig. 6D). The effect of the temporal filtering was prominent of the empirical features for the Schaefer atlas, where the performance was significantly increased for the LF condition compared with the others (Fig. 6D, the 'Emp.' column for the Schaefer atlas). On the other hand, the HF condition showed low performances on the empirical features, in particular, with very low specificities down to zero (Fig. 6B and D) and very high sensitivities up to 1 (Supplementary Fig. 8), where the LF filtering seems again to be a beneficial condition for Parkinson's disease prediction. Summarizing, the temporal filtering conditions influenced the model performance and the LF band-pass filtering resulted in the most effective prediction relying on the connectome relationships. The other considered narrow-band HF filtering condition is not advisable for Parkinson's disease classification. However, involving the simulated connectomes is still of advantage also under this condition as compared with using only empirical features.

We also compared the prediction performance when the simulated connectomes obtained from the neuroimaging and behavioural model fittings were considered separately. This resulted in two additional feature conditions (see Supplementary Fig. 8). The neuroimaging model fitting in most cases led to a weaker prediction performance compared with the behavioural model fitting or to the composite case when the features of both fittings are merged. This justifies the introduction of the behavioural model fitting for subject classification.

Furthermore, we applied the current approach to the balanced subject configuration (99 subjects, see Supplementary Table 1 for the demography). The prediction performance

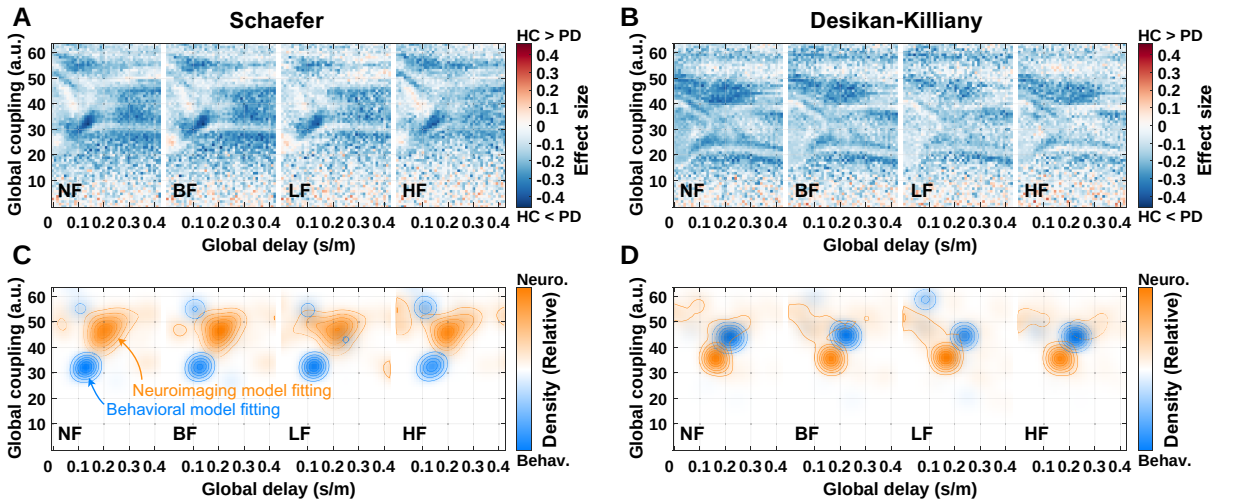

Figure 4 Parameter maps of the effect size of the difference between goodness-of-fit (GoF) values (eFC-sFC correlation) of healthy and Parkinsonian groups used for the behavioural model fitting. The filtering conditions are indicated in the plots for (**A**) the Schaefer atlas and (**B**) the Desikan–Killiany atlas. Effect sizes in the (τ_{global}, C)-parameter plane were calculated by a non-parametric Wilcoxon rank-sum two-tailed test between patients and controls in the GoF values for each parameter point. (**C, D**) Distributions of optimal parameters derived from the neuroimaging model fitting (orange, all subjects, $n = 116$) and the behavioural model fitting (blue, repeated subsampling, $n = 1000$) for **(C)** the Schaefer atlas and (**D**) the Desikan–Killiany atlas.

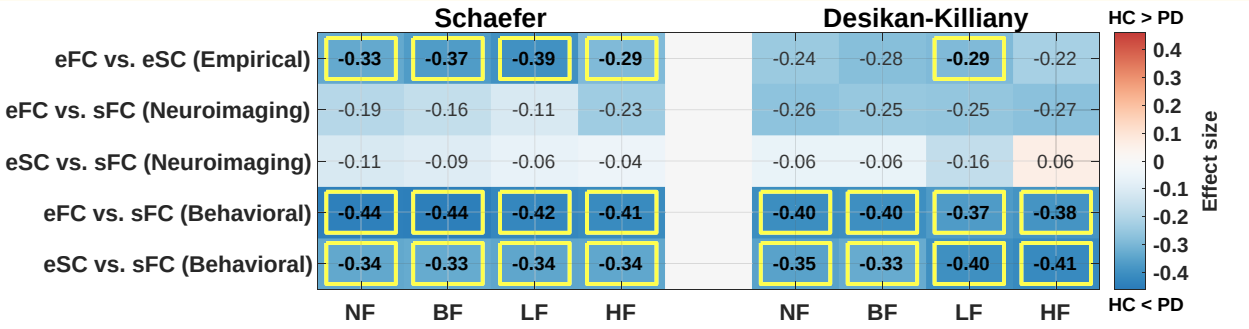

Figure 5 Differentiation between healthy and Parkinsonian subjects as reflected by the relationships between empirical and simulated connectomes. (**Left**) The Schaefer atlas and (**Right**) the Desikan–Killiany atlas. The simulated connectomes are calculated for the optimal model parameters of the neuroimaging and behavioural model fitting as indicated on the vertical axis. Summary tables of the effect sizes (numbers) of the differences between Parkinsonian and healthy subject groups are calculated by the Rosenthal formula and shown in negative for HC < Parkinson's disease and positive for HC > Parkinson's disease. The significant cases are indicated by rectangles as given by the Bonferroni corrected *P*-values of the Wilcoxon rank-sum two-tail test.

was consistent with the main findings of the entire cohort (116 subjects, Fig. 6). In other words, complementing empirical data with simulated results using LF filtering involving multi-parcellation (concatenating both atlases) is advisable for Parkinson's disease classification (Supplementary Fig. 9).

Figure 6 shows the well-known measures characterizing the prediction performance as median values and interquartile ranges of distributions. Although these measures clearly reflect how well the machine learning approach is commonly working, we may also be interested in how every test is performing for the classification of individual unseen subjects. In this respect, Fig. 7 illustrates the results of classification/prediction probabilities of all tests performed on individual subjects from the test sets. The prediction probabilities were collected and related to the probability calibration curves.

We can interpret the probability calibration plots (Fig. 7A–C) according to two aspects. Feature conditions using simulated results (red and yellow curves) resulted in predictions that are more closely aligned with the ideal case (the diagonal black line) than the empirical relationship. Indeed, for the Schaefer atlas and the multi-parcellation case, the distance to the diagonal as given by the mean-squared error of the predicted probabilities against the actual classes calculated according to the Brier score[76] is minimal for the composed features, including the empirical and simulated

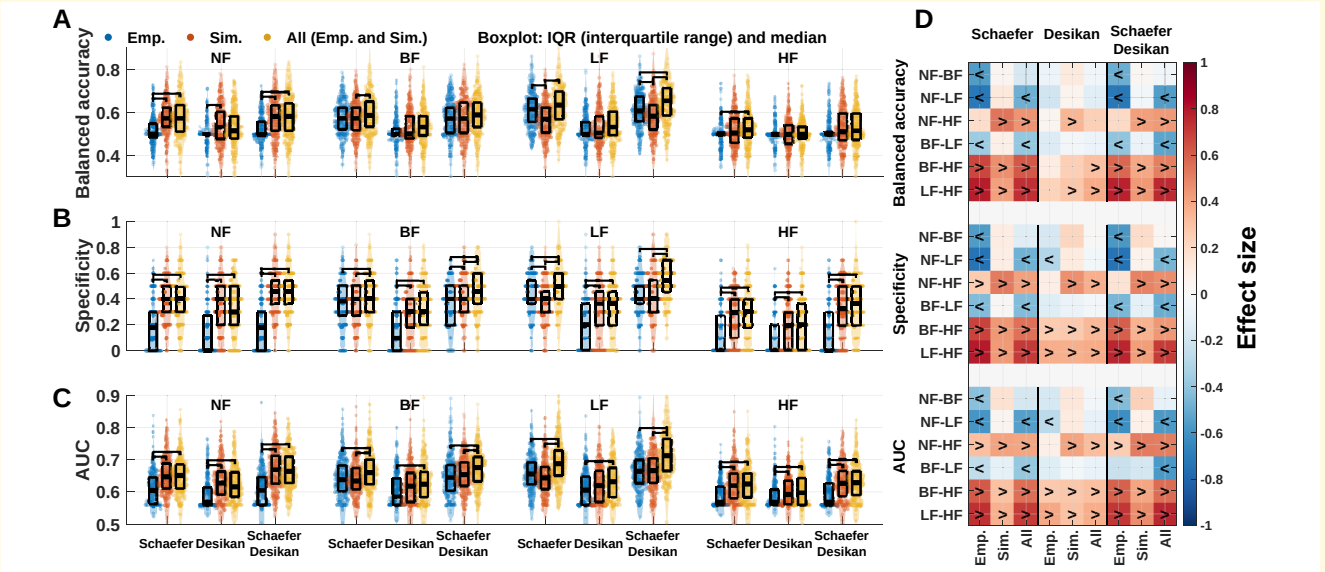

Figure 6 Summary of the performance of Parkinson's disease classification using the three different feature conditions: empirical features (left distribution), simulated features (middle distribution) and all features (right distribution) after incorporating the age controlling and the behavioural model fitting during the nested CV (Fig. 2). The median values of the balanced accuracy, specificity and AUC of the ROC curves for all considered parcellations and filtering conditions are shown in each panel for **(A)** balanced accuracy and (**B**) specificity and **(C)** AUC. The error bars indicate the interquartile range of 250 tests represented as data points in the plots across 50 iterations of the outer loop (5-fold) of the nested CV procedure (Fig. 2). The horizontal brackets connecting two coloured distributions indicate significantly different performance between feature conditions (Bonferroni corrected $P < 0.05$; Wilcoxon signed-rank two-tail test). (**D**) Effect sizes between filtering conditions for each feature condition. The signs '<' and '>' indicate which condition is significantly larger than the other. For example, '<' sign for 'NF-LF' indicated on the vertical axes means NF < LF for a given feature condition indicated on the horizontal axes. The Wilcoxon signed-rank two-tail test was used for comparisons across feature and filtering conditions (Bonferroni corrected statistics). The Desikan–Killiany atlas is shortend as 'Desikan'.

connectomes for the LF filtering condition (Fig. 7E). As a second aspect, the prediction probabilities derived from the empirical features are more narrowly distributed around 0.5 (blue curves in Fig. 7D) compared with the case of all features (yellow curves in Fig. 7D). This can be quantified by the minimum cost of turning the observed distribution into a uniform distribution using the Wasserstein distance[77] (Fig. 7F). In the latter case, the predicted probabilities derived from all features show widely spreading distribution that also reach the low and high probability values, which indicates high confidence.[75] In other words, in our predictive modelling, the prediction results, where the empirical data were complemented by simulated features, were better calibrated in some cases as compared with the case of the empirical data only (Fig. 7C). As mentioned above, the Wasserstein distance in Fig. 7F clearly shows which filtering condition and which feature condition can be the best beneficial configuration for Parkinson's disease classification. In particular, the LF filtering of the BOLD signals and involving of the simulated connectomes together with the empirical ones for the Schaefer atlas and multi-parcellation case can improve the prediction results and the confidence of the prediction model. The same conclusion was drawn above based on the Brier scores, which confirm their robustness and may be relevant for the application of the discussed modelling and prediction approaches to clinical data and disease diagnosis.

Discussion

The main objective of this study is to effectively apply whole-brain dynamical modelling and the derived simulated connectomes to Parkinson's disease classification. Whole-brain simulations allow us to explore various regimes of brain dynamics corresponding to different values of free model parameters. To extract features from the simulated results, it is essential to evaluate which model fitting is appropriate. The detected optimal model parameters can differ when we use different model fitting approaches. In other words, whole-brain dynamics with proper model parameters can disclose group differences between Parkinson's disease and HC subjects and provide a way to extract effective features for Parkinson's disease classification. In this study, we introduced the behavioural model fitting approach and showed that it captured differences between Parkinson's disease and HC better than the conventionally used neuroimaging model fitting approach. Then, we applied it to Parkinson's disease classification. Based on our findings, we can conclude that using proper model validation in whole-brain dynamical modelling may provide effective features to machine learning and provide information complementary to empirical features.

In addition to whole-brain dynamical modelling for classification, data processing is also important because, as we have shown, different data processing influences model

Table 3 Comparisons between goodness-of-fit values of the considered filtering conditions (Bonferroni corrected *P*-values of the Wilcoxon signed-rank two-tail test) and the corresponding effect sizes by Rosenthal formula[61]

P (effect size)	NF versus BF	NF versus LF	NF versus HF	BF versus LF	BF versus HF	LF versus HF
Schaefer	**0.000 (0.70)**	**0.000 (0.84)**	**0.000 (0.86)**	**0.000 (0.81)**	**0.000 (0.70)**	0.998 (0.04)
Desikan–Killiany	**0.000 (0.66)**	**0.000 (0.77)**	**0.000 (0.85)**	**0.000 (0.69)**	**0.000 (0.70)**	0.838 (0.10)

Bold fonts indicate that the goodness-of-fit values are significantly different between filtering conditions.

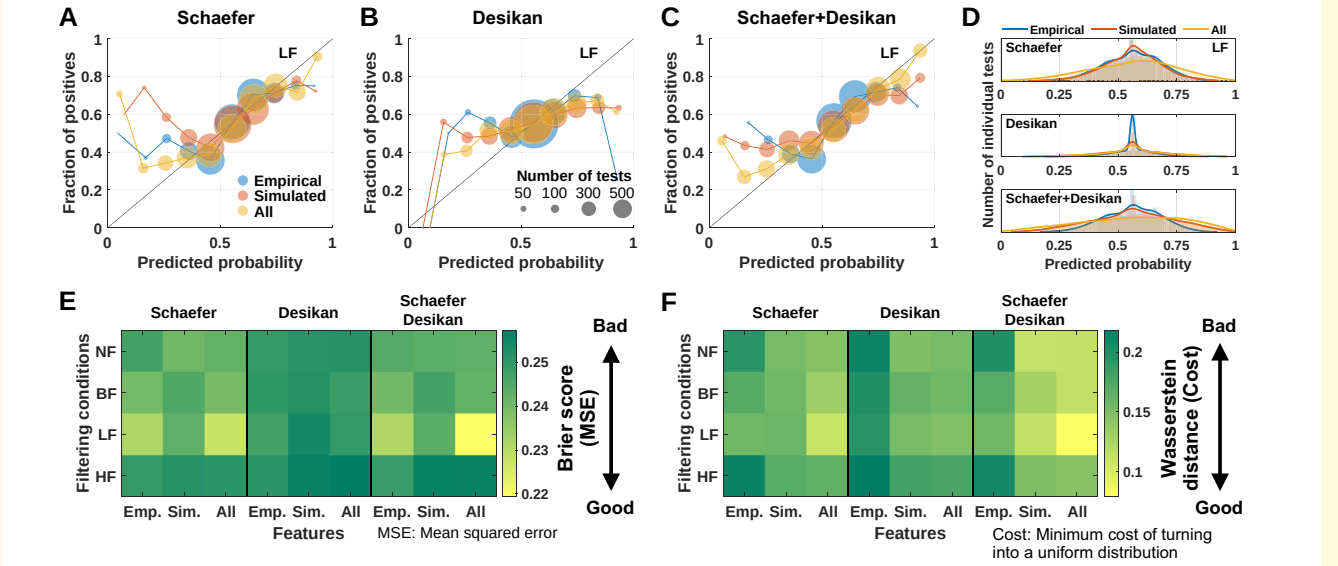

Figure 7 Performance of the trained prediction model regarding the predicted probabilities for individual subjects. (***Top* row**) Plots of the probability calibrations from 5800 predictions for (**A**) the Schaefer atlas, (**B**) Desikan–Killiany atlas, and (**C**) multiple atlases, where the fraction of true positives is plotted versus the probability of them predicted by the trained model for individual subjects. The sizes of the circles indicate the number of individual subject tests for the three considered feature conditions as indicated in the legend in plot (**A**). (**D**) Histograms of the predicted probabilities (5800 predictions) for each feature condition, as indicated in the legend. The case of the LF band-pass filtering condition is illustrated in plots (**A**–**D**). (**E**) Table of the Brier scores (mean-squared error to the correct classes) for all considered filtering and feature conditions. (**F**) Tables of the Wasserstein distances between distributions of predicted probabilities and a uniform distribution for all conditions. Desikan, Desikan–Killiany; Emp., empirical features; Sim., simulated features; All, empirical and simulated features.

validation.[6,30,35,79] In this respect, we investigated how temporal filtering of BOLD signals and brain parcellation influence empirical and simulated results regarding model fitting, group difference and prediction performance. Based on our results, we can conclude that the resting-state whole-brain simulations with appropriate data processing and model validation reflect personal traits of individual subjects, which may contribute to disease classification based on the whole-brain connectivity relationships with potential relevance in medicine.

Effect of temporal filtering on model fitting and prediction

The effect of temporal filtering on functional MRI has been the focus of neuroimaging research for a long time.[80–83] One related study considered different temporal filters for MRI data processing and reported distinguishable BOLD dynamics in task-driven and resting-state brain activity between low and high-frequency band-pass filtering.[38] Furthermore, temporal filtering can influence the classification performance for patients with Alzheimer's disease as compared across several low- and high-band-pass filtering conditions.[39] In this study, we found that the neuroimaging model fitting resulted in significantly different distributions of the maximal GoF values for individual subjects under different filtering conditions. Furthermore, the empirical structure-function connectivity relationship and the maximal GoF values of the neuroimaging model fitting were diminishing for the narrower filtering bands (Supplementary Fig. 4).

Another study investigated Parkinson's disease classification via machine learning on brain networks derived from the empirical resting-state FC with a high pass temporal filtering (> 0.01 Hz) of BOLD signals,[36] which corresponds to the case of the NF condition in our study. According to our prediction results, we suggest to consider the low-frequency band-pass filtering, i.e. the LF condition, which

can improve the differentiation and classification of Parkinson's disease also for the case when only empirical features are used.

An appropriate selection of the filtering condition (broad- or narrow-, high- or low-frequency band) appears to be important for the prediction performance, as reflected by several integrative measures considered in this study. In particular, a detailed evaluation of individual tests indicates that selecting a proper band-pass filter for the empirical and simulated BOLD signals can improve the prediction performance (Figs. 6 and 7).

In a broader perspective, changing parameter values or algorithms in a data processing pipeline can affect empirical results such as structural and functional connectivities, which in turn influence simulation results. In previous studies, for instance, we reported the impact of data processing on simulated results by whole-brain dynamical modelling: WBT densities,[30] region granularities,[6] parcellation schemes,[6,30,79,84] whole-brain simulation models[6,79,84] and model fitting approaches.[6,30] In the current study, we showed that applying temporal filtering to BOLD signals and using different brain parcellations and their combinations, as well as the neuroimaging and behavioural types of model fitting, can impact empirical and simulated results and their classification performance. Subsequently, we therefore investigated the impact of the considered parameter conditions of the data processing and model simulation on classification performance. By doing so, the conditional pipeline, which gives the highest performance, can be considered as contributing to the extent of the data and model personalization, which is important for subject classification based on clinical or behavioural data and their simulations.

Biophysical interpretation of model parameters

Under the assumption that the resting-state brain activity is governed by a complex dynamical system, we can interpret the optimal model parameters of the neuroimaging model fitting as parameters of that system with potential neuroscientific/physical meaning. Since the optimal parameters were determined by distinct model validations, they can differ when a given model fitting approach changes as observed in our previous studies[6,30] and demonstrated by the results in the current study (Fig. 4C–D). Furthermore, the parcellations also impact on the locations of the optimal parameters. For instance, the optimal global coupling parameters derived from the behavioural model fitting suggest weaker optimal couplings than those from the neuroimaging model fitting for the Schaefer atlas (Fig. 4C). On the other hand, the situation for the Desikan–Killiany atlas is opposite (Fig. 4D).

In our model, we used the reconstructed PLs of the tractography streamlines in the white matter, which approximate the actual lengths of the anatomical axonal connections in the brain. The considered model simulates the electrical activity of the excitatory and inhibitory neuronal populations in the brain regions, as reflected by the dynamics of the respective PSP signals. We can thus evaluate and interpret the optimal model parameters for the propagation of the simulated electrical signals (EPSP) along the brain pathways. We, in particular, found that the neuroimaging model fitting resulted in the optimal delay of the signal propagation in the electrophysiologically plausible range[78] (Fig. 3D and H). This confirms the applicability of the used dynamical model for simulating brain dynamics. Furthermore, the optimal delay of the behavioural model fitting obtained from repeated subsampling for different subject configurations is located in the same biologically reasonable range as well, which validates the behavioural model fit (Fig. 4C–D). Further parameters of the considered model and the simulated electrical PSP signals (Table 2) may have biologically plausible interpretations and ranges. Here we may mention, for example, the excitation-inhibition balance of the intra-regional coupling or the time constants responsible for controlling slow or fast oscillations of electrical neuronal activity.

In Parkinson's disease research, a neural model generating such oscillations in a certain frequency range is essential to engaging the pathological neural activity during rest. Previous studies reported that the resting-state cortico-cortical FC of Parkinson's disease patients changed in the 8–10 Hz range (in the alpha-rhythm) for early-stage and moderately advanced Parkinson's disease patients[85] and cortico-cortical coupling for oscillations between 10 and 35 Hz correlated with the severity of Parkinson's disease in the electroencephalogram study.[86] High oscillatory synchrony in the basal ganglia at frequencies of 8–35 Hz was also associated with Parkinson's disease based on spectral power changes between off- and on-drug (levodopa dose).[87] With this respect, we may also investigate the relationship between frequencies of neural activity and models by varying the scale factor R of the current whole-brain dynamical model.

Exploring parameter landscapes

The neuroimaging model fitting is a well-established model validation as though maximizing GoF values of the model is the main objective of the model validation. Nevertheless, brain dynamics for non-optimal model parameters may also provide additional useful properties. They can contribute to the application of the dynamical models to analyse the brain and behaviour. In particular, brain modelling with virtual brains or *in silico* models for brain abnormalities has been used for clinical purposes.[26–28] To this end, we explored the parameter landscapes of GoF values and searched for parameter points that provide optimal GoF values to effectively answer the current research question. As we reported in the results, there exist hotspots of the densely located optimal model parameters, where either neuroimaging or behavioural model fitting is the most effective, although these hotspots may not coincide (Fig. 4C-D, the distributions in blue and orange). This should be linked to the definition of the atlas and, hence, regions. We also observed an impact of brain parcellations on the distributions

of the optimal parameters.[6,30,79,84] A detailed investigation of this phenomenon will require considering more parcellation schemes to systematically describe their influence on the modelling results, as we already initiated in our previous studies.[6,30,79,84] Therefore, a systematic exploration of parameter landscapes allows us to find proper model parameters for a given purpose, which may be different in locations and other properties from one modelling condition and research question to another. Accordingly, we conclude that exploring parameter landscapes of the whole-brain dynamical models using behavioural/phenotypical measures might reveal optimal model parameters best suited for research goals related to inter-individual variability and prediction approaches.

Classification of Parkinsonian patients

In this study, we did not aim at obtaining the highest prediction accuracy, which might have required extensive testing of many simulation and prediction conditions, feature spaces, and learning algorithms. Nevertheless, the obtained prediction performance (65.2% as median accuracy using empirical features) is comparable with that reported, for example, in the study of Plaschke *et al.*[36] which had a median accuracy of 65.5% over considered brain networks.

When we considered the simulated data for Parkinson's disease classification, the features from the neuroimaging model fitting had much lower performance in most considered cases as compared with the features from the behavioural model fitting (Supplementary Fig. 8). Therefore, we suggest that the behavioural model fitting can be used to validate the model against behavioural data for probing the simulated whole-brain dynamics to improve the model correspondence to phenotypical characteristics of subjects and prediction results. Such an approach may be of crucial importance in clinical research and the reported results showed promising confirmations.

In this study, we also explored the impact of a few data processing choices and model simulation on the differentiation and prediction performance. For example, composing predictive features including empirical and simulated connectomes from multiple brain atlases can provide complementary features leading to even better prediction performance (Supplementary Fig. 7). We further showed that also filtering conditions of empirical and simulated BOLD signals can play an important role in model validation and subject classification, where in particular, prediction specificity may vary significantly across filtering conditions as well as the number of false positives of the trained model can be reduced by appropriate filtering (Fig. 6).

Modern neuroimaging research dedicated to prediction analysis and based on machine learning techniques has shown enhanced performance for clinical data and in radiology in particular.[67,88] Those predictive results and developed approaches have faced the issue of translation of their analysis and interpretation of the obtained outcomes to clinical application.[89] In this respect, the current study illustrated the characteristics of individual prediction probabilities to bridge the gap between modelling and prediction results and their translation for diagnosis in clinical research. The analysis included in the present study explored the calibration of the predicted probabilities for individual subjects and provided additional reliable information for the interpretation of the classification results. This can be achieved when the prediction probabilities are considered at the level of individual subjects, for example, when new, unseen patients are tested for diagnostic purposes. Furthermore, the discussed probability analysis delivered additional evidence that the whole-brain simulation results can be useful for complementing empirical data for prediction and classification in clinical research. Consequently, involving the whole-brain dynamical models in the training of machine learning models can improve individual prediction, which can potentially help a clinician better gauge a diagnosis during the examination of individual patients.

Future work

For further studies, other phenotypical properties can be used for the behavioural model fitting, for instance, age or sex. Of course, cognitive or clinical scores such as the Montreal Cognitive Assessment, Mattis dementia rating scales and the unified Parkinson's disease rating scales are also applicable. The suggested approach to behavioural model fitting is similar to the brain mapping of various behavioural or phenotypic measures on the cortical surface and can thus be generalized. In other words, we can map the parameter space using cognitive or clinical scores, which can be referred to as *phenotypical mapping* on the model parameter space like the behavioural model fitting that we introduced in the present study.

Summary

We simulated whole-brain resting-state dynamics and calculated the relationships between structural and functional empirical and simulated connectomes for a variety of conditions and data processing, options including brain parcellation and temporal filtering of BOLD signals. We introduced the behavioural model fitting paradigm and found that the ensuing modelling results can lead to enhanced differentiation of disease and control groups and improved classification of Parkinsonian patients by machine learning approaches. Thus, the involvement of simulated connectomes, especially, in combination with empirical ones, is of great advantage, where the individual probabilities approach the ideal case as compared with the purely empirical feature space. We showed that band-pass filtering in the low-frequency band can have a beneficial effect on the prediction performance. On the other hand, the high-frequencies of the empirical and simulated BOLD signals should be considered with care

and may not immediately be recommended for subject-level classification. In addition, we demonstrated that the prediction performance can differ for different or multiple brain parcellation schemes. Our findings can contribute to a better understanding of empirical and simulated whole-brain dynamics and their relationship to disease. They further suggest an avenue for application of the results of whole-brain simulations for cognitive or clinical investigation of inter-individual differences and disease diagnosis.

Acknowledgements

The authors greatly acknowledge the contribution of Dr. Christian Mathys, Dr. Martin Südmeyer and Dr. Christian Hartmann for the assessment of the Parkinson's disease data. The authors are also grateful to Shraddha Jain for the MRI data quality check. The authors gratefully acknowledge the computing time granted through JARA on the supercomputer JURECA at Forschungszentrum Jülich.

Funding

This work was supported by the Portfolio Theme Supercomputing and Modeling for the Human Brain by the Helmholtz association (https://www.helmholtz.de/en), the Human Brain Project and the European Union's Horizon 2020 Research and Innovation Programme (https://cordis.europa.eu) under Grant Agreements 785907 (HBP SGA2), 945539 (HBP SGA3) and 826421 (VirtualBrainCloud). Open access publication was funded by the Deutsche Forschungsgemeinschaft (DFG, German Research Foundation)—491111487. The funders had no role in study design, data collection and analysis, decision to publish or preparation of the manuscript.

Competing interests

The authors report no competing interests.

Supplementary Material

Supplementary material is available at *Brain Communications* online.

Data availability

The raw empirical data used in this study are not immediately available for public sharing because the given informed consent of the included patients did not include public sharing. The simulated data that support the findings of this study are available from the corresponding author upon a reasonable request.

References

1. Park HJ, Friston K. Structural and functional brain networks: From connections to cognition. *Science*. 2013;342(6158):1238411.
2. Greicius MD, Supekar K, Menon V, Dougherty RF. Resting-state functional connectivity reflects structural connectivity in the default mode network. *Cereb Cortex*. 2009;19(1):72-78.
3. van den Heuvel MP, Mandl RC, Kahn RS, Hulshoff Pol HE. Functionally linked resting-state networks reflect the underlying structural connectivity architecture of the human brain. *Hum Brain Mapp*. 2009;30(10):3127-3141.
4. van den Heuvel MP, Sporns O, Collin G, *et al*. Abnormal rich club organization and functional brain dynamics in schizophrenia. *JAMA Psychiatry*. 2013;70(8):783-792.
5. Batista-Garcia-Ramo K, Fernandez-Verdecia CI. What we know about the brain structure-function relationship. *Behav Sci (Basel)*. 2018;8(4):39.
6. Popovych OV, Jung K, Manos T, *et al*. Inter-subject and inter-parcellation variability of resting-state whole-brain dynamical modeling. *NeuroImage*. 2021;236:118201.
7. Gu Z, Jamison KW, Sabuncu MR, Kuceyeski A. Heritability and interindividual variability of regional structure-function coupling. *Nat Commun*. 2021;12(1):4894.
8. Zamani Esfahlani F, Faskowitz J, Slack J, Misic B, Betzel RF. Local structure-function relationships in human brain networks across the lifespan. *Nat Commun*. 2022;13(1):2053.
9. Finn ES, Shen X, Scheinost D, *et al*. Functional connectome fingerprinting: Identifying individuals using patterns of brain connectivity. *Nat Neurosci*. 2015;18(11):1664-1671.
10. Cocchi L, Harding IH, Lord A, Pantelis C, Yucel M, Zalesky A. Disruption of structure-function coupling in the schizophrenia connectome. *Neuroimage Clin*. 2014;4:779-787.
11. Wirsich J, Perry A, Ridley B, *et al*. Whole-brain analytic measures of network communication reveal increased structure-function correlation in right temporal lobe epilepsy. *Neuroimage Clin*. 2016;11:707-718.
12. Zarkali A, McColgan P, Leyland LA, Lees AJ, Rees G, Weil RS. Organisational and neuromodulatory underpinnings of structural-functional connectivity decoupling in patients with Parkinson's disease. *Commun Biol*. 2021;4(1):86.
13. Honey CJ, Sporns O, Cammoun L, *et al*. Predicting human resting-state functional connectivity from structural connectivity. *Proc Natl Acad Sci U S A*. 2009;106(6):2035-2040.
14. Deco G, Tononi G, Boly M, Kringelbach ML. Rethinking segregation and integration: Contributions of whole-brain modelling. *Nat Rev Neurosci*. 2015;16(7):430-439.
15. Naskar A, Vattikonda A, Deco G, Roy D, Banerjee A. Multiscale dynamic mean field (MDMF) model relates resting-state brain dynamics with local cortical excitatory–inhibitory neurotransmitter homeostasis. *Netw Neurosci*. 2021;5(3):757-782.
16. Cabral J, Kringelbach ML, Deco G. Functional graph alterations in schizophrenia: A result from a global anatomic decoupling? *Pharmacopsychiatry*. 2012;45(Suppl 1):S57-S64.
17. Cabral J, Fernandes HM, Van Hartevelt TJ, James AC, Kringelbach ML, Deco G. Structural connectivity in schizophrenia and its impact on the dynamics of spontaneous functional networks. *Chaos*. 2013;23(4):046111.
18. Yang GJ, Murray JD, Repovs G, *et al*. Altered global brain signal in schizophrenia. *Proc Natl Acad Sci U S A*. 2014;111(20):7438-7443.
19. Anticevic A, Hu X, Xiao Y, *et al*. Early-course unmedicated schizophrenia patients exhibit elevated prefrontal connectivity associated with longitudinal change. *J Neurosci*. 2015;35(1):267-286.
20. Zimmermann J, Perry A, Breakspear M, *et al*. Differentiation of Alzheimer's disease based on local and global parameters in personalized virtual brain models. *Neuroimage Clin*. 2018;19:240-251.
21. van Hartevelt TJ, Cabral J, Deco G, *et al*. Neural plasticity in human brain connectivity: The effects of long term deep brain stimulation

of the subthalamic nucleus in Parkinson's disease. *Plos One*. 2014; 9(1):e86496.
22. Saenger VM, Kahan J, Foltynie T, *et al.* Uncovering the underlying mechanisms and whole-brain dynamics of deep brain stimulation for Parkinson's disease. *Sci Rep*. 2017;7(1):9882.
23. Falcon MI, Riley JD, Jirsa V, McIntosh AR, Chen EE, Solodkin A. Functional mechanisms of recovery after chronic stroke: Modeling with the virtual brain. *eNeuro*. 2016;3(2):ENEURO.0158–15.2016.
24. Deco G, Kringelbach ML, Jirsa VK, Ritter P. The dynamics of resting fluctuations in the brain: Metastability and its dynamical cortical core. *Sci Rep*. 2017;7(1):3095.
25. Popovych OV, Tass PA. Control of abnormal synchronization in neurological disorders. *Front Neurol*. 2014;5:268.
26. Popovych OV, Tass PA. Adaptive delivery of continuous and delayed feedback deep brain stimulation—a computational study. *Sci Rep*. 2019;9(1):10585.
27. Aerts H, Schirner M, Dhollander T, *et al.* Modeling brain dynamics after tumor resection using the virtual brain. *NeuroImage*. 2020; 213:116738.
28. An S, Fousek J, Kiss ZHT, *et al.* High-resolution virtual brain modeling personalizes deep brain stimulation for treatment-resistant depression: Spatiotemporal response characteristics following stimulation of neural fiber pathways. *NeuroImage*. 2022;249: 118848.
29. Cabral J, Vidaurre D, Marques P, *et al.* Cognitive performance in healthy older adults relates to spontaneous switching between states of functional connectivity during rest. *Sci Rep*. 2017;7(1):5135.
30. Jung K, Eickhoff SB, Popovych OV. Tractography density affects whole-brain structural architecture and resting-state dynamical modeling. *NeuroImage*. 2021;237:118176.
31. Varikuti DP, Hoffstaedter F, Genon S, Schwender H, Reid AT, Eickhoff SB. Resting-state test-retest reliability of a priori defined canonical networks over different preprocessing steps. *Brain Struct Funct*. 2017;222(3):1447-1468.
32. Botvinik-Nezer R, Holzmeister F, Camerer CF, *et al.* Variability in the analysis of a single neuroimaging dataset by many teams. *Nature*. 2020;582(7810):84-88.
33. Bhagwat N, Barry A, Dickie EW, *et al.* Understanding the impact of preprocessing pipelines on neuroimaging cortical surface analyses. *Gigascience*. 2021;10(1):giaa155.
34. Borrelli P, Cavaliere C, Salvatore M, Jovicich J, Aiello M. Structural brain network reproducibility: Influence of different diffusion acquisition and tractography reconstruction schemes on graph metrics. *Brain Connect*. 2022;12(8):754-767.
35. Popovych OV, Manos T, Hoffstaedter F, Eickhoff SB. What can computational models contribute to neuroimaging data analytics? *Front Syst Neurosci*. 2019;12:68.
36. Plaschke RN, Cieslik EC, Muller VI, *et al.* On the integrity of functional brain networks in schizophrenia, Parkinson's disease, and advanced age: Evidence from connectivity-based single-subject classification. *Hum Brain Mapp*. 2017;38(12):5845-5858.
37. Rubbert C, Mathys C, Jockwitz C, *et al.* Machine-learning identifies Parkinson's disease patients based on resting-state between-network functional connectivity. *Br J Radiol*. 2019;92(1101): 20180886.
38. Baria AT, Baliki MN, Parrish T, Apkarian AV. Anatomical and functional assemblies of brain BOLD oscillations. *J Neurosci*. 2011;31(21):7910-7919.
39. Wee CY, Yap PT, Denny K, *et al.* Resting-state multi-spectrum functional connectivity networks for identification of MCI patients. *Plos One*. 2012;7(5):e37828.
40. Hou Y, Wu X, Hallett M, Chan P, Wu T. Frequency-dependent neural activity in Parkinson's disease. *Hum Brain Mapp*. 2014;35-(12):5815-5833.
41. Schaefer A, Kong R, Gordon EM, *et al.* Local-global parcellation of the human cerebral cortex from intrinsic functional connectivity MRI. *Cereb Cortex*. 2018;28(9):3095-3114.
42. Desikan RS, Segonne F, Fischl B, *et al.* An automated labeling system for subdividing the human cerebral cortex on MRI scans into gyral based regions of interest. *NeuroImage*. 2006;31(3): 968-980.
43. Lopes da Silva FH, Hoeks A, Smits H, Zetterberg LH. Model of brain rhythmic activity. The alpha-rhythm of the thalamus. *Kybernetik*. 1974;15(1):27-37.
44. Jansen BH, Rit VG. Electroencephalogram and visual evoked potential generation in a mathematical model of coupled cortical columns. *Biol Cybern*. 1995;73(4):357-366.
45. Mathys C, Caspers J, Langner R, *et al.* Functional connectivity differences of the subthalamic nucleus related to Parkinson's disease. *Hum Brain Mapp*. 2016;37(3):1235-1253.
46. Caspers J, Mathys C, Hoffstaedter F, *et al.* Differential functional connectivity alterations of two subdivisions within the right dlPFC in Parkinson's disease. *Front Hum Neurosci*. 2017;11:288.
47. Dale AM, Fischl B, Sereno MI. Cortical surface-based analysis. I. Segmentation and surface reconstruction. *NeuroImage*. 1999;9(2):179-194.
48. Smith SM, Jenkinson M, Woolrich MW, *et al.* Advances in functional and structural MR image analysis and implementation as FSL. *NeuroImage*. 2004;23(Suppl 1):S208-S219.
49. Tustison NJ, Avants BB, Cook PA, *et al.* N4ITK: Improved N3 bias correction. *IEEE Trans Med Imaging*. 2010;29(6):1310-1320.
50. Tournier JD, Smith R, Raffelt D, *et al.* MRtrix3: A fast, flexible and open software framework for medical image processing and visualisation. *NeuroImage*. 2019;202:116137.
51. Cox RW. AFNI: Software for analysis and visualization of functional magnetic resonance neuroimages. *Comput Biomed Res*. 1996; 29(3):162-173.
52. Fischl B, van der Kouwe A, Destrieux C, *et al.* Automatically parcellating the human cerebral cortex. *Cereb Cortex*. 2004;14(1): 11-22.
53. Jeurissen B, Tournier JD, Dhollander T, Connelly A, Sijbers J. Multi-tissue constrained spherical deconvolution for improved analysis of multi-shell diffusion MRI data. *NeuroImage*. 2014;103: 411-426.
54. Tournier JD, Calamante F, Connelly A. Improved probabilistic streamlines tractography by 2nd order integration over fibre orientation distributions. *Proc Int Soc Magn Reson Med*. 2010;18:1670.
55. Virtanen P, Gommers R, Oliphant TE, *et al.* Scipy 1.0: Fundamental algorithms for scientific computing in python. *Nat Methods*. 2020; 17(3):261-272.
56. van der Walt S, Colbert SC, Varoquaux G. The NumPy array: A structure for efficient numerical computation. *Comput Sci Eng*. 2011;13(2):22-30.
57. Moran R, Pinotsis DA, Friston K. Neural masses and fields in dynamic causal modeling. *Front Comput Neurosci*. 2013;7:57.
58. Havlicek M, Roebroeck A, Friston K, Gardumi A, Ivanov D, Uludag K. Physiologically informed dynamic causal modeling of fMRI data. *NeuroImage*. 2015;122:355-372.
59. Buxton RB, Wong EC, Frank LR. Dynamics of blood flow and oxygenation changes during brain activation: The balloon model. *Magn Reson Med*. 1998;39(6):855-864.
60. Friston KJ, Harrison L, Penny W. Dynamic causal modelling. *NeuroImage*. 2003;19(4):1273-1302.
61. Rosenthal R. Parametric measures of effect size. In: Cooper H and Hedges L, eds. *The handbook of research synthesis*. Russell Sage Foundation; 1994:621(2):231-244.
62. Worsley KJ, Evans AC, Marrett S, Neelin P. A three-dimensional statistical analysis for CBF activation studies in human brain. *J Cereb Blood Flow Metab*. 1992;12(6):900-918.
63. Ashburner J, Friston KJ, Penny W. *Human brain function*. 2nd edn. Academic Press; 2003.
64. Shimizu Y, Yoshimoto J, Toki S, *et al.* Toward probabilistic diagnosis and understanding of depression based on functional MRI data analysis with logistic group LASSO. *Plos One*. 2015;10(5): e0123524.

65. Schouten TM, Koini M, Vos F, *et al*. Individual classification of Alzheimer's disease with diffusion magnetic resonance imaging. *NeuroImage*. 2017;152:476-481.
66. Priya S, Liu Y, Ward C, *et al*. Machine learning based differentiation of glioblastoma from brain metastasis using MRI derived radiomics. *Sci Rep*. 2021;11(1):10478.
67. Mei J, Desrosiers C, Frasnelli J. Machine learning for the diagnosis of Parkinson's disease: A review of literature. *Front Aging Neurosci*. 2021;13:633752.
68. Tibshirani R. Regression shrinkage and selection via the lasso. *J R Stat Soc Ser B (Methodological)*. 1996;58(1):267-288.
69. Hastie T, Tibshirani R, Friedman J. *The elements of statistical learning*. 2nd edn. Springer; 2009.
70. Tanner CM, Goldman SM. Epidemiology of Parkinson's disease. *Neurol Clin*. 1996;14(2):317-335.
71. de Lau LML, Breteler MMB. Epidemiology of Parkinson's disease. *Lancet Neurol*. 2006;5(6):525-535.
72. More S, Eickhoff SB, Caspers J, Patil KR. Confound removal and normalization in practice: A neuroimaging based sex prediction case study. In: Dong Y, Ifrim G, Mladenić D, Saunders C, Van Hoecke S, eds. *Machine Learning and Knowledge Discovery in Databases. Applied Data Science and Demo Track: European Conference, ECML PKDD 2020*, Ghent, Belgium, September 14–18, 2020. Lecture Notes in Computer Science, Vol 12461. Springer; 2021:3-18.
73. Vabalas A, Gowen E, Poliakoff E, Casson AJ. Machine learning algorithm validation with a limited sample size. *Plos One*. 2019;14-(11):e0224365.
74. Fawcett T. An introduction to ROC analysis. *Pattern Recognit Lett*. 2006;27(8):861-874.
75. Kompa B, Snoek J, Beam AL. Second opinion needed: Communicating uncertainty in medical machine learning. *NPJ Digit Med*. 2021;4(1):4.
76. Brier GW. Verification of forecasts expressed in terms of probability. *Mon Weather Rev*. 1950;78(1):1-3.
77. Kantorovich LV. Mathematical methods of organizing and planning production. *Manage Sci*. 1960;6(4):366-422.
78. Caminiti R, Carducci F, Piervincenzi C, *et al*. Diameter, length, speed, and conduction delay of callosal axons in macaque monkeys and humans: Comparing data from histology and magnetic resonance imaging diffusion tractography. *J Neurosci*. 2013;33-(36):14501-14511.
79. Domhof JWM, Jung K, Eickhoff SB, Popovych OV. Parcellation-induced variation of empirical and simulated brain connectomes at group and subject levels. *Netw Neurosci*. 2021;5(3):798-830.
80. Friston KJ, Josephs O, Zarahn E, Holmes AP, Rouquette S, Poline J. To smooth or not to smooth? Bias and efficiency in fMRI time-series analysis. *NeuroImage*. 2000;12(2):196-208.
81. Zuo XN, Di Martino A, Kelly C, *et al*. The oscillating brain: Complex and reliable. *NeuroImage*. 2010;49(2):1432-1445.
82. Boubela RN, Kalcher K, Huf W, Kronnerwetter C, Filzmoser P, Moser E. Beyond noise: Using temporal ICA to extract meaningful information from high-frequency fMRI signal fluctuations during rest. *Front Hum Neurosci*. 2013;7:168.
83. Vergara VM, Mayer AR, Damaraju E, Hutchison K, Calhoun VD. The effect of preprocessing pipelines in subject classification and detection of abnormal resting state functional network connectivity using group ICA. *NeuroImage*. 2017;145(Pt B):365-376.
84. Domhof JWM, Eickhoff SB, Popovych OV. Reliability and subject specificity of personalized whole-brain dynamical models. *NeuroImage*. 2022;257:119321.
85. Stoffers D, Bosboom JL, Deijen JB, Wolters E, Stam CJ, Berendse HW. Increased cortico-cortical functional connectivity in early-stage Parkinson's disease: An MEG study. *NeuroImage*. 2008;41(2):212-222.
86. Silberstein P, Pogosyan A, Kuhn AA, *et al*. Cortico-cortical coupling in Parkinson's disease and its modulation by therapy. *Brain*. 2005;128(Pt 6):1277-1291.
87. Kuhn AA, Tsui A, Aziz T, *et al*. Pathological synchronisation in the subthalamic nucleus of patients with Parkinson's disease relates to both bradykinesia and rigidity. *Exp Neurol*. 2009;215(2):380-387.
88. Burgos N, Colliot O. Machine learning for classification and prediction of brain diseases: Recent advances and upcoming challenges. *Curr Opin Neurol*. 2020;33(4):439-450.
89. Caspers J. Translation of predictive modeling and AI into clinics: A question of trust. *Eur Radiol*. 2021;31(7):4947-4948.

Supplementary material

Simulated BOLD signals

The neurovascular coupling describes that the changes of the induced signals $s(t)$ driven by the EPSP input link to the changes in the cerebral blood flows (CBF) $f(t)$ as the blood inflow

$$\dot{s}(t) = -\kappa s(t) - \gamma(f(t) - 1) + \frac{y_{EPSP}(t)}{A}, \quad (1)$$

$$\dot{f}(t) = s(t). \quad (2)$$

Equations 1 and 2 govern the dynamics of the induced signal and CBF, respectively. Parameters κ and γ are the rate constants that regulate ultra-slow endogenous fluctuations at around 0.09 Hz.[1] The normalized neural response, i.e., $y_{EPSP}(t)$ divided by the amplitude A of the parameter in the electrical model, drives the induced slow fluctuation. Consequently, CBF signals simultaneously influence the changes of the cerebral blood volume (CBV) $v(t)$ and deoxyhemoglobin content (DOH) $q(t)$ as described by the following equations:

$$\dot{v}(t) = \frac{1}{t_{MTT}}[f(t) - f_{out}(v,t)], \quad (3)$$

$$\dot{q}(t) = \frac{1}{t_{MTT}}\left[f(t)\frac{E(f)}{E_0} - f_{out}(v,t)\frac{q(t)}{v(t)}\right]. \quad (4)$$

The mean transit time t_{MTT} scales both differential equations for passing a bolus of the blood through the vein. To estimate CBV changes, Equation 3 models a difference between the blood inflow $f(t)$ and the blood outflow $f_{out}(v,t)$. Subsequently, we can calculate the changes of DOH using the dynamics of CBF and CBV by regarding oxygen extraction fraction $E(f)$ in Equation 4. Parameter E_0 is the net oxygen extraction fraction at rest,

$$f_{out}(v) = v^{1/\alpha}, \quad (5)$$

$$E(f) = 1 - (1 - E_0)^{1/f}. \quad (6)$$

Equation 5 provides the relationship between CBF and CBV, where Grubb *et al.*[2] empirically found α is 0.38. Equation 6 is a non-linear function of CBF, and describes an effect of CBF on the oxygen extraction fraction, see the reference[1] for details. Using CBV and DOH, we can calculate simulated BOLD signals y_{BOLD}:

$$y_{BOLD} = V_0\left[k_1(1-q) + k_2\left(1 - \frac{q}{v}\right) + k_3(1-v)\right], \quad (7)$$

where V_0 is the resting blood volume fraction, and parameters k_1, k_2, and k_3 depend on the magnetic field strength as follows:

$$k_1 = 4.3 \cdot \vartheta_0 \cdot E_0 \cdot TE, \qquad k_2 = \varepsilon \cdot r_0 \cdot E_0 \cdot TE, \qquad k_3 = 1 - \varepsilon. \quad (8)$$

Parameters ϑ_0, TE, ε, and r_0 are the frequency offset for 3 T scanner, the echo time, the ratio of intra/extra-vascular signal, and the sensitivity of changes in intra-vascular signal relaxation rate with changes in oxygen saturation, respectively.[1] The parameter values of the BW model for BOLD signals are given in Table 2.

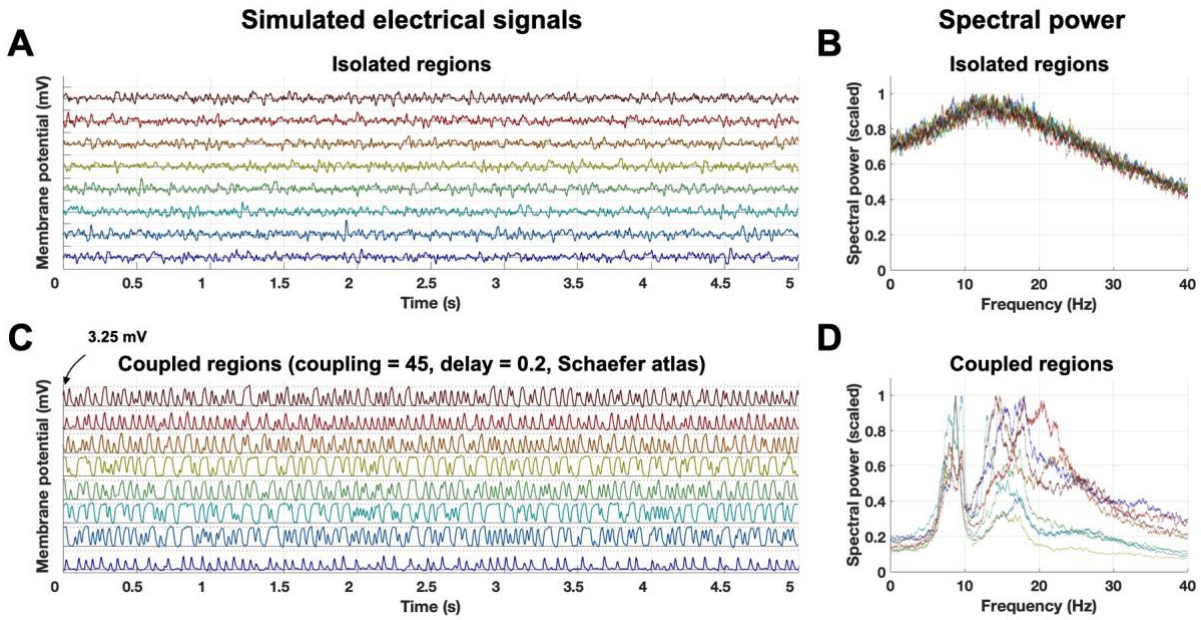

Supplementary Figure 1. Examples of **(A, C)** time courses of the simulated excitatory post-synaptic potentials (EPSP) and **(B, D)** their spectral power distributions of a few brain regions for **(A, B)** isolated (global coupling = 0) and **(C, D)** coupled cases for the Schaefer atlas. In the latter case, global coupling = 45 and global delay = 0.2 are the optimal model parameters of the neuroimaging model fitting. The peaks of the maximal spectral power for the isolated regions in (B) are around 13 Hz. The dotted horizontal lines in (C) indicate the maximum EPSP (3.25 mV), which is the specified value as the maximal EPSP kernel in Table 2.

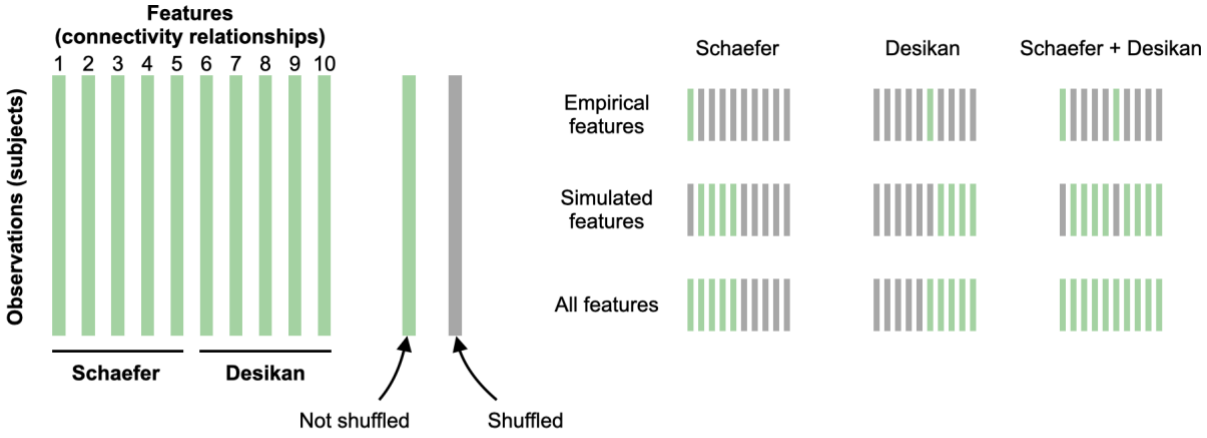

10 features

1. Corr(eFC, eSC) (Empirical, Schaefer)
2. Corr(eFC, sFC) (Neuroimaging, Schaefer)
3. Corr(eSC, sFC) (Neuroimaging, Schaefer)
4. Corr(eFC, sFC) (Behavioral, Schaefer)
5. Corr(eSC, sFC) (Behavioral, Schaefer)
6. Corr(eFC, eSC) (Empirical, Desikan-Killiany)
7. Corr(eFC, sFC) (Neuroimaging, Desikan-Killiany)
8. Corr(eSC, sFC) (Neuroimaging, Desikan-Killiany)
9. Corr(eFC, sFC) (Behavioral, Desikan-Killiany)
10. Corr(eSC, sFC) (Behavioral, Desikan-Killiany)

Supplementary Figure 2. Features and feature conditions used for PD classification. Ten connectivity relationships listed in the plot were used during machine-learning training and testing for PD classification as features. To investigate the impact of simulated results on the prediction performance, we considered 9 feature conditions as illustrated in the right part of the plot. Here, a few features of interest were selected (green bars), while the other features were randomly shuffled across subjects (gray bars). Shuffling is done for each feature separately, i.e., shuffling within a feature gives the same distribution of the values but randomized feature values across subjects, which destroys the correspondence between the (brain) feature and behavioral labels (PD or HC). The shuffled feature is supposed to not contribute to classification performance, but we always keep the same number (ten) of features in all feature conditions of the machine-learning experiments. Abbreviations: FC = functional connectivity; PD = Parkinson's disease; SC = streamline count.

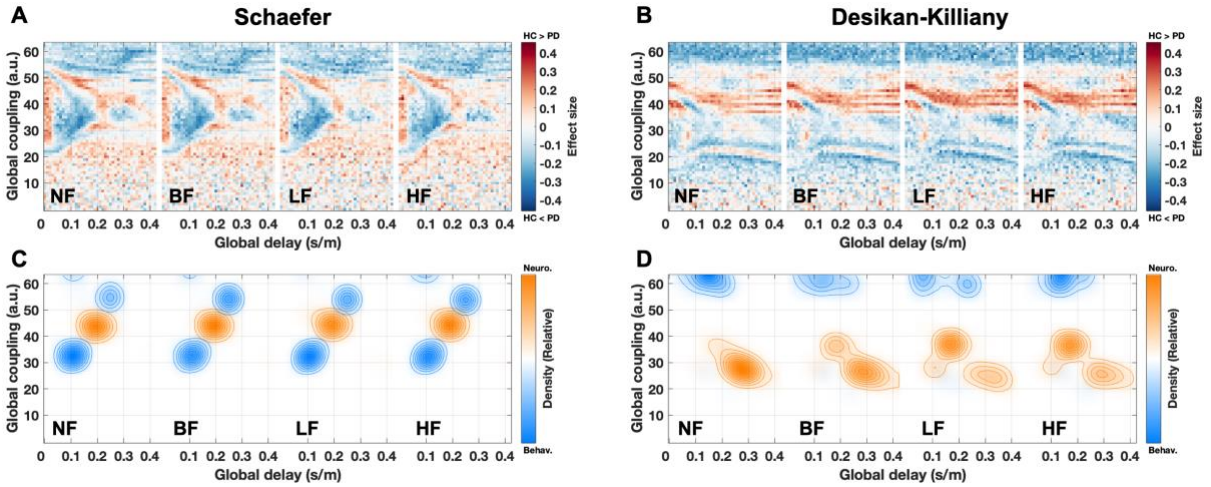

Supplementary Figure 3. Parameter maps of the effect size of the difference of eSC-sFC correlation values between PD and HC subject groups used for the behavioral model fitting. The filtering conditions are indicated in the plots for **(A)** the Schaefer atlas and **(B)** the Desikan-Killiany atlas. Effect sizes in the (τ_{global}, C)-parameter plane were calculated by a non-parametric Wilcoxon rank-sum two-tailed test between HC and PD subject groups in the eSC-sFC correlation values for each parameter point. **(C, D)** Distributions of optimal parameters derived from the neuroimaging model fitting (orange, all subjects, n=116) and the behavioral model fitting (blue, repeated sub-sampling, n=1000) for **(C)** the Schaefer atlas and **(D)** the Desikan-Killiany atlas. Abbreviations: PD = Parkinson's disease; HC = healthy controls; NF = no filtering; BF = broad band ([0.01,0.1] Hz); LF = low-frequency band ([0.01,0.05] Hz); HF = high-frequency band ([0.05,0.1] Hz).

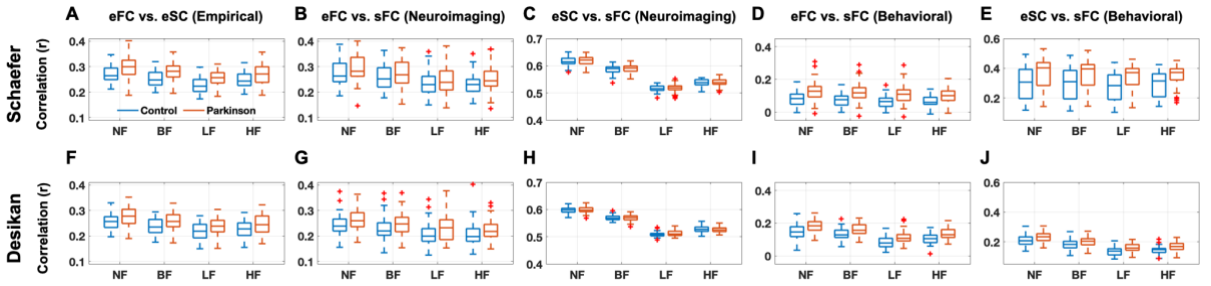

Supplementary Figure 4. Comparison of connectivity correspondences between HC and PD subject groups as reflected by the connectivity relationships of empirical and simulated results for **(A-E)** the Schaefer atlas and **(F-J)** the Desikan-Killiany atlas for **(A, F)** the empirical structure-function relationship (eFC vs. eSC), **(B, C, G, H)** functional (eFC vs. sFC) and structure-function (eSC vs. sFC) relationships for the neuroimaging model fitting, and **(D, E, I, J)** connectome relationships (eFC vs. sFC and eSC vs. sFC) for the behavioral model fitting. Abbreviations: NF = no filtering; BF = broad band ([0.01,0.1] Hz); LF = low-frequency band ([0.01,0.05] Hz); HF = high-frequency band ([0.05,0.1] Hz); FC = functional connectivity; SC = streamline count.

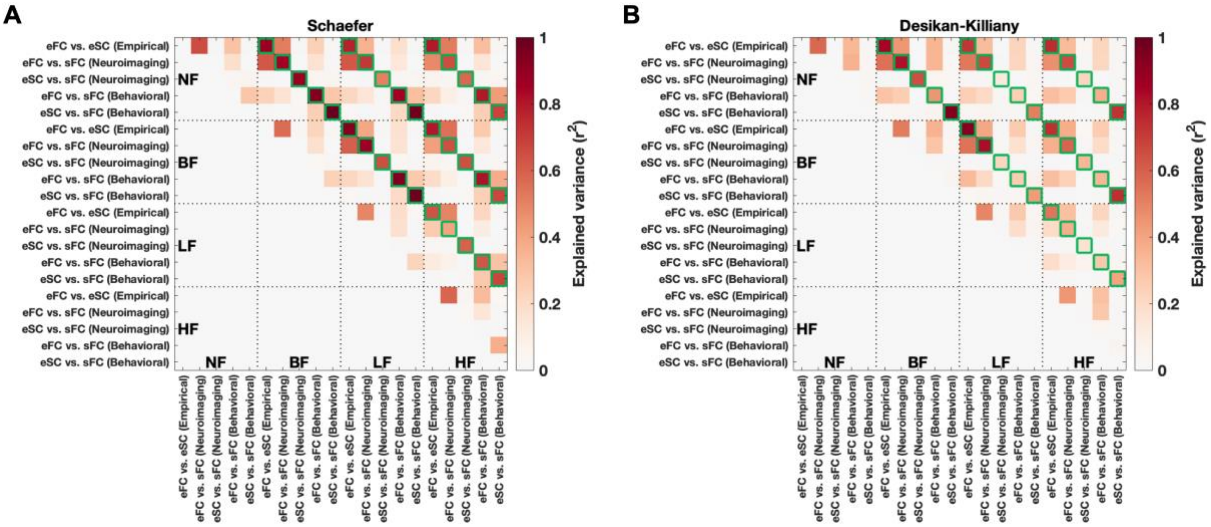

Supplementary Figure 5. Explained variances (EV, squared correlation r^2) between five connectivity relationships for **(A)** the Schaefer atlas and **(B)** the Desikan-Killiany atlas. The five connectivity relationships are corr(eSC, eFC) (empirical), corr(eFC, sFC) (neuroimaging), corr(eSC, sFC) (neuroimaging), corr(eFC, sFC) (behavioral), and corr(eSC, sFC) (behavioral). Due to the four considered temporal filtering conditions of NF, BF, LF, and HF indicated in the plots, the intra-/inter-condition EVs were obtained using 20 connectivity relationships (see the axes). The green boxes are for the same types of connectivity relationships under different filtering conditions. Abbreviations: NF = no filtering; BF = broad band ([0.01,0.1] Hz); LF = low-frequency band ([0.01,0.05] Hz); HF = high-frequency band ([0.05,0.1] Hz).

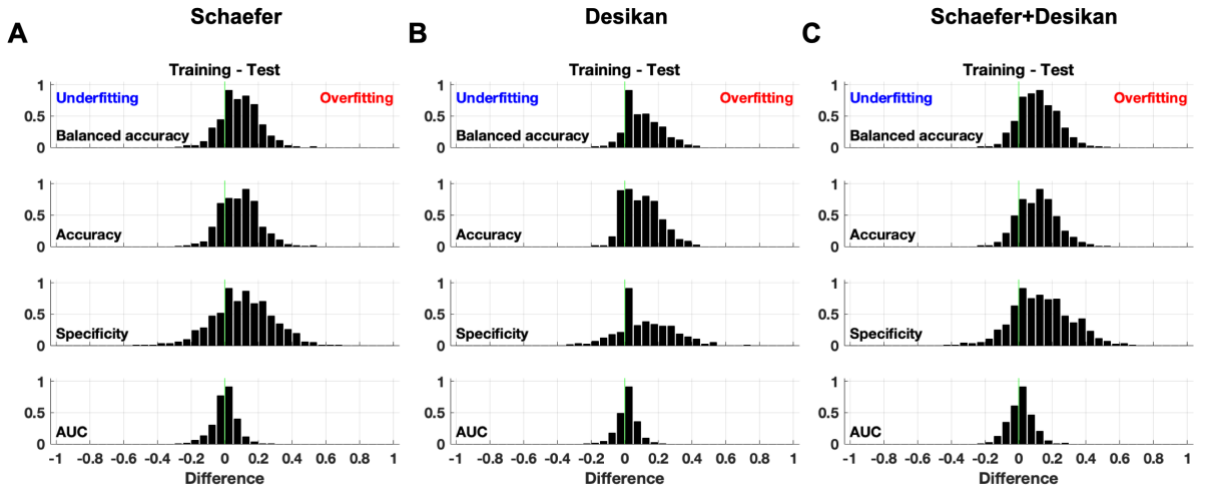

Supplementary Figure 6. Differences of model performance between training and test sets (Training – Test) for PD prediction including all filtering conditions and all features for the **(A)** Schaefer atlas, **(B)** Desikan-Killiany atlas, and **(C)** multiple atlases, i.e., the Schaefer and Desikan-Killiany atlases. The considered performance measures are indicated in the plots. The green vertical lines indicate zero differences. The positive differences are overfitting cases, and the negative ones are underfitting. Abbreviation: AUC = area-under-curve.

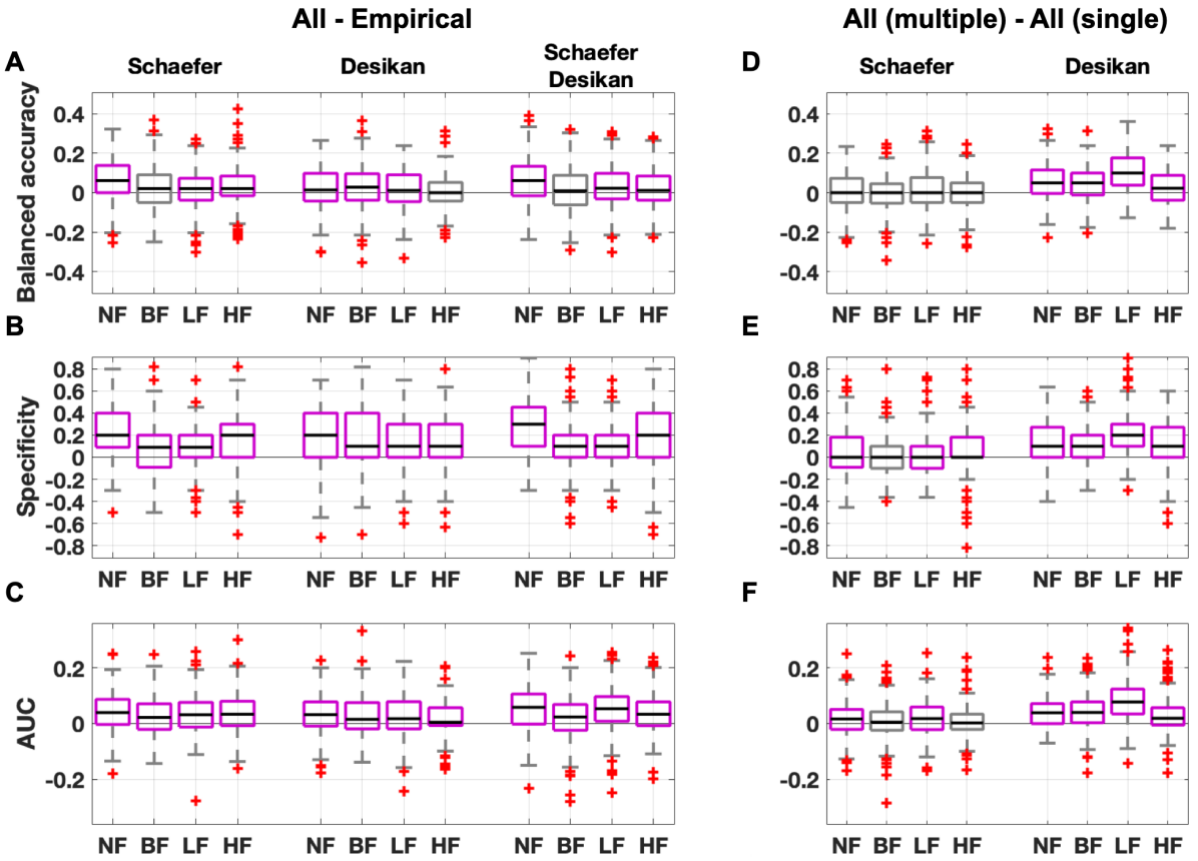

Supplementary Figure 7. Comparisons of the prediction performance between the feature conditions used for the subject classification, see Supplementary Figure 2. The differences in the performance measures are illustrated as box plots for (A-C) "All features" versus "Empirical features" (All - Empirical) for the Schaefer, Desikan-Killiany, and multiple (Schaefer and Desikan-Killiany) atlases as indicated on the top of the plot (A) and for **(D-F)** "All features" for the multiple atlases versus "All features" for single atlases (All(multiple) – All (single)) as indicated on top of plot (D). The performance measures are **(A, D)** balanced accuracy, **(B, E)** specificity, and **(C, F)** AUC of ROC curves. The filtering conditions are given on the horizontal axes. The purple boxes depict significantly different performance (Wilcoxon signed-rank two-tail test and Bonferroni corrected $p < .05$). Abbreviations: NF = no filtering; BF = broad band ([0.01,0.1] Hz); LF = low-frequency band ([0.01,0.05] Hz); HF = high-frequency band ([0.05,0.1] Hz).

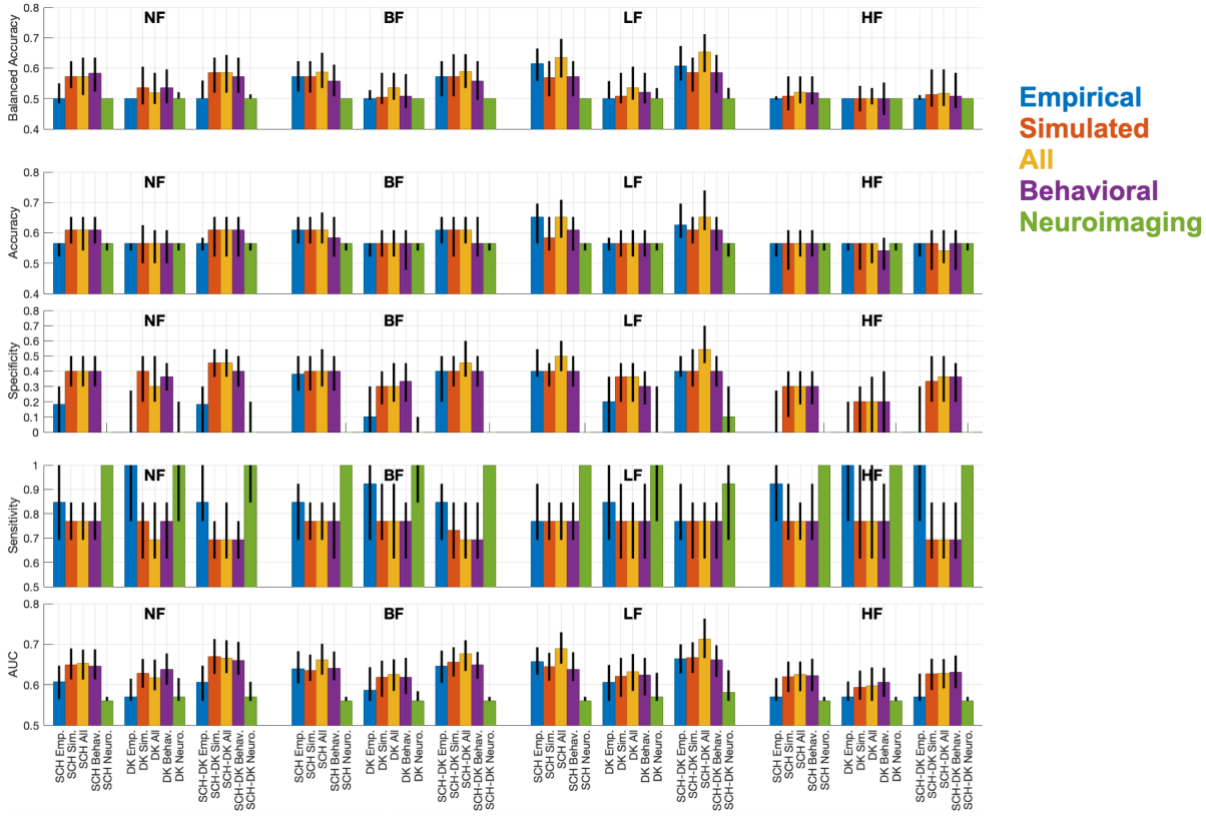

Supplementary Figure 8. Prediction performance as given by the balanced accuracy, accuracy, specificity, sensitivity, and AUC of ROC curves using optimal simulated connectomes (corresponding to the optimal model parameters) from the behavioral fitting only (purple) and from the neuroimaging fitting only (green) as additional feature conditions to those presented in Supplementary Figure 2 (also depicted here for comparison, see the legend). The error bars indicate interquartile ranges, and the heights of bars are the medians. The filtering conditions are indicated in the plots. Abbreviations: NF = no filtering; BF = broad band ([0.01,0.1] Hz); LF = low-frequency band ([0.01,0.05] Hz); HF = high-frequency band ([0.05,0.1] Hz); SCH = Schaefer; DK = Desikan-Killiany, Emp. = Empirical features, Sim. = Simulated features, All = All features, Neuro. = Simulated features from the neuroimaging model fitting only, and Behav. = Simulated features from the behavioral model fitting only.

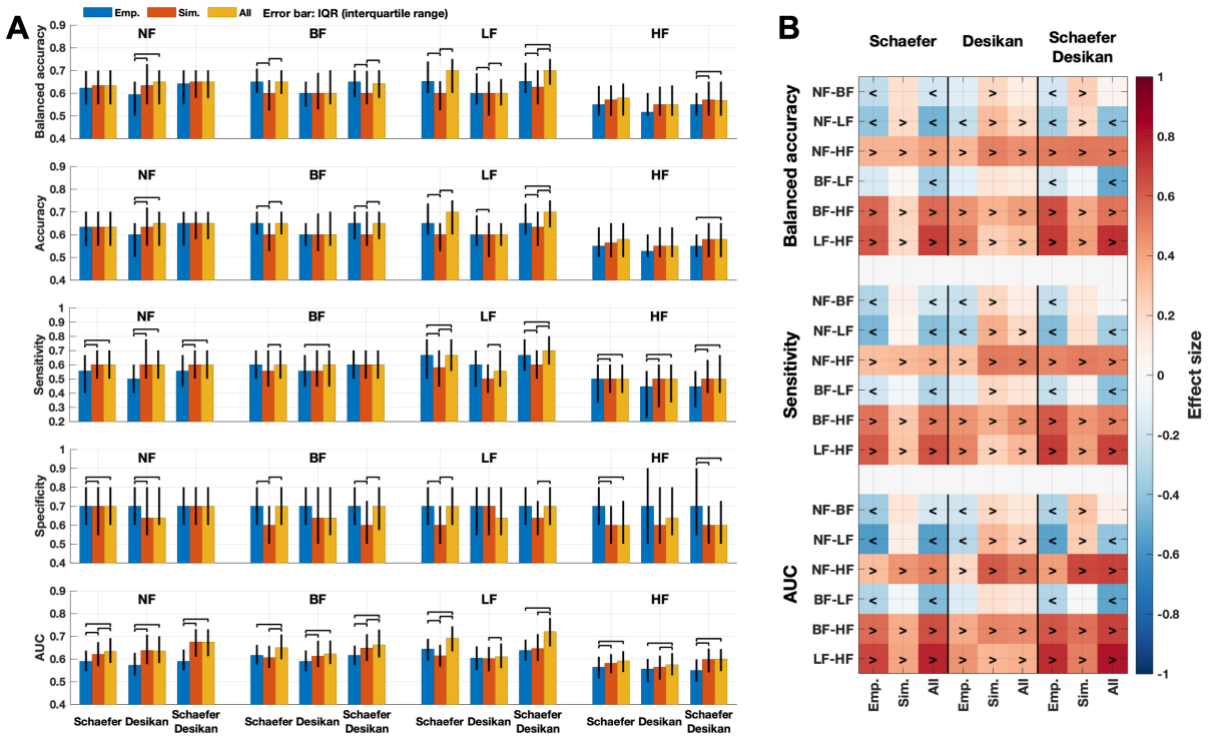

Supplementary Figure 9. Summary of the performance of PD classification using the three different feature conditions: empirical features (blue bars), simulated features (red bars), and all features (yellow bars) for the balanced subject configuration (n=99, Supplementary Table 1) controlled for the balanced age and sex and size of subject groups (HC versus PD). **(A)** Median values of the balanced accuracy, accuracy, sensitivity, specificity and area-under-curve (AUC) of the receiver operating characteristics (ROC) curves for all considered parcellations and filtering conditions are shown in each panel. The error bars indicate the interquartile range across iterations of the outer loop of the nested cross-validation procedure (see Fig. 2 in the main text). The black lines connecting two conditions indicate significantly different performance between feature conditions. **(B)** Effect sizes between filtering conditions for each feature condition. The signs '<' and '>' indicate which condition is significantly larger than the other. For example, '<' sign for 'NF-LF' indicated on the vertical axes means NF < LF for a given performance indicated on the horizontal axes. The Wilcoxon signed-rank two-tail test was used for comparisons across feature and filtering conditions (Bonferroni corrected statistics). Abbreviations: PD = Parkinson's disease; NF = no filtering; BF = broad band ([0.01,0.1] Hz); LF = low-frequency band ([0.01,0.05] Hz; HF = high-frequency band ([0.05,0.1] Hz).

Supplementary Table 1 Demography of a balanced subject configuration (excluding 17 oldest patients from 116 subjects).

Groups	Mean (standard deviation) years		Statistical tests	*p*-values
	All subjects		**Chi-square goodness-of-fit test**	
All	56.62 (9.24)		99 subjects	0.235
	Healthy controls	**Patients**	**Wilcoxon rank-sum two-tail test**	
All	55.02 (9.69)	58.31 (8.42)	51 healthy controls versus 48 patients	0.062
Female	56.52 (9.40)	60.80 (8.96)	21 healthy controls versus 20 patients	0.201
Male	53.97 (9.74)	56.54 (7.53)	30 healthy controls versus 28 patients	0.156
	Females	**Males**	**Wilcoxon rank-sum two-tail test**	
All	58.61 (9.43)	55.21 (8.84)	41 females versus 58 males	0.095

References

1. Havlicek M, Roebroeck A, Friston K, Gardumi A, Ivanov D, Uludag K. Physiologically informed dynamic causal modeling of fMRI data. *NeuroImage.* 2015;122:355-372.

2. Grubb RL, Jr., Raichle ME, Eichling JO, Ter-Pogossian MM. The effects of changes in PaCO2 on cerebral blood volume, blood flow, and vascular mean transit time. *Stroke.* 1974;5(5):630-639.

5 Discussion

The main objective of this dissertation is to delineate and investigate the impact of data processing on whole-brain dynamical modeling via the systematically planned workflow illustrated in Fig. 3. From the results of the three studies in this project, the impact on the modeling involves four aspects: data processing parameters, optimal model parameters, personalized whole-brain models, and model fitting approaches. Based on these aspects, this dissertation formulates whole-brain models as a mathematical or biophysical *in silico* framework for interacting among brain regions via the whole-brain connectome. Subsequently, the following sections discuss our findings from the performed studies and address the impact of data processing on the whole-brain modeling and its applications.

5.1 Impact of data processing

Whole-brain models generate brain dynamics based on empirical data as a backbone of intrinsic interactions between brain regions. Whole-brain simulation studies, however, have used study-specific data processing or one from the literature. Due to no consensus pipeline for MRI data processing, various data processing parameters can affect empirical data. Thus, the effect of data processing parameters should be carefully tested by systematically prepared experiments. Otherwise, empirical data and analyzed results can be less reliable, and subsequently, the corresponding conclusions will be less replicable across studies. Therefore, we performed simulation experiments with systematically designed conditions based on the current project workflow and investigated the impact of MRI data processing parameters on the whole-brain dynamical models.

5.1.1 Impact of structural pipeline on modeling

In study 1, varying WBT density (the number of streamlines in the WBT) affects whole-brain structural architecture, such as SC and their graph theoretical network properties. As mentioned, SC is used for whole-brain models, thus using different SCs can affect simulated results. For instance, previous studies have shown that manipulating SC edges could result in a better fit for model validation (Cabral et al., 2012; Deco et al., 2014; Proix et al., 2016). Because of many possible ways of SC variation for the model validation, we should consider data processing parameters of the structural pipeline on top of state-of-the-art techniques for WBT calculation (Tournier et al., 2019). For example, average path lengths of streamlines between brain regions are sensitive to disconnection or re-connection of edges across WBT density conditions rather

than streamline counts. Therefore, long-range or interhemispheric connections have relatively small numbers of streamlines and can influence the structural connectome while varying WBT density. Accordingly, simulated BOLD signals by whole-brain models will differ across applied structural pipeline conditions. In addition, the simulated FCs calculated by the simulated BOLD signals from the varied WBT density conditions impact whole-brain dynamical modeling.

In study 1, we suggested that the applicable range of WBT density is 50,000 streamlines as a sparse one and 2,000,000 streamlines as a dense one. Some of the considered graph-theoretical network properties are highly sensitive to the varied WBT densities in this range. Therefore, using different WBT densities can clearly impact model validation because it provides the brain network architecture serving as a backbone for the modeling of brain dynamics (Cabral et al., 2011; Endo et al., 2019; Honey et al., 2009; Zimmermann et al., 2018). Correspondingly, we addressed the relationship between graph-theoretical network properties and goodness-of-fit (GoF, *i.e.*, similarity between empirical and simulated data) values across varied WBT densities. In addition to the impact of the WBT densities, we applied different parcellation schemes for the modeling and found that the results have different patterns across the WBT density conditions when we use different parcellation schemes. Thus, WBT densities and brain parcellation schemes are intermingled as a mutual impact on the modeling. I will discuss this in the subsection 5.1.3 later.

5.1.2 Impact of functional pipeline on modeling

Data processing parameters in the functional pipeline influence BOLD signals and, accordingly, empirical FC will be affected by the different BOLD signals (Caballero-Gaudes and Reynolds, 2017). For instance, signal processing of BOLD signals has been an issue in neuroimaging research for a long time (Boubela et al., 2013; Friston et al., 2000; Vergara et al., 2017; Zuo et al., 2010). The literature showed that applying temporal filters with different frequency ranges influences empirical BOLD signals and FC for healthy subjects (Baria et al., 2011) and patients (Hou et al., 2014; Wee et al., 2012). In study 3, we also observed that temporal filtering with different frequency ranges for empirical and simulated BOLD signals influences empirical and simulated FC and subsequently impacts model fitting results. Based on the correspondence between empirical and simulated data, we trained a prediction model for classification of patients with Parkinson's disease using a machine learning method and observed that the prediction performances are clearly different across the temporal filtering conditions. So applying the temporal filtering conditions for BOLD signals influences empirical and simulated FC simultaneously. Therefore, data processing parameters in the functional pipeline do not only

affect empirical FC but also impact the results of whole-brain model fitting. In addition to the impact of the functional processing parameters, we applied two parcellation schemes to whole-brain dynamical modeling and found that the prediction performances are also different across parcellation schemes. In consequence, different temporal filtering conditions and brain parcellation schemes impact the whole-brain dynamical modeling and the patient classification. I will discuss this in the next subsection.

5.1.3 Impact of parcellation schemes on modeling

As we reviewed brain parcellation schemes in the recent study (Domhof et al., 2021), various parcellation schemes have been published using different criteria and algorithms, such as cytoarchitectures regarding cell distribution (Pijnenburg et al., 2021; Scholtens et al., 2018), structural architectures based on gyri- or sulci-formation in the neocortex (Desikan et al., 2006; Destrieux et al., 2010; Tzourio-Mazoyer et al., 2002), and functional analyses of resting-state or task-driven functional MRI (Craddock et al., 2012; Schaefer et al., 2018; Shen et al., 2013; Urchs et al., 2019). However, choosing an optimal parcellation scheme is still under debate, and it can be study-dependent in considering research methods and questions.

In study 1, we used two parcellation schemes and found the mutual impact on the model validation in two factors: WBT densities and parcellation schemes. With the 12 configurations of conditions (6 WBT densities and 2 parcellation schemes), whole-brain dynamical modeling resulted in different maximal GoF profiles across WBT density conditions for each parcellation scheme. One remarkable observation is that the cortical parcellation exhibits differentiable modeling behavior across subjects, such as subject stratification in study 1 and parcellation-induced variation at group and subject level summarized by our recent study (Domhof et al., 2021). Consequently, we infer that individual subjects can have different results of whole-brain dynamical modeling when disparate brain parcellation schemes are used for data processing.

In study 2, we also used three parcellation schemes with varied region-granularity (the number of parcels of the neocortex) and region-probability conditions (different region sizes with the same number of parcels). We observed that using disparate parcellation schemes provides different results of whole-brain dynamical model fitting because the brain parcellation is used to calculate empirical FC and SC. In other words, parcellation schemes are not only related with empirical data, but also simultaneously influencing simulated FC derived by the whole-brain models that employed empirical data as a backbone. Therefore, it is difficult to understand how brain parcellation schemes impact whole-brain dynamical modeling. For instance, our findings

in study 2, which was focusing on the impact of varying parcellation schemes, showed different relationships between data variables of empirical connectome (FC and SC) and maximal GoF values across individuals, *i.e.*, inter-subject variability. Besides, the results also showed different correspondences of maximal GoF values between the empirical data variables and brain parcellation families, *i.e.*, inter-parcellation variability. Although this dissertation does not assert which parcellation scheme is generally optimal for whole-brain dynamical modeling in the data-driven approach, these findings support the argument about the impact of data processing of using different parcellation schemes on whole-brain dynamical modeling.

5.2 Optimal model parameters in data processing and analyses

Optimizing parameters of whole-brain models means searching for parameter values in the parameter space (free parameters) corresponding to the model that gives the maximal GoF value (or the minimal value of a loss function) against empirical data. Simulated data derived by the optimal model can provide properties of whole-brain dynamics complying with the applied model fitting (or applied objective function). Therefore, optimal model parameters can be different when we consider various model fitting approaches, for instance, similarity between simulated FC and empirical FC and similarity between simulated FC and empirical SC. With this, whole-brain models with different optimal parameters can represent different dynamics of simulated data depending on the applied model fitting. In the three studies of this thesis, we considered a couple of model fitting approaches for whole-brain modeling and investigated optimal model parameters in each case.

5.2.1 Optimal delay plays a role in varied tractography densities

In the literature of computational neuroscience, some researchers used whole-brain models without delay in coupling for ultraslow BOLD dynamics (Deco et al., 2019; Ponce-Alvarez et al., 2015). In study 1, we employed free parameters of delayed coupling between regions based on empirical path lengths (the anatomical white-matter path lengths of streamlines between brain regions) for the Kuramoto model (Kuramoto, 1984; Yeung and Strogatz, 1999) and performed whole-brain dynamical modeling to find optimal couplings and delays. As a result, whole-brain models with the optimal parameters (couplings and non-zero delays) exhibited enhanced GoF values compared to the models with zero delays. Although structural architecture showed similar tendencies of the graph-theoretical network properties across varied WBT densities, the distributions of optimal delays differently behave when we use disparate parcellation schemes via the model fitting to the empirical SC, *i.e.*, searching for the maximal

correspondence between empirical SC and simulated FC. Furthermore, the optimal model parameters based on the different model fitting approaches can also play roles in distinct behaviors between the two parcellation schemes. Consequently, varying WBT density can reveal the changing distributions of optimal delays in whole-brain dynamical modeling.

In addition to the impact of varying WBT density on the distributions of optimal delays, the optimal parameter values can also be related with apparent criteria for subject stratification. For instance, stratified subjects based on different patterns of optimal delays showed discrete maximal GoF values between the two distributions of optimal delays across WBT densities, *i.e.*, small delays (nearly zero) and large delays. Furthermore, we also observed that the optimal delays have negative correlations with natural frequencies of oscillators corresponding to the maximal spectral peaks (the most dominant frequency) of empirical BOLD signals of each region. Therefore, the optimal signal propagation speeds of the model can be regulated by the mean intrinsic temporal frequencies of oscillators of the brain regions. Consequently, structural data processing parameters does not impact only optimal parameters but also reveals relationships between subject stratification and whole-brain dynamical modeling.

5.2.2 Optimal parameter distributions in whole-brain models

In study 2, we also observed similar distributions of optimal model parameter points when we use various parcellation schemes for whole-brain dynamical modeling using the model fitting to empirical SC, and besides, we used two different whole-brain models, *i.e.*, a coupled phase oscillator model (Kuramoto, 1984; Yeung and Strogatz, 1999) and a coupled generic limit-cycle oscillator model (Kuznetsov et al., 1998). As a result, by using the both models, we found that the optimal model parameter points distribute in similar locations on the parameter space across two model conditions (the phase oscillators and the generic limit-cycle oscillators) and different parcellation schemes with regional granularity or region-probability conditions. On the other hand, in study 3, we observed that optimal model parameter points corresponding to the maximal GoF values were located in different hot spots from the results in studies 1 and 2 when we applied a convolution-based (critically damped oscillators) two-population model (Jansen and Rit, 1995; Lopes da Silva et al., 1974) for electrical neural responses. Moreover, the optimal model parameters were located in a range where optimal delays are biologically feasible (Caminiti et al., 2013). On the contrary, the other two models in the published studies 1 and 2 showed that the distributions of optimal model parameter values were almost zero delays via the same model fitting approach, *i.e.*, the model fitting to empirical FC. As a consequence of the results, these studies of the thesis show a manifest effect of that using different whole-brain

models can influence model-fitting results showing different distributions of optimal model parameter points in whole-brain dynamical modeling. In addition, disparate whole-brain models of mathematical or biophysical neural updates can result in different landscapes of model-fitting values across data processing parameters. Consequently, using different types of whole-brain models allows us to investigate the impact of data processing parameters on whole-brain dynamical modeling.

5.2.3 Exploring parameters with model fitting approaches

Exploring a given free parameter space with several model fitting approaches can also provide a way to reveal effective and latent simulated results for answering research questions. In light of the unlimited number of whole-brain models with free parameters, exploring a landscape of model-fitting values using different objective functions allows us to investigate the impact of data processing parameters on whole-brain dynamical modeling in more details. For instance, one model parameter point can be optimal in terms of revealing a pronounced difference between subject groups, and another distinct parameter point can disclose relationships (*e.g.*, correlation) between simulated data and behavioral measures. With this, we can also apply varied data processing parameters for whole-brain dynamical modeling, and subsequently simulated results can be influenced by the data processing conditions. By doing so, we can show how the whole-brain dynamical modeling can be affected by varying data processing parameters regarding model fitting approaches, which can reveal relationships between simulated data and objective functions connected with research questions.

In study 3, we reported that optimal model parameter points were distributed in different areas on the applied parameter space when we introduced a new model fitting approach compared to the model fitting that we used in studies 1 and 2. The new model fitting searches for optimal model parameter values corresponding to the maximal difference between healthy subjects and patients with Parkinson's disease. In addition to the different distributions of optimal model parameter points, we found that using different parcellation schemes for whole-brain dynamical modeling affects the distributions. With this, we showed that the simulated result derived by the new model fitting leads to a better performance for patient classification. At the same time, we also reported that the data processing parameters impact the classification performance. Thus, we addressed that whole-brain dynamical modeling can exhibit different simulated results via varying model fitting approaches with different objective functions. Furthermore, we illustrated how simulated results can be utilized by varying data processing parameters.

5.3 Personalized whole-brain modeling

In the previous sections, we discussed the impact of data processing on whole-brain modeling. An intriguing point we have observed is that varying data processing parameters did not induce the same inter-subject changes of simulated results in whole-brain dynamical modeling. In other words, introducing data processing parameter conditions induces different simulated results across subjects (inter-subject variability). Therefore, we can consider individualized optimal data processing configurations, which give the best model fitting values for each subject. The optimal data processing configuration, here, can be a personalized data processing for whole-brain dynamical modeling. In this section, we discuss the impact of data processing on inter-individual variability of model fitting as personalized modeling and show an example of clinical applications.

In study 1, we reported the impact of varying WBT density on whole-brain modeling. We found that subjects can be stratified via the following three criteria from data processing and model fitting, and subsequently, the major subgroups throughout the stratification showed different simulation results. First, the relationship between graph-theoretical network properties of structural connectome in varied WBT densities allows us to split subjects into two groups that are showing positive or negative correlations with the maximal GoF values. Second, we split subjects into two groups based on the optimal delay profiles across WBT density conditions. Third, we also split subjects into two groups that are showing positive or negative slopes of maximal GoF values across WBT density conditions. With these criteria, we demonstrated that the three steps with regard to the criteria for whole-brain dynamical modeling can involve the impact of data processing in subject-specific manners.

In study 2, we also discussed inter-subject variability through varied parcellation schemes based on relationships between maximal GoF values and empirical data variables. Furthermore, the multiple linear regression showed that the empirical data variables are correlated with the maximal GoF values of individuals. Although the results of the multiple linear regression of empirical data variables estimated the maximal GoF values, in contrast, the contribution of the empirical data variables was various in the results of each parcellation scheme. These results clearly showed that choosing a parcellation scheme is crucial for inter-subject variability.

As a clinical application, in study 3, we varied functional data processing (different temporal filters for empirical and simulated BOLD signals) with two parcellation schemes. With this, we investigated the impact of the functional data processing on whole-brain dynamical modeling

for patient classification of Parkinson's disease. We examined classification performances derived from the considered data processing conditions and showed that the performances differed across the data processing conditions, *i.e.*, temporal filtering and parcellation scheme conditions. Furthermore, we suggested that the low-frequency bandpass filtering with multiple parcellation schemes could be an advisable conditional configuration of whole-brain dynamical modeling for classification of patients with Parkinson's disease. Therefore, we assert that data processing should be optimally configured for a better performance because data processing impacts inter-subject variability, which induces different prediction performances.

5.4 Utilizing model fitting approaches for further analysis

Whole-brain simulation results in different dynamics across model parameters. In particular, we observed that some ranges in a free parameter space depict apparent changes of model fitting results when model parameters vary. Usually, one model fitting searches for the optimal model parameter point in the parameter space as a single point. For instance, the neuroimaging model fitting searches for the optimal parameters corresponding to the maximal GoF value, *i.e.*, the maximal similarity between empirical and simulated connectomes. This is a well-established model fitting in the literature (Deco et al., 2015; Honey et al., 2009; Naskar et al., 2021). However, whole-brain dynamical models with non-optimal model parameter points can also reveal additional traits with different model fitting approaches for answering research questions. For instance, when we use different objectives for whole-brain model fitting, it can show different model parameter values as optimal ones. In studies 1 and 2, we have already shown that different model fitting methods, *i.e.*, similarity between empirical FC and simulated FC and similarity between empirical SC and simulated FC, have different distributions of optimal model parameters. Based on the subject-stratification results using the two neuroimaging model fitting approaches in study 1, we suggested that applying multiple model-fitting methods can be possible metrics to utilize whole-brain dynamical modeling. This way can also contribute to a better understanding of whole-brain model fitting for personalized modeling. In other words, we can utilize model fitting approaches for further analysis.

In study 3, we used the neuroimaging model fitting methods for the maximal correspondence between empirical and simulated data. In addition, we introduced a novel model fitting approach, termed behavioral model fitting, which searches for the optimal model parameter points corresponding to the maximal group difference between healthy subjects and patients with Parkinson's disease. Through this, we again explored the parameter space and found optimal points corresponding to the connectome relationships, which effectively answer the

research question that we had, *i.e.*, which model (parameter points) can show the largest effect size for the group difference between healthy subjects and patients. As reported in study 3, we found two hotspots of densely located optimal model parameters, where either neuroimaging or behavioral model fitting is the most effective, although these hotspots did not coincide. Therefore, we suggested that applying a proper model fitting approach allows us to find the optimal parameters of whole-brain models for answering research questions. Consequently, we used simulation data derived by whole-brain models with the optimal parameters to improve the classification of patients with Parkinson's disease.

The concept of the behavioral model fitting has a great potential for further applications. For example, demographical or phenotypical properties can be used for this method, such as age, sex, or group difference of cohorts. Of course, cognitive or clinical measures such as the Montreal cognitive assessment, Mattis dementia rating scales, the unified Parkinson's disease rating scales are also applicable to search for the optimal model parameter points corresponding to the strongest relationship with simulated results. The suggested concept of the model fitting approach is similar to the brain mapping of various behavioral or phenotypical measures on the cortical surfaces (Glasser et al., 2016; Huth et al., 2016; Raichle, 2009) and can thus be generalized. Consequently, we can map the parameter space using cognitive or clinical scores, which can be referred to as phenotypical mapping on the model parameter space like the behavioral model fitting of the group difference that we scrutinized in study 3.

5.5 Conclusion

The thesis aims to disclose the impact of data processing on whole-brain dynamical modeling. Due to the lack of ground truth of the human brain, neuroimaging studies of MRI have been using a pipeline with study-specific data processing parameters for a given research question or those from the literature, which has no consensus among studies. Therefore, I proposed the study workflow of an MRI processing pipeline which is able to fully control data processing parameters that can influence the empirical whole-brain connectome. With this, the hypothesis here is that varying data processing parameters impact whole-brain dynamical modeling. In this project, I verified the hypothesis by showing that conditional data processing with varied parameter values impacts the results of whole-brain dynamical modeling. Accordingly, the three performed simulation experiments in this dissertation delineate the proof of the concepts of this assertion.

The three studies in the dissertation focused on experimental conditions including structural data processing, functional data processing, and model fitting approach. Furthermore, the effects of these conditions can also intermingle because they are not independent but implanted in the pipeline. In other words, to generalize the impact of data processing on the whole-brain dynamical modeling, we should consider configurations of the conditions, which cover all possible cases for data-driven approaches. At the same time, empirical and simulated results across experimental conditions can differ. Moreover, the simulated results showed inconsistent relationships via different model fitting approaches. For instance, GoF values or effect sizes of group differences showed different landscapes across data processing conditions, such as the varied WBT densities, temporal filters for BOLD signals, and brain parcellation schemes.

We can further infer that the data-driven approach provides subject-specific features across data processing conditions and individual subjects, which implies inter-individual variability via the whole-brain dynamical modeling. If we use the same data processing parameters for the entire cohort of subjects, the optimal model parameter points can be found by a model fitting. Then, the optimal model parameters can represent subject-specific variability. Furthermore, by using different (or optimal) data processing configurations doing likewise in this project, we can also enhance the subject-specific variability. Therefore, optimizing data processing parameters also means that inter-individual variability goes to personalized whole-brain modeling. In other words, to have the best fitting, each subject might need a subject-specific data processing as a personalized pipeline. Hence, we can apply this attribute for subject stratification or subject classification, as we showed in the published studies. Remarkably, the impacts of data processing evidently differed across parcellation conditions. Thus, we should always consider the impact of parcellation schemes that can make the inter-individual variability more complicated. It does not mean that we need the best brain parcellation scheme, but we can optimize a way of using parcellation schemes. For instance, we demonstrated in study 3 that using multiple parcellation schemes provides complementing features of inter-individual variability from each parcellation scheme.

Exploring a free parameter space for whole-brain dynamical modeling can provide a potential way to answer research questions via using phenotypic or cognitive measures for model fitting. Utilizing model fitting also allows us to investigate latent entities of whole-brain models via model fitting with varying hidden model parameters. Then, we can delineate relationships between the optimal hidden parameters and results of model fitting, which can be applied to any kind of measures. Besides, the free parameter space has unlimited sizes. Thus, we should

apply a systematic approach for whole-brain dynamical modeling. With varied data processing and their impacts on the simulation results, this dissertation outlines the systematic data-driven approach for whole-brain dynamical modeling. Conclusively, we can contribute to a better understanding of the human brain and develop an advanced model for further applications.

6 Reference list

Amunts, K., Mohlberg, H., Bludau, S., Zilles, K., 2020. Julich-Brain: A 3D probabilistic atlas of the human brain's cytoarchitecture. Science 369, 988-992.

An, S., Fousek, J., Kiss, Z.H.T., Cortese, F., van der Wijk, G., McAusland, L.B., Ramasubbu, R., Jirsa, V.K., Protzner, A.B., 2022. High-resolution virtual brain modeling personalizes deep brain stimulation for treatment-resistant depression: Spatiotemporal response characteristics following stimulation of neural fiber pathways. Neuroimage 249, 118848.

Ashburner, J., Friston, K.J., 2000. Voxel-based morphometry--the methods. Neuroimage 11, 805-821.

Bajada, C.J., Schreiber, J., Caspers, S., 2019. Fiber length profiling: A novel approach to structural brain organization. Neuroimage 186, 164-173.

Bansal, K., Nakuci, J., Muldoon, S.F., 2018. Personalized brain network models for assessing structure-function relationships. Curr Opin Neurobiol 52, 42-47.

Baria, A.T., Baliki, M.N., Parrish, T., Apkarian, A.V., 2011. Anatomical and functional assemblies of brain BOLD oscillations. J Neurosci 31, 7910-7919.

Bernal-Casas, D., Lee, H.J., Weitz, A.J., Lee, J.H., 2017. Studying Brain Circuit Function with Dynamic Causal Modeling for Optogenetic fMRI. Neuron 93, 522-532 e525.

Botvinik-Nezer, R., Holzmeister, F., Camerer, C.F., Dreber, A., Huber, J., Johannesson, M., Kirchler, M., Iwanir, R., Mumford, J.A., Adcock, R.A., Avesani, P., Baczkowski, B.M., Bajracharya, A., Bakst, L., Ball, S., Barilari, M., Bault, N., Beaton, D., Beitner, J., Benoit, R.G., Berkers, R., Bhanji, J.P., Biswal, B.B., Bobadilla-Suarez, S., Bortolini, T., Bottenhorn, K.L., Bowring, A., Braem, S., Brooks, H.R., Brudner, E.G., Calderon, C.B., Camilleri, J.A., Castrellon, J.J., Cecchetti, L., Cieslik, E.C., Cole, Z.J., Collignon, O., Cox, R.W., Cunningham, W.A., Czoschke, S., Dadi, K., Davis, C.P., Luca, A., Delgado, M.R., Demetriou, L., Dennison, J.B., Di, X., Dickie, E.W., Dobryakova, E., Donnat, C.L., Dukart, J., Duncan, N.W., Durnez, J., Eed, A., Eickhoff, S.B., Erhart, A., Fontanesi, L., Fricke, G.M., Fu, S., Galvan, A., Gau, R., Genon, S., Glatard, T., Glerean, E., Goeman, J.J., Golowin, S.A.E., Gonzalez-Garcia, C., Gorgolewski, K.J., Grady, C.L., Green, M.A., Guassi Moreira, J.F., Guest, O., Hakimi, S., Hamilton, J.P., Hancock, R., Handjaras, G., Harry, B.B., Hawco, C., Herholz, P., Herman, G., Heunis, S., Hoffstaedter, F., Hogeveen, J., Holmes, S., Hu, C.P., Huettel, S.A., Hughes, M.E., Iacovella, V., Iordan, A.D., Isager, P.M., Isik, A.I., Jahn, A., Johnson, M.R., Johnstone, T., Joseph, M.J.E., Juliano, A.C., Kable, J.W., Kassinopoulos, M., Koba, C., Kong, X.Z., Koscik, T.R., Kucukboyaci, N.E., Kuhl, B.A., Kupek, S., Laird, A.R., Lamm, C., Langner, R., Lauharatanahirun, N., Lee, H., Lee, S., Leemans, A., Leo, A., Lesage, E., Li, F., Li, M.Y.C., Lim, P.C., Lintz, E.N., Liphardt, S.W., Losecaat Vermeer, A.B., Love, B.C., Mack, M.L., Malpica, N., Marins, T., Maumet, C., McDonald, K., McGuire, J.T., Melero, H., Mendez Leal, A.S., Meyer, B., Meyer, K.N., Mihai, G., Mitsis, G.D., Moll, J., Nielson, D.M., Nilsonne, G., Notter, M.P., Olivetti, E., Onicas, A.I., Papale, P., Patil, K.R., Peelle, J.E., Perez, A., Pischedda, D., Poline, J.B., Prystauka, Y., Ray, S., Reuter-Lorenz, P.A., Reynolds, R.C., Ricciardi, E., Rieck, J.R., Rodriguez-Thompson, A.M., Romyn, A., Salo, T., Samanez-Larkin, G.R., Sanz-Morales, E., Schlichting, M.L., Schultz, D.H., Shen, Q., Sheridan, M.A., Silvers, J.A., Skagerlund, K., Smith, A., Smith, D.V., Sokol-Hessner, P., Steinkamp, S.R., Tashjian, S.M., Thirion, B., Thorp, J.N., Tinghog, G., Tisdall, L., Tompson, S.H., Toro-Serey, C., Torre Tresols, J.J., Tozzi, L., Truong, V., Turella, L., van 't Veer, A.E., Verguts, T., Vettel, J.M.,

Vijayarajah, S., Vo, K., Wall, M.B., Weeda, W.D., Weis, S., White, D.J., Wisniewski, D., Xifra-Porxas, A., Yearling, E.A., Yoon, S., Yuan, R., Yuen, K.S.L., Zhang, L., Zhang, X., Zosky, J.E., Nichols, T.E., Poldrack, R.A., Schonberg, T., 2020. Variability in the analysis of a single neuroimaging dataset by many teams. Nature 582, 84-88.

Boubela, R.N., Kalcher, K., Huf, W., Kronnerwetter, C., Filzmoser, P., Moser, E., 2013. Beyond Noise: Using Temporal ICA to Extract Meaningful Information from High-Frequency fMRI Signal Fluctuations during Rest. Front Hum Neurosci 7, 168.

Breakspear, M., Heitmann, S., Daffertshofer, A., 2010. Generative models of cortical oscillations: neurobiological implications of the kuramoto model. Front Hum Neurosci 4, 190.

Breakspear, M., Terry, J., Friston, K., 2003. Modulation of excitatory synaptic coupling facilitates synchronization and complex dynamics in a biophysical model of neuronal dynamics. Network: Computation in Neural Systems 14, 703-732.

Brodmann, K., 1909. Vergleichende Lokalisationslehre der Grosshirnrinde in ihren Prinzipien dargestellt auf Grund des Zellenbaues. Barth.

Buxton, R.B., Uludag, K., Dubowitz, D.J., Liu, T.T., 2004. Modeling the hemodynamic response to brain activation. Neuroimage 23 Suppl 1, S220-233.

Buxton, R.B., Wong, E.C., Frank, L.R., 1998. Dynamics of blood flow and oxygenation changes during brain activation: the balloon model. Magn Reson Med 39, 855-864.

Buzsaki, G., 2006. Rhythms of the Brain. Oxford University Press.

Caballero-Gaudes, C., Reynolds, R.C., 2017. Methods for cleaning the BOLD fMRI signal. Neuroimage 154, 128-149.

Cabral, J., Hugues, E., Kringelbach, M.L., Deco, G., 2012. Modeling the outcome of structural disconnection on resting-state functional connectivity. Neuroimage 62, 1342-1353.

Cabral, J., Hugues, E., Sporns, O., Deco, G., 2011. Role of local network oscillations in resting-state functional connectivity. Neuroimage 57, 130-139.

Caminiti, R., Carducci, F., Piervincenzi, C., Battaglia-Mayer, A., Confalone, G., Visco-Comandini, F., Pantano, P., Innocenti, G.M., 2013. Diameter, length, speed, and conduction delay of callosal axons in macaque monkeys and humans: comparing data from histology and magnetic resonance imaging diffusion tractography. J Neurosci 33, 14501-14511.

Craddock, R.C., James, G.A., Holtzheimer, P.E., 3rd, Hu, X.P., Mayberg, H.S., 2012. A whole brain fMRI atlas generated via spatially constrained spectral clustering. Hum Brain Mapp 33, 1914-1928.

Deco, G., Cruzat, J., Cabral, J., Tagliazucchi, E., Laufs, H., Logothetis, N.K., Kringelbach, M.L., 2019. Awakening: Predicting external stimulation to force transitions between different brain states. Proc Natl Acad Sci U S A 116, 18088-18097.

Deco, G., McIntosh, A.R., Shen, K., Hutchison, R.M., Menon, R.S., Everling, S., Hagmann, P., Jirsa, V.K., 2014. Identification of optimal structural connectivity using functional connectivity and neural modeling. J Neurosci 34, 7910-7916.

Deco, G., Ponce-Alvarez, A., Mantini, D., Romani, G.L., Hagmann, P., Corbetta, M., 2013. Resting-state functional connectivity emerges from structurally and dynamically shaped slow linear fluctuations. J Neurosci 33, 11239-11252.

Deco, G., Tononi, G., Boly, M., Kringelbach, M.L., 2015. Rethinking segregation and integration: contributions of whole-brain modelling. Nat Rev Neurosci 16, 430-439.

Desikan, R.S., Segonne, F., Fischl, B., Quinn, B.T., Dickerson, B.C., Blacker, D., Buckner, R.L., Dale, A.M., Maguire, R.P., Hyman, B.T., Albert, M.S., Killiany, R.J., 2006. An automated labeling system for subdividing the human cerebral cortex on MRI scans into gyral based regions of interest. Neuroimage 31, 968-980.

Destrieux, C., Fischl, B., Dale, A., Halgren, E., 2010. Automatic parcellation of human cortical gyri and sulci using standard anatomical nomenclature. Neuroimage 53, 1-15.

Domhof, J.W.M., Jung, K., Eickhoff, S.B., Popovych, O.V., 2021. Parcellation-induced variation of empirical and simulated brain connectomes at group and subject levels. Netw Neurosci 5, 798-830.

Eickhoff, S.B., Yeo, B.T.T., Genon, S., 2018. Imaging-based parcellations of the human brain. Nat Rev Neurosci 19, 672-686.

Endo, H., Hiroe, N., Yamashita, O., 2019. Evaluation of Resting Spatio-Temporal Dynamics of a Neural Mass Model Using Resting fMRI Connectivity and EEG Microstates. Front Comput Neurosci 13, 91.

Esteban, O., Markiewicz, C.J., Blair, R.W., Moodie, C.A., Isik, A.I., Erramuzpe, A., Kent, J.D., Goncalves, M., DuPre, E., Snyder, M., Oya, H., Ghosh, S.S., Wright, J., Durnez, J., Poldrack, R.A., Gorgolewski, K.J., 2019. fMRIPrep: a robust preprocessing pipeline for functional MRI. Nat Methods 16, 111-116.

Fischl, B., Salat, D.H., Busa, E., Albert, M., Dieterich, M., Haselgrove, C., van der Kouwe, A., Killiany, R., Kennedy, D., Klaveness, S., Montillo, A., Makris, N., Rosen, B., Dale, A.M., 2002. Whole brain segmentation: automated labeling of neuroanatomical structures in the human brain. Neuron 33, 341-355.

Fischl, B., van der Kouwe, A., Destrieux, C., Halgren, E., Segonne, F., Salat, D.H., Busa, E., Seidman, L.J., Goldstein, J., Kennedy, D., Caviness, V., Makris, N., Rosen, B., Dale, A.M., 2004. Automatically parcellating the human cerebral cortex. Cereb Cortex 14, 11-22.

Fitzhugh, R., 1961. Impulses and Physiological States in Theoretical Models of Nerve Membrane. Biophys J 1, 445-466.

Frackowiak, R., Markram, H., 2015. The future of human cerebral cartography: a novel approach. Philos Trans R Soc Lond B Biol Sci 370.

Friston, K.J., Harrison, L., Penny, W., 2003. Dynamic causal modelling. Neuroimage 19, 1273-1302.

Friston, K.J., Josephs, O., Zarahn, E., Holmes, A.P., Rouquette, S., Poline, J., 2000. To smooth or not to smooth? Bias and efficiency in fMRI time-series analysis. Neuroimage 12, 196-208.

Girard, G., Caminiti, R., Battaglia-Mayer, A., St-Onge, E., Ambrosen, K.S., Eskildsen, S.F., Krug, K., Dyrby, T.B., Descoteaux, M., Thiran, J.P., Innocenti, G.M., 2020. On the cortical connectivity in the macaque brain: A comparison of diffusion tractography and histological tracing data. Neuroimage 221, 117201.

Glasser, M.F., Coalson, T.S., Robinson, E.C., Hacker, C.D., Harwell, J., Yacoub, E., Ugurbil, K., Andersson, J., Beckmann, C.F., Jenkinson, M., Smith, S.M., Van Essen, D.C., 2016. A multi-modal parcellation of human cerebral cortex. Nature 536, 171-178.

Gupta, K., Sekhar, N., Vigneault, D.M., Scott, A.R., Colvert, B., Craine, A., Raghavan, A., Contijoch, F.J., 2021. Octree Representation Improves Data Fidelity of Cardiac CT Images and Convolutional Neural Network Semantic Segmentation of Left Atrial and Ventricular Chambers. Radiol Artif Intell 3, e210036.

Hagmann, P., Cammoun, L., Gigandet, X., Meuli, R., Honey, C.J., Wedeen, V.J., Sporns, O., 2008. Mapping the structural core of human cerebral cortex. PLoS Biol 6, e159.

Havlicek, M., Roebroeck, A., Friston, K., Gardumi, A., Ivanov, D., Uludag, K., 2015. Physiologically informed dynamic causal modeling of fMRI data. Neuroimage 122, 355-372.

Havlicek, M., Uludag, K., 2020. A dynamical model of the laminar BOLD response. Neuroimage 204, 116209.

Herculano-Houzel, S., 2012. The remarkable, yet not extraordinary, human brain as a scaled-up primate brain and its associated cost. Proc Natl Acad Sci U S A 109 Suppl 1, 10661-10668.

Hodgkin, A.L., Huxley, A.F., 1952. A quantitative description of membrane current and its application to conduction and excitation in nerve. J Physiol 117, 500-544.

Honey, C.J., Sporns, O., Cammoun, L., Gigandet, X., Thiran, J.P., Meuli, R., Hagmann, P., 2009. Predicting human resting-state functional connectivity from structural connectivity. Proc Natl Acad Sci U S A 106, 2035-2040.

Hou, Y., Wu, X., Hallett, M., Chan, P., Wu, T., 2014. Frequency-dependent neural activity in Parkinson's disease. Hum Brain Mapp 35, 5815-5833.

Hubel, D.H., Wiesel, T.N., 1962. Receptive fields, binocular interaction and functional architecture in the cat's visual cortex. J Physiol 160, 106-154.

Huth, A.G., de Heer, W.A., Griffiths, T.L., Theunissen, F.E., Gallant, J.L., 2016. Natural speech reveals the semantic maps that tile human cerebral cortex. Nature 532, 453-458.

Jansen, B.H., Rit, V.G., 1995. Electroencephalogram and visual evoked potential generation in a mathematical model of coupled cortical columns. Biol Cybern 73, 357-366.

Jirsa, V.K., Proix, T., Perdikis, D., Woodman, M.M., Wang, H., Gonzalez-Martinez, J., Bernard, C., Benar, C., Guye, M., Chauvel, P., Bartolomei, F., 2017. The Virtual Epileptic Patient: Individualized whole-brain models of epilepsy spread. Neuroimage 145, 377-388.

Jones, R., Maffei, C., Augustinack, J., Fischl, B., Wang, H., Bilgic, B., Yendiki, A., 2021. High-fidelity approximation of grid- and shell-based sampling schemes from undersampled DSI using compressed sensing: Post mortem validation. Neuroimage 244, 118621.

Jung, K., Kang, J., Chung, S., Park, H.J., 2019. Dynamic causal modeling for calcium imaging: Exploration of differential effective connectivity for sensory processing in a barrel cortical column. Neuroimage 201, 116008.

Keller, P.J., Ahrens, M.B., 2015. Visualizing whole-brain activity and development at the single-cell level using light-sheet microscopy. Neuron 85, 462-483.

Knutson, B., Westdorp, A., Kaiser, E., Hommer, D., 2000. FMRI visualization of brain activity during a monetary incentive delay task. Neuroimage 12, 20-27.

Kriegeskorte, N., Douglas, P.K., 2018. Cognitive computational neuroscience. Nat Neurosci 21, 1148-1160.

Kuramoto, Y., 1984. Chemical Oscillations, Waves, and Turbulence.

Kuruvilla, A., Flink, R., 2003. Intraoperative electrocorticography in epilepsy surgery: useful or not? Seizure 12, 577-584.

Kuznetsov, Y.A., Kuznetsov, I.A., Kuznetsov, Y., 1998. Elements of applied bifurcation theory. Springer.

Le Bihan, D., Mangin, J.F., Poupon, C., Clark, C.A., Pappata, S., Molko, N., Chabriat, H., 2001. Diffusion tensor imaging: concepts and applications. J Magn Reson Imaging 13, 534-546.

Lee, H., Jung, K., Kang, D.W., Kim, N., 2020. Fully Automated and Real-Time Volumetric Measurement of Infarct Core and Penumbra in Diffusion- and Perfusion-Weighted MRI of Patients with Hyper-Acute Stroke. J Digit Imaging 33, 262-272.

Lindquist, M., 2020. Neuroimaging results altered by varying analysis pipelines. Nature.

Logothetis, N.K., Pauls, J., Augath, M., Trinath, T., Oeltermann, A., 2001. Neurophysiological investigation of the basis of the fMRI signal. Nature 412, 150-157.

Lopes da Silva, F.H., Hoeks, A., Smits, H., Zetterberg, L.H., 1974. Model of brain rhythmic activity. The alpha-rhythm of the thalamus. Kybernetik 15, 27-37.

Maffei, C., Girard, G., Schilling, K.G., Aydogan, D.B., Adluru, N., Zhylka, A., Wu, Y., Mancini, M., Hamamci, A., Sarica, A., Teillac, A., Baete, S.H., Karimi, D., Yeh, F.C., Yildiz, M.E., Gholipour, A., Bihan-Poudec, Y., Hiba, B., Quattrone, A., Quattrone, A., Boshkovski, T., Stikov, N., Yap, P.T., de Luca, A., Pluim, J., Leemans, A., Prabhakaran, V., Bendlin, B.B.,

Alexander, A.L., Landman, B.A., Canales-Rodriguez, E.J., Barakovic, M., Rafael-Patino, J., Yu, T., Rensonnet, G., Schiavi, S., Daducci, A., Pizzolato, M., Fischi-Gomez, E., Thiran, J.P., Dai, G., Grisot, G., Lazovski, N., Puch, S., Ramos, M., Rodrigues, P., Prckovska, V., Jones, R., Lehman, J., Haber, S.N., Yendiki, A., 2022. Insights from the IronTract challenge: Optimal methods for mapping brain pathways from multi-shell diffusion MRI. Neuroimage 257, 119327.

Maier-Hein, K.H., Neher, P.F., Houde, J.C., Cote, M.A., Garyfallidis, E., Zhong, J., Chamberland, M., Yeh, F.C., Lin, Y.C., Ji, Q., Reddick, W.E., Glass, J.O., Chen, D.Q., Feng, Y., Gao, C., Wu, Y., Ma, J., He, R., Li, Q., Westin, C.F., Deslauriers-Gauthier, S., Gonzalez, J.O.O., Paquette, M., St-Jean, S., Girard, G., Rheault, F., Sidhu, J., Tax, C.M.W., Guo, F., Mesri, H.Y., David, S., Froeling, M., Heemskerk, A.M., Leemans, A., Bore, A., Pinsard, B., Bedetti, C., Desrosiers, M., Brambati, S., Doyon, J., Sarica, A., Vasta, R., Cerasa, A., Quattrone, A., Yeatman, J., Khan, A.R., Hodges, W., Alexander, S., Romascano, D., Barakovic, M., Auria, A., Esteban, O., Lemkaddem, A., Thiran, J.P., Cetingul, H.E., Odry, B.L., Mailhe, B., Nadar, M.S., Pizzagalli, F., Prasad, G., Villalon-Reina, J.E., Galvis, J., Thompson, P.M., Requejo, F.S., Laguna, P.L., Lacerda, L.M., Barrett, R., Dell'Acqua, F., Catani, M., Petit, L., Caruyer, E., Daducci, A., Dyrby, T.B., Holland-Letz, T., Hilgetag, C.C., Stieltjes, B., Descoteaux, M., 2017. The challenge of mapping the human connectome based on diffusion tractography. Nat Commun 8, 1349.

Maldonado, P.E., Godecke, I., Gray, C.M., Bonhoeffer, T., 1997. Orientation selectivity in pinwheel centers in cat striate cortex. Science 276, 1551-1555.

Markram, H., Muller, E., Ramaswamy, S., Reimann, M.W., Abdellah, M., Sanchez, C.A., Ailamaki, A., Alonso-Nanclares, L., Antille, N., Arsever, S., Kahou, G.A., Berger, T.K., Bilgili, A., Buncic, N., Chalimourda, A., Chindemi, G., Courcol, J.D., Delalondre, F., Delattre, V., Druckmann, S., Dumusc, R., Dynes, J., Eilemann, S., Gal, E., Gevaert, M.E., Ghobril, J.P., Gidon, A., Graham, J.W., Gupta, A., Haenel, V., Hay, E., Heinis, T., Hernando, J.B., Hines, M., Kanari, L., Keller, D., Kenyon, J., Khazen, G., Kim, Y., King, J.G., Kisvarday, Z., Kumbhar, P., Lasserre, S., Le Be, J.V., Magalhaes, B.R., Merchan-Perez, A., Meystre, J., Morrice, B.R., Muller, J., Munoz-Cespedes, A., Muralidhar, S., Muthurasa, K., Nachbaur, D., Newton, T.H., Nolte, M., Ovcharenko, A., Palacios, J., Pastor, L., Perin, R., Ranjan, R., Riachi, I., Rodriguez, J.R., Riquelme, J.L., Rossert, C., Sfyrakis, K., Shi, Y., Shillcock, J.C., Silberberg, G., Silva, R., Tauheed, F., Telefont, M., Toledo-Rodriguez, M., Trankler, T., Van Geit, W., Diaz, J.V., Walker, R., Wang, Y., Zaninetta, S.M., DeFelipe, J., Hill, S.L., Segev, I., Schurmann, F., 2015. Reconstruction and Simulation of Neocortical Microcircuitry. Cell 163, 456-492.

Messe, A., 2020. Parcellation influence on the connectivity-based structure-function relationship in the human brain. Hum Brain Mapp 41, 1167-1180.

Moran, R., Pinotsis, D.A., Friston, K., 2013. Neural masses and fields in dynamic causal modeling. Front Comput Neurosci 7, 57.

Mori, S., Zhang, J., 2006. Principles of diffusion tensor imaging and its applications to basic neuroscience research. Neuron 51, 527-539.

Mountcastle, V.B., 1997. The columnar organization of the neocortex. Brain 120 (Pt 4), 701-722.

Nagumo, J., Arimoto, S., Yoshizawa, S., 1962. An Active Pulse Transmission Line Simulating Nerve Axon. Proceedings of the IRE 50, 2061-2070.

Naskar, A., Vattikonda, A., Deco, G., Roy, D., Banerjee, A., 2021. Multiscale dynamic mean field (MDMF) model relates resting-state brain dynamics with local cortical excitatory-inhibitory neurotransmitter homeostasis. Netw Neurosci 5, 757-782.

Neumann-Haefelin, T., Wittsack, H.J., Wenserski, F., Siebler, M., Seitz, R.J., Modder, U., Freund, H.J., 1999. Diffusion- and perfusion-weighted MRI. The DWI/PWI mismatch region in acute stroke. Stroke 30, 1591-1597.

Niedworok, C.J., Brown, A.P., Jorge Cardoso, M., Osten, P., Ourselin, S., Modat, M., Margrie, T.W., 2016. aMAP is a validated pipeline for registration and segmentation of high-resolution mouse brain data. Nat Commun 7, 11879.

Ogawa, S., Tank, D.W., Menon, R., Ellermann, J.M., Kim, S.G., Merkle, H., Ugurbil, K., 1992. Intrinsic signal changes accompanying sensory stimulation: functional brain mapping with magnetic resonance imaging. Proc Natl Acad Sci U S A 89, 5951-5955.

Owen, J.P., Li, Y.O., Ziv, E., Strominger, Z., Gold, J., Bukhpun, P., Wakahiro, M., Friedman, E.J., Sherr, E.H., Mukherjee, P., 2013. The structural connectome of the human brain in agenesis of the corpus callosum. Neuroimage 70, 340-355.

Park, H.J., Friston, K., 2013. Structural and functional brain networks: from connections to cognition. Science 342, 1238411.

Parkes, L., Fulcher, B., Yucel, M., Fornito, A., 2018. An evaluation of the efficacy, reliability, and sensitivity of motion correction strategies for resting-state functional MRI. Neuroimage 171, 415-436.

Penny, W.D., Friston, K.J., Ashburner, J.T., Kiebel, S.J., Nichols, T.E., 2011. Statistical parametric mapping: the analysis of functional brain images. Elsevier.

Pijnenburg, R., Scholtens, L.H., Ardesch, D.J., de Lange, S.C., Wei, Y., van den Heuvel, M.P., 2021. Myelo- and cytoarchitectonic microstructural and functional human cortical atlases reconstructed in common MRI space. Neuroimage 239, 118274.

Polimeni, J.R., Lewis, L.D., 2021. Imaging faster neural dynamics with fast fMRI: A need for updated models of the hemodynamic response. Prog Neurobiol 207, 102174.

Ponce-Alvarez, A., Deco, G., Hagmann, P., Romani, G.L., Mantini, D., Corbetta, M., 2015. Resting-state temporal synchronization networks emerge from connectivity topology and heterogeneity. PLoS Comput Biol 11, e1004100.

Popovych, O.V., Manos, T., Hoffstaedter, F., Eickhoff, S.B., 2019. What Can Computational Models Contribute to Neuroimaging Data Analytics? Front Syst Neurosci 12, 68.

Prasad, G., Nir, T.M., Toga, A.W., Thompson, P.M., 2013. Tractography Density and Network Measures in Alzheimer's Disease. Proc IEEE Int Symp Biomed Imaging 2013, 692-695.

Proix, T., Spiegler, A., Schirner, M., Rothmeier, S., Ritter, P., Jirsa, V.K., 2016. How do parcellation size and short-range connectivity affect dynamics in large-scale brain network models? Neuroimage 142, 135-149.

Raichle, M.E., 2009. A brief history of human brain mapping. Trends Neurosci 32, 118-126.

Roberts, J.A., Gollo, L.L., Abeysuriya, R.G., Roberts, G., Mitchell, P.B., Woolrich, M.W., Breakspear, M., 2019. Metastable brain waves. Nat Commun 10, 1056.

Rodrigues, F.A., Peron, T.K.D.M., Ji, P., Kurths, J., 2016. The Kuramoto model in complex networks. Physics Reports-Review Section of Physics Letters 610, 1-98.

Rosch, R.E., Hunter, P.R., Baldeweg, T., Friston, K.J., Meyer, M.P., 2018. Calcium imaging and dynamic causal modelling reveal brain-wide changes in effective connectivity and synaptic dynamics during epileptic seizures. PLoS Comput Biol 14, e1006375.

Sanz-Leon, P., Knock, S.A., Spiegler, A., Jirsa, V.K., 2015. Mathematical framework for large-scale brain network modeling in The Virtual Brain. Neuroimage 111, 385-430.

Schaefer, A., Kong, R., Gordon, E.M., Laumann, T.O., Zuo, X.N., Holmes, A.J., Eickhoff, S.B., Yeo, B.T.T., 2018. Local-Global Parcellation of the Human Cerebral Cortex from Intrinsic Functional Connectivity MRI. Cereb Cortex 28, 3095-3114.

Schilling, K.G., Nath, V., Hansen, C., Parvathaneni, P., Blaber, J., Gao, Y., Neher, P., Aydogan, D.B., Shi, Y., Ocampo-Pineda, M., Schiavi, S., Daducci, A., Girard, G., Barakovic, M., Rafael-Patino, J., Romascano, D., Rensonnet, G., Pizzolato, M., Bates, A., Fischi, E., Thiran, J.P., Canales-Rodriguez, E.J., Huang, C., Zhu, H., Zhong, L., Cabeen, R., Toga, A.W., Rheault, F.,

Theaud, G., Houde, J.C., Sidhu, J., Chamberland, M., Westin, C.F., Dyrby, T.B., Verma, R., Rathi, Y., Irfanoglu, M.O., Thomas, C., Pierpaoli, C., Descoteaux, M., Anderson, A.W., Landman, B.A., 2019. Limits to anatomical accuracy of diffusion tractography using modern approaches. Neuroimage 185, 1-11.

Schilling, K.G., Rheault, F., Petit, L., Hansen, C.B., Nath, V., Yeh, F.C., Girard, G., Barakovic, M., Rafael-Patino, J., Yu, T., Fischi-Gomez, E., Pizzolato, M., Ocampo-Pineda, M., Schiavi, S., Canales-Rodriguez, E.J., Daducci, A., Granziera, C., Innocenti, G., Thiran, J.P., Mancini, L., Wastling, S., Cocozza, S., Petracca, M., Pontillo, G., Mancini, M., Vos, S.B., Vakharia, V.N., Duncan, J.S., Melero, H., Manzanedo, L., Sanz-Morales, E., Pena-Melian, A., Calamante, F., Attye, A., Cabeen, R.P., Korobova, L., Toga, A.W., Vijayakumari, A.A., Parker, D., Verma, R., Radwan, A., Sunaert, S., Emsell, L., De Luca, A., Leemans, A., Bajada, C.J., Haroon, H., Azadbakht, H., Chamberland, M., Genc, S., Tax, C.M.W., Yeh, P.H., Srikanchana, R., McKnight, C.D., Yang, J.Y., Chen, J., Kelly, C.E., Yeh, C.H., Cochereau, J., Maller, J.J., Welton, T., Almairac, F., Seunarine, K.K., Clark, C.A., Zhang, F., Makris, N., Golby, A., Rathi, Y., O'Donnell, L.J., Xia, Y., Aydogan, D.B., Shi, Y., Fernandes, F.G., Raemaekers, M., Warrington, S., Michielse, S., Ramirez-Manzanares, A., Concha, L., Aranda, R., Meraz, M.R., Lerma-Usabiaga, G., Roitman, L., Fekonja, L.S., Calarco, N., Joseph, M., Nakua, H., Voineskos, A.N., Karan, P., Grenier, G., Legarreta, J.H., Adluru, N., Nair, V.A., Prabhakaran, V., Alexander, A.L., Kamagata, K., Saito, Y., Uchida, W., Andica, C., Abe, M., Bayrak, R.G., Wheeler-Kingshott, C., D'Angelo, E., Palesi, F., Savini, G., Rolandi, N., Guevara, P., Houenou, J., Lopez-Lopez, N., Mangin, J.F., Poupon, C., Roman, C., Vazquez, A., Maffei, C., Arantes, M., Andrade, J.P., Silva, S.M., Calhoun, V.D., Caverzasi, E., Sacco, S., Lauricella, M., Pestilli, F., Bullock, D., Zhan, Y., Brignoni-Perez, E., Lebel, C., Reynolds, J.E., Nestrasil, I., Labounek, R., Lenglet, C., Paulson, A., Aulicka, S., Heilbronner, S.R., Heuer, K., Chandio, B.Q., Guaje, J., Tang, W., Garyfallidis, E., Raja, R., Anderson, A.W., Landman, B.A., Descoteaux, M., 2021. Tractography dissection variability: What happens when 42 groups dissect 14 white matter bundles on the same dataset? Neuroimage 243, 118502.

Schlaug, G., Benfield, A., Baird, A.E., Siewert, B., Lovblad, K.O., Parker, R.A., Edelman, R.R., Warach, S., 1999. The ischemic penumbra: operationally defined by diffusion and perfusion MRI. Neurology 53, 1528-1537.

Scholtens, L.H., de Reus, M.A., de Lange, S.C., Schmidt, R., van den Heuvel, M.P., 2018. An MRI Von Economo - Koskinas atlas. Neuroimage 170, 249-256.

Series, P., Lorenceau, J., Fregnac, Y., 2003. The "silent" surround of V1 receptive fields: theory and experiments. J Physiol Paris 97, 453-474.

Shen, X., Tokoglu, F., Papademetris, X., Constable, R.T., 2013. Groupwise whole-brain parcellation from resting-state fMRI data for network node identification. Neuroimage 82, 403-415.

Soares, J.M., Marques, P., Alves, V., Sousa, N., 2013. A hitchhiker's guide to diffusion tensor imaging. Frontiers in Neuroscience 7.

Spiegler, A., Hansen, E.C., Bernard, C., McIntosh, A.R., Jirsa, V.K., 2016. Selective Activation of Resting-State Networks following Focal Stimulation in a Connectome-Based Network Model of the Human Brain. eNeuro 3.

Spiegler, A., Jirsa, V., 2013. Systematic approximations of neural fields through networks of neural masses in the virtual brain. Neuroimage 83, 704-725.

Sporns, O., 2011. The human connectome: a complex network. Year in Cognitive Neuroscience 1224, 109-125.

Sporns, O., Tononi, G., Kotter, R., 2005. The human connectome: A structural description of the human brain. PLoS Comput Biol 1, e42.

Stehling, M.K., Turner, R., Mansfield, P., 1991. Echo-planar imaging: magnetic resonance imaging in a fraction of a second. Science 254, 43-50.

Stephan, K.E., Weiskopf, N., Drysdale, P.M., Robinson, P.A., Friston, K.J., 2007. Comparing hemodynamic models with DCM. Neuroimage 38, 387-401.

Tournier, J.D., Smith, R., Raffelt, D., Tabbara, R., Dhollander, T., Pietsch, M., Christiaens, D., Jeurissen, B., Yeh, C.H., Connelly, A., 2019. MRtrix3: A fast, flexible and open software framework for medical image processing and visualisation. Neuroimage 202, 116137.

Tzourio-Mazoyer, N., Landeau, B., Papathanassiou, D., Crivello, F., Etard, O., Delcroix, N., Mazoyer, B., Joliot, M., 2002. Automated anatomical labeling of activations in SPM using a macroscopic anatomical parcellation of the MNI MRI single-subject brain. Neuroimage 15, 273-289.

Urchs, S., Armoza, J., Moreau, C., Benhajali, Y., St-Aubin, J., Orban, P., Bellec, P., 2019. MIST: A multi-resolution parcellation of functional brain networks. MNI Open Research 1.

Vergara, V.M., Mayer, A.R., Damaraju, E., Hutchison, K., Calhoun, V.D., 2017. The effect of preprocessing pipelines in subject classification and detection of abnormal resting state functional network connectivity using group ICA. Neuroimage 145, 365-376.

von Economo, C.F., Koskinas, G.N., 1925. Die cytoarchitektonik der hirnrinde des erwachsenen menschen. J. Springer.

Wee, C.Y., Yap, P.T., Denny, K., Browndyke, J.N., Potter, G.G., Welsh-Bohmer, K.A., Wang, L., Shen, D., 2012. Resting-state multi-spectrum functional connectivity networks for identification of MCI patients. Plos One 7, e37828.

Wilson, H.R., Cowan, J.D., 1972. Excitatory and inhibitory interactions in localized populations of model neurons. Biophys J 12, 1-24.

Wong, K.F., Wang, X.J., 2006. A recurrent network mechanism of time integration in perceptual decisions. J Neurosci 26, 1314-1328.

Yeh, C.H., Jones, D.K., Liang, X., Descoteaux, M., Connelly, A., 2021. Mapping Structural Connectivity Using Diffusion MRI: Challenges and Opportunities. J Magn Reson Imaging 53, 1666-1682.

Yendiki, A., Aggarwal, M., Axer, M., Howard, A.F.D., van Walsum, A.V.C., Haber, S.N., 2022. Post mortem mapping of connectional anatomy for the validation of diffusion MRI. Neuroimage, 119146.

Yeung, M.K.S., Strogatz, S.H., 1999. Time Delay in the Kuramoto Model of Coupled Oscillators. Physical Review Letters 82, 648-651.

Zimmermann, J., Perry, A., Breakspear, M., Schirner, M., Sachdev, P., Wen, W., Kochan, N.A., Mapstone, M., Ritter, P., McIntosh, A.R., Solodkin, A., 2018. Differentiation of Alzheimer's disease based on local and global parameters in personalized Virtual Brain models. Neuroimage Clin 19, 240-251.

Zuo, X.N., Di Martino, A., Kelly, C., Shehzad, Z.E., Gee, D.G., Klein, D.F., Castellanos, F.X., Biswal, B.B., Milham, M.P., 2010. The oscillating brain: complex and reliable. Neuroimage 49, 1432-1445.

7 Acknowledgements

I want to thank all the people who supported my research journey in pursuing my life question. Dr. Gyoungho Lee gave me a lot of chances to formulate a goal in academia. After establishing my life question, I have continuously motivated myself and never doubted the direction of the journey. Dr. Choongkil Lee trained me a lot as being a thorough scientist in neuroscience. He supported me when I was not proficient in neuroimaging research.

I learned clinical neuroimaging data processing from Dr. Namkug Kim and researchers and doctors working at Asan Medical Center in South Korea. Dr. Yongjun Chang showed how researchers successfully collaborate with others. Without his scientific paragon, my research experience would be monotonous. Discussions and discourses with Dr. Seunghyun Choi have inspired me to understand the synthetic perspective contemplating the human brain as a bio-mechanical system. I learned scientific discussions with researchers from Dr. Hae-Jeong Park. He showed how we can find current research topics and formulate intriguing questions.

When I arrived in Germany for my Ph.D. program, Dr. Oleksandr V. Popovych heartfully welcomed and helped me. As a doctoral supervisor (I like the German word ‘der Doktorvater’), he advised me a lot and talked about the attitude of scientists and researchers. He sometimes indicated weak points in my progress, but I liked his positive mind toward the difficulties. I also thank Dr. Esther Florin. We discussed workflows and each step of my Ph.D. project, and she gave supervision about my progress.

I really enjoyed the wonderful environment in Forschungszentrum Jülich. Such a place is the best for doing research. Moreover, I want to thank Dr. Simon B. Eickhoff. He gave essential comments and feedback on my studies. Although he had a full of schedule, he showed efficient ways to improve my work. All other colleagues in the institutes in Jülich and Düsseldorf were kind and made a productive research condition. Kevin J. Wischnewski helped me in difficulty of mathematical questions. Justin W. M. Domhof inspired me as doing systematic analysis. In particular, Kevin, Chris, Mehran, and Shammi are close friends, and thanks to them, I enjoyed life in Germany. I also gratefully acknowledge the computing time granted through JARA on the supercomputer JURECA at Forschungszentrum Jülich.

My parents supported me for all educational tracks in South Korea. I will never forget their devotion. Finally, I am very grateful to my wife and son. I should say that my lovely wife and son have always supported me on such a long journey.

Review note